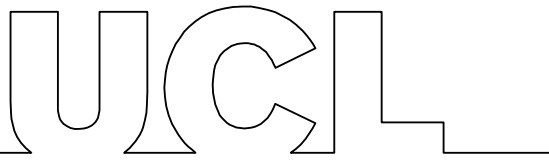

The spectroscopy of bound and predissociating Rydberg states of NO in external electric fields

Nicholas Jones

A thesis submitted for the degree of

Doctor of Philosophy

University College London

September 2008

I, Nicholas Jones, confirm that the work presented in this thesis is my own. Where information has been derived from other sources, I confirm that this has been indicated in the thesis.

- My soul, she cried, I thought you'd died

Amid fumes of formaldehyde

You have been gone for so long

I felt the lapping of an ebbing tide -

Carrion - British Sea Power

Dedicated to Alex and Amy

Abstract

This thesis reports the application of static and ramped electric fields to the Rydberg states of NO. Chapter 1 introduces the history of Rydberg states, their exotic properties, decay mechanisms, and the effect of an applied electric field. Chapter 2 details the experimental set-up used for the experiments presented in this thesis. Chapter 3 describes the structure of NO and multiphoton excitation scheme utilised for the work presented in this thesis.

Chapter 4 investigates the effect of applied DC electric fields in the range 0 – 150 V cm^{-1} on the predissociating Rydberg states of NO below the $v^+ = 0$ ionisation limit, with principal quantum numbers n = 25 – 30. The Stark states are accessed by two-colour, double-resonance excitation *via* the $v' = 0, N' = 0$, 1, 2, and 4 rovibrational states of the $A^2\Sigma^+$ state. The N (^{2}D) atoms produced by predissociation are measured by (2 + 1) resonance-enhanced multiphoton ionization. The zero field and predissociation spectra are analysed using a matrix diagonalisation method. In Chapter 5, initial progress on simulating the spectra is presented. The predissociation spectra are compared with pulsed-field ionization spectra of the bound Rydberg state population providing an almost complete picture of the Rydberg state dynamics.

In Chapter 6, ramped fields of varying slew rates are applied to the bound Rydberg states of NO, and the ionisation time profiles are obtained. The development of the experimental chamber and investigation into sources of electrical noise required to achieve this is discussed. It is shown that the rotational quantum state composition of field-ionised molecules can be controlled by varying the slew rate of the applied electric field.

This thesis is based on the following publications

Chapter 4:

N.J.A. Jones, R.S. Minns, R. Patel and H.H. Fielding,

Observation of the Stark effect in Rydberg states of NO: A comparison between predissociating and bound states

J. Phys. B **41** 185102 (2008)

Chapter 5:

R. Patel, N. J. A. Jones and H. H. Fielding, Observation of the Stark effect in $v^+ = 0$ Rydberg states of NO with a matrix-diagonalization analysis

J. Phys. B **40** 1369-1381 (2007)

Chapter 6:

R. Patel, N.J.A. Jones and H.H. Fielding, Rotation-state selective field ionization of Rydberg states of NO

Phys. Rev. A. **76** 043313 (2007)

Acknowledgements

First, I would like to thank Professor Helen Fielding for giving me the opportunity to work on this research project. I would also like to thank all of those that helped me to reduce that noise; in particular Professor Steve Price for his help and limitless knowledge. The infinite darkness that is the black art of electrical noise reduction would have been a lot murkier without it. The Chemistry workshop at UCL has also been vital to my PhD, especially Jim who deciphered my scribblings and made it into a big metal reality, and Len who used the largest resistor I have ever seen.

My lab partners have born an equal share of the many difficulties and deserve buckets of thanks. Rakhee was vital to most of the bound state work presented in this thesis, and was above all a great friend. Russell's green fingers are legendary and helped me out of a sticky situation by getting something to actually work. Rob's knowledge, understanding and boundless enthusiasm was a source of constant motivation during the early difficulties. I would also like to thank group members past and present for making our group such a fun and friendly place to work: Rob, Liz, Rakhee, Corrine, Toni, Kiera, Abigail, Russell, Adam K, Adam M, Emma, Jadranka and Eva.

I'd like to thank my family for the continuing support, even if they're not exactly sure what it is I actually do; without them none of this would be possible. I'd also like to thank my moustache (and my friends for pretending it was acceptable) for keeping me occupied during the times when I had neither the money nor time to have a real social life. Finally I'd like to thank Alex. Without her it is unlikely I would have ever attempted a PhD, although I don't blame her for that, and without her love and understanding I would not have been able to finish.

List of Contents

List of Figures

List of Tables

1. Introduction

1.1. History of Rydberg States

Atoms excited to high values of principal quantum number n, played an important role in the development of atomic models during the late 19th and early 20th centuries. Early advances in spectroscopic techniques enabled the radiation emitted from excited atoms to be recorded. The observed "line spectra" showed discrete emission lines at specific wavelengths, unique to the species under investigation. In 1885 Balmer produced an empirical formula relating the wavelength, λ, of a series of atomic lines in the emission spectrum of hydrogen to a pair of integers, n and m where $n = 2$ and $m = 3$, 4, 5, and 6 (equation 1.1.1) [1]. This series was later named the Balmer series in honour of his discovery. Further lines predicted by the equation were subsequently discovered.

$$\lambda = \frac{m^2 h}{m^2 - n^2}. \qquad (1.1.1)$$

In 1890, Johannes Rydberg succeeded in producing a general formula, which related the position of the emission lines in wavenumbers, $1/\lambda$, to a pair of integers, n_1 and n_2 where $n_2 > n_1$ [2]. A constant was introduced, R_x, that was dependent on the system under investigation, x, and was initially determined by experimental observations.

$$\frac{1}{\lambda} = R_x\left(\frac{1}{n_1^2} - \frac{1}{n_2^2}\right). \qquad (1.1.2)$$

In 1897, J.J. Thompson discovered the electron by applying electric and magnetic fields to cathode ray tubes [3]. Thompson proposed that the atom was composed of a cloud of positive charge, in which the electrons were suspended. The electrons were free to move in the cloud, and formed orbital rings stabilised by electron interactions. Attempts by Thompson to fit observed spectral lines to the energy difference between orbital rings proved unsuccessful; however, in 1910 A. C. Haas used the model to derive a formula for the Rydberg constant containing only fundamental constants. Haas's paper was rejected after Rutherford's analysis of the 1909 experiments by Geiger and Marsden discounted the Thompson model [4]. Geiger and Marsden had directed a beam of alpha particles onto a thin gold film, and found that a small number were deflected by more than 90° [5]. Rutherford proposed a new planetary model for the atom based on a compact highly positively charged nucleus orbited by small negatively charged electrons. Haas's derivation of R had succeeded despite the inaccuracies of the Thompson model due to the stabilised electron orbitals, which were characterised by a discrete parameter: the radius of the orbital sphere. In 1913, Bohr combined the discrete spheres of rotation with Rutherford's planetary model to fully define R in terms of fundamental constants [6]. Recent advances in the theory of quantum mechanics had found that the quantisation of parameters existed in many systems and that the size of these quanta was related to Planck's constant, h. In his derivation of the Rydberg constant, Bohr quantised the angular momentum of the electron by setting it equal to an integer multiple of the reduced Planck's constant, $\hbar = h/2\pi$.

$$mvr = n\hbar, \tag{1.1.3}$$

where m is the electron mass, v is the velocity of the electron and r is the orbital radius. Next, the electron was assumed to be in a circular orbit in the Coulomb potential of the positive nucleus. Newton's law for uniform circular motion states that

$$F = \frac{ke^2Z}{r^2} = \frac{mv^2}{r} \tag{1.1.4}$$

where $k = 1/4\pi\varepsilon_0$, ε_0 is the permittivity of free space, e is the charge of an electron, and Z is the positive charge of the nucleus. Substituting equation 1.1.3 into 1.1.4 leads to

$$r = \frac{n^2\hbar^2}{ke^2mZ}. \tag{1.1.5}$$

The energy of an electronic state is the sum of the kinetic and potential energy

$$E = \frac{mv^2}{2} - \frac{kZe^2}{r}. \tag{1.1.6}$$

Substituting the value of r from equation 1.1.5 leads to

$$E = \frac{-k^2Z^2e^4m}{2\hbar^2} \times \frac{1}{n^2}. \tag{1.1.7}$$

Therefore, by comparing equation 1.1.2 to ΔE, the energy difference between two states of principal quantum number n_1 and n_2, calculated using equation 1.17 the Rydberg constant can be shown to be

$$R = \frac{k^2Z^2e^4m}{2\hbar^2}. \tag{1.1.8}$$

From the Bohr interpretation, it is clear that the Balmer equation (equation 1.1.1) is a specific example of the more general Rydberg equation (1.1.2) and describes the transition between the n_1 = 2 and the n_2 = 3, 4, 5, and 6 electronic energy levels of hydrogen.

1.2. Scaling Laws

The Bohr model revealed a number of important scaling laws for the classical properties of the electron (table 1.2.1).

	Symbol	Scaling	n = 1	n = 40
Binding energy	$E(n)$	n^{-2}	109 737 cm^{-1}	69 cm^{-1}
Energy Spacing	$\Delta E(n)$	n^{-3}	220 000 cm^{-1}	3 cm^{-1}
Kepler orbital radius	$r(n)$	n^2	53 pm	85 nm
Kepler orbital period	τ_{cl}	n^3	152 as	10 ps

Table 1.2.1: A selection of physical laws for Rydberg systems with values calculated using the Bohr model for two electronic states of atomic hydrogen.

Equation 1.1.5 relates the electron orbital radius to the principal quantum number n, showing an n^2 dependence. The classical period of the electron scales as n^3 (equation 1.2.1); however, the time the electron spends near the nucleus at the inner turning point of the orbit is independent of n.

$$\tau_{cl} = 2\pi n^3 . \qquad (1.2.1)$$

It is a consequence of these scaling laws that systems other than hydrogen possess Rydberg states. A Rydberg state is an excited electron in a hydrogenic orbital; an electron that experiences a single positive point charge from the central nucleus so that the Schrödinger equation describing the motion is identical to that of hydrogen. For all systems other than hydrogen, the core region is not a single point charge; however as n increases the rapid increase in r leads to electrons in orbits distant from the remainder of the core. Whilst the electron is outside of the core radius, r_c, it experiences only a single positive charge from the core, as any extra charge is

shielded by the inner electrons. The total orbit period increases as n^3, whilst the time spent in the core region is independent of n: hence the probability of finding the electron in the core scales as n^{-3}. In molecular systems, this means that during the short transit time of the electron through the core region the internal core motion can be regarded as fixed, and so the electronic motion is considered to be uncoupled to the internal motion of the core. The degree of interaction of the electron with the core region depends on the electronic angular momentum. This will be discussed in the next section.

The scaling laws revealed by the Bohr model also show the exotic properties of Rydberg states. As shown in table 1.2.1, many of the properties of a state with $n = 40$ are on a macroscopic scale. The exaggerated properties also make Rydberg states ideal systems to study experimentally as the large loosely bound orbits are greatly perturbed by applied fields, and the electrons can be easily ionised and subsequently detected. In molecular systems, the orbit period of the electron is long with respect to the internal motion of the ion core, leading to a breakdown in the Born Oppenheimer approximation..

The final scaling law of particular relevance to the work described in this thesis concerns the spacing between energy levels. It is possible to show that the spacing between energy levels is equal to the derivative of equation 1.1.7, and so scales as n^{-3}.

$$\begin{aligned} \frac{dE_n}{dn} &= \frac{E_{n+1} - E_n}{n+1-n} = \Delta E_n \\ E_n &= -\frac{1}{2n^2} \\ \Delta E_n &= -\frac{1}{2}\left(2n^{-3}\right) = n^{-3} \end{aligned} \qquad (1.2.2)$$

All lines of equation 1.2.2 are in atomic units. Therefore, states get progressively closer together in energy as n increases. The development of ultra-fast, broad

bandwidth laser systems [7] allows the excitation of a coherent superposition of a number of Rydberg states. The electronic wavepackets formed are the experimental realisation of an idea first proposed by Schrödinger in 1926; a wave group can be formed that moves in a quantised Kepler orbit and is the representation of the hydrogen atom in wave mechanics [8]. Wavepackets have a high uncertainty in energy, and therefore it follows from the Heisenberg uncertainty principle that they are localised in time and space. Thus, wavepackets inhabit the boundary between particle-like classical and wave-like quantum behaviour. The first atomic wavepackets were observed by ten Wolde and co-workers [9] in 1988, and the first molecular wavepackets were observed by Stavros and co-workers ten years later [10, 11]. Over time, the focus has shifted from observation to control over the properties of the wavepacket [12-15]. In our own group control has been exerted over the rotational angular momentum of electronic wavepackets in atoms [16-18] and molecules [19] and the branching ratio between different decay mechanisms [20]. An experiment by Carley and co-workers [16] is of particular relevance to this thesis as the wavepacket characterisation technique (ramped field ionisation) is explored in Chapter 6.

1.3. The Quantum Defect

A Rydberg electron spends most of the orbit period at the outer turning point, experiencing only the net single positive charge of the core. As it returns to the core region and penetrates the outer radius, r_c, the inner structure becomes important. An analysis of the inner and outer turning points of the electron orbit (equation 1.3.1) shows that the inner turning point scales as $l(l+1)/2$ for $l(l+1)/2 << n^2$, where l is the orbital angular momentum of the electron.

$$r_{\pm} = n^2\left(1 \pm \sqrt{1 - l(l+1)/n^2}\right). \qquad (1.3.1)$$

Therefore, only the low l states ($l \leq 2$) will penetrate the non-Coulombic inner ion core. The motion of the non penetrating states ($l > 2$) can be described using the Schrödinger equation for a hydrogenic atom or ion with nuclear charge +*Ze* orbited by a single electron.

$$\left(E + \frac{Ze^2}{4\pi\varepsilon_0 r}\right)\psi + \frac{-\hbar^2}{2m_e}\nabla^2\psi = 0, \tag{1.3.2}$$

where ∇^2 is the Laplacian operator (expressed in spherical coordinates in equation 1.3.3), r is the electron-nucleus distance, E is the total energy and ψ is the wavefunction.

$$\begin{aligned}\nabla^2 &= \frac{1}{r^2}\frac{\partial}{\partial r}\left(r^2\frac{\partial}{\partial r}\right) + \frac{1}{r^2\sin\theta}\frac{\partial}{\partial\theta}\left(\sin\theta\frac{\partial}{\partial\theta}\right) + \frac{1}{r^2\sin\theta}\frac{\partial^2}{\partial\varphi^2} \\ &= \frac{1}{r^2}\frac{\partial}{\partial r}\left(r^2\frac{\partial}{\partial r}\right) - \frac{\hat{L}^2}{\hbar^2 r^2}\end{aligned} \tag{1.3.3}$$

where $\hat{L}^2$ is the angular momentum operator. Assuming the solution of equation 1.3.2 can be written as a product of radial and angular functions, $\psi = Y(\theta,\varphi)R(r)$, the separated form of equation 1.3.2 can be found.

$$\frac{1}{2m}\frac{\hat{L}^2 Y}{Y} = Er^2 - \left[\frac{-\hbar^2}{2m}\frac{1}{R}\frac{\partial}{\partial r}\left(r^2\frac{\partial R}{\partial r}\right) - \frac{Ze^2 r}{4\pi\varepsilon_0}\right]. \tag{1.3.4}$$

The equation can now be broken down into angular and radial components dependent on *Y* and *R* respectively. As both sides of equation 1.3.4 are equal the solution to each can be written as an arbitrary constant λ. For example the left hand side of equation 1.3.4 can be written

$$\frac{1}{2m}\frac{\hat{L}^2 Y_{lm}(\theta,\phi)}{Y_{lm}(\theta,\phi)} = \lambda. \tag{1.3.5}$$

Equation 1.3.5 is the eigenvalue condition for the total angular momentum operator $\hat{L}^2$ and so by using the normalised spherical harmonics for Y it is possible to find the corresponding eigenfunctions and eigenvalues.

$$\begin{aligned}\hat{L}^2 Y_{lm}(\theta,\phi) &= (\lambda 2m) Y_{lm}(\theta,\phi) \\ &= \hbar^2 l(l+1) Y_{lm}(\theta,\phi)\end{aligned} \tag{1.3.6}$$

and λ is found to be $\hbar^2 l(l+1)/2m$. Substituting this value for λ and defining a new function as $R(r) = \rho(r)/r$ allows the radial component of equation 1.3.4 to be written as

$$E\rho = -\frac{\hbar^2}{2m}\frac{\partial^2 \rho}{\partial r^2} + \left[\frac{l(l+1)\hbar^2}{2mr^2} - \frac{Ze^2}{4\pi\varepsilon_0 r}\right]\rho . \tag{1.3.7}$$

This form of the radial component corresponds to one-dimensional motion with the terms in the square brackets equivalent to an effective potential, $V_{\text{eff}}(r)$, consisting of a centrifugal potential in terms of $l(l+1)/r^2$ and a Coulombic potential in terms of $1/r$. A plot of these two potentials and the resultant effective potential is shown in figure 1.3.1. At large *r*, the Coulombic potential dominates. At low *r* the centrifugal potential dominates, and the value of *l* determines if the electron can overcome the centrifugal barrier and penetrate the core region. The overall wavefunction is the bound hydrogen wavefunction.

$$\psi_{nlm}(\theta,\varphi,r) = \frac{Y_{lm}(\theta,\varphi) f(E,l,r)}{r} . \tag{1.3.8}$$

For all systems other than hydrogen, an electron penetrating the core will experience a larger attraction to the positive core, as it is no longer shielded by the inner electrons. At low *r*, the potential for the non-hydrogen system is deeper and the energy of the electron is lowered. The lower potential shifts the phase of the radial wavefunction by

$\pi\delta_l$. The wavefunction for a Rydberg state belonging to a system with a finite core can be written as

$$\psi_{nlm}(\theta,\varphi,r) = Y_{lm}(\theta,\varphi)\frac{\left[f(E,l,r)\cos\pi\delta_l - g(E,l,r)\sin\pi\delta_l\right]}{r}, \qquad (1.3.9)$$

where f and g are the regular and irregular Coulomb functions. The energy of the state is

$$E = -\frac{1}{2(n-\delta_l)^2}, \qquad (1.3.10)$$

where n is the principal quantum number, and δ_l is the quantum defect.

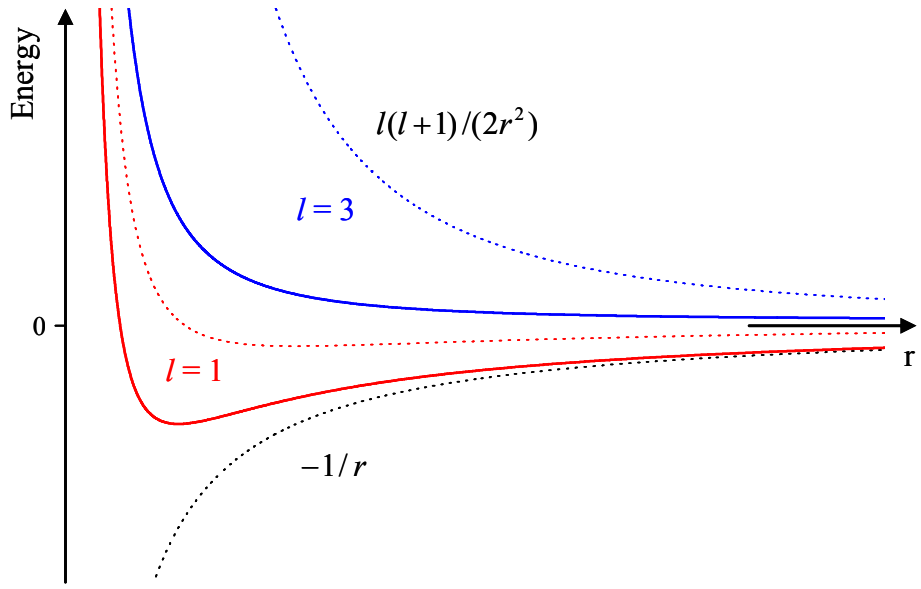

Figure 1.3.1: Schematic showing effective potentials experienced by a Rydberg electron with electronic angular momentum l = 1 (solid red lines) and l = 3 (solid blue lines). The Coulomb potential is shown as a dotted black line and the l = 1 and l = 3 centrifugal potentials are shown as dotted red and blue lines respectively.

A form of equation 1.3.10 was first used by Rydberg to fit the experimentally observed emission line spectra of Na to series of different electronic angular momentum, with δ_l an experimentally determined parameter. However, the quantum

defect can also be considered as a *l*-dependent parameter describing the penetration of the electron into the ion core, or as a phase shift on the wavefunction of hydrogen.

1.4. Molecular Rydberg States

Despite the early observations of atomic Rydberg states, the first Rydberg states of a molecular system were not observed until 1915 by Fowler in emission spectra taken by Curtis [21]. In 1935 Price interpreted a number of Rydberg series in acetylene using the Rydberg formula, proving that it was applicable for molecular systems [22].

As discussed in Section 1.2, the internal rovibrational motion of the core is independent of the electronic motion, and can be labelled using the ionic quantum numbers: rotational angular momentum, N^+ , and vibrational motion, v^+ . The energy of a molecular Rydberg state is given in equation 1.4.1, where $I_{N^+v^+}$ is the ionisation energy for a specific core state.

$$E = I_{N^+v^+} - \frac{R_M}{(n-\delta_{lN^+})^2}. \qquad (1.4.1)$$

R_M is the corrected Rydberg constant, which takes into account the core mass of species *M*. It can be written in terms of the Rydberg constant R_∞, the mass of the electron m_e, and the mass of the ion core, $m_{\text{ion-core}}$. This formula also applies to atomic Rydberg series.

$$R_M = \frac{R_\infty}{1 + m_e / m_{\text{ion-core}}}. \qquad (1.4.2)$$

For each quantum state of the ion core in a molecular Rydberg system there will exist a Rydberg series converging to the associated ionisation energy. This leads to a high density of states and increased opportunities for interseries coupling. The increasing

complexity in Rydberg systems from hydrogen, to molecules is shown in figure 1.4.1. The core structure also allows electron-core scatter interactions leading to ionisation (autoionisation) and core fragmentation (predissociation).

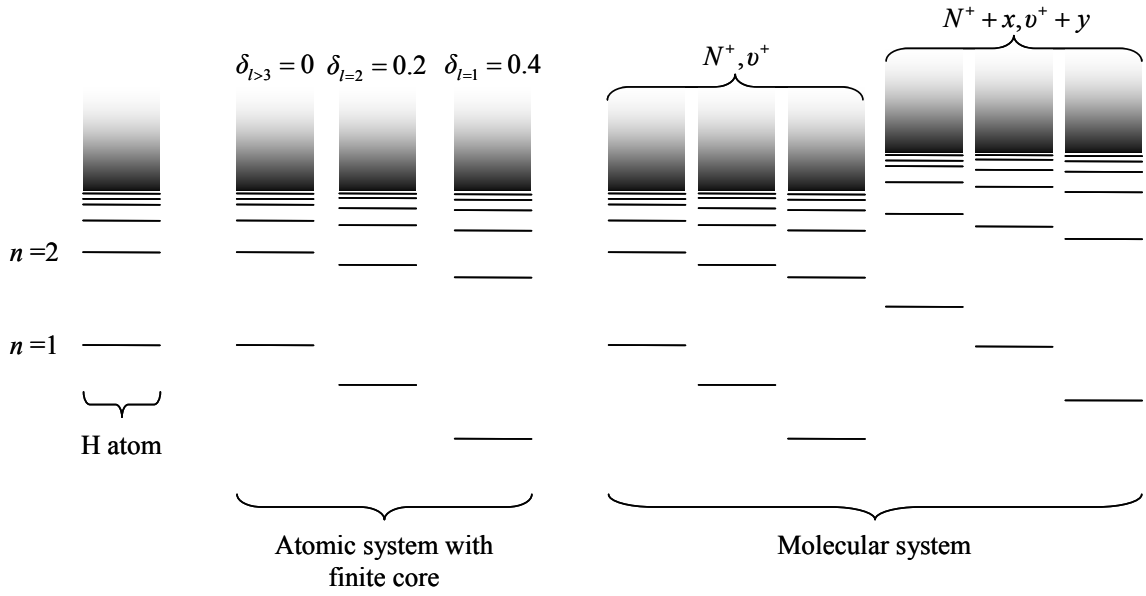

Figure 1.4.1: Schematic showing the increasing complexity of a Rydberg system moving from the hydrogen atom to molecular systems. Atomic systems other than hydrogen posses a finite core, and the energy of the penetrating low electronic angular momentum states, i.e $l < 3$, is lowered by interactions with the core. States of high l do not interact with the core. Molecular systems possess groups of series converging to the ionisation limit of each rovibrational state of the ion core, labeled using the rotational, N^+, and vibrational, v^+, quantum numbers. The y-axis is energy, increasing from bottom to top. The x-axis shows the increasing complexity going from the simplest system on the left (hydrogen) to the more complex molecular system on the right.

1.4.1. Electron-Core Decay Mechanisms

Rydberg states are long lived with respect to radiative decay; however interactions between the electron and ion core allow rapid electron scatter decay processes. These electron-core decay mechanisms involve discrete states that are degenerate with a continuum associated with a lower energy state of the ion core. Autoionisation can occur when the core can exist in a state of lower rovibrational energy in a molecular

system or lower spin-orbit energy in an atomic system. The spin-orbit case is not relevant to this thesis, and so will not be considered. Autoionisation can be viewed from either a classical or quantum mechanical perspective. Classically, as the electron returns to the core region, it undergoes an inelastic collision with the core. The core can impart rovibrational energy to the electron in the form of kinetic energy, allowing the electron to escape the Coulomb potential. Conservation of energy means that the core is left in a lower rovibrational state. In the quantum picture, a Rydberg state of non-zero rovibrational energy is bound with respect to its own direct ionisation, but coupled to the ionisation continuum of a lower ionic state. The wavefunction is quasibound with respect to ionisation from this lower channel. Figure 1.4.2A shows autoionisation occurring for discrete states of non-zero vibrational energy. High lying states of the $v^+ = 1$ series can decay into the ionisation continuum associated with the $v^+ = 0$ series, whereas states belonging to the higher $v^+ = 2$ series can decay into either of the two lower continua.

Predissociation can only occur in molecular systems. Classically, as an electron returns to the core it has high momentum and if there is a collision, energy can be imparted into a vibrational mode leading to dissociation. This occurs when the Rydberg state crosses a bound electronic state above its dissociation limit, or a repulsive electronic state (figure 1.4.2B). The molecule fragments into neutral components, and can form different products depending on the particular potential into which it decays.

$$\mathrm{AB}^*(E^*) \rightarrow \mathrm{A}(E^A) + \mathrm{B}(E^* - E^A)$$

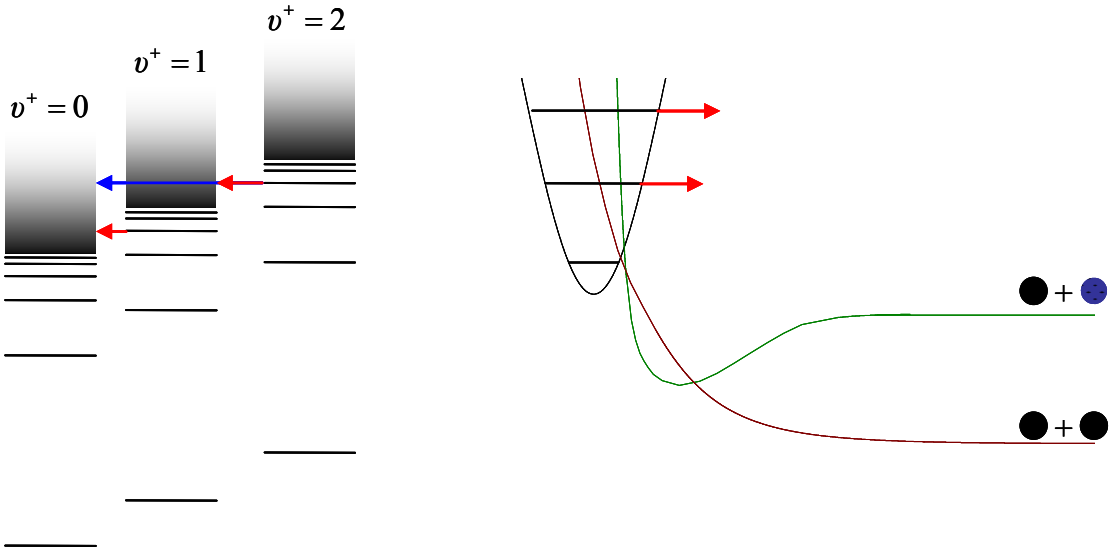

A **B**

Figure 1.4.2: Schematics showing the two possible electron scatter ionisation mechanisms in molecular Rydberg systems:
A: Vibrational autoionisation from states belonging to the v_1^+ series to the continuum associated with the v_2^+ series, where $v_1^+ > v_2^+$.
B: Predissociation can occur from states degenerate with the dissociation continuum associated with the fragmented molecule. In the example above, the states are degenerate with a continuum associated with a repulsive state and a continuum above the dissociation limit of a bound state. The molecule can fragment into different components along different potentials.

In the quantum picture, the Rydberg state is quasibound with respect to a dissociation continuum of another state. There is a non-zero probability of moving onto the dissociative surface resulting in fragmentation of the core. The transition probability from a discrete state, $|\varphi\rangle$, to a dissociative continuum, $|\varepsilon\rangle$, of equal energy is

$$P = (4\pi^2 / h)\left|\langle \varepsilon | H' | \varphi \rangle\right|, \qquad (1.4.3)$$

where H' is the Hamiltonian of the perturbation responsible for the predissociation. The magnitude of equation 1.4.3 is approximately equal to the overlap of the two vibrational parts of the total wavefunction as labelled with a superscript v, $\langle \varepsilon^v | \varphi^v \rangle$ [23], which is governed by the relative positions and forms of the potential

curves associated with the discrete and dissociative states. Therefore, the probability of predissociation is higher from Rydberg states into dissociative continua with potentials of the same symmetry. Below the lowest ionisation limit, only predissociation can occur. Above the lowest ionisation limit autoionisation and predissociation compete and this is shown experimentally by an increased rate of decay. For example, in NO, np($v^+ = 0$) states show a decay rate of $1610/n^3$ cm^{-1} [24] whereas the np($v^+ = 1$) states, which are above the $v^+ = 0$ ionisation limit and are susceptible to autoionisation, show an increased decay rate of $4000/n^3$ cm^{-1} [25]. It has previously been shown that it is possible to control the branching ratio between these two processes by coherent control in electronic wave packet experiments [20].

1.5. Lifetimes of Rydberg States

The radiative lifetime of a Rydberg state is given by

$$\tau_{nl} = \left[\sum_{n'l'} A_{n'l',nl} \right]^{-1}, \tag{1.5.1}$$

where $A_{n'l',nl}$ is the Einstein A coefficient, which gives the spontaneous decay rate of a Rydberg state, nl, to a lower state, $n'l'$, separated by $\omega_{n'l',nl}$.

$$A_{n'l',nl} = \frac{-2e^2 \omega_{n'l',nl}^{\ 2}}{\hbar c^3} \bar{f}_{n'l',nl}, \tag{1.5.2}$$

where $\bar{f}_{n'l',nl}$ is the average oscillator strength and is given by

$$\bar{f}_{n'l',nl} = \omega_{n'l',nl} \frac{2l_{\max}}{3(2l+1)} \left| \langle n'l' | r | nl \rangle \right|^2. \tag{1.5.3}$$

The decay rate is proportional to the cube of the separation between the two states, $\omega_{n'l',nl}$. This means that the highest frequency transitions dominate, and so for all states except the s states the transition to the lowest (l – 1) state dominates.

The decay rate due to stimulated emission or absorption by black body radiation is given as

$$K_{n'l',nl} = \bar{n} A_{n'l',nl}, \tag{1.5.4}$$

where $\bar{n}$ is the photon occupation number (the number of photons per mode of radiation) and is given by Planck's radiation law as a function of frequency ω, temperature T, and the Boltzmann constant k.

$$\bar{n} = \frac{1}{\mathrm{e}^{\omega/kT} - 1}. \tag{1.5.5}$$

In contrast to spontaneous emission, the $\bar{n}$ dependence of stimulated emission and adsorption caused by black body radiation favours low frequency transitions to nearby states. This mainly affects high lying Rydberg states for which the energy spacing is small and $\omega << kT$ allowing the photon occupation number to be approximated as kt/ω. The lifetime with respect to stimulated emission and absorption can then be written as

$$\tau_{nl} = \left[\sum_{n'l'} \frac{-2e^2 kT\omega_{n'l',nl}}{hc} \bar{f}_{n'l',nl} \right]^{-1}. \tag{1.5.6}$$

Rydberg states move in large valence orbits and have little overlap with the ground states, *i.e.* $\langle n'l' | r | nl \rangle$ is small. Due to the stability of Rydberg states to spontaneous and stimulated radiative decay the dominant decay process is by the various electron-core interactions discussed in Section 1.4.1. As these decay processes depend on the interaction of the Rydberg electron with the ion core they are proportional to the orbit period of the electron, and therefore scale as n^3. The degree of core penetration is also important with the experimentally determined zero field decay parameters, $\Gamma_0(l)$, showing a strong l dependence. The total lifetime of a Rydberg state of principal

quantum number n can be calculated from the experimentally determined decay parameters by using equation 1.5.7.

$$\Gamma(n,l) = \Gamma_0(l)/n^3 . \qquad (1.5.7)$$

1.6. Lineshapes

In an ideal system an absorptive transition would show an infinitely narrow line shape, *i.e.* a delta function; in reality, a number of effects change the observed spectral line shape. Inhomogeneous broadening, in which there exists an inhomogeneous spread of conditions in the sample, creates a Gaussian lineshape. An example of an inhomogeneous effect is Doppler broadening. In a molecular beam, there is a spread in the velocity of molecules relative to the excitation laser pulse and this results in a spread in the excitation frequency. A second broadening effect arises from the uncertainty principle, which states there is a relationship between the lifetime and energy width of a state. All excited states have a finite lifetime, τ, and the energy of the state must be uncertain by an amount of order $\hbar/\tau$. For a transition, ω_{ba}, between two states the maximum intensity is observed at $\omega = \omega_{ba} = (E_b - E_a)/\hbar$, and decreases to one half the maximum at

$$\omega = \omega_{ba} \pm 1/(2\tau_b) = (E_b - E_a \pm \Gamma_b/2)/\hbar , \qquad (1.6.1)$$

where $\Gamma_b = \hbar/\tau_b$. A Lorentzian distribution is ideally suited to fit this behaviour and the line shape is proportional to the function

$$f(\omega) = \frac{(\Gamma_b/2\hbar)^2}{(\omega-\omega_{ba})^2 + (\Gamma_b/2\hbar)^2} . \qquad (1.6.2)$$

Autoionising and predissociating states also show asymmetric Fano line shapes due to interference effects [26]. Transitions to states embedded in an ionisation or

dissociation continuum can be considered as transitions to the continuum *via* a direct and indirect pathway. The indirect pathway involves the Rydberg state embedded in the continuum and is therefore part discrete and part continuous. The interference between the two pathways is constructive on one side of the resonance and destructive on the other, and leads to an asymmetric line shape. A line shape formula can be derived from the ratio between the transition probabilities from an initial state *i* to the mixed state φ and featureless continuum $\psi_{E'}$.

$$R = \frac{\left|\langle \varphi | D | i \rangle\right|^2}{\left|\langle \psi_{E'} | D | i \rangle\right|^2} = \frac{(q+\varepsilon)^2}{(1+\varepsilon)^2}, \qquad (1.6.3)$$

where q is the Fano line shape parameter and ε is a measure of the detuning from the resonance energy E_0, and is equal to $2(E - E_0)/\Gamma$. The symmetry of the Fano line shape depends on the line shape parameter, q, and approaches a Lorentzian profile as $q \to \infty$.

1.7. Rydberg States in Applied Fields: The Stark Effect

In the same year as Bohr's derivation of R from first principles, Johannes Stark observed the splitting in the spectral lines of hydrogen under an applied field of 100000 V cm^{-1} [27]. Using the Bohr model, Epstein and Schwarzschild independently derived the equations for the linear and quadratic Stark effect in hydrogen [28, 29]. Each Rydberg state of principal quantum number n has (n-1) l states where l is electronic orbital momentum. With no applied field the non-penetrating ($l > 3$) states are degenerate. The application of an external electric field reduces the symmetry of the Rydberg system from spherical (due to the Coulomb potential) to axial. The change in symmetry lifts the degeneracy of the high-l states and creates a saddle point

in the Coulombic potential. The saddle point, and resulting possibility of field ionisation, will be explored in detail in the next section.

To understand the splitting of the high-*l* states, it is useful to consider the simplest system, hydrogen, in which all *l* states belonging to a particular *n* are degenerate. An electron at a distance *r* from an origin has a dipole moment of $\boldsymbol{\mu} = -e\mathbf{r}$ where *e* is the charge on the electron. The interaction between the dipole moment and applied field, *F*, is $\hat{H}^{(1)} = \boldsymbol{\mu}.\mathbf{F}$. For a field applied along the *z*-axis, the Stark Hamiltonian can be written as -*eFz*, and can be included in the Schrödinger equation for hydrogen (previously shown in equation 1.3.2).

$$\left(E + \frac{Ze^2}{4\pi\varepsilon_0 r} - eFz\right)\psi + \frac{-\hbar^2}{2m_e}\nabla^2\psi = 0\,. \qquad (1.7.1)$$

The matrix elements of the Stark perturbation are shown in equation 1.7.2 and the non-zero matrix elements are those of $m = m'$ and $l' = l + 1$

$$\langle nlm|eFz|n'l'm'\rangle = eF\langle nlm|r\cos\theta|n'l'm'\rangle\,. \qquad (1.7.2)$$

The simplest state in hydrogen that undergoes splitting has principal quantum number *n* = 2, and contains four degenerate states. The states can be labelled using ψ_{nlm} notation as ψ_{200}, ψ_{21-1}, ψ_{210}, and ψ_{211}. For simplicity, ψ_{210} and ψ_{200} are labelled $|i\rangle$ and $|j\rangle$ respectively and the Hamiltonians coupling the wavefunctions are labelled H_{ij} and H_{ji}. The non-zero matrix elements can be written in atomic units as

$$H_{ij} = H_{ji} = 3F\,. \qquad (1.7.3)$$

Degenerate perturbation theory (used for systems in which the unperturbed states are degenerate) gives a set of secular equations that can be used to find the perturbed wavefunctions. It assumes that the correct zero order eigenfunction representing a

degenerate pair of functions is a combination of the two *i.e.* in this case a combination of the $2p_0$ and $2s_0$ wavefunctions, $\varphi = c_1\psi_{210} + c_2\psi_{200}$. It can be shown that

$$\begin{pmatrix} H_{11} - E_0^{(1)} & H_{12} \\ H_{21} & H_{22} - E_0^{(1)} \end{pmatrix} \begin{pmatrix} c_1 \\ c_2 \end{pmatrix} = 0 , \qquad (1.7.4)$$

where $E_0^{(1)}$ is the first order perturbation state energy. Using the values of H_{12} and H_{21} in equation 1.7.3, and solving the determinant of the first matrix gives

$$E_0^{(1)} = \pm 3F , \qquad (1.7.5)$$

i.e. the first order splitting of the degenerate levels by the field is proportional to the field strength. Substituting the value of $E_0^{(1)}$ back into 1.7.4 gives the (unnormalised) eigenfunctions of the perturbed states (equation 1.7.6). The Stark energy diagram for the $n = 2$ level of hydrogen is shown in figure 1.7.1.

$$\varphi = \psi_{200} \pm \psi_{210} . \qquad (1.7.6)$$

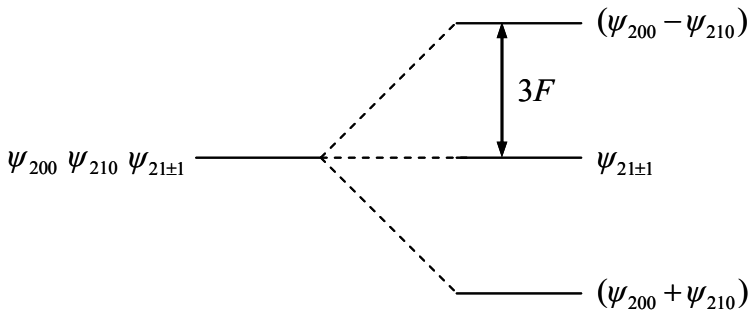

Figure 1.7.1: Energy levels of $n = 2$ electronic level of atomic hydrogen. In an electric field, F, the four degenerate states split. The two $m_l = \pm1$ states are unchanged, but the field mixes the $m_l = 0$ levels which are shifted in energy by $3F$ (in atomic units). The wavefunctions of the states are labeled using ψ_{nlm} notation where n is the principal quantum number, l is the electronic angular momentum, and m is the projection of l onto the internuclear axis.

A more generalised treatment of the linear Stark effect can be carried out by using parabolic coordinates, so that the Schrödinger equation remains separable. In two

dimensions, the parabolic coordinate lines are confocal parabolas, where the foci lie at the origin. A three dimensional system (as used here) is obtained by rotating about the symmetry axis of the parabolas. The parabolic coordinates are defined as a combination of the Cartesian and spherical coordinates, such that constant ξ and η are paraboloids of revolution about the *z*-axis [30].

$$\begin{aligned} \xi &= r + z = r(1 + \cos\theta) \\ \eta &= r - z = r(1 - \cos\theta) \\ \varphi &= \tan^{-1}(y / x) \end{aligned} \tag{1.7.7}$$

Using the parabolic coordinate system, the Schrödinger equation can be written as

$$\left[\frac{-\nabla^2}{2} - \frac{2}{\xi + \eta} + \frac{F(\xi + \eta)}{2}\right]\psi = E\psi\,, \tag{1.7.8}$$

where

$$\nabla^2 = \frac{4}{\xi + \eta}\frac{\partial}{\partial\xi}\left(\xi\frac{\partial}{\partial\xi}\right) + \frac{4}{\xi + \eta}\frac{\partial}{\partial\eta}\left(\eta\frac{\partial}{\partial\eta}\right) + \frac{1}{\xi\eta}\frac{\partial^2}{\partial\varphi^2}\,. \tag{1.7.9}$$

By assuming equation 1.7.8 is separable, with a solution of $\psi = U_1(\xi) + U_2(\eta) + \mathrm{e}^{im\varphi}$, it is possible to find the zero field parabolic wave functions. These wavefunctions contain the parabolic quantum numbers n_1 and n_2, which correspond to the number of nodes in the U_1 and U_2 functions. n_1 and n_2 are related to *n* and *m* by

$$n = n_1 + n_2 + |m| + 1\,. \tag{1.7.10}$$

The loss in *l* degeneracy arises from the reduction in the symmetry due to the field. *l* now precesses rapidly around the field vector (as shown in figure 1.7.2) and *l* is no longer defined. Instead a new quantum number, *k*, is introduced where

$$k = n_1 - n_2\,. \tag{1.7.11}$$

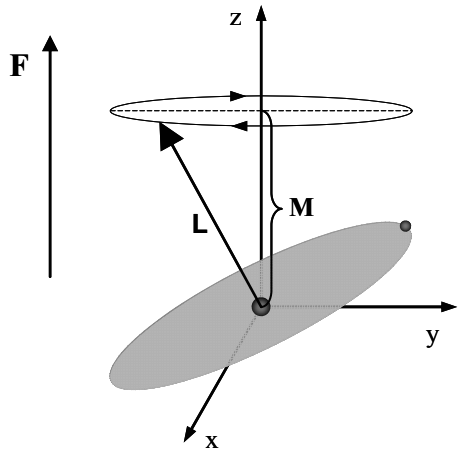

Figure 1.7.2: Schematic representation of the vectors governing the motion of a Rydberg electron in an electric field. **F** is the direction of the electric field, along the z axis. The grey disc is the plane of the orbit of the Rydberg electron, and the angular momentum vector, **L** , acts at right angles to this plane. The addition of the field causes **L** to precess around the direction of the field vector; however the projection of **L** onto the internuclear axis, **M**, does not change.

Under an applied field, each l state splits into a manifold of (n - m) k states where k takes a value from $(n-l-m)$ to $-(n-l-m)$. The value of m populated in the Stark manifold depends on the polarisation of the exciting laser pulse with respect to the polarisation of the electric field; if the two fields are parallel then $\Delta m_l = 0$ transitions are allowed whereas $\Delta m_l = 1$ transitions occur if the two fields are perpendicular. For example, table 1.7.1 shows the various parabolic quantum numbers of the Stark states populated if a manifold of n = 5 is accessed from a m_l = 0 launch state using laser light that is parallel or perpendicular to the electric field.

The energy of a Stark state to second order is given in atomic units by equation 1.7.12. The term containing F is the linear Stark shift, as calculated for the n = 2 state of hydrogen in equation 1.7.5. The term containing F^2 is the quadratic shift, which is important at high fields. The quadratic shift always moves the line position to lower energies and lifts the m_l degeneracy.

$$E = -\frac{1}{2n^2} + \frac{3nk}{2}F - \frac{n^2}{16}F^2\left(17n^2 - 3k^2 - m_l^2 + 19\right). \qquad (1.7.12)$$

Systems with a finite sized core show a number of important differences. As previously discussed, penetrating states ($l \leq 2$) are non-degenerate with the high-l manifolds even in zero fields, as the electron-core interaction lowers the state energy. An applied field lifts the high-l degeneracy and forms a Stark manifold; however the penetrating states do not join the manifold until higher fields. A second effect of the finite core is that n_1 and n_2 are no longer good quantum numbers and the red and blue states of a manifold are coupled in the core region. The field at which the extreme red and blue of the respective (n + 1) and n manifolds cross is called the Inglis Teller limit.

$$F_{\mathrm{IT}} = \frac{1}{3n^5}. \qquad (1.7.13)$$

In atomic hydrogen, there is no interaction between states of different n but equal m and adjacent manifolds cross. The core interaction in all other systems, and resulting loss of n_1 and n_2 as good quantum numbers, means that states from adjacent manifolds create avoided crossings.

	Parallel	**Perpendicular**
$n_1 + n_2 + \lvert m \rvert + 1 = n$	$n_1 + n_2 + 1 = 5$	$n_1 + n_2 + 2 = 5$
n_1	4, 3, 2, 1, 0	3, 2, 1, 0
n_2	0, 1, 2, 3, 4	0, 1, 2, 3
$k = n_1 - n_2$	4, 2, 0, -2, -4	3, 1, -1, -3

Table 1.7.1: Parabolic quantum numbers of Stark states populated in the n =5 manifold using laser light parallel and perpendicular to an applied electric field.

1.8. Rydberg States in Applied Fields: Field Ionisation

The application of an electric field to a Rydberg system breaks the spherical symmetry of the Coulomb potential leading to the creation of a saddle point (labelled sp in figure 1.8.1). The saddle point of the combined Coulomb-Stark potential occurs at $r_{sp} = -1/\sqrt{F}$, with a potential of $V_{sp} = -2\sqrt{F}$. The effective potential experienced by the electron as shown in figure 1.8.1 is a sum of the potential due to the field, and Coulombic potential.

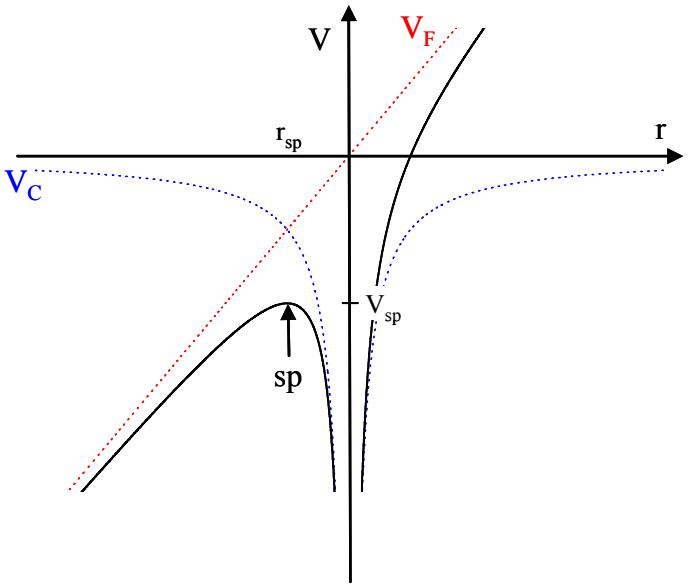

Figure 1.8.1: Schematic representation of the effective potential experienced by the electron (black line), which is a combination of the Coulomb potential (dotted blue, labeled V_c) and the field potential (dotted red, labeled V_F). The potential and radial position of the saddle point are labeled as V_{sp} and r_{sp} respectively.

Ignoring the splitting of states due to the electric field, classical ionisation of a Rydberg state occurs when the energy of the saddle point is equal to the state energy. The field at which this occurs is related to the principal quantum number by

$$F = \frac{1}{16n^4} \qquad (1.8.1)$$

The energy at which an electron can escape the Coulomb-Stark potential is given in cm^{-1} by $E_{sp} = -6.12\sqrt{F}$. Taking into account the Stark shift on the extreme red state of the Stark manifold, and using the approximation $n = k$, which is valid for large n, the ionisation field can be expressed as

$$F = \frac{1}{9n^4}. \tag{1.8.2}$$

If population is initially excited to a single Rydberg state in zero field and then a ramped ionising field pulse is applied, the population travels along the Stark manifold towards ionisation. At each avoided crossing population can be transferred either diabatically or adiabatically. The probability of a diabatic crossing can be expressed using the Landau-Zener approximation.

$$P_{dia} = \exp\left[\frac{2\pi|V_{12}|^2}{h(dW_{12}/dt)}\right], \tag{1.8.3}$$

where

$$\frac{dW_{12}}{dt} = \frac{dF}{dt}\left(\frac{dE_1}{dF} - \frac{dE_2}{dF}\right). \tag{1.8.4}$$

dF/dt is the slew rate of the ionising field, V_{12} is the coupling matrix element that causes the avoided crossing, and dE_x/dF is the gradient of the Stark state, x, at the crossing. An ionising pulse with a fast ramp will lead to mainly diabatic crossings, and ionisation occurs at the field given by equation 1.8.2. The use of a slowly ramped field leads to an adiabatic crossing at the first avoided crossing (at the Inglis-Teller limit), and at all subsequent crossing. Ionisation occurs at a field close to the classical ionisation limit (equation 1.8.1). Experimentally, the slew rate of the field can be changed to exploit the passage through the Stark manifold. Fast ramped fields are used in pulsed field ionisation investigations, to concentrate population into a purely

diabatic route to ionisation [31-33]. This reduces the spread in time of ionisation, and reduces the width of the detected ionisation signal. A slow ramped field can be used to characterise the population components in a wavepacket. Population is ionised from the constituent states at different fields, and are therefore detected at different times. By analysing the ionisation time profile, and taking into account the possibility of some adiabatic crossings, the initial Rydberg state components of the wavepacket can be found [16, 34-36].

The field ionisation process is further complicated by the relative stabilities of the blue and red Stark states to field ionisation. The solutions to equation 1.7.1 show that the extreme k states are localised along the + z-axis (as can be seen in the simple example given by equation 1.7.6), whilst the $k = 0$ wavefunction is localised near the $z = 0$ plane. The maximum of the bluest Stark state is located on the opposite side of the core to the saddle point, whereas the highest red state is located in the region of the saddle point. Therefore, blue states are kinetically more stable to classical ionisation *i.e.* any state located above the saddle point is ionised. The coupling of states in the core introduces an ionising process similar to autoionisation. The interaction by blue and red states due to coupling in the core destabilises all states other than the extreme red state. In a classical picture, as a stable blue state passes through the core it can scatter into the degenerate continuum and ionise.

1.9. Summary

The exotic properties of Rydberg states and sensitivity to external perturbations make them ideal systems to study experimentally. Molecular Rydberg states show unique decay processes that are investigated in experiments presented in this thesis. The application of an electric field reduces the symmetry of a Rydberg system and removes the degeneracy of the l states as investigated in Chapter 4. In an electric field

Rydberg states also show interesting ionisation characteristics as discussed in Chapter 6.

2. Experimental Set-up

2.1. Introduction

Since the development of lasers, multiphoton excitation schemes have been used to investigate Rydberg states in many systems. A resonance-enhanced multiphoton scheme involves an initial transition to an intermediate state, followed by a second transition to a Rydberg state governed by strict selection rules. Exciting a Rydberg level *via* an intermediate state allows transitions to levels that are forbidden with a single photon transition from the ground state, and also reduces the spectral congestion normally observed due to transitions from many thermally populated rotational levels of the ground electronic state. Breaking the excitation scheme down in a number of smaller transitions allows the use of commercially available light sources and has the advantage of exploiting one photon transition selection rules to selectively populate specific states. Resonance enhanced multi-photon schemes have been used to study the autoionisation process in Rydberg states of NO as the decay process forms an electron and positive ion, both of which can then be detected. The predissociating and bound states require a secondary ionisation process to form charged products that can then be detected. To study predissociation, an extra light source is needed to photoionise the neutral fragments formed. The bound molecular Rydberg states can be studied using pulsed field ionisation, in which an electrical pulse with a fast rise time creates a saddle point in the Coulomb potential allowing the bound electron to escape.

The experiments described in this thesis use both of these techniques to study the predissociating and bound Rydberg states of NO from n = 25 to 30. The field ionisation of the bound states is studied using a variety of electrical pulses to ionise the electron, altering the path the electron takes through the Stark manifold before reaching the saddle point. The effect of a static DC electric field on predissociating states is used to investigate state mixing by the external field, and allows the observation of many states that are forbidden by a single photon transition in zero field.

The predissociation and field ionisation studies presented in this thesis are both performed using the same basic set-up of a resonance enhanced multiphoton excitation scheme in a linear time of flight apparatus. The full development of the vacuum chamber and time-of-flight apparatus is detailed in Chapter 6, including the many developments necessary to carry out the field ionisation studies. The previous studies of the bound states shown in Chapter 6 used an earlier time-of-flight set-up, although the principles are the same. This set-up is described in Section 6.2 of Chapter 6.

2.2. Laser system

The frequency spectra presented in this thesis use a resonance enhanced multiphoton excitation scheme to access the Rydberg states of NO, and the spectroscopy is introduced in Chapter 3. Briefly, one photon is used to access a specific rovibrational level of the $A^2\Sigma^+$ intermediate state and a second then excites to a Rydberg state. The two photons are generated by two narrow bandwidth nanosecond dye lasers pumped by a Q-switched Nd:YAG laser operating at 20 Hz. The Nd:YAG (Continuum Powerlite 8010) generates pulses of light at 1064 nm and 6 ns duration with a

bandwidth of 1 cm^{-1}. Around 8 W (450 mJ) of the second harmonic at 532 nm is produced and used to pump the two dye lasers.

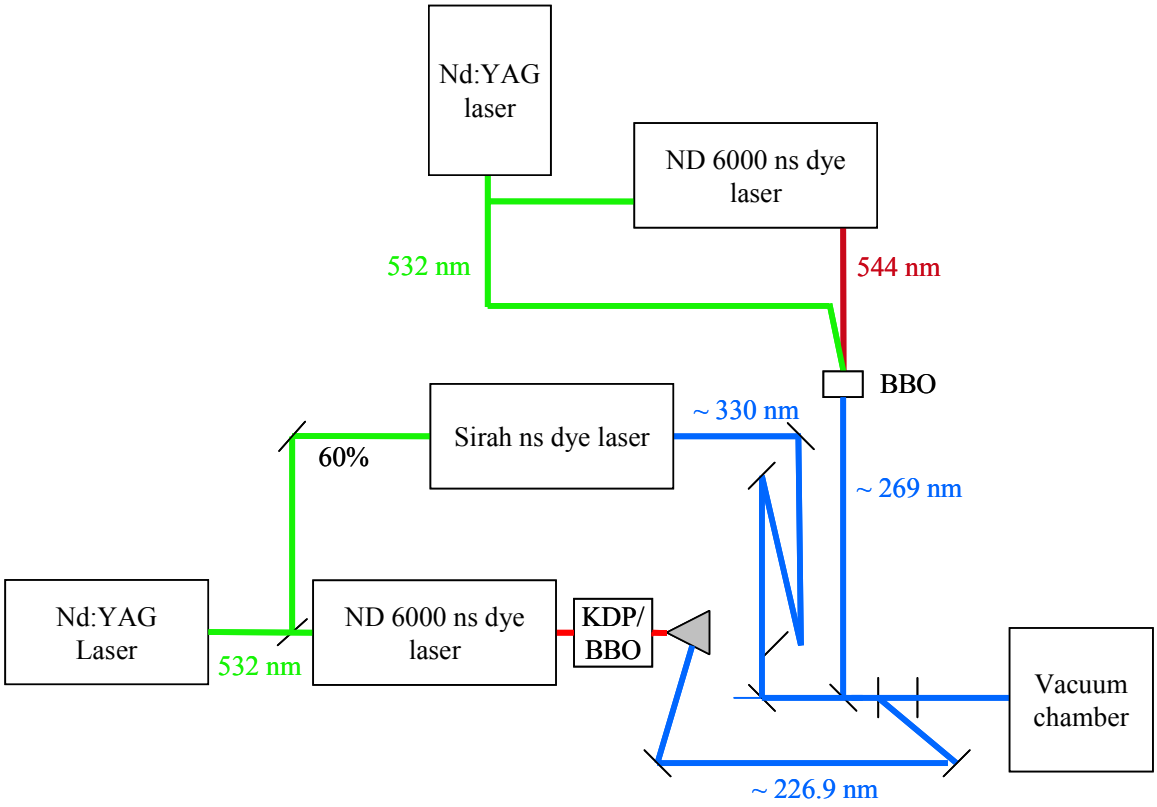

Figure 2.2.1: Schematic showing optical layout of laser system. Two ns dye lasers pumped by a Nd:YAG access the Rydberg states *via* an intermediate state. To get the required wavelength for the ground to intermediate transition the frequency of the output from the first dye laser is tripled using an array of optics and crystals (KDP/BBO). The two beams are combined at a dichroic mirror and directed into the vacuum chamber. To detect the nitrogen produced by predissociation it is ionized using 269 nm light generated using a second Nd:YAG and third ns dye laser.

40 % of the Nd:YAG output is used to pump the first dye laser (ND6000) which is used to access the $A^2\Sigma^+$ intermediate state. The dye used is Pyridine 1 dissolved in ethanol, and generates light in the range of 645-730 nm, with energy of 15 mJ per pulse and a bandwidth of 0.05 cm^{-1}. The transition to the $A^2\Sigma^+$ state requires UV light, and this is generated from the visible red output of the laser using a series of non-linear crystals. The output beam is collimated and reduced in diameter using a pair of lenses, and then passed through a potassium dihydrogen phosphate (KDP) doubling

crystal. A half waveplate then rotates the polarisation of the fundamental light by 90° and finally the fundamental and doubled light are mixed in a β-barium borate (BBO) crystal to generate UV light in the region of 215-243 nm. This is separated from the remaining fundamental and doubled light using a Pellin Broca prism. Transitions to the $A^2\Sigma^+$ intermediate states that are accessed in the work presented in this thesis are in the range of 226.9 - 227 nm. It is necessary to reduce the intensity of the mixed light to avoid resonance enhanced multiphoton ionisation (REMPI) from the intermediate state. This is achieved by rotating the half waveplate and reducing the efficiency of the frequency mixing process.

The remaining 60 % of the Nd:YAG output is used to pump a second dye laser (Sirah Cobra Stretch) accessing the transition from the intermediate A state to the Rydberg levels. The dye used is DCM dissolved in dimethyl sulfoxide (DMSO), producing light in the range of 626 - 685 nm with a peak output at 651 nm. A frequency doubling unit attached to the laser generates 10 mJ of UV pulses in the range of 313 – 343 nm with a bandwidth of approximately 0.05 cm^{-1}, and duration 8 ns. The crystal angle inside the doubling unit is computer controlled to ensure that the power of the doubled light remains constant as the wavelength is scanned. The wavelength scan is controlled by a Labview programme, and this is discussed in Section 2.6.

The beams from the two dye lasers are then combined at a dichroic beam splitter and directed through a UV grade fused silica window and into the vacuum chamber, where they cross a molecular beam of the sample gas. It is necessary to delay the Sirah beam by about 3 ns with respect to the ND6000, and this is carried out using a number of mirrors to increase the path length. The beams pass through the chamber and leave from a second silica window. The Sirah beam is then collected by focusing it into a fibre optic cable which is connected to a wavemeter (Angstrom WS – 7).

Wavelength collection is synchronised with the triggered scanning of the Sirah laser, and will be discussed in Section 2.6.

The predissociation experiments require a further set of lasers to generate the 269 nm necessary to photo-ionise nitrogen atoms using a (2+1) REMPI scheme *via* the $^2S_{1/2}$ intermediate state. A second Nd:YAG generates 575 mJ of 532 nm light. 40 % is used to pump a third dye laser (ND6000) operating with fluorescein 548, generating 250 mJ of light at 544 nm. This is then frequency mixed with 10 % of the Nd:YAG output in a BBO crystal to generate 45 mJ of light at 269 nm. The REMPI beam is then overlapped with the first two laser beams using a second dichroic mirror and all three are focused (f = 250 mm) onto the interaction region. For the predissociation experiments it is necessary to detune the doubling crystal in the Sirah to reduce the power of the UV light to less than 1.5 mJ. This is to avoid power broadening effects in which the edge of the laser pulse saturates a transition, broadening the observed peaks.

2.3. Vacuum chamber

The vacuum apparatus (figure 2.3.1) consists of three chambers differentially pumped with a combination of two turbo molecular pumps and one diffusion pump all backed by two rotary pumps. Each pump can be isolated from the chamber with a manual valve; a butterfly valve for the diffusion pump and gate valves for both turbo pumps.

The source chamber holds the gas nozzle and is pumped using a 700 l s^{-1} diffusion pump (Edwards 160/700 M). With the nozzle closed the source chamber is held at a pressure of 10^{-7} mbar, rising to 10^{-5} mbar whilst the nozzle is in operation. The diffusion pump is backed by a two stage rotary pump (Edwards E2M18). The interaction chamber holds the field optics between which the laser beams cross the

molecular beam. It is separated from the source chamber by a beam skimmer, which extracts the centreline of the molecular beam and isolates it from interference from the rest of the beam expansion. The interaction chamber is pumped using a turbo molecular pump (Leybold Turbovac 361) backed by a rotary pump (Leybold D16B). With the nozzle closed the pressure is 10^{-8} mbar, rising to 10^{-7} mbar with the nozzle open. The detection region is also pumped using a turbo molecular pump (Edwards EXT-250), backed using the same rotary pump. The pressure is 10^{-8} mbar and only increases by 0.5×10^{-8} mbar when the nozzle is open.

Both rotary pumps are connected to the different vacuum pumps through an adsorption trap, and a valve that allows the backing line to be closed. A Pirani type pressure gauge is also used to measure the pressure on either rotary in order to check that it does not exceed 10^{-2} mbar. The turbo and diffusion pumps both require the chamber pressure to be at a low value before they can be used. It is possible to rough out the chamber down to the starting pressure required by the turbo molecular pumps (10^{-3} mbar) using the two rotary pumps. All of the valves connecting the vacuum pumps to the rotary and chamber must be closed. The source chamber can then be roughed out using a valve on the diffusion pump that closes the backing line to the diffusion and opens a second line directly into the chamber just above the butterfly valve. The interaction and detection chambers are roughed out by opening a valve that connects the rotary pump used to back the two turbo molecular pumps to a port on the detection chamber. The turbo molecular pumps are then opened to the chamber, and once the pressure reaches 10^{-5} mbar the valve isolating the diffusion pump can also be opened.

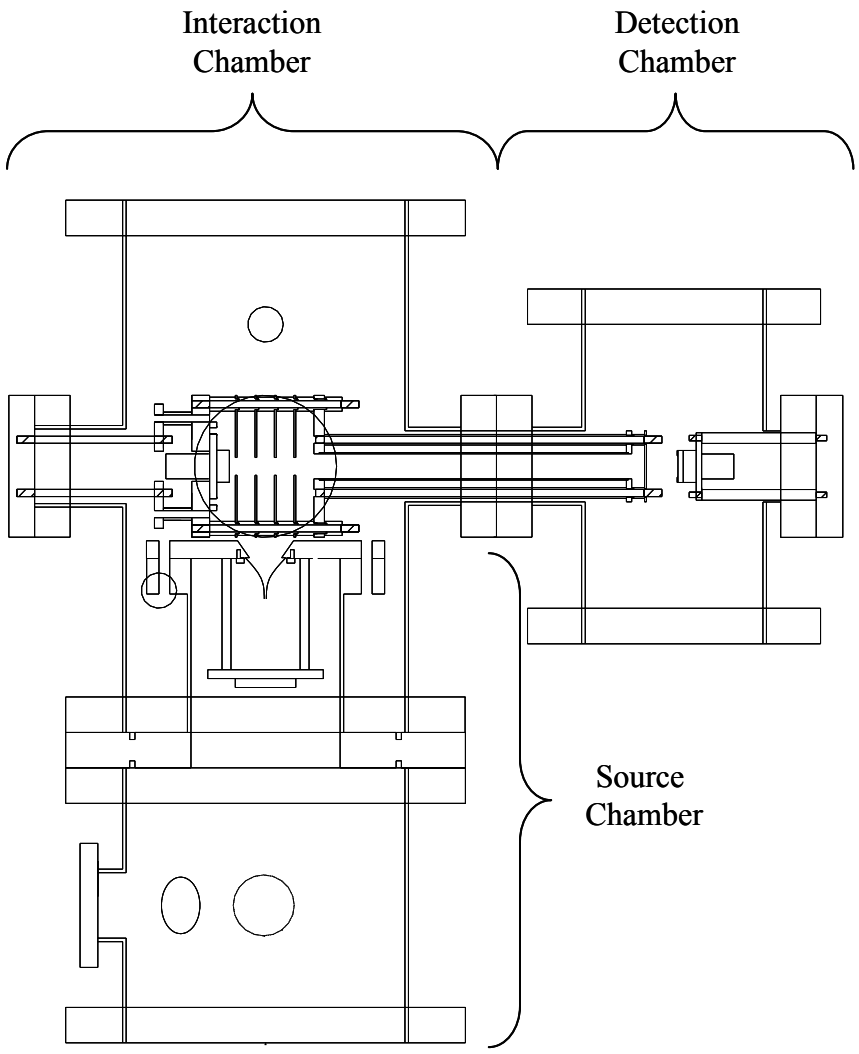

Figure 2.3.1: Cross section (to scale) of the vacuum apparatus. The set-up consists of three chambers, each connected to a separate pump. The source chamber holds the gas nozzle and is pumped by a diffusion pump. It is separated from the interaction chamber by a beam skimmer. The interaction chamber holds the field optics, between which the molecular beam crosses the laser beams. It is pumped by a turbo molecular pump. The detection chamber holds the ion MCP and is pumped by a second turbo molecular pump.

The addition of the skimmer results in an increase in the signal to noise ratio. This is observed as a decrease in the baseline for bound Rydberg state frequency spectra recorded using pulsed field ionisation (figure 2.3.2). However, due to the smaller gas flow reaching the interaction region, the overall signal intensity is decreased reducing the detection efficiency of bound states with a principal quantum number of less than 32.

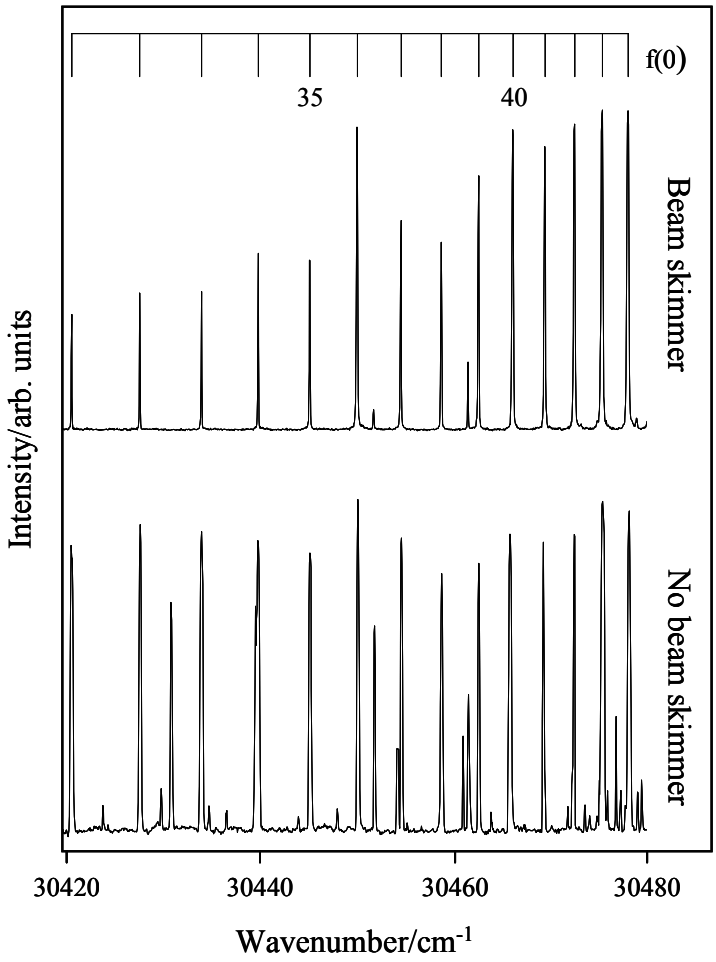

Figure 2.3.2: Pulsed field ionization spectra recorded with and without a molecular beam skimmer. The spectrum recorded with a beam skimmer shows a flatter background line and thinner peaks. These are due to an increase in the quality of the molecular beam at the point where it crosses the laser, and also a decrease in the pressure of the interaction/electron detection chamber. The comb shows the expected positions of the f(0) Rydberg series, labeled using $l(N^+)$ where l is the orbital angular momentum of the Rydberg electron, and N^+ is the rotational angular momentum of the ion core. The x-axis is wavenumbers and the y-axis is intensity of the signal in arbitrary units.

2.4. Time-of-flight

A linear time of flight set-up consists of an array of field plates used to extract and then direct charged species towards a detector. The external field applied to the plates accelerates all species at the same point in the acceleration region to the same energy. Particles of the same kinetic energy, but different masses will travel at different

velocities making it possible to separate particles of different mass during a long field free time-of-flight. The point at which the laser beams perpendicularly cross the skimmed molecular beam is designated the interaction region. This is located midway between two field plates (interaction plates) separated by 10 mm. Behind each of these plates is located another plate that is connected to ground.

For electrons to be detected a negative electric field is pulsed onto the interaction plate furthest from the electron detector, with the opposite plate held at ground. The potential generated accelerates electrons towards the detector. Due to the small mass of an electron the time of flight from the acceleration region to the detector is on the order of a few ns.

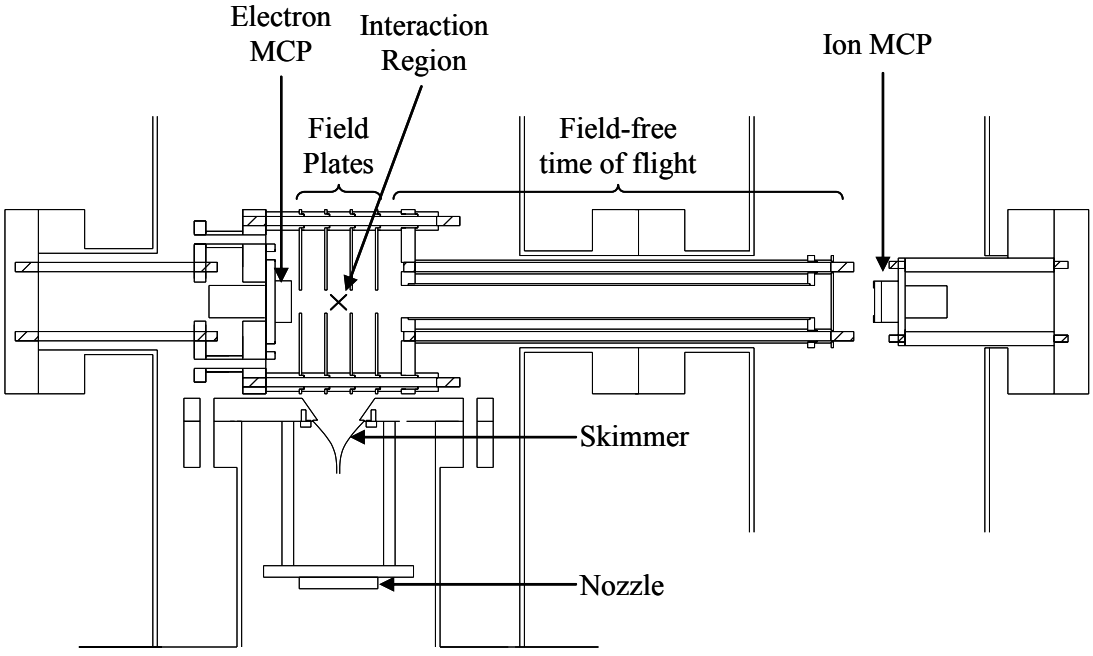

Figure 2.4.1: To scale cross section showing time of flight apparatus. The X marks the point at which the molecular beam perpendicularly crosses the laser beam (out of page). A pulsed electrical field is applied to a field plate on one side of the X to send charged particles to the opposite detector. The other field optics are held at ground.

For ions, the polarity of the pulsed field and the field plate onto which it is directed are swapped. The ions are accelerated out of the acceleration region, and directed

along a field free time-of-flight tube 179 mm in length. The time taken for an ion of mass m to travel a distance d in the zero field region to the detector is given by equation 2.3.1, where U is the applied voltage and q is the charge of the particle.

$$t = \frac{d}{\sqrt{2U}}\left(\sqrt{\frac{m}{q}}\right). \qquad (2.3.1)$$

For the predissociation spectra, the N^+ signal is measured as a product of the predissociation process. Therefore, the signal due to N^+ ions needs to be distinguished from the signal due to NO^+ ions produced by field ionisation of bound Rydberg population. Using equation 2.3.1, the time of flights of the N^+ and NO^+ ions are calculated as 1.77 and 2.59 μs respectively for a total field free distance of 208 mm at 2000 V (*i.e.* 1000 V from interaction region to edge of acceleration region). An oscilloscope trace taken of both the NO^+ and N^+ signals is shown in figure 2.4.2, and confirms these calculations.

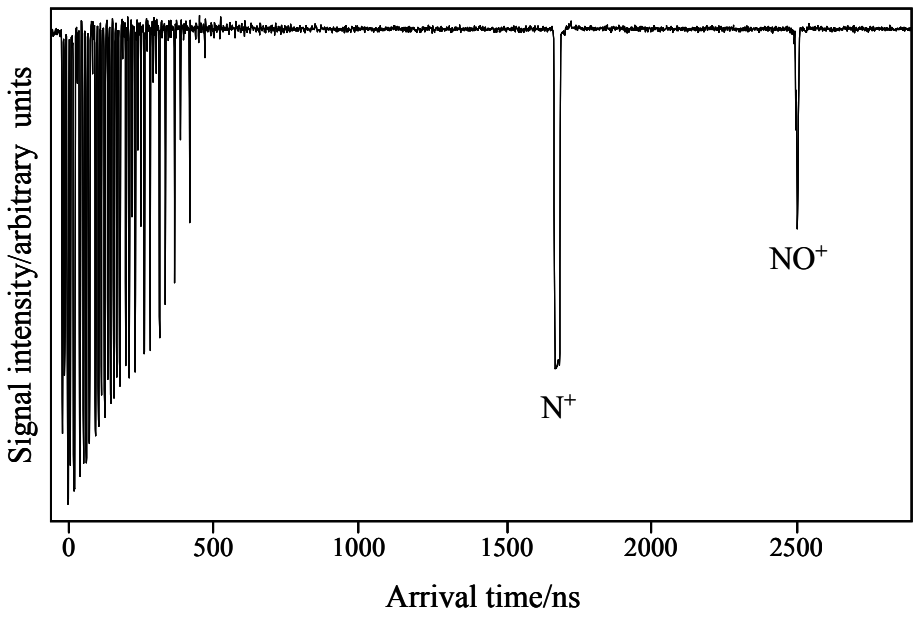

Figure 2.4.2: Oscilloscope trace showing signals due to the arrival of the N^+ and NO^+ ions at the ion MCP detector. The start of the electrical pulse (*i.e.* t_0) is taken as the peak of the electrical noise generated by the pulsed field. The arrival times of both peaks are close to the calculated values of 1770 ns and 2590 ns for the N^+ and NO^+ ions respectively.

The Stark experiments are performed by applying a constant DC field over the interaction region. Applied fields of up to 5 V cm^{-1} are generated with an offset on a low voltage pulse generator (Stanford Research Systems DS345) that is connected to the interaction plate usually attached to ground. To generate fields of up to 160 V cm^{-1} a high voltage wideband amplifier (Tabor Electronics 9100) is added in series with the pulse generator. For fields over 160 V cm^{-1} a high voltage box (Stanford Research System PS350) is used.

Bound state experiments require the pulsed electric field to field ionise the bound electron by reducing one side of the Coulomb potential generated by the ion core. For the frequency resolved experiments, it is then possible to detect either the ionised electron or the corresponding NO^+ ion, depending on the polarity of the ionising field. In general, the electron signal is stronger and easier to detect. The ramped field ionisation experiments of bound states detect the intensity of the released electrons as a function of time. This provides a probe of the path taken to ionisation by the electron and can be used as a "fingerprint" for a particular state. A resistor in series and a capacitor to ground are used to generate ramped high voltage pulses (figure 2.4.3). The value of *R* is increased to increase the rise time of the electrical pulse. The arrival time of electrons to the electron MCP is then monitored using the digital oscilloscope. A second function of the RC circuit is to reduce the high frequency noise entering the signal circuit. A resistor of 47 Ω can be used to slow the high voltage point to a rise time of about 50 ns. As with the unaltered pulse the electron follows a single route to ionisation and so the arrival time of field ionised electrons from a single Rydberg state is effectively constant.

The microchannel plate detectors (MCP) used to detect electrons and ions operate on the same basic principles. Each MCP is made up of a parallel array of flat highly resistive ceramic discs. Each plate is perforated by a large number of tiny parallel

holes running diagonally at a small angle with respect to the surface from one face of the plate to the other. The small angle guarantees that as a charged particle is accelerated into a channel it will strike the wall and eject a cascade of secondary electrons. This sets up an amplifying chain reaction as the released electrons strike the channel wall and eject further electrons. The electrons exit the channel, and are detected by measuring the current at an anode.

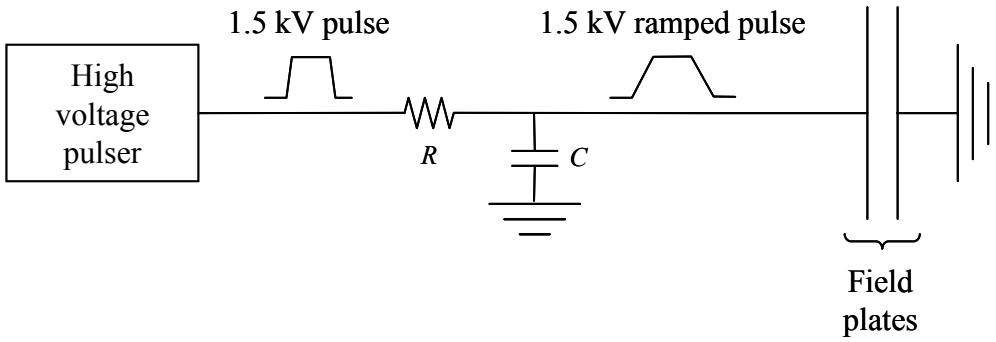

Figure 2.4.3: Schematic showing RC circuit used to slow the rise time of the high voltage electrical pulses before it is applied to a field plate.

The current set-up uses two Hamamatsu MCPs, which both consist of a pair of plates with an effective diameter of 14.5 mm, and a channel diameter of 12 μm. The plates are rotated 180° with respect to each other, producing a chevron shape. Positive ions are measured using a F4655-10 MCP, the front face of which has a large negative bias with respect to the anode that is held at ground. Electrons are detected with a F4655-12 MCP, the front face of which is held at ground, with a large positive bias on the anode. The bias is usually 2000 V, but can be increased for more sensitive experiments.

2.5. Timing

The timing setup controls the relative arrival of the gas pulse, the intermediate and Rydberg laser pulses and the ionising/extracting electrical pulse. For the

predissociation experiments, it is also necessary to control the arrival of the third REMPI laser pulse. Figure 2.5.1 shows the full timing set-up. Initially, a pulse generator (Thandar TG105) generates two TTL (transistor-transitor logic) pulses. The first triggers the pulsed nozzle controller (IOTA ONE), whilst the second is delayed by about 5ms before triggering a digital delay generator (Stanford Research DG535). The pulsed nozzle controller has an adjustable delay which is set at 5121 μs. The delay generator produces three TTL pulses, with independent delays. Two TTL pulses of 10 μs duration trigger the flash lamps (after a 99.1 μs delay) and Q-switch (394.1 μs delay) of the Nd:YAG laser. The remaining trigger (99.1 μs delay) initiates a second delay generator, which after further intervals of 295 and 298 μs triggers a high voltage pulse generator (DEI PVE-4140) and digital oscilloscope (Lecroy Waverunner LT372 500 MHz). The high voltage pulse has a rise time of less than 15 ns and the timing of the rising and falling edge is controlled by the timings of the trigger pulse. The voltage required for the pulse generator is provided by a high voltage power supply (Stanford Research System PS350), which is set to produce pulses with amplitude ± 1.5 to 2.2 kV.

For the predissociation experiments an extra set of TTL pulses are required to trigger the flash lamps and Q-switch for the second Nd:YAG. The trigger pulse comes from the first DG535 delay generator, and has the same timings as the flashlamp trigger. It is sent to a third DG535 delay generator, which waits for 20 μs before triggering another delay generator. This delay generator (Quantum Computers Plus 9514PG) then triggers the flashlamps, before triggering the Q-switch 275 μs later.

The timings are regularly optimised to generate the maximum signal. The Q-switch trigger is altered to optimise the power out of the Nd:YAG. The timing of reference point A (corresponding to 99.1 μs) out of the first delay generator is used to move all of the experimental triggers an equal amount with respect to the nozzle trigger. The

arrival times of the three laser pulses is observed using a photodiode and the relative arrival of the electrical pulse field can then be optimised. However, the arrival time of the field is kept at least 50 ns after the last laser pulse to avoid the presence of any external fields as the molecules are excited. The predissociation experiments also require optimisation of the arrival of the third probe laser pulse. It was found that the optimum arrival time was less than 10 ns after the arrival of the Rydberg excitation laser pulse (Sirah).

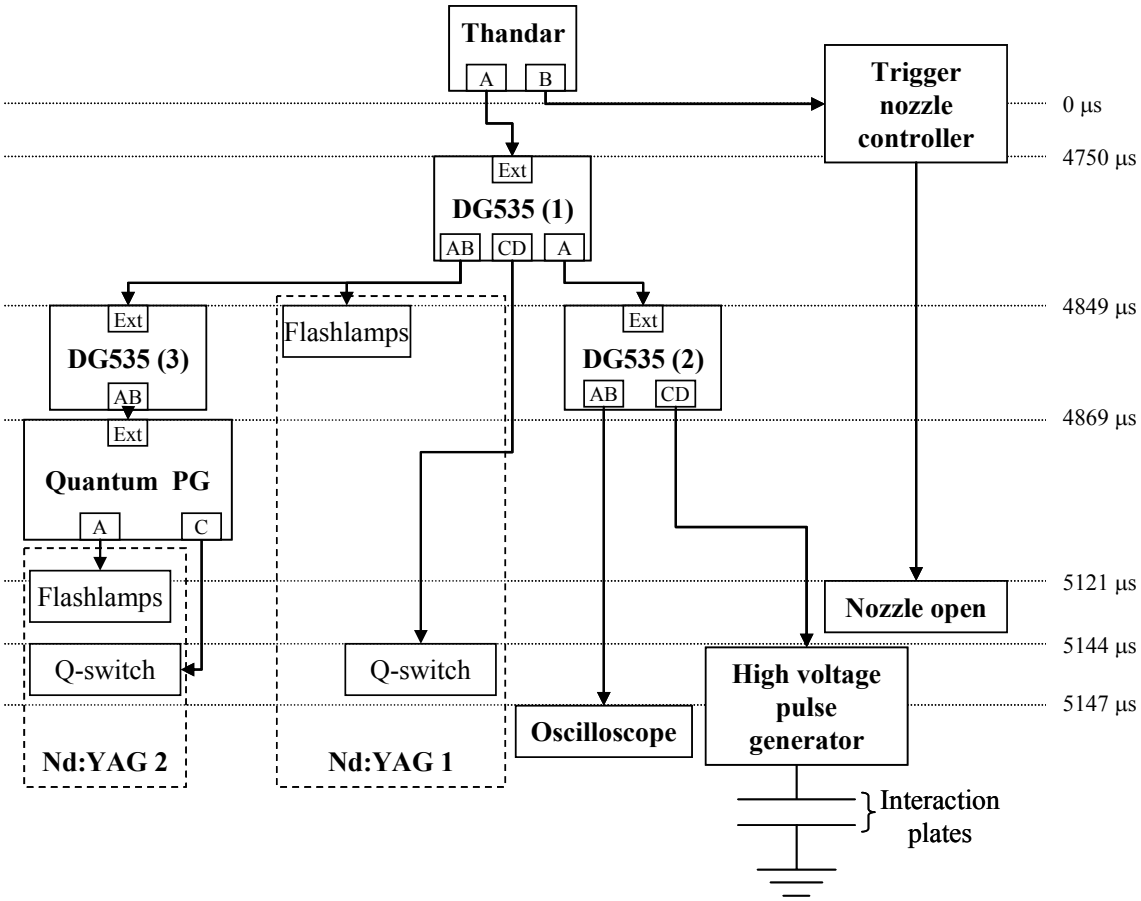

Figure 2.5.1: Schematic showing timing of electronics. Not to scale. Timings on the right indicate delays entered into the four TTL pulse delay generators. The actual timings will be affected by cable lengths and instrument response times.

Due to the lower repetition rate of the data transfer from the oscilloscope to a computer the speed of the measurement system is not synched to individual laser shots and instead takes an average of many events. The recording of these events is

synchronised to the change of the laser wavelength as described in the following section. The data averaging is also necessary to reduce the signal to noise ratio.

2.6. Data collection

A charged particle arriving at the associated detector will create a current on the MCP anode. The signal current is then carried by a BNC cable through a fast pre-amplifier (Ortec VT120C) and monitored on a 500 MHz digital oscilloscope (Lecroy Waverunner LT372) as a function of time. The scope trace is transferred *via* a GPIB (General Purpose Interface Bus) to a PC, where data collection is controlled by one of two Labview programmes.

For the frequency spectra, the relevant data are the signal intensity at a given wavelength. To do this a new Labview programme was created to perform triggered scanning of the Sirah (Rydberg) laser (figure 2.6.1). A switch on the control panel allows triggered scanning to be turned off, and the constant speed scan mode used instead. Constant speed scans are quicker, and more suited to test scans, however the accuracy in the wavelength reading is reduced. Triggered scanning has three input parameters; start wavelength, end wavelength and increment. A basic schematic of the control programme is shown in figure 2.6.2. The triggered scan mechanism relies on two control loops; one on the Sirah control computer and one for the Labview control program on the data collection PC. The Sirah has two BNC ports labelled IN and OUT. These are connected to two user defined signal ports on a shielded connector block (National Instruments BNC 2110) connected *via* a 64 pin connector to a DAQ device (National Instruments PCI-6032E) inside the data collection personal computer (PC). To start, the Sirah control program is initialised, and the laser moved to the starting wavelength. Once in position, the Sirah OUT port is set to high, and this is detected by the Labview control programme triggering data collection. A specified

number of traces are recorded from the oscilloscope, integrated and the average found and recorded to a file. Once saved, the Labview program sends out a set number of TTL pulses to the Sirah IN port.

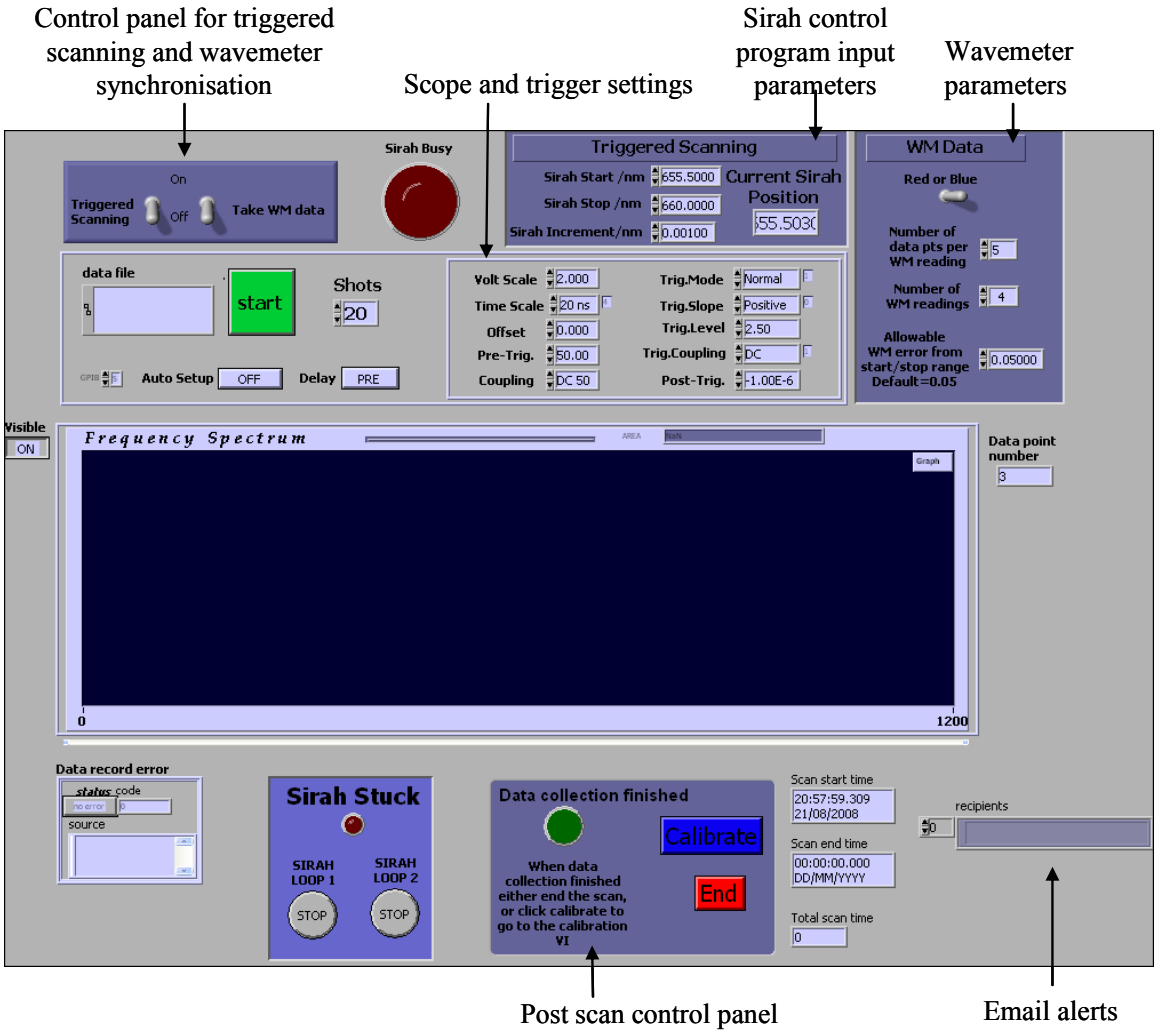

Figure 2.6.1: Front panel of Labview triggered scanning control program. The top left control panels allows triggered or constant speed scans to be recorded, with or without wavemeter data. The other panels along the top set the various experimental parameters. The email alert box will send an email to any addresses entered when the scan is finished, and if the wavemeter fails to take a reading after 15 attempts. When the scan is finished the bottom panel ends the program or opens the calibration subprogram.

It was found that setting the number of trigger events to 2 or more decreased the likelihood of accidental triggering of the Sirah. Once the set number of events has been read in, the Sirah OUT port is set to low and the laser is moved one increment.

When it arrives at the required wavelength, the OUT port is set to high and the data collection starts again. Once the wavelength reaches the end wavelength both control loops end.

The increased accuracy of the triggered scan programme with respect to a constant speed scan arises from the added synchronisation with the wavemeter. The wavemeter control PC is connected to the data collection PC *via* the serial ports. If there is a pause in the reading of the wavelength during a constant speed scan then the wavelength of the laser will have moved from the point at which the intensity information was recorded. An inherent error in the wavemeter means that void values are sometimes read. If this occurs for a large number of consecutive readings then the subsequent calibration of the spectrum will have a larger error. For triggered scanning, the wavelength is measured at one point for every y signal measurements (usually 4). At each measurement point the wavelength is read z amount of times (usually 5) and saved to a file. If the wavemeter reading is far outside the expected range, then another reading is taken until a value within a certain error range is measured. Once the scan is finished a Labview calibration subprogram is initiated, reading in the laser increment, the intensity readings between each wavemeter reading, y, and the number of wavelength readings taken at each measurement step, z.

As shown in the graph on the Labview panel in figure 2.6.3, the wavelength readings are prone to systematic errors leading to two parallel calibration lines. A comparison between spectra calibrated using either line and the expected line positions show that the highest of these lines is correct. The second calibration line is only 0.007 nm below the true value and so cannot be automatically ignored during the scan. The wavemeter also measures points located on another line but this is far from the true value, and so can easily be ignored by the data collection programme during the scan.

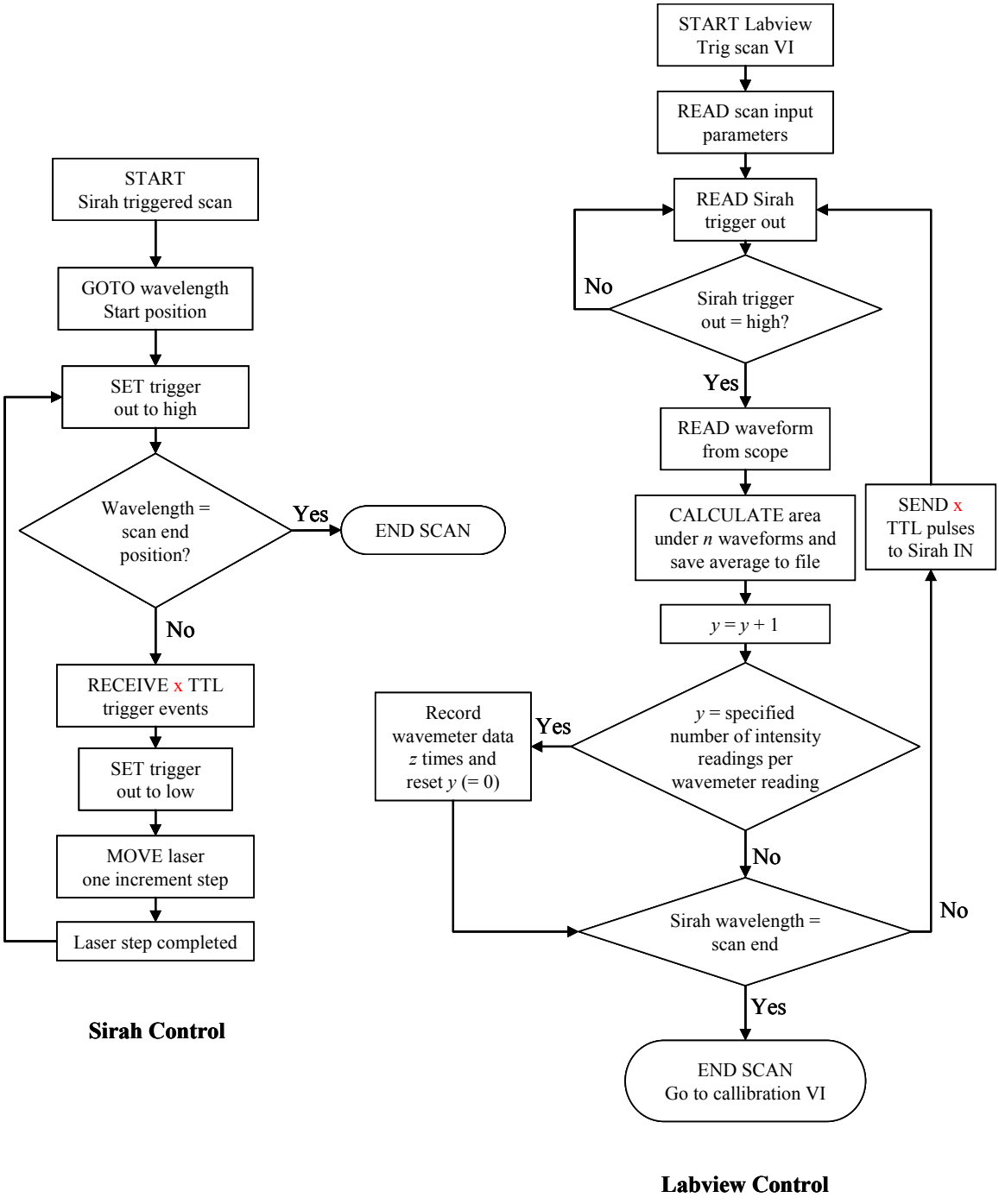

Figure 2.6.2: Two flow charts showing the loops that control triggered scanning of the Sirah laser. The left flow chart is the Sirah internal loop. The right flow chart shows the mechanism of the Labview control program assuming that wavemeter data is also to be recorded. Due to the slow connection between the wavemeter and data collection computers the wavemeter is only read once the intensity has been recorded *y* times.

The calibration subprogram displays the collected wavelength data as a graph. The user must choose a point that lies on the true calibration line, by specifying the point

number and correct array. The calibration then moves along this true line, taking averages of data lying within a range smaller than 0.0005 nm. If no data points can be found along the expected true calibration line then the identical gradient of the parallel incorrect calibration line can be exploited by taking a point from this line, some number of wavelength data points along. If no wavelength within the error range can be found, then an approximate step is added, using the laser increment per intensity reading and number of intensity readings per wavemeter reading. Once the average calibration line is calculated then a spline is performed between each data point to give each intensity point a corresponding wavelength value. A read out panel details the method by which each wavelength step was calibrated, giving an idea of the accuracy of the calibration process.

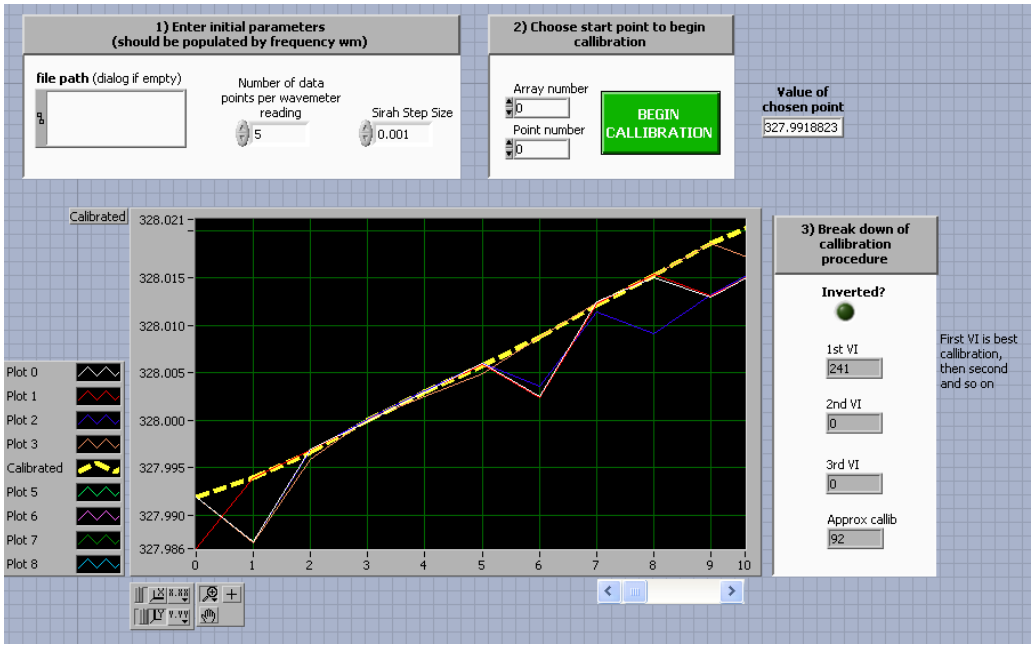

Figure 2.6.3: Labview calibration program front panel. The wavelength file is read as a number of arrays (coloured solid lines). Once the calibration is performed the calculated value is displayed on the graph (dotted yellow line) allowing it to be checked against the measured values.

Labview is not naturally suited to this kind of algebraic operation and a FORTRAN program was also written to simplify the calibration method. However, the accuracy

of the Labview programme is comparable and offers the advantage of a user interface that links directly to the triggered scan control programme. This allows the calibration to be quickly performed and checked against the measured data as soon as a frequency scan is finished.

2.7. Summary

This chapter has described the basic experimental set-up used to investigate the Rydberg states of NO in the frequency domain. The Rydberg states are accessed *via* a resonance enhanced multiphoton excitation scheme. The Rydberg states are then probed by a secondary technique to create ions or electrons. The bound states are probed by field ionisation using a high voltage pulsed field. The field ionisation process with pulses of varying rise times is also investigated to give ionisation profiles as a function of time. The predissociating states are investigated by measuring the nitrogen fragments of the predissociation process using a (2+1) REMPI scheme to ionise the nitrogen atoms produced. An electrical field perturbation can be added to the interaction region to investigate the Stark effect on Rydberg states.

3. The Spectroscopy of NO

3.1. Introduction

All Rydberg systems other than atomic hydrogen possess a finite sized core. The interaction between the Rydberg electron and the inner structure of the core lifts the degeneracy of states with low orbital angular momentum and leads to complex spectroscopy. The spectroscopy of molecular Rydberg systems is further complicated by the vibrational and rotational energy of the core. Each rovibrational state of the core has an associated set of Rydberg series, leading to a high density of states. Electron-core interactions also allow the Rydberg electron to decay *via* interactions with the dissociative and ionisation continua. A state that is degenerate with a dissociation continuum has a non-zero probability of moving onto the dissociative surface causing the core to fragment (predissociation). States above the first ionisation limit can decay into the ionisation continuum of a lower rovibrational state (autoionisation).

NO is an ideal system to study molecular Rydberg states experimentally. The ionisation limit can be easily reached using the output of two commercially available lasers. This allows bound and predissociating states to be investigated as well as autoionising states above the first ionisation limit. It is also an attractive system to study because the closed ground state configuration of the NO^+ molecular ion has no core angular momentum, which as a result simplifies theoretical treatments. The spectroscopy of NO has been studied extensively over the past half-century. An initial exhaustive study was performed by Miescher and collaborators using high resolution

vacuum ultraviolet (UV) absorption spectroscopy. [37-45]. These studies provided many important observations including the first assignment of the quantum defects of the low angular momentum states ($l \leq 3$) [42] and broadening of the p series, which provided evidence of predissociation [45]. However, absorption spectroscopy probes transitions to many levels in a system simultaneously. The many overlapping absorption bands produce congested spectra making assignment difficult. The development of lasers opened up a new range of spectroscopic techniques; in particular, double resonance techniques offer a distinct advantage over absorption spectroscopy. In this technique, a level is accessed *via* an intermediate resonance and transitions from this intermediate resonance are governed by strict selection rules. Consequently only a few final states are accessed, removing the congestion. Interestingly, Miescher used the laser properties of the $F^2\Delta$ and $C^2\Pi$ levels in NO to probe the rotational structure of the two levels [40]. A population inversion was generated by the lower $C^2\Pi$ level depopulating *via* predissociation. Therefore, by populating the upper $F^2\Delta$ level using an electrical discharge, laser transitions to the rotational levels of the lower state could be observed. Highly excited autoionising states, which lie above the first ionisation limit have been studied extensively using multi-photon ionisation (MPI) [46-50] and photoelectron spectroscopy [51]. These states are coupled to the ionisation continuum of a lower ionic state, and decay to form molecular ions that can then be detected. For example, in the work by Anezaki and coworkers, a laser is tuned to a specific rovibrational level of the $A^2\Sigma^+$ state, and a second is tuned to a one photon transition to a Rydberg state above the first ionisation limit [48]. The autoionising states decay into the NO^+ molecular ion, which is brought into the detection region by a positively charged repeller plate and detected using a channel multiplier. The spectra obtained can be assigned in terms of the ns($\upsilon^+ = 1$), np($\upsilon^+ = 1$), and nf($\upsilon^+ = 1$) Rydberg series. Below the first ionisation limit, bound states have been investigated using collision induced ionisation in a gas cell [52, 53].

However, collision induced ionisation is inefficient for states of low principal quantum number, *n*, and the experimental resolution is poor. Spectral resolution can be increased by using a molecular beam, and a pulsed electric field can then be used to field ionise bound states [31-33] as long as the lifetime of the state is longer than the delay between the laser and field. Four wave mixing has also been employed to observe bound states [54, 55].

There have been many theoretical techniques applied to the investigation of the decay of molecular Rydberg states, both below [56, 57] and above the first ionisation limit where autoionisation and predissociation compete [58-61]. Jungen investigated the f series using a long range model for the interaction of the NO^+ core, and then expanded the method to incorporate the penetration effects of the s and d orbitals, including the s-d orbital mixing [62]. The results were in good agreement with previous emission spectra taken by Huber and Miescher [43].

The excitation scheme employed to excite the Rydberg levels of NO is outlined in the following sections of this chapter, including details of the relevant intermediate and ground energy levels. In the work presented in this thesis, the predissociating states of NO are also investigated, requiring a second excitation scheme to produce N^+ ions. A discussion of the literature and excitation scheme is introduced in Section 3.2.7.

3.2. Excitation scheme

All of the experiments described in this thesis employ a $(1+1')$ excitation scheme to access the bound and predissociating Rydberg states of NO in the range of n = 10 - 100. It is beneficial to use a resonant multi-photon excitation scheme for a variety of reasons. One of the main advantages is the accessibility of the Rydberg states; these states cannot be reached by a one photon transition without the use of a VUV source, which is technically demanding to implement. Another benefit is spectral simplification; many rotational and vibrational states of the ground electronic state are occupied even when using a molecular beam expansion to cool the gas. Therefore, excitation directly from the ground state to a target Rydberg state would involve transitions from all of the occupied rovibronic levels of the ground electronic state, resulting in congested spectra. By exciting a specific rovibrational level of an intermediate state, the subsequent transition to a Rydberg state is from a single initial vibrational and rotational state with well defined quantum numbers. The excitation from the launch state is then governed by the single-photon selection rules. By selecting different launch states transitions can occur to Rydberg series that would otherwise be inaccessible using a single photon, and this allows greater control over the final angular momentum of the Rydberg states accessed.

A schematic diagram of our excitation scheme is shown in figure 3.2.1, and the various levels and transitions are discussed in detail in the following sections. Also shown in figure 3.2.1 is the (2 + 1) REMPI scheme employed to ionise the nitrogen fragments generated *via* predissociation. This is described in more detail in Section 3.2.7.

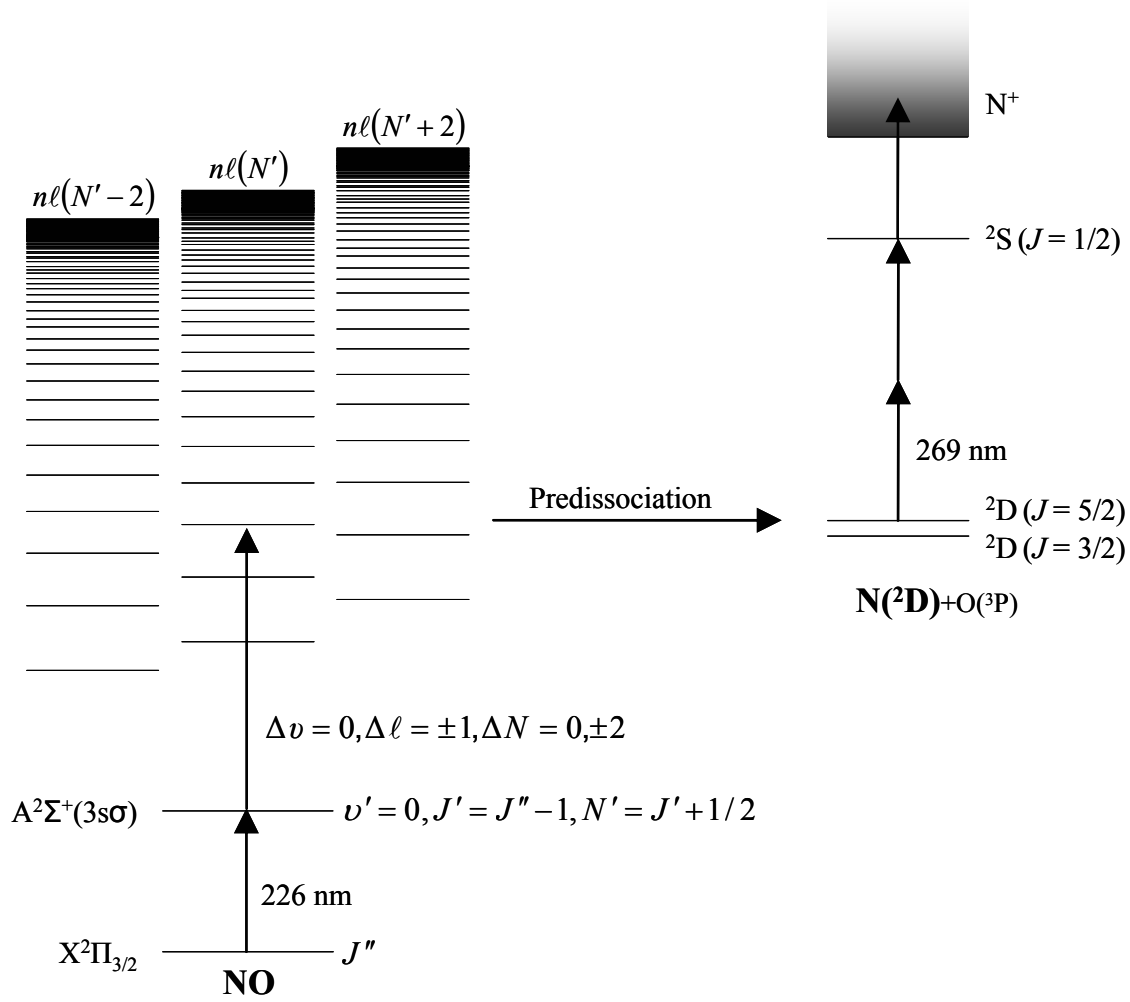

Figure 3.2.1: Schematic excitation scheme showing $(1+1')$ Rydberg transition followed by $(2+1)$ REMPI of the N(^{2}D) fragment produced by predissociation. l is the electronic orbital momentum of the Rydberg electron, N is the rotational angular momentum of the ion core, v is the vibrational quantum number of the core, and J is the total angular momentum. The prime and double prime refer to the first excited and ground state respectively. For the experiments described in this thesis, intermediate states of N' = 0,1,2, and 4 are accessed. The Rydberg levels accessible are labeled as $nl(\Delta N' = 0, \pm 2)$, based on the selection rules discussed in Section 3.2.6.

3.2.1. Angular momentum coupling in NO

To describe the different coupling schemes between the various sources of angular momentum in NO, it is useful to introduce Hund's cases. These are idealized situations used to demonstrate the different angular momentum coupling that can exist

in diatomic molecules. There are five angular momenta involved and it is also necessary to define the projections of the electronic angular momenta onto the internuclear axis:

Angular momentum vector	**Quantum number**	**Description**
L	l	Total electronic orbital angular momentum
S	s	Total electronic spin angular momentum
J	$J = \lvert\mathbf{N}' + \mathbf{S}\rvert \ldots \lvert\mathbf{N}' - \mathbf{S}\rvert$	Total angular momentum
$\mathbf{N}'$	$N' = \lvert\mathbf{N} + \mathbf{L}\rvert \ldots \lvert\mathbf{N} - \mathbf{L}\rvert$	Total angular momentum excluding spin
N	N	Rotational angular momentum of nuclei
Λ	Λ	Projection of total electronic orbital angular momentum onto internuclear axis
Σ	Σ	Projection of total electronic spin angular momentum onto internuclear axis
Ω	$\Omega = \lvert\mathbf{\Lambda} + \mathbf{\Sigma}\rvert \ldots \lvert\mathbf{\Lambda} - \mathbf{\Sigma}\rvert$	Projection of total electronic angular momentum onto internuclear axis

Table 3.2.1: Table listing angular momentum vectors and projections onto internuclear axis necessary to describe angular momentum coupling in diatomic systems.

Most ground states and lowest excited states of diatomics can be described using cases (a) and (b) or an intermediate between these. Rydberg systems can be described using case (d) or (e).

Hund's case (a)

In NO, for low values of total angular momentum J, the $^2\Pi$ ground electronic state can be well described by the angular momentum coupling of Hund's case (a). In this coupling scheme, the total orbital angular momentum **L** is strongly coupled to the internuclear axis, by electrostatic forces. The total electronic spin angular momentum

S is also strongly coupled to the internuclear axis by spin-orbit coupling. Both **L** and **S** precess rapidly around the nuclear axis, and are no longer good quantum numbers; although the projections of **L** and **S** onto the internuclear axis are well defined. These couple so that $\mathbf{\Sigma} + \mathbf{\Lambda} = \mathbf{\Omega}$. This then couples with the angular momentum of the rotating nuclei so that $\mathbf{J} = \mathbf{\Omega} + \mathbf{N}$. **L** and **S** can precess about the axis in either direction. Therefore, they can have either positive or negative values *i.e.* $\Omega = |\mathbf{\Lambda} + \mathbf{\Sigma}| \ldots |\mathbf{\Lambda} - \mathbf{\Sigma}|$. This can lead to two-fold degeneracy, which in certain cases can be lifted by the molecular rotation. The notation for these cases is ${}^{2S+1}\mathbf{\Lambda}_{\mathbf{\Omega}}$

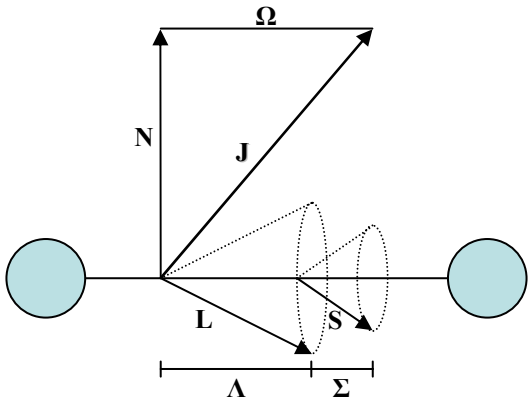

Figure 3.2.2: Vector coupling diagram for Hund's case (a). **L** and **S** are the total orbital angular momentum and total spin angular momentum, and **Λ** and **Σ** are the respective projections onto the internuclear axis. **Ω** is the total projection of electronic angular momentum onto the internuclear access *i.e.* **Λ** + **Σ**. **N** is the total rotational angular momentum of the nuclei and **J** is the total angular momentum.

Hund's case (b)

For high values of **J**, the ground electronic state of NO is described as an intermediate coupling scheme between Hund's case (a) and (b). In the case (b) scheme the spin-orbit coupling is weak, **S** is no longer coupled to the internuclear axis, and **Ω** is not well defined. As in case (a), **L** precesses rapidly about the axis, and the projection onto the internuclear axis is **Λ**. **Λ** then couples to the rotation of the molecule so that $\mathbf{N} + \mathbf{\Lambda} = \mathbf{N}'$. $\mathbf{N}'$ then couples to **S** to give $\mathbf{J} = \mathbf{N}' + \mathbf{S}$. The notation for these cases is

$^{2S+1}\Lambda^{p}$, where p is the parity of the system. This describes the behaviour of the electron wavefunction, when reflected in the plane of the internuclear axis.

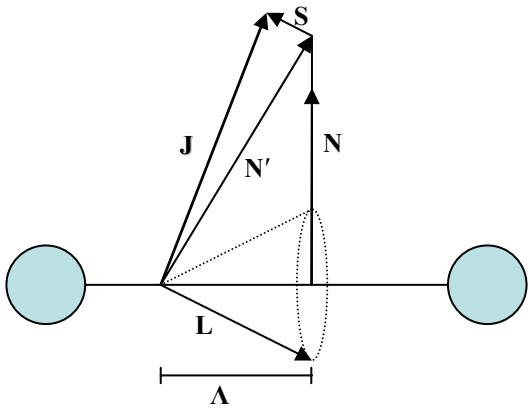

Figure 3.2.3: Vector coupling diagram for Hund's case (b). See text for explanation of symbols Vector coupling diagram for Hund's case a. **L** is the total orbital angular momentum and **Λ** is the projection of **L** onto the internuclear axis. **Ω**. **N** is the total rotational angular momentum of the nuclei, **N′** is the total angular momentum excluding the total spin angular momentum, **S**, and **J** is the total angular momentum *i.e.* $\mathbf{J} = \mathbf{N}' + \mathbf{S}$

Hund's case (c)

Although this case does not apply to NO, it is included here for completeness. For heavy molecules, in which there is strong spin orbit coupling and the electron is under a moderate field, the coupling between **L** and **S** is stronger that the interaction with the internuclear axis and so the projections **Σ** and **Λ** are not defined. Instead **L** and **S** couple first to form $\mathbf{J_a}$, with axial component **Ω**. The projection **Ω** couples to **N** so that the total angular momentum is $\mathbf{J} = \mathbf{J_a} + \mathbf{N}$.

Hund's case (d)

The Rydberg states of NO are best described using a Hund's case (d) coupling scheme, which describes a system in which there is weak spin-orbit coupling and a weak interaction between the electron and the molecular core. The electron spin, **S**, is uncoupled from the nuclear axis and so s is a good quantum number. The rotation of the core, **N**, is independent to the electron and so can be considered as the rotation of

an ion core. The coupling between **L** and **N** is stronger than the coupling between **L** and the axis, so that $\mathbf{L} + \mathbf{N} = \mathbf{N}'$. The resultant angular momentum, $\mathbf{N}'$, then couples with the electron spin so that $\mathbf{N}' + \mathbf{S} = \mathbf{J}$.

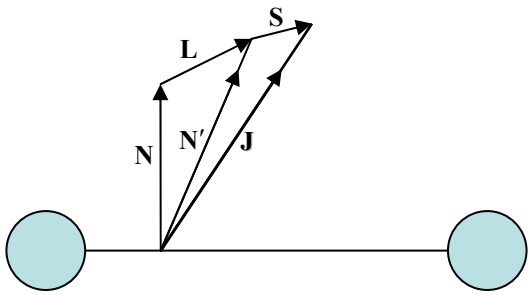

Figure 3.2.4: Vector coupling diagram for Hund's case (d). **L** and **S** are the total orbital angular momentum and total spin angular momentum. **N** is the total rotational angular momentum of the molecular ion core. **L** and **N** couple to form $\mathbf{N}'$, which then couples to the electron spin to form the total angular momentum, **J**.

Hund's case (e)

A Rydberg system with strong spin orbit coupling is best described using a Hund's case (e) coupling scheme *e.g.* the high *n* Rydberg states of O_2. This does not apply to NO; however it is introduced here for completeness. In this scheme **L** and **S** are strongly coupled forming the resultant $\mathbf{J_a}$ but the interaction of **L** and **S** with the internuclear axis is weak. $\mathbf{J_a}$ couples with the rotation of the ion core **N** so that $\mathbf{J} = \mathbf{J_a} + \mathbf{N}$.

3.2.2. The X state of NO

The $X^2\Pi$ ground state of NO can be well described using an angular momentum coupling scheme that is intermediate between Hund's cases (a) and (b); but for low values of the total angular momentum, *J*, it can be described adequately using Hund's case (a). The ground state has a single unpaired electron in a π*2p orbital and so $\Lambda = +1$ and $\Sigma = \pm 1/2$. As introduced in Section 3.2.1, the $\mathbf{\Sigma}$ and $\mathbf{\Lambda}$ axial components couple to form $\mathbf{\Omega}$, which for the $X^2\Pi$ state of NO has values of 1/2 and 3/2. Using the

notation introduced in Section 3.2.1, the two non-degenerate spin orbit components of the electronic ground states are labelled $^2\Pi_{1/2}$ and $^2\Pi_{3/2}$ and are separated by 119.77 cm^{-1} *i.e.* the energy of an electron "spin flip" [63]. In the following equations the $^2\Pi_{1/2}$ and $^2\Pi_{3/2}$ states are labelled using i with a value of 1 and 2 respectively. Assuming a Boltzmann distribution the ratio of the two levels, $P_{3/2}/P_{1/2,}$ at room temperature is 1.09 and so both levels are almost equally populated. Therefore, if Rydberg states were accessed directly *via* a transition from the ground electronic state both spin orbit components would need to be considered.

The total energy, T_i, of a specific rotational and vibrational state can be calculated using equation 3.2.1 [64]. The double prime indicates that we are considering the ground state of the system. It is convenient to calculate the energy of the two spin orbit components of the ground electronic state from the same set of equations. Therefore, the first three terms of equation 3.2.1 contribute to a υ-dependent energy based around an average of the two states. The remaining terms depend on i, with a value of 1 or 2 for the $^2\Pi_{1/2}$ and $^2\Pi_{3/2}$ states respectively.

$$T_i\left(J'',\upsilon''\right)=T_e''+G_\upsilon''-D_\upsilon''+\left(-1\right)^i\times a_\upsilon''/2+B_{\upsilon i}''\left(J''+1/2\right)^2-D_{\upsilon i}''\left(J''+1/2\right)^4+H_{\upsilon i}''\left(J''+1/2\right)^6. \tag{3.2.1}$$

T_e'' is the electronic energy of the state in wavenumber units. The zero energy of the system is taken as the bottom of the $^2\Pi_{1/2}$ potential well. The average electronic energy of the two spin orbit states is

$$T_e''=\frac{a_\upsilon''}{2}, \tag{3.2.2}$$

where a_υ'' accounts for the difference in electronic energy of the two spin orbit states

$$a_\upsilon''=A_\upsilon''-2B_\upsilon''+\frac{2B_\upsilon''^2}{A_\upsilon''}. \tag{3.2.3}$$

D_v'' and B_v'' are the true rotational constants. G_v'' is the total vibrational energy

$$G_v'' = \omega_e''(v''+1/2) - \omega_e\chi_e''(v''+1/2)^2 + \omega_e y_e''(v''+1/2)^3, \quad (3.2.4)$$

where ω_e is the frequency, $\omega_e x_e$ is the first order anharmonicity constant, and $\omega_e y_e$ is the second order anharmonicity constant. The remaining terms are all dependent on the specific spin orbit state being considered and are calculated using the *i*-dependent equations 3.2.5 - 3.2.7. B_{vi}, D_{vi} and H_{vi} are effective rotational constants and represent the rotational energy of the system, using the rotational quantum number, J''.

$$B_{vi}'' = B_v'' + D_v'' + (-1)^i B_v''\left(\lambda_v'' + 2\lambda_v''^2 + ...\right), \quad (3.2.5)$$

$$D_{vi}'' = D_v'' + (-1)^i B_v''\left(\lambda_v''^3 + 6\lambda_v''^4 + ...\right), \quad (3.2.6)$$

$$H_{vi}'' = (-1)^i B_v''\left(2\lambda_v''^5 + 20\lambda_v''^6 + ...\right). \quad (3.2.7)$$

λ_v has been defined previously as [64]:

$$\lambda_v'' = \frac{A_v''}{B_v''} \approx 73. \quad (3.2.8)$$

However, in an increasing power expansion the main term must be less than one and so we assume that equation 3.2.8 should be:

$$\lambda_v'' = \frac{B_v''}{A_v''} \cong 0.014. \quad (3.2.9)$$

This assumption would appear to be valid as our calculations of energy levels using equation 3.2.9 agree with the values tabulated in reference [64] and also agree with our own experimental values [32].

The constants used in equations 3.2.1 – 3.2.9 are given in table 3.2.2.

	$X^2\Pi_{1/2}$	$X^2\Pi_{3/2}$
ω_e''	1904.204	1904.04
$\omega_e\chi_e''$	14.075	14.1
$\omega_e y_e''$	0.0077	0.011
i	1	2
A_v''	123.209	
B_v''	1.696	
D_v''	5.47E-06	

Table 3.2.2: Table of constants [63, 64] used to calculate the total energy of the NO ground state. All values are quoted in wavenumbers (cm^{-1}).

3.2.3. The A state

The energy levels of the first excited state of NO are well described using a Hund's case (b) coupling scheme. Using the notation introduced in Section 3.2.1, this state can be labelled $A^2\Sigma^+$. This state is used as an intermediate state, to excite to the higher Rydberg series in our double resonance experiments.

The total energy of the A state, E'_{TOT} is given by [65]:

$$E'_{TOT} = T'_e + G'_v + F'_v , \qquad (3.2.10)$$

where T'_e is the electronic energy with respect to the zero energy of the system *i.e.* the bottom of the $X^2\Pi_{1/2}$ (i = 1) potential well. G'_v is the vibrational energy, and has the same form as equation 3.2.4 but with the double prime, replaced by the single prime to indicate that we are considering an intermediate state.

F_v' is the rotational energy of the intermediate state.

$$F'_{v(J)} = B'_v\left[N'(N'+1)\right] - D'_v\left[N'(N'+1)\right]^2 , \qquad (3.2.11)$$

where

$$B'_{\upsilon} = B'_{\mathrm{e}} - \alpha'_{\mathrm{e}}\left(\upsilon' + 1/2\right) - \gamma'_{\mathrm{e}}\left(\upsilon' + 1/2\right)^2, \tag{3.2.12}$$

$$D'_{\upsilon} = D'_{\mathrm{e}} + \beta'_{\mathrm{e}}\left(\upsilon' + 1/2\right). \tag{3.2.13}$$

N' is the rotational state of the core *i.e.* rotational angular momentum quantum number of a pair of nuclei. υ' is the vibrational quantum number. D'_{υ} is a vibrationally dependent centrifugal distortion correction.

The constants given in table 3.2.3 (all values given in cm^{-1}) were used in equations 3.2.11 – 3.2.13 to calculate the energies of the rotational levels of the A-state.

ω'_{e}	2374.31
$\omega_{\mathrm{e}}\chi'_{\mathrm{e}}$	16.106
$\omega_{\mathrm{e}}y'_{\mathrm{e}}$	-0.0465
T'_{e}	43965.7
α'_{e}	0.01915
B'_{e}	1.9965
D'_{e}	4.9×10^{-6}
γ'_{e}	negligible
β'_{e}	negligible

Table 3.2.3: Table of constants [63, 66] used to calculate the energy of the rotational levels of the $A^2\Sigma^+$ state in equations 3.2.11 – 3.2.13. All values are given in cm^{-1}.

3.2.4. The A to X transition

Transitions from the ground state to the intermediate launch state are governed by the usual selection rules: $\Delta J = 0, \pm 1$ and $\Delta \Lambda = 0, \pm 1$ where J is the total angular momentum quantum number and Λ is the projection of the electronic angular

momentum onto the internuclear axis. The chosen intermediate is the $A^2\Sigma^+$ state corresponding to a transition from the ground state satisfying $\Delta\Lambda$= -1. The intermediate can be well-described by Hund's case (b) coupling scheme. This means that due to spin-rotation coupling each N' rotational state splits into two sub levels of $J = N' \pm s'$, where s' = 1/2 is the spin quantum number of the electron. These two cases are labelled as *f*: the $N' + s'$ state is labelled as f = 1 and the $N' - s'$ state is labelled f = 2. The $X^2\Pi_{1/2}$ and $X^2\Pi_{3/2}$ sub levels of the ground electronic state are labelled i = 1 or 2 respectively as introduced in Section 3.2.2.

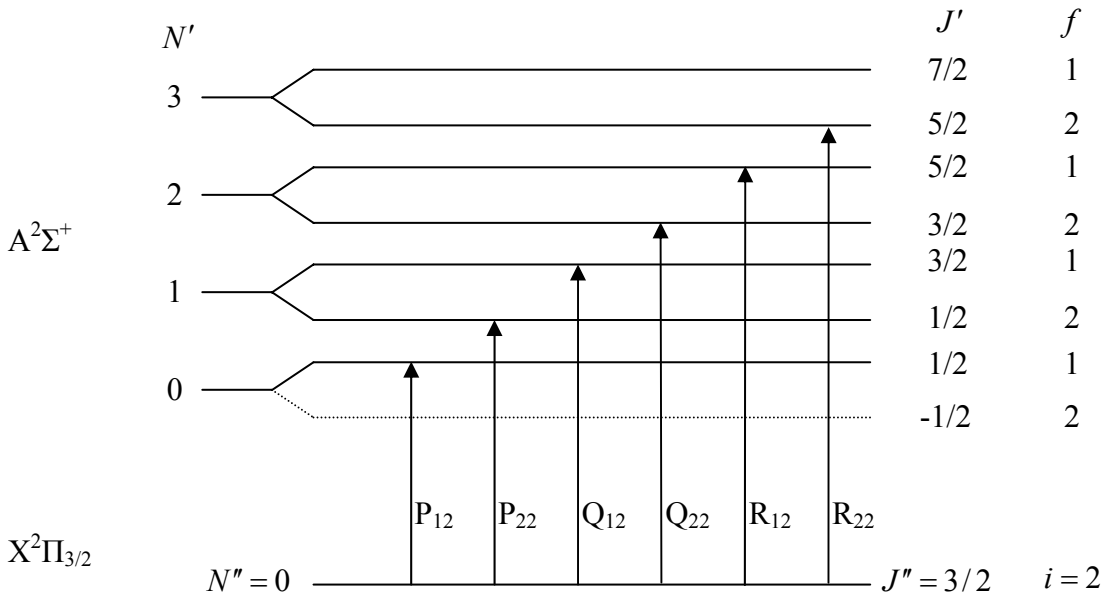

Figure 3.2.5: Schematic diagram showing all possible $A^2\Sigma^+ \leftarrow X^2\Pi_{3/2}$ transitions in NO. All six transitions can be labelled using ΔJ_{if} notation as introduced in the text.

Electronic transitions from the X-state to the A-state are labelled using standard spectroscopic notation *i.e.* P, Q, and R for transitions of $\Delta J = -1,0,+1$. A subscript, *fi*, is used to denote the initial and final rotational terms *i* and *f* as previously defined for the X-state and A-state respectively. Using the ΔJ_{fi} notation, all possible $A^2\Sigma^+ \leftarrow X^2\Pi_{3/2}$ transitions can be separated into six possible branches; P_{12}, P_{22}, Q_{12},

Q_{22}, R_{12}, and R_{22} (figure 3.2.5). The A-X transitions that are relevant to the work presented in this thesis are listed in table 3.2.4.

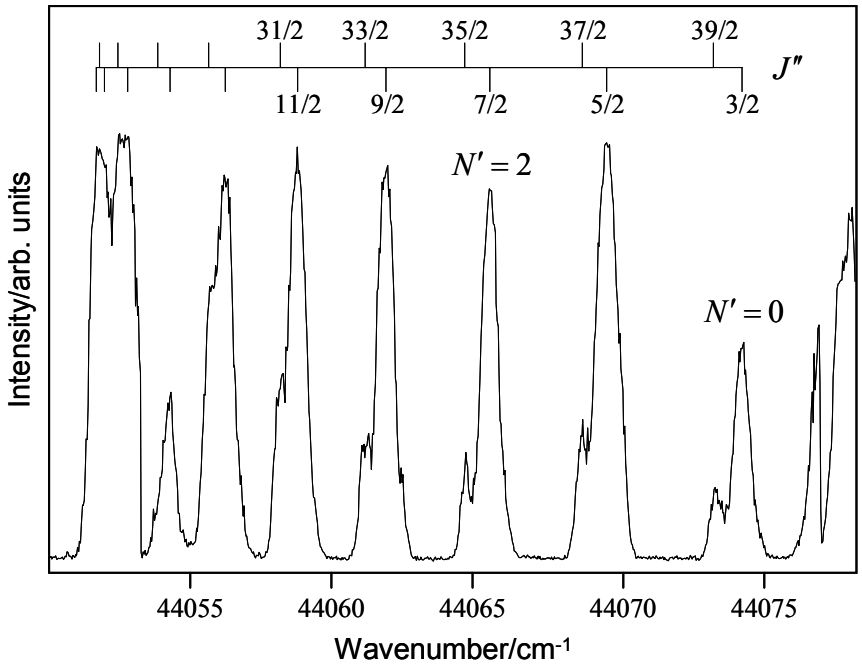

Figure 3.2.6: Frequency spectrum showing a portion of the P_{12} branch of the A←X transition in NO. In the experiments presented in this thesis the N' = 0, 1, 2 and 4 states are used as intermediate launch states. This region of the spectrum is clear of other rotational branches, allowing individual states to be accessed cleanly.

The splitting of the N' states of the $A^2\Sigma^+$ intermediate into the F_1 and F_2 sublevels is less than 0.01 cm^{-1}. With the resolution of the lasers in the current set-up (0.05 cm^{-1}), transitions to different branches of the same N' cannot be resolved. In the work described in this thesis we are concerned only with transitions to $J = N' + 1/2$.

Initial State	Final State	Transition energy/cm^{-1}
$X^2\Pi_{3/2}\ (\upsilon''=0, J''=3/2)$	$A^2\Sigma^+\ (N'=0, J'=1/2, \upsilon'=0)$	44073.77
$X^2\Pi_{3/2}\ (\upsilon''=0, J''=5/2)$	$A^2\Sigma^+\ (N'=1, J'=3/2, \upsilon'=0)$	44069.26
$X^2\Pi_{3/2}\ (\upsilon''=0, J''=7/2)$	$A^2\Sigma^+\ (N'=2, J'=5/2, \upsilon'=0)$	44065.33
$X^2\Pi_{3/2}\ (\upsilon''=0, J''=9/2)$	$A^2\Sigma^+\ (N'=4, J'=7/2, \upsilon'=0)$	44061.99

Table 3.2.4: Table of P_{12} transitions from the ground X state to intermediate $A^2\Sigma^+$ state, used in this thesis (all in cm^{-1}). Transitions are calculated using equations 3.2.1 - 3.2.13, and constants taken from ref [65, 66].

3.2.5. Rydberg state energies

Rydberg states are electronic states with hydrogenic orbits. The electron moves in the Coulomb potential of the ion core, and spends most of its orbit period outside of the core region. The most appropriate coupling scheme is Hund's case (d). The hydrogenic nature of the Rydberg electron allows the energy of the state to be calculated using the well known Rydberg equation, introduced in Chapter 1. For consistency with the notation used throughout this chapter, the Rydberg formula can be written as

$$T_{\upsilon^+N^+Nnl} = T_{\upsilon^+N^+} - \frac{R_{NO}}{(n-\delta_{\upsilon^+N^+lN})^2}, \qquad (3.2.14)$$

where $T_{\upsilon^+N^+Nnl}$ is the energy of a molecular Rydberg state with principal quantum number n and orbital angular momentum l orbiting a molecular ion core with rotational angular momentum N^+, vibrational quantum number υ^+ and total angular momentum excluding spin N. The Rydberg series is converging on the ionisation limit $T_{\upsilon^+N^+}$ of the (N^+, υ^+) rovibrational state of the ion core. R_{NO} is the Rydberg constant for NO as calculated using equation 1.4.2 in Chapter 1, and is equal to 109735.3 cm^{-1} [66]. $\delta_{\upsilon^+N^+lN}$ is the quantum defect of the series with quantum numbers (υ^+, N^+, l, N) as introduced in Chapter 1. The quantum defect describes how the

system differs from the single proton ion core of hydrogen. As the electron penetrates the inner region of the molecular ion core it is no longer shielded by the inner electrons and experiences the full +*Z* attractive potential of the protons in the ion core. The value of $\delta_{\upsilon^+ N^+ lN}$ depends strongly on the degree the electron penetrates the ion core, and so is strongly dependent on *l*. In the matrix diagonalisation calculations described later in this thesis it is necessary to use a Hund's case (b) coupling scheme to describe the electronic energy of the Rydberg state, and then use a frame transformation to Hund's case (d). The Hund's case (b) quantum defects are listed in table 3.2.5, and are labelled $\mu_{l\lambda}$ where λ is the projection of *l* onto the internuclear axis. The frequency combs used to assign various spectra presented in this thesis use the Hund's case (d) defects taken from ref [67] and also listed in table 3.2.5.

The ionisation potential from $X^2\Pi_{1/2}$ to Rydberg series converging to $X^1\Sigma^+(\upsilon^+ = 0, N^+ = 0)$ is 74721.5 cm^{-1} determined by an extrapolation of selected rotational lines [39]. For a Rydberg series with non-zero values of N^+ and υ^+ the ionization potential can be calculated using equation 3.2.15.

$$IP = 74721.5\,\mathrm{cm}^{-1} - F_{\upsilon(J)^+} + G_{\upsilon^+} - G_{\upsilon^+=0} \ . \qquad (3.2.15)$$

	$\mu_{l\lambda}$				δ_l
l	λ = 0	λ = 1	λ = 2	λ = 3	
0	0.210				1.1
1	0.7038	0.7410			0.7
2	0.05	-0.05	0.089		0.02
3	0.0182	0.0172	0.0128	0.0057	0.01

Table 3.2.5: Table of Hund's case (b) and (d) quantum defects as used in equation 3.2.14 taken from ref [24] and [67] respectively.

Literature values of Rydberg states are usually based on the separation between the Rydberg state and the $X^2\Pi_{1/2}$ ground state. When considering the $X^2\Pi_{3/2}$ state, this separation is reduced by the equivalent of the energy difference between the lowest rovibrational levels of the two *i* states, *i.e.* 119.77 cm^{-1}.

$$IP(X^2\Pi_{3/2}) = IP(X^2\Pi_{1/2}) - 119.77\ cm^{-1}. \quad (3.2.16)$$

3.2.6. Transitions from A to Rydberg Series

Table 3.2.6 contains all of the relevant quantum numbers and quantities necessary to describe transitions from the A-state to Rydberg states [68]:

A state	N'	Rotational angular momentum of core
	s'	Spin of electron
	l'	Orbital angular momentum of electron
	J'	Total angular momentum
	p'	Parity of intermediate state
Rydberg state	N^+	Rotational angular momentum of ion core
	s	Spin of Rydberg electron
	l	Orbital angular momentum of Rydberg electron
	p^+	Parity of Rydberg state
Photon	γ'	Angular momentum of photon

Table 3.2.6: Quantum numbers used to describe the Hund's case d Rydberg states and Hund's case b intermediate state.

The transition from the intermediate A-state to a Rydberg state requires the absorption of a photon. The conservation of angular momentum requires that the total angular momentum of the A-state, J', and photon, γ, is equal to that of the total angular momentum of the resultant Rydberg state, $J = N^+ + l + s$.

i.e. $J' + \gamma = N^+ + l + s$. (3.2.17)

The total angular momentum of the intermediate state is the sum of the electron spin and core rotation as described in Section 3.2.4:

$$J' = N' + s' . \qquad (3.2.18)$$

The spin of the outer electron is conserved, *i.e.* $s = s'$, therefore by combining equations 3.2.17 and 3.2.18 both spins cancel to leave

$$N' + \gamma = N^+ + l . \qquad (3.2.19)$$

The rotation spectator model states that the photon imparts angular momentum to the outer electron and not the core. The angular momentum of the Rydberg state is therefore the sum of the intermediate angular momentum, plus the unit angular momentum of the photon

$$l = l' + 1 . \qquad (3.2.20)$$

Equations 3.2.19 and 3.2.20 are combined to give equation 3.2.21. From this expression and the $\Delta l = \pm 1$ selection rule, it is possible to calculate the values of N^+ and l accessed in a one photon transition from a known intermediate state.

$$N^+ = N' + l' . \qquad (3.2.21)$$

Parity must also be considered. The parity of a photon is odd, and the parity of the intermediate is $p' = (-1)^{N'}$. The parity of the final Rydberg state is given by

$$p^+ = (-1)^{N+l} . \qquad (3.2.22)$$

The requirement for an overall change in the parity leads to equation 3.2.23.

$$p^+ p' = -1 . \qquad (3.2.23)$$

Although the $A^2\Sigma^+$ state is referred to as the lowest Rydberg state, and is labelled 3sσ, it is not purely s in character but 94 % s character, 5 % d character, 0.2 % p character

and 0.8 % higher angular momentum character [69, 70]. Therefore, it follows from equation 3.2.20 that transitions to Rydberg states of different electronic angular momentum are possible. Based on the selection rules discussed above, the dominant Rydberg levels accessed from the $A^2\Sigma^+(N'=0, J'=1/2, v'=0)$ intermediate would belong to the *n*p(0) series using $nl(N^+)$ notation where *n* is principal quantum number, *l* is electronic angular momentum and N^+ is rotational angular momentum of the core. There would also be a some contribution from the *n*p(2), and *n*f(2) series and minor contributions from the *n*s(1), *n*d(1) and *n*d(3) series; however, the frequency spectrum shown in figure 3.2.7 is dominated by the *n*f(2) series, with only occasional *n*p(0) states. The p states have short lifetimes due to predissociation, and so decay before the pulsed field can ionise them. The predissociation spectra shown in Chapter 4 are dominated by p series, and also show evidence of s and d series, suggesting that these states also have a short predissociation lifetime.

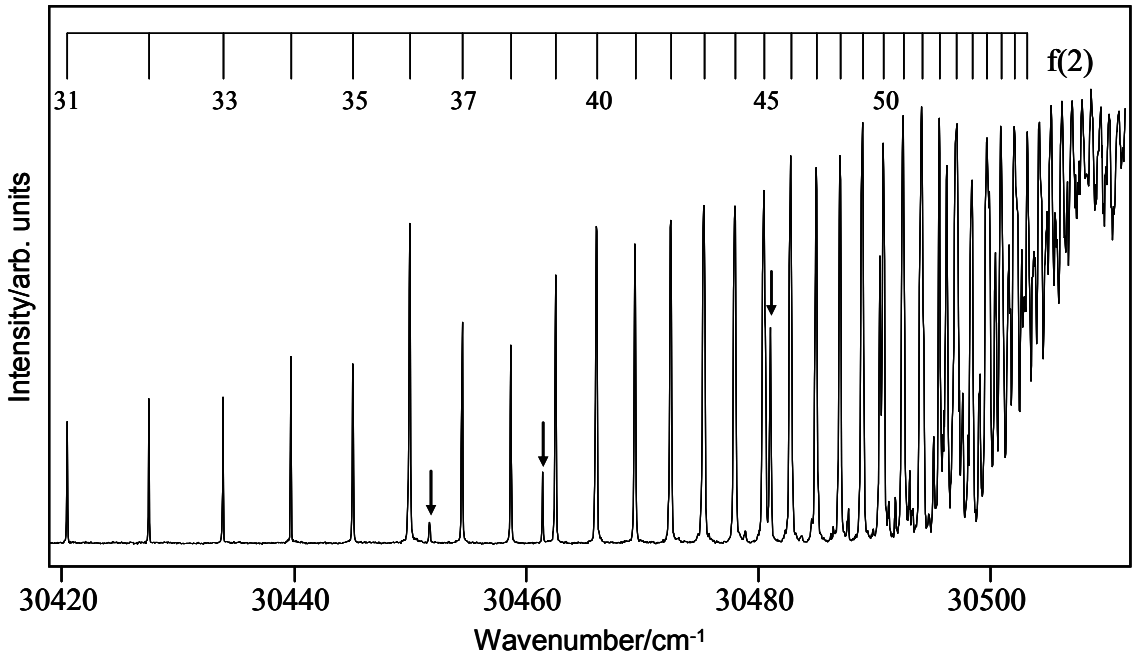

Figure 3.2.7: Pulsed field ionisation frequency spectrum taken using a $(1+1')$ transition *via* the $A^2\Sigma^+(N'=0, J'=1/2, v'=0)$ intermediate state. As discussed in the text, the *n*f(2) series is dominant, with the states of $l \leq 2$ decaying before the pulsed field arrives. The comb shows the zero field positions of the *n*f(2) series. The three peaks labeled with arrows belong to the 40p(0), 43p(0), and 52p(0) states.

3.2.7. Predissociation

When a discrete energy level in a molecular system is excited that is degenerate with a dissociative continuum, there is a non-zero probability that the population will move into the continuum and the core will fragment. A detailed description of predissociation in NO and other species can be found in a review by Kato and Baba [23]. A theoretical treatment is outlined in Chapter 5. NO has a number of dissociation limits but only three are relevant to this thesis as shown in figure 3.2.8; the ground state NO^+ potential curve closely resembles that of a Rydberg state and so can be used when considering potential crossings. In this energy region autoionisation is not possible, and so predissociation is the main decay pathway. The energetically lowest dissociation limit forms $N(^4S) + O(^3P)$ and couples to the NO^+ potential energy curve *via* the $A'^2\Sigma^+$ valence state, which crosses the NO^+ potential at around $v^+ = 2$. The next limit is due to $N(^4S) + O(^1D)$. The third, and most relevant to this thesis, is the $N(^2D) + O(^3P)$ limit which lies 9 eV above the NO ground state. This couples to the NO^+ curve *via* dissociative valence states; $L^2\Pi$, $B''^2\Delta$, $I^2\Sigma^+$ and $B^2\Pi$. $L^2\Pi$ crosses the NO^+ curve around $v^+ = 2$, whilst the other two cross at $v^+ = 0$. $B^2\Pi$ is the major channel (90%) for p to dissociate into $N(^2D)$ due to the Π character of the p state [61]. The s states have a weak dissociation route to the $N(^2D) + O(^3P)$ products *via* the $I^2\Sigma^+$ state although these is a stronger coupling to the $N(^4S) + O(^3P)$ products *via* the $A'^2\Sigma$ state.

The $N(^2D)$ fragment is probed using (2+1) REMPI *via* the $3p(^2S)$ level. Fine structure is present in the form of spin orbit coupling, splitting the ground energy level of the $N(^2D)$ into $J = 3/2$ and 5/2. The $J = 5/2$ level has a much larger signal due to its larger degeneracy therefore we only consider the REMPI transition from the $J = 5/2$ level. The other predissociation products can be ionised using similar (2 + 1) REMPI schemes *via* different intermediate states.

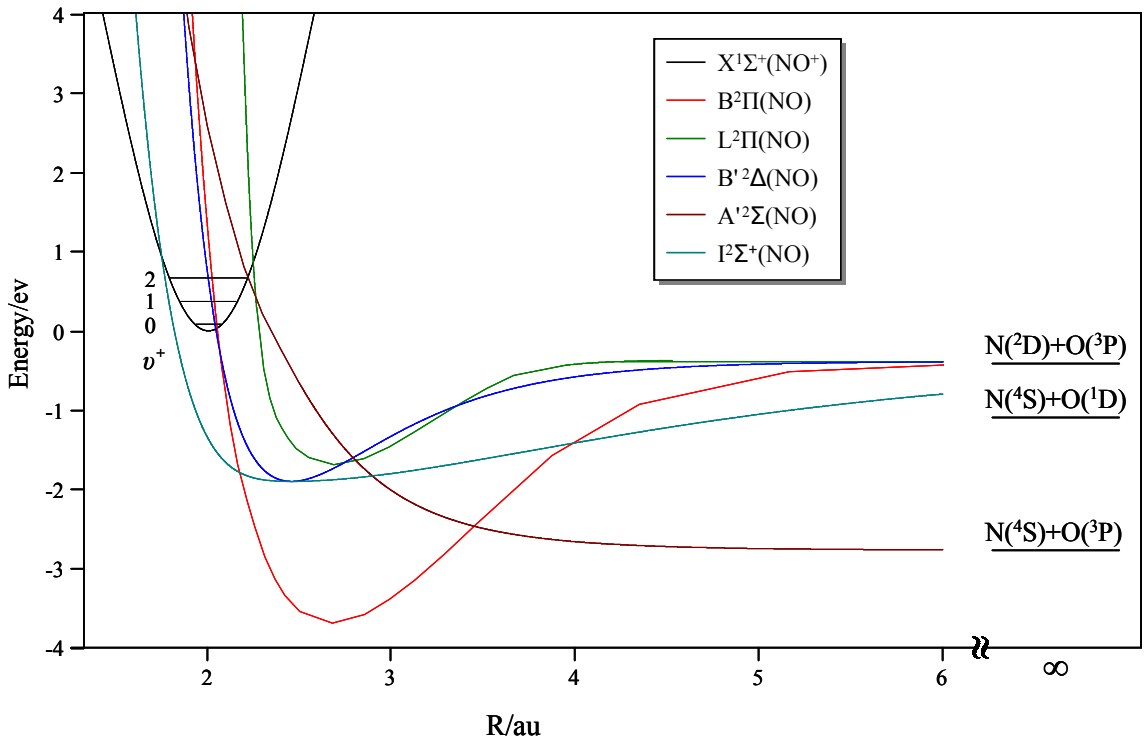

Figure 3.2.8: Schematic showing potential curves important in predissociation. The potential of the ground state of NO^+ closely resembles that of a Rydberg electron. On the right, the two main dissociation limits are shown. The central curves show the valence states that couple the dissociative limits to the Rydberg potential.

The effects of predissociation have been observed in a number of experimental investigations of the Rydberg states of NO [40, 48, 54, 71]. However, it was only first probed directly by Gad and Jusinski in 1989 [72]. Two photons at 268 - 279 nm were used to access the high Rydberg states and a third photon was employed to ionise the molecule forming NO^+ ions. Two electrodes were placed either side of the interaction region with one held at + 220 V DC with respect to the second. The voltage bias on the electrodes drew the positive ions towards the second electrode, and the current generated was then converted by an analogue processor and recorded. A second laser at 269 nm was then introduced, and an enhancement of the total ion count was observed. This can be explained in terms of a (2 + 1) REMPI scheme of atomic nitrogen (as shown in figure 3.2.1). Two photons of 269 nm correspond to a $^2S_{1/2} \leftarrow {}^2D_{5/2}$ transition in atomic nitrogen, from which a third photon of 269 nm can ionise to

form N^+. Therefore, upon application of the second laser, $N(^2D)$ formed *via* predissociation is ionised and the total ion count ($N^+ + NO^+$) increases. However, the experimental resolution was insufficient to resolve fully the different signals due to N^+ and NO^+. An extensive study of predissociation in NO was undertaken by Fujii and Morita, in which one laser was used to scan through Rydberg levels, and a second was tuned to a particular (2 + 1) REMPI pathway of nitrogen. The NO^+ and N^+ signals were separated by their time of flights along a Wiley-McLaren mass spectrometer allowing cleaner spectra to be obtained [73-77]. Fujii and Morita also employed fluorescence dip spectroscopy and NO^+ detection to observe the excitation efficiency of Rydberg levels and subsequent autoionisation. When analysed in conjunction with (2+1) REMPI of nitrogen it was then possible to investigate the competition between predissociation and autoionisation [74]. In these experiments, a first laser was fixed to be in resonance with the $A^2\Sigma^+(v' = 1, N' = 0) \leftarrow X^2\Pi$ transition and a second scanned through the $nl(v^+ = 1) \leftarrow A^2\Sigma^+(v' = 1, N' = 0)$ transition. Monitoring the NO^+ ion signal produced an autoionisation spectra that showed Rydberg series with orbital angular momentum of s, p and f. However, the (2 + 1) REMPI of the $N(^2D)$ predissociation product showed a spectrum dominated by the p series with a strongly *n*-dependent contribution from the f states, in which intensity was only observed for states with principal quantum number 8 and 11. No series due to s states were observed due to the rapid decay *via* autoionisation. Calculations showed that the actual rate of autoionisation was four times larger for the p Rydberg states than it was for the s Rydberg states illustrating that thinking purely in terms of the individual decay rate can be counter-intuitive, and instead the ratio of the rates due to the two different decay pathways should be considered. In the case of NO, this ratio favours predissociation for p Rydberg states and autoionisation for s Rydberg states. In these experiments, Fujji and Morita also investigated states below the $v^+ = 0$ ionisation limit where the core is in the lowest ionic state. Therefore,

electronic states could not couple to an ionisation continuum and so were unable to decay *via* autoionisation. In this region, the p states again dominated the N(^{2}D) predissociation spectrum, but now the s states had a larger contribution. The appearance of the f Rydberg states again depended strongly on the principal quantum number, *n*. A (2 + 1) REMPI from the ^{4}S state of atomic nitrogen showed that states absent in the N(^{2}D) predissociation yield spectrum, appeared in the N(^{4}S) yield spectrum. Therefore, the N + O products formed by predissociation of the f Rydberg states of NO showed a strong dependence on *n*.

4. The Stark effect in the predissociating Rydberg states of NO

4.1. Introduction

Weakly bound Rydberg states are highly susceptible to external perturbations making them ideal systems to study the effect of an applied electric field. An external field mixes states with angular momentum $\Delta l = \pm 1$ allowing the observation of states that can not be accessed *via* a one photon transition in zero field. A molecular system has a high density of states and many more inter series interactions. This large number of states provides a larger and more complex testing ground for various molecular parameters such as inter series coupling, quantum defects and decay rates. NO provides an ideal testing ground for these types of experiments; the Rydberg states are accessible and are easily field ionised whilst the closed shell structure of the ion core has zero angular momentum. Numerous groups have investigated the spectroscopy of the Rydberg states of NO, with many focusing on the autoionising states which lie above the first ionization limit [46-50]. Below the ionization limit, there have been a number of studies of the bound states usually using pulsed field ionisation [31-33]. However, this method can only detect long lived states that are not susceptible to predissociation. Initial investigations by Fujii and Morita [74] studied the predissociation of the low Rydberg states (n = 8 – 12) in zero field by probing the fragmentation products, which is the methodology used for the predissociation studies presented in this thesis. The effect of an external field on the Rydberg states of NO has been investigated in the autoionising [25] and bound states [32], and on the predissociating Rydberg states of molecular hydrogen [78, 79]. The high Rydberg

ZEKE bound states (n = 70 – 120) have been investigated using pulsed field ionisation, and the predissociation lifetimes determined from the observed linewidths [24]. However, there have been few Stark studies on the predissociating states of NO. A recent paper by Clarson and co-workers investigated the Stark effect in the low Rydberg states of NO (n = 13 – 16) [80].

Complementary to these, the experiments presented in this chapter focus on the intermediate Rydberg states (n = 25 – 30) converging to the $v^+ = 0$ ionisation limit. In this region, the rotational and electronic spacings are comparable leading to the breakdown of the Born Oppenheimer approximation. The bound states in this region have already been investigated within our group, and the analysis of both bound and predissociating spectra provides an almost complete picture of the Rydberg state dynamics. The analysis of the spectra is carried out using a matrix diagonalisation technique based on that developed by Vrakking [24]. This will now be introduced.

4.2. Analysis of Stark spectra

4.2.1. Introduction

Two approaches are usually utilised for the theoretical description of Rydberg states and the effect of an external electric field. Matrix diagonalisation is used to interpret and simulate the spectra presented in this thesis and will be discussed in detail in the following sections. Briefly, it is a perturbative technique in which a Hamiltonian matrix is constructed using a diagonal zero field basis set and an off-diagonal perturbation due to the field. The matrix is then diagonalised to obtain the eigenvalues and eigenvectors which are equivalent to the energy and the weighting of the basis set states in the mixed Stark state respectively. A complementary theoretical technique is multi-channel quantum defect theory (MQDT), in which the Rydberg molecule is

considered as a scattering problem between the electron and ion core, and a scattering matrix is constructed. The behaviour of the electron is separated into a number of regions separated by frame transformations, and each region has a number of channels; a channel is a set of discrete and continuum states for which the electron and core configuration is the same, except for principal quantum number, *n*. If no external field is present, then the system can be separated into two regions. Far from the core the electron moves slowly in the Coulomb potential of the ion core, $V = -1/r$, and the inverse Born Oppenheimer approximation is valid. The core wavefunction, labelled using $|i\rangle = |v^+ N^+\rangle$, is represented by the vibrational, v^+, and rotational, N^+, quantum numbers of the ion core and can be described using a Hund's case (d) coupling scheme. In the core region the electron moves with a large velocity compared to the motion of the core, and the Born Oppenheimer approximation is valid. The large velocity results in the electron spending little time in the core region, and so the core structure can be approximated as fixed. The vibration of the nucleus is now represented as a fixed internuclear distance, *R*, and the ion core couples the electron to the internuclear axis, Λ. The wavefunction is labelled with $|\alpha\rangle = |R\Lambda\rangle$ and follows a Hund's case (b) coupling scheme. As the electron moves through the core region, an electronic reaction matrix can scatter the electron into a different channel. As the electron moves between these two regions a transformation matrix, $U_{i\alpha}$, projects from a $|v^+ N^+\rangle$ channel to a $|R\Lambda\rangle$ channel and vice versa. If an external field is added, a third region must be defined. The potential for this region now includes the effect of the field, $V = -1/r + Fz$, and a further frame transformation is required. MQDT has been used to simulate Stark spectra of the Rydberg series in a variety of systems [81-83], including NO [25, 80].

4.3. Matrix diagonalisation

4.3.1. Introduction

Matrix diagonalisation is a perturbative technique involving the construction of a matrix containing the various Hamiltonians required to describe the system. This is demonstrated in equation 4.3.1, in which the Hamiltonian for the whole system, H, is a function of the unperturbed zero field Hamiltonian, H_0, and the perturbative Stark Hamiltonian H_F.

$$H = H_0 + H_F \,. \tag{4.3.1}$$

The form of the Hamiltonians used depends on the chosen basis set, and therefore this choice has an effect on the complexity and speed of the diagonalisation calculation. The basis set should be chosen so that the zero field Hamiltonian, H_0, is close to diagonal. The off-diagonal elements resulting from the perturbation, H_F, are then added. After the diagonalisation calculation, the eigenvalues and eigenvectors can be easily found. The eigenvalues at field F correspond to the energy of a Stark state, E_k, and the eigenvectors give the weighting of the zero field basis set states present in the Stark state. For example, if a Hund's case (d) basis set is chosen, then the calculated Stark states, φ_k, will be a linear combination of the case (d) basis states, $\varphi_i^{(d)}$, of the form shown in equation 4.3.2

$$\varphi_k = \sum_i c_{ki} \varphi_i^{(d)} \,. \tag{4.3.2}$$

The work presented in this thesis follows the form of the matrix Hamiltonian developed by Vrakking [24], which is a hybrid quantum defect/diagonalisation approach. All of the expressions used in the matrix calculations are taken from [24, 25].

A schematic of the Hamiltonian matrix for NO is shown in figure 4.3.1, showing just the low angular momentum states ($l < 4$) for a single n. The zero field Hamiltonian H_0 runs mainly along the diagonal (*i.e.* the sum of the electronic and rotational Hamiltonians), but there are also off-diagonal terms specific to NO. These will be described in the following sections.

N^+			0				2								
	l		s	p	d	f	s	p			d				
		N	0	1	2	3	2	1	2	3	0	1	2	3	4
0	s	0	H_{el}	H_F							H_{sd}				
	p	1	H_F	H_{el}	H_F			H_{core}							
	d	2		H_F	H_{el}	H_F	H_{sd}						H_{core}		
	f	3			H_F	H_{el}									
2	s	2			H_{sd}		$H_{el} + H_{rot}$			H_F					
	p	1		H_{core}				$H_{el} + H_{rot}$			H_F		H_F		
		2							$H_{el} + H_{rot}$			H_F		H_F	
		3					H_F			$H_{el} + H_{rot}$			H_F		H_F
	d	0	H_{sd}					H_F			$H_{el} + H_{rot}$				
		1							H_F			$H_{el} + H_{rot}$			
		2			H_{core}		H_{sd}	H_F		H_F			$H_{el} + H_{rot}$		
		3							H_F					$H_{el} + H_{rot}$	
		4								H_F					$H_{el} + H_{rot}$

Figure 4.3.1: A schematic showing a portion of the Hamiltonian matrix corresponding to the states of $l < 4$ for a single Rydberg state, n. The diagonal elements correspond to the electronic and rotational Hamiltonians. The off diagonal elements in black are the short range coupling Hamiltonians due to sσ-dσ and $l - l$ couplings. The red elements are due to couplings induced by the external electric field.

4.3.2. Diagonal elements of H_0

The choice of basis set determines the efficiency of the diagonalisation calculation on the Hamiltonian matrix. Rydberg states are best described using a case (d) basis, and the form of the rotational Hamiltonian in this basis is diagonal. The case (d) rotational Hamiltonian is shown in equation 4.3.3, where $B_0 = 1.987892$ cm^{-1} is the rotational

constant and $D_0 = 5.64 \times 10^{-6}$ cm^{-1} is a centrifugal distortion term for the NO ion core with $v^+ = 0$ [66]. N is the total angular momentum excluding spin, N^+ is the rotational angular momentum of the ion core and l is the electronic orbital angular momentum.

$$H_{\text{rot}}^{(\text{d})}\left[l, N, N^+; l, N, N^+\right] = B_{v^+} N^+(N^+ + 1) - D_{v^+}[N^+(N^+ + 1)]^2 \ . \qquad (4.3.3)$$

The case (d) rotational Hamiltonian is diagonal, whilst the case (b) rotational coupling terms are complicated. However, when considering the electronic part of the Hamiltonian it is advantageous to use the near-diagonal case (b) electronic Hamiltonian. The case (b) Hamiltonian is given in equation 4.3.4 in terms of $\mu_{l\Lambda}$, the case (b) quantum defect, and v, the effective principal quantum number. Λ denotes the projection of the orbital electronic angular momentum, l, onto the internuclear axis. The values used for $\mu_{l\Lambda}$ are listed in table 4.3.1

$$H_{el}^{(b)}\left[l, N, \Lambda; l, N, \Lambda\right] = -\frac{\mu_{l\Lambda}}{v^3}. \qquad (4.3.4)$$

As previously stated, high-n Rydberg states are best described using the Hund's case (d) quantum numbers, l and N^+, and so a case (d) basis is preferential. Therefore, the case (b) electronic Hamiltonian requires a frame transformation to case (d) as given in equation 4.3.5

$$H_{el}^{(d)}\left[l, N, N^+; l', N', N^{+\prime}\right] = \sum_{\Lambda\Lambda'} A_{N^+\Lambda} H_{el}^{(b)}\left[l, N, \Lambda; l', N', \Lambda'\right] A_{N^{+\prime}\Lambda'}, \qquad (4.3.5)$$

where

$$A_{N^+\Lambda} = (-1)^{l+\Lambda-N^+} \begin{pmatrix} l & N & N^+ \\ -\Lambda & \Lambda & 0 \end{pmatrix} (2N^+ + 1)^{1/2} [2/(1+\delta_{\Lambda 0})]^{1/2}. \qquad (4.3.6)$$

$A_{N^+\Lambda}$ is a Clebsch-Gordan coefficient, which describes the overlap between the different angular momentum in the two Hund's cases. The first term is a phase term, the second a 3-j symbol describing the addition of two angular momenta vectors, and the last is a normalisation factor.

For $N^+ = 0$, the diagonal elements are H_{el}. For $N^+ \neq 0$, the diagonal elements are $H_{el} + H_{rot}$.

Λ / l	**0**	**1**	**2**	**3**
0	0.210			
1	0.7038	0.7410		
2	0.05	-0.053	0.089	
3	0.0182	0.0172	0.0128	0.0057

Table 4.3.1: Hund's case (b) quantum defects used in equation 4.3.4. All values are taken from [24] except values for $l = 3$, which are taken from [25].

4.3.3. Non-diagonal elements of H_0

The case (b) electronic Hamiltonian is almost diagonal; however there are a few non-diagonal elements to include due to short range electron-core interactions. The configuration mixing between sσ-dσ in NO has been described in detail by Fredin and co-workers who quantified the mixing as a parameter θ, with a value of 38.7° [84]. The mixing is described using modified forms of the case (b) Hamiltonian (equations 4.3.7 to 4.3.9) and so requires a frame transformation to case (d) using equation 4.3.5. This coupling also exists for the diagonal electronic Hamiltonians with $l = l'$ and $l = 0$ or 2. The off diagonal elements are labelled H_{sd} in figure 4.3.1.

$$H_{el}^{(b)}[s,N,0;s,N,0] = -(\mu_{s\sigma}\cos^2\theta + \mu_{d\sigma}\sin^2\theta)/v_{s\sigma}^{3/2}v_{d\sigma}^{3/2}, \quad (4.3.7)$$

$$H_{el}^{(b)}[d,N,0;d,N,0] = -(\mu_{s\sigma}\sin^2\theta + \mu_{d\sigma}\cos^2\theta)/v_{s\sigma}^{3/2}v_{d\sigma}^{3/2}, \quad (4.3.8)$$

$$H_{el}^{(b)}[s,N,0;d,N,0] = -\frac{\sin^2\theta}{2}(\mu_{s\sigma} - \mu_{d\sigma})/v_{s\sigma}^{3/2}v_{d\sigma}^{3/2}. \quad (4.3.9)$$

A short range electron-core interaction also exists between Rydberg series of the same N and l, in which the quadrupole of the ion core couples states of $\Delta N^+ = \pm 2, \pm 4$. This coupling also exists between series of different l when $l = 0$ and 2. This coupling is labelled as H_{core} in figure 4.3.1 and the case (d) Hamiltonian can be written as

$$H_{core}^{(d)}\left[l,N,N^+;l,N,N^+\pm 2,\pm 4\right]=\sum_{\Lambda\Lambda'}A_{N^+\Lambda}H_{el}^{(b)}\left[l,N,\Lambda;l',N,\Lambda'\right]A_{N^{+'}\Lambda'},$$

where $A_{N^{+'}\Lambda'}$ is of the same form as given in equation 4.3.6.

4.3.4. Matrix elements due to Stark perturbation - H_F

An applied electric field along the z-axis introduces an off-diagonal perturbation, as described by the Hamiltonian in equation 4.3.11 and labelled H_F [24].

$$H_{\mathrm{F}}^{(\mathrm{d})}\left[l,N,N^+;l',N,N^{+'}\right]=-eF\left\langle vlN^+NM_N\left|z\right|v'l'N^{+'}N'M'_N\right\rangle, \qquad (4.3.11)$$

which using the Wigner-Eckart theorem can be expressed as

$$H_{\mathrm{F}}^{(\mathrm{d})}\left[l,N,N^+;l',N,N^{+'}\right]=-eF(-1)^{N-M_N+l+N^++N'+1}\left[(2N+1)(2N'+1)\right]^{1/2}\times \begin{pmatrix} N & 1 & N' \\ -M_N & 0 & M'_N \end{pmatrix}\begin{Bmatrix} 1 & N & N^+ \\ N' & l' & 1 \end{Bmatrix}\left\langle vl\|r\|vl\right\rangle\delta_{N^+N^{+'}}. \qquad (4.3.12)$$

The last term in equation 4.3.12, $\delta_{N^+N^{+'}}$, is a Kronecker delta from which it can be determined that the mixing of states is governed by $\Delta N^+ = 0$. The first term in equation 4.3.12 is a phase term, and the term in the square brackets is a normalisation factor. The next two terms are 3-j and 6-j symbols, used to describe the addition of angular momentum. The 3-j symbol describes the coupling of the total angular momentum in both states and shows that the field couples states for which $\Delta N = 0, \pm 1$ and $\Delta M_N = 0$. The 6-j symbol describes the mixing of three angular momenta and shows a $\Delta l = \pm 1$ coupling. The next term in equation 4.3.12, $\left\langle vl\|r\|vl\right\rangle$, is a reduced matrix element as given in equation 4.3.13. Considering the reduced matrix element

as a single electron problem allows it to be evaluated using standard angular momentum algebra [85].

$$\langle vl\|r\|v'l'\rangle = \begin{cases} -\sqrt{l+1}\langle vl|r|v'(l+1)\rangle \\ \sqrt{l}\langle vl|r|v'(l-1)\rangle \end{cases} \quad l' = l \pm 1 . \tag{4.3.13}$$

The radial integrals can be calculated using an approach by Edmonds and co-workers, which obtained equation 4.3.14. This approach uses a one electron Coulomb approximation followed by extrapolation to high *n* and so is more reliable for the non-penetrating high-*l* Rydberg states.

$$\langle vl|r|v'l'\rangle = \left\{ \frac{3}{2} v_c^2 \left[1 - \left(\frac{l_c}{v_c} \right)^2 \right]^{\frac{1}{2}} \right\} \sum_{p=0}^{3} \gamma^p g_p(s) , \tag{4.3.14}$$

where $l_c = \max(l, l')$, $v_c = 2/[(1/v) - (1/v')]$, $\Delta l = l' - l$, $\gamma = \Delta l (l_c / v_c)$, $s = v - v'$ and the $g_p(s)$ functions are tabulated in [86].

Transitions to Stark states are governed by a further selection rule for the projection of the total angular momentum excluding spin, M_N, which depends on the relative polarisation of the laser with respect to the electric field. If the laser polarisation is parallel to the electric field, then transitions are governed by $\Delta M_N = 0$. If the two polarisations are perpendicular then the transition is to states of $\Delta M_N = \pm 1$.

4.3.5. Comparison of theoretical techniques

Both matrix diagonalisation and MQDT require a limited basis set, due to computational restrictions. Matrix diagonalisation requires a separate entry for each state resulting in a large matrix, *i.e.* a different matrix element is needed for every combination of n, l, N^+, and N. MQDT requires a smaller basis set; a single channel includes all values of n including the continuum. The inclusion of the continuum in MQDT helps to simplify the treatment of discrete-continuum interactions such as for autoionising states; however the inclusion of the dissociation continuum is non-trivial. Despite the larger basis set, matrix diagonalisation is a computationally simpler technique, requiring only a single calculation to calculate the energy and eigenvectors of a Rydberg state at a given field. On the other hand, MQDT involves a number of matrix operations repeated at each step along a fine energy mesh resulting in a greater number of calculations. A comparison between the two methods carried out by Goodgame and co-workers [25] showed that both techniques were able to accurately simulate autoionising Stark spectra.

Ten to fifteen years ago, matrix diagonalisation techniques were severely limited by computing power. Today, modern computers are able to cope with the large basis sets required for matrix diagonalisation approaches and it is now a viable option for calculating large Stark maps. The matrix calculations used to generate the Stark maps presented in the thesis required basis sets of between 1099 and 5000 states. To calculate the maps used to analyse states in the range n = 26 – 30 as shown in the spectra recorded *via* the $A^2\Sigma^+(v' = 0,\ N' = 0)$ intermediate (Section 4.4.2), a basis set of 1099 case (d) wave functions was used. At one value of external field, the diagonalisation calculation takes less than 10 seconds on a Mac Pro workstation with 2 dual-core 3 GHz Intel Xeon processors and 8 Gb memory. The memory required to hold a $M \times N$ matrix is equal to $M \times N \times mm$ where mm is the precision dependant

memory requirement for each matrix element. The 8 Gb Mac Pro workstation can hold a square matrix with over twenty thousand elements per row. The time taken for a matrix calculation is a non-linear function of the size of the matrix, the operation required and the CPU. Many operations scale exponentially with increasing matrix size. Therefore, to calculate the relative efficiencies of MQDT and matrix diagonalisation to calculate a Stark map for a specific region of the Rydberg energy space, it would be necessary to analyse the CPU time taken for the many calculations required in the MQDT technique and compare it to the single step required by diagonalisation. In general, the region of Rydberg states investigated would govern the choice of theoretical technique. For a limited range of low Rydberg states, the large spacing between states means that MQDT requires many small energy steps to include the positions of a small number of states. In comparison, matrix diagonalisation requires only a few matrix elements to cover the same region, and would be the obvious choice. For a region of high *n* the high density of states would favour MQDT.

4.4. Results

4.4.1. Predissociation spectra excited *via* $A^2\Sigma^+(N', v' = 0)$ in the absence of electric field

Predissociating states are accessed by a $(1+1')$ multiphoton transition. The nitrogen fragmentation product is ionised using a (2+1) REMPI scheme and detected in a linear time of flight. N^+ yield spectra recorded *via* the $A^2\Sigma^+(v' = 0, N')$ intermediate state with $N' = 0$ and 2 are presented in figures 4.4.2 and 4.4.4 respectively. States are labelled using $l(N^+)$ notation, where l is the orbital angular momentum and N^+ is the rotational angular momentum of the ion core. As a comparison it is useful to first introduce bound spectra recorded from the same intermediates, as presented in figure

4.4.1. The bound states are excited *via* the same $(1+1')$ multiphoton scheme, and then field ionised using a high voltage pulsed field with an amplitude greater than 1500 V cm^{-1}. Based on the angular momentum character of the intermediate [69, 70] and the selection rules introduced in Section 3.2.6 it would be expected that Rydberg series of p($N^+ = N'$) character would dominate the bound spectra, with a smaller contribution from the p($N^+ = N' \pm 2$) and f($N^+ = N' \pm 2$) series. However, both spectra in figure 4.4.1 are dominated by only Rydberg series of f character. The predissociation lifetime of Rydberg states of p character is less than the delay between the exciting laser pulses and ionising field and so these penetrating states rapidly predissociate and are not observed. The top spectrum in figure 4.4.1, recorded *via* the $A^2\Sigma^+(v' = 0,\ N' = 0)$ intermediate, is dominated by the f(2) series, with occasional p(0) states. The lower spectrum in figure 4.4.1 recorded *via* the $A^2\Sigma^+(v' = 0,\ N' = 2)$ intermediate shows greater congestion. This is due to the presence of f states belonging to series of different N^+; mainly states of f(2) and f(0) character with a smaller contribution from states belonging to the f(4) series. The bound spectra show a characteristic increase in signal as *n* increases. As *n* increases the orbit period, and hence rate of predissociation, decreases leading to the appearance of the *n*p(0) and *n*p(2) series in the bound spectra. This leads to a high density of states that can not be resolved with the resolution of the lasers in the current set-up.

The predissociation spectrum recorded *via* the $A^2\Sigma^+(v' = 0,\ N' = 0)$ intermediate state presented in figure 4.4.2 shows a greater complexity than the bound state equivalent. The p(0) series now dominate, as expected from the selection rules discussed previously, and there is also a significant contribution from the p(2), s(1) and f(2) series. A number of lines can be also attributed to the f(0), d(3), and s(3) series. The single photon transition to states belonging to the s(3) series is forbidden and so the appearance must be due to sσ-dσ coupling to the allowed d(3) state. A small number of lines exist that do not belong to any of the expected Hund's case (d) series, and

may be due to interloper states belonging to series of N^+ greater than four or v^+ greater than zero.

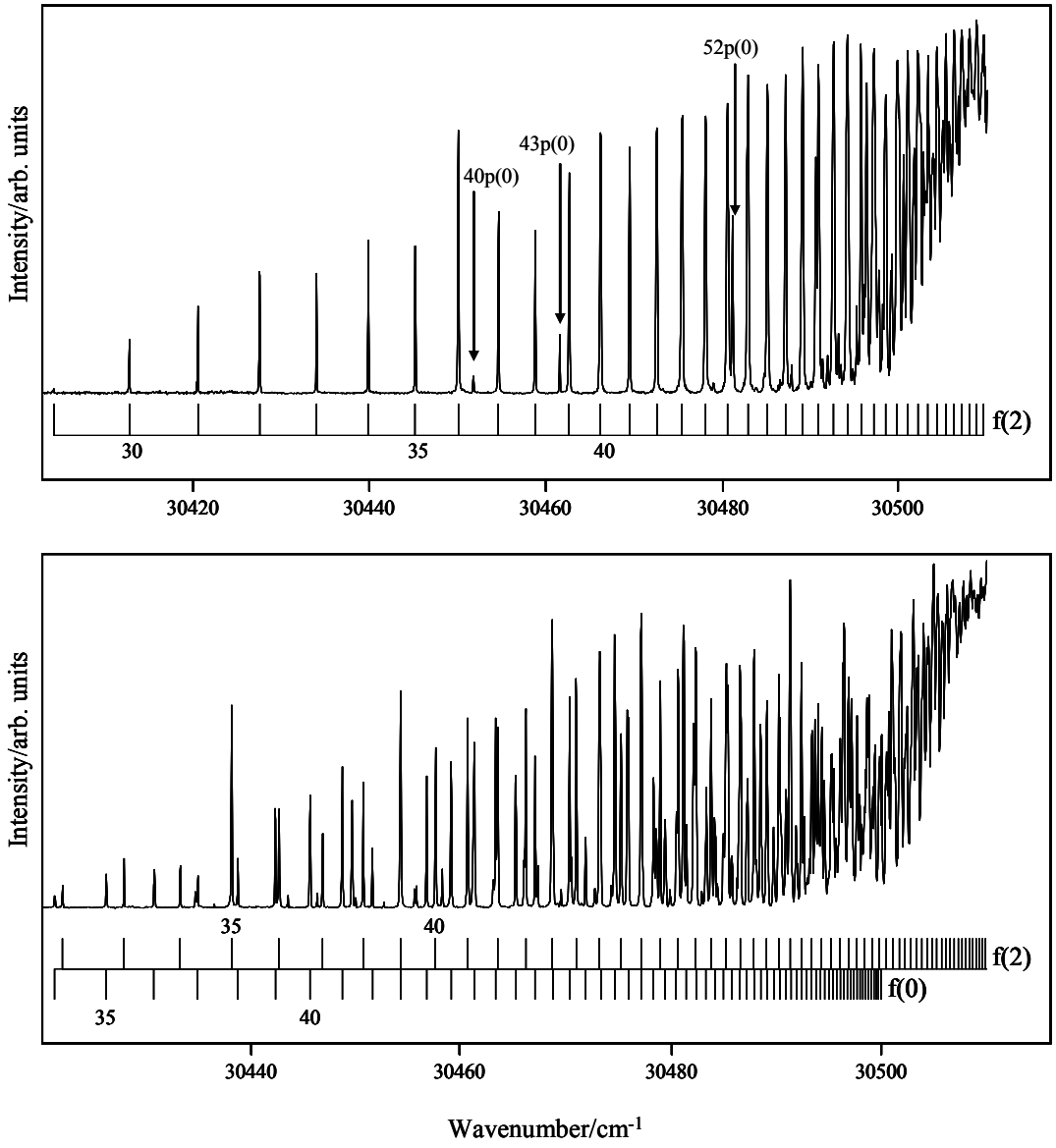

Figure 4.4.1: Zero field pulsed field ionisation spectra of the Rydberg states of NO converging on the $v^+ = 0$ ionisation limit. The upper spectrum was recorded *via* the $A^2\Sigma^+(v' = 0,\ N' = 0)$ intermediate, and the lower spectrum *via* the $A^2\Sigma^+(v' = 0,\ N' = 2)$ intermediate. The ladders show the dominant Rydberg series, labeled using the $l(N^+)$ notation where l is the orbital angular momentum, and N^+ is the rotational angular momentum of the core. Both spectra are dominated by the f series, as states of lower orbital angular momentum decay rapidly *via* predissociation. The few np(0) states observed in the upper spectrum are labeled.

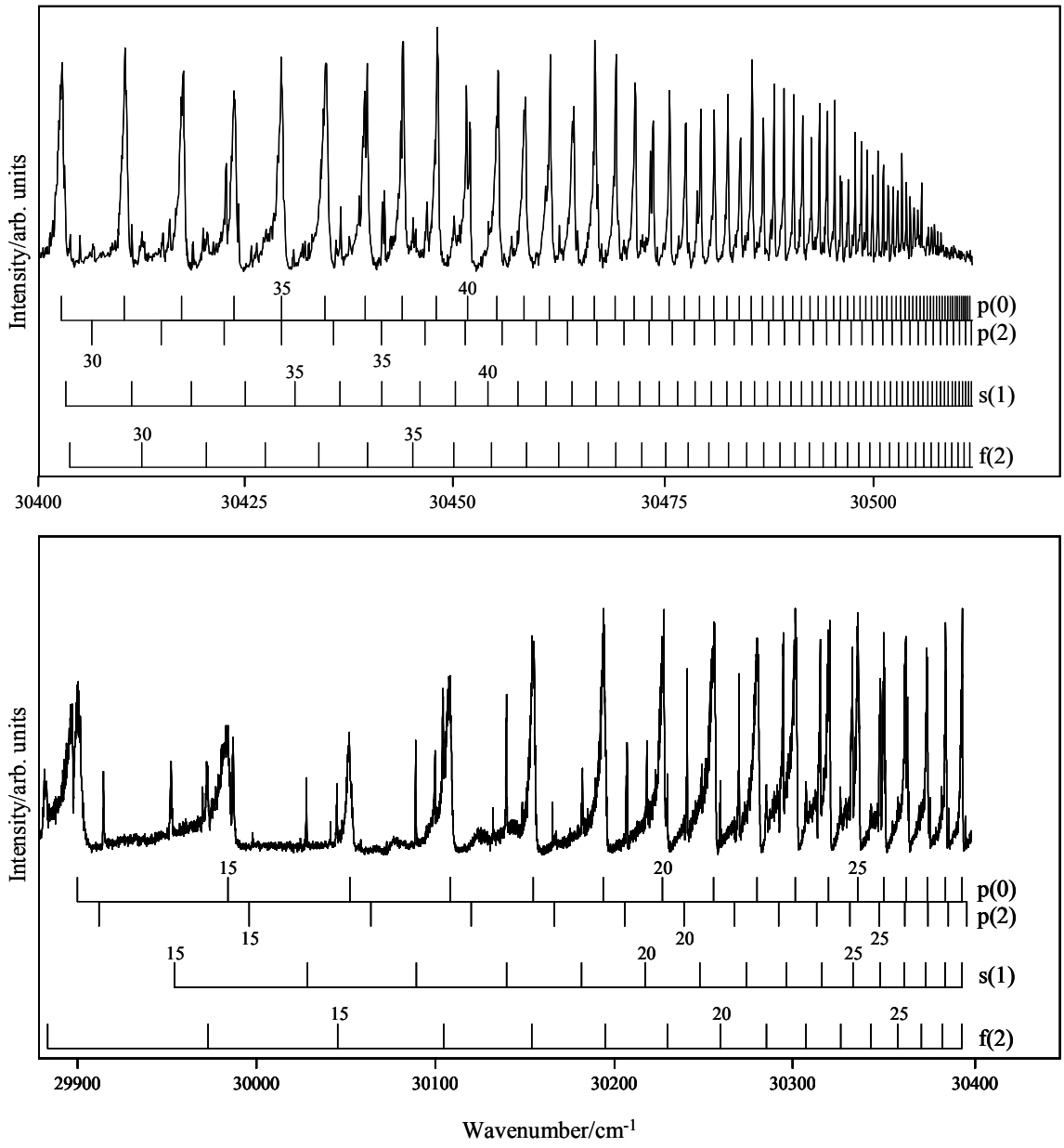

Figure 4.4.2: Zero field N^+ yield spectrum of the predissociating states of NO converging on the $v^+ = 0$ ionisation limit excited *via* the $A^2\Sigma^+(v' = 0, N' = 0)$ intermediate state. The complexity of the spectrum is greater than the equivalent bound state spectrum, due to the presence of many more series. The p(0) series dominates, but there are also significant contributions from the p(2), s(1), and f(2) series, with small contributions from the f(0), d(3) and s(3) series.

The p(0) states show a strong Fano lineshape; the broader width of which obscures the spectra more than the sharp Lorentzian lineshapes observed for bound states. The width of the Fano lineshape decreases with increasing *n* due to the drop in penetration between the Rydberg orbit and the core [87]. In contrast to the bound spectra, the

predissociaton signal decreases with increasing *n*. Again, this is due to the decrease in the rate of predissociation with increasing *n*. Instead of obscuring the spectrum as observed in the bound spectra, this decrease in signal allows states up to $n = 86$ to be resolved. States of low *n* can also now be observed as the signal no longer depends on the ionising field. States down to $n = 14$ are observed in the spectra presented in this thesis although states as low as $n = 9$ have previously been reported [74].

It is interesting to note that the integrated intensity of the p(2) series displays a large *n* dependence (figure 4.4.3). Over the range $n = 18$ to 26 the series grows in intensity as *n* increases until it reaches a max for 26p(2). The p(0) series dominates the whole spectrum except at this point at which the 26p(2) peak is actually more intense than the 27p(0) peak. The next 27p(2) peak overlaps the 28p(0) peak and so cannot be resolved. At this point the relative position of the p(2) series moves from the low to the high energy side of the p(0) series. The next p(2) peak, 28p(2), is barely resolvable and few subsequent p(2) states show any significant intensity. The sudden drop in intensity could be explained as another predissociation channel becoming accessible to *n*p(2) states in this energy region. However, this energy region does not correspond to any previously calculated crossings between the valence state potentials and the Rydberg state potential [74]. It is these crossings that couple the p states to the $N(^2D) + O(^3P)$ dissociation continuum. Alternatively, a second possible explanation is that the two indirect routes to dissociation, *via* the *n*p(0) and *n*p(2) "doorway" states, interfere with one another and that this interference is constructive or destructive depending on their relative energy separation and ordering.

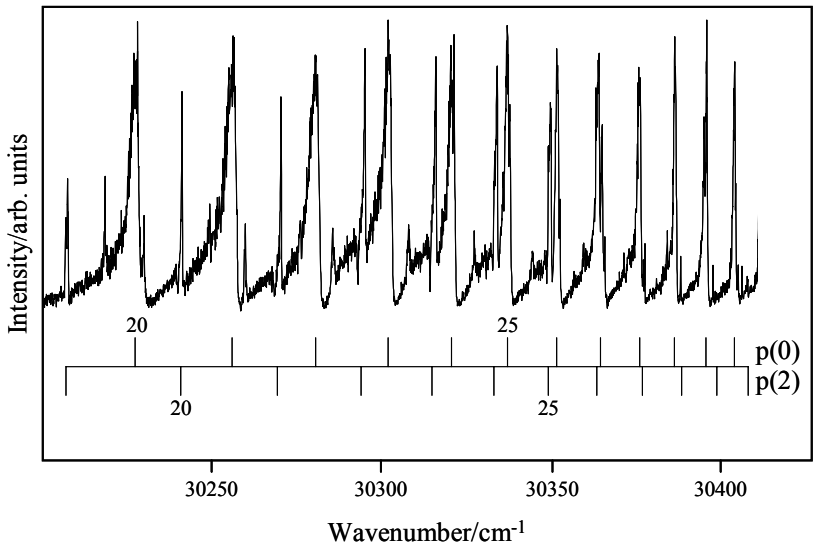

Figure 4.4.3: Zoom of zero field spectrum presented in figure 4.4.2. The combs represent the states of the $l(N^+)$ Rydberg series. The p(2) series grows in intensity as it approaches the dominant p(0) peaks before suddenly dropping in intensity as it passes through.

The predissociation spectrum recorded *via* the $A^2\Sigma^+(v' = 0,\ N' = 2)$ intermediate state is presented in figure 4.4.4. As observed in the bound spectra, the spectral complexity increases with N'. However, the greater number of series observed in the predissociation spectra leads to an even greater complexity. Assignment can be difficult due to the many overlapping series; a problem that increases with n as the energy spacing between states decreases as n^{-3}. For low n, it is possible to assign the dominant series as p(2), with significant contributions from the p(0), f(2), f(0) and d(1) series and smaller contributions from the p(4), d(5) and f(4) series. As observed in the predissociation spectrum recorded *via* the $A^2\Sigma^+(v' = 0,\ N' = 0)$ intermediate state, the width of the Fano lineshape decreases with n and the intensity dies off as the Rydberg states converge to the ionisation limit. It is possible to resolve states up to the region of 100p(2).

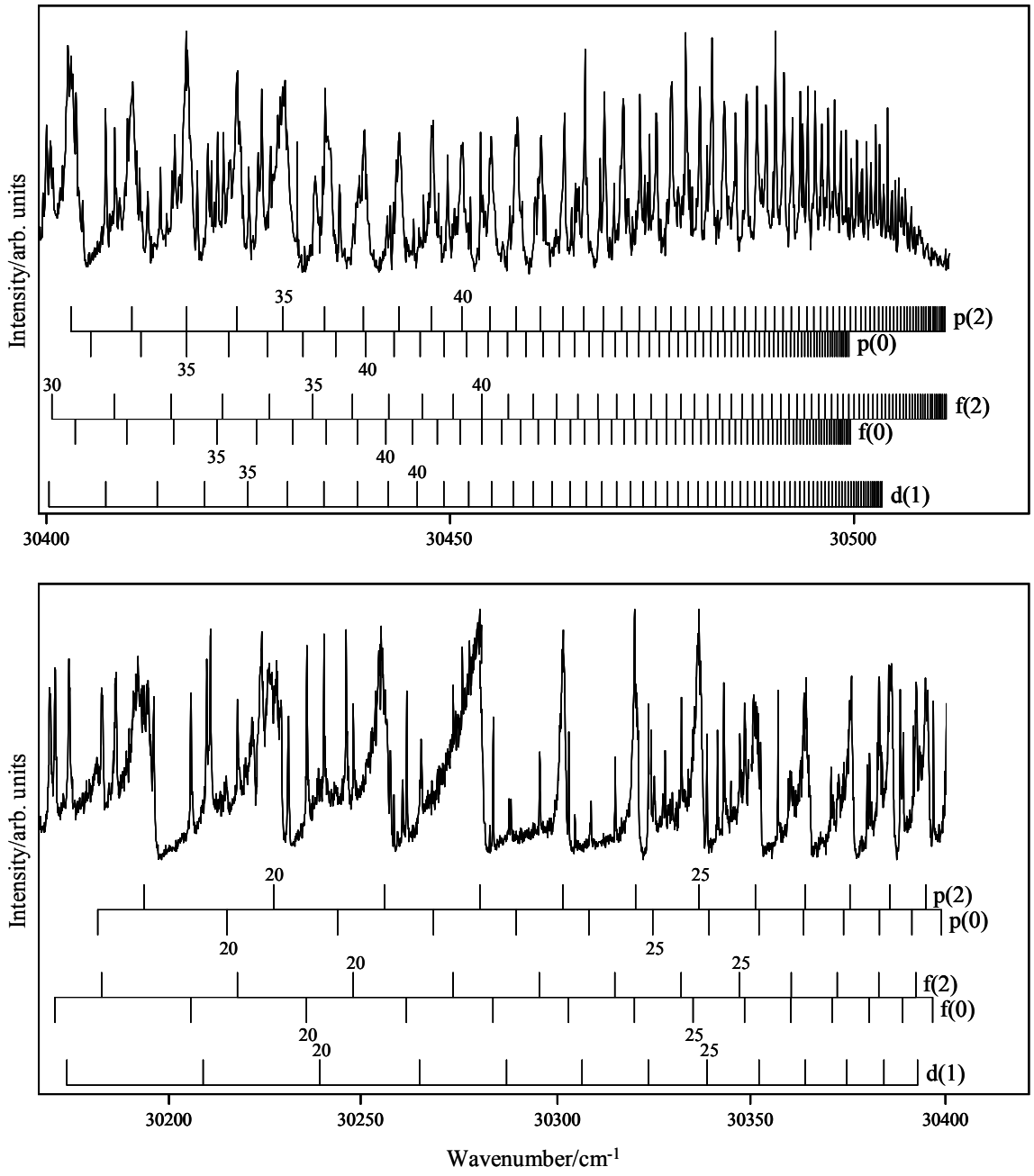

Figure 4.4.4: Zero field N^+ yield spectrum of the predissociating states of NO converging on the $v^+ = 0$ ionisation limit excited *via* the $A^2\Sigma^+(v' = 0,\ N' = 2)$ intermediate state. The spectral complexity has increased to a level that now makes assignment difficult due to the many overlapping series. The p(0) series dominates, but there are also significant contributions from the p(2), d(1), and f(2) series, with small contributions from the f(2), d(3) and s(3) series.

4.4.2. Predissociation spectra excited *via* $A^2\Sigma^+(N' = 0, v' = 0)$ in the presence of an electric field

A series of N^+ yield spectra are presented in figure 4.4.5 recorded under a number of applied fields *via* the $A^2\Sigma^+(N' = 0, v' = 0)$ intermediate state. As observed in the longer zero field spectra presented in the previous section, the *n*p(0) series dominates, with a smaller contribution from the *n*p(2) and *n*f(2) series. The peaks arising from states of p character show the characteristic broad asymmetric Fano lineshape [26]. On this smaller scale, the sudden disappearance of the p(2) series as it passes through the p(0) series can be clearly observed.

To fully analyse the Stark spectra, Stark maps were calculated from 0 to 160 Vcm^{-1} containing states from 25*l*(0) and 24*l*(2) to 31*l*(0) and 30*l*(2) forming a total basis set of 1099 states. Figures 4.4.6 and 4.4.8 show the recorded predissociation Stark spectra (black lines) overlaid on the calculated $N^+ = 0$ and 2 Stark maps (grey lines). To simplify the data analysis, it is convenient to define three regions of the Rydberg spectrum characterised by the relative energies of the zero field $N^+ = 0$ and 2 manifolds. In region (*i*) the 24(2) and 25(2) manifolds are lower in energy than the 25(0) and 26(0) manifolds. In region (*ii*) the 27(0) manifold is 0.1 cm^{-1} below the 26(2) manifold *i.e.* they are almost degenerate. Finally, region (*iii*) is the reverse of (*i*), and the 27(2) and 28(2) manifolds are higher in energy than the 28(0) and 29(0) manifolds.

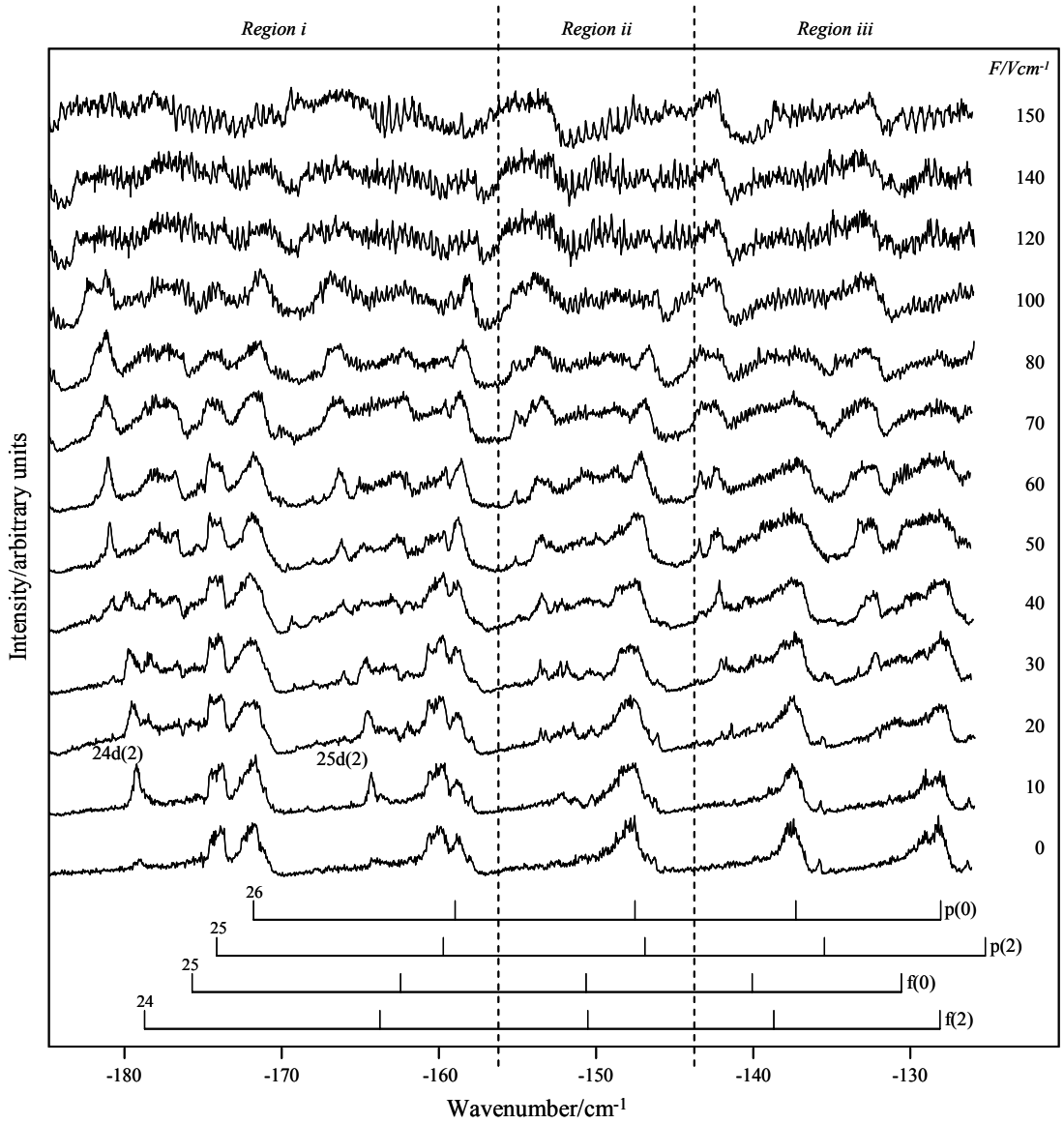

Figure 4.4.5: Stark spectra of the predissociating Rydberg states of NO converging to the $v^+ = 0$ ionisation limit with principal quantum number n = 26 – 31 excited *via* the $A^2\Sigma^+(N' = 0, v' = 0)$ state. The x-axis is the binding energy with respect to the lowest ionisation limit ($N^+ = 0$, $v^+ = 0$). The y-axis is the intensity of the nitrogen REMPI signal in arbitrary units. The spectra are arranged from bottom to top in order of increasing applied electric field. The zero-field positions of the *n*p(0) and *n*p(2) Rydberg states are marked, together with the zero-field positions of the *n*f(0) and *n*f(2) series, which are almost degenerate with the high-l manifolds associated with the $N^+ = 0$ and 2 ionisation limits.

A portion of the spectrum from region (*i*) is reproduced in figure 4.4.6. The 24(2) and 25(2) manifolds are lower in energy than the 25(0) and 26(0) manifolds, and as the field is increased the blue-shifted Stark states of the $N^+ = 2$ manifolds mix with the

red-shifted states of the $N^+ = 0$ manifolds. Specifically, as the field increases, the 24d(2) and 25s(2) states begin to mix with the high angular momentum 24*l*(2) manifold and gain intensity. The 24d(2) state lies only 0.3 cm^{-1} below the 24(2) manifold in zero field; it mixes into the manifold readily and is observed to have significant intensity even at 10 V cm^{-1}. The 25s(2) state lies 0.9 cm^{-1} below the 24(2) manifold in zero field and gains intensity slowly with increasing electric field strength until 50 V cm^{-1} when it joins the edge of the 24(2) manifold and suddenly becomes quite significant. Similar features are observed in the vicinity of the 25(2) and 26(0) manifolds. In many respects, the $N^+ = 2$ states behave in the same way as an atomic Rydberg series and are relatively unperturbed by the presence of the $N^+ = 0$ Rydberg states.

For a state to have intensity in a predissociation spectrum it must be susceptible to decay *via* predissociation, and also have a non-zero transition moment from the chosen intermediate state. It is likely that the increase in the d(2) and s(2) peak intensity during mixing into the high-*l* *n*(2) manifold arises from one of two mechanisms. As discussed in Section 3.2.6 the f(2) states have some transition intensity as a result of the 5 % d component of the intermediate A state. However, at this value of *n* they are relatively immune to predissociation and are only weakly observed at zero fields. As the s and d states mix with the f state, the resulting Stark state has a mixture of the high predissociation rate of the low *l* states and the transition strength of the f state; the combination required to observe a signal in the predissociation spectrum. The second mechanism arises from mixing between the 24p(2) and 23p(2) Rydberg states and the 24*l*(2) manifold giving intensity to the high *l* manifold. This is then shared with the s and d states as they mix into the manifold.

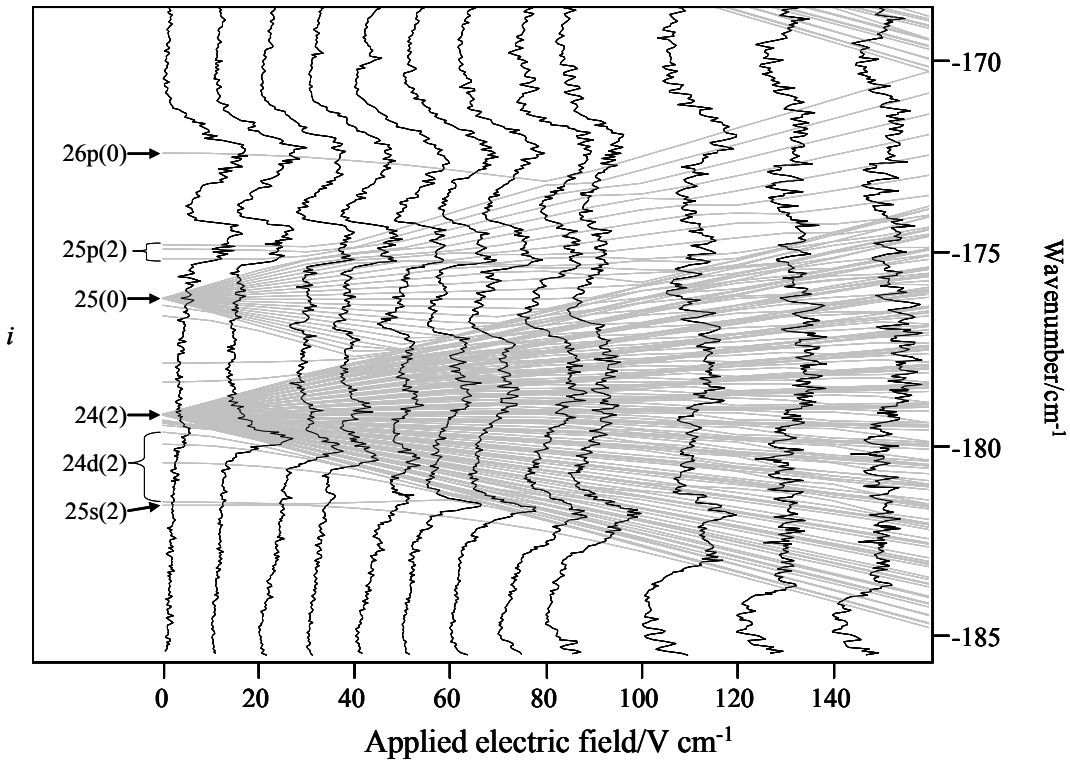

Figure 4.4.6: Zoom of Stark spectra of the predissociating Rydberg states of NO converging to the $v^+ = 0$ ionisation limit as shown in figure 4.4.5, superimposed on Stark maps calculated using the matrix diagonalisation method outlined in the text and including Rydberg states with even core rotational angular momentum quantum numbers $N^+ = 0$ and 2. Individual Rydberg states are labeled $nl(N^+)$. The positions of the zero field manifolds ($l > 3$) are labeled using the notation $n(N^+)$. In the region shown the 24(2) manifold is lower in energy than the 25(0) manifold. This is an example of Region *i* as discussed in the text.

An analysis of the eigenvectors produced by the matrix diagonalisation calculation shows little change in the composition of the 25s(2) state as it mixes into the manifold (figure 4.4.7A). With no applied field, the state has 98 % 25s(2) character, falling to 93 % at 60 V cm^{-1}. Over this range the proportion of 24p(2) and 24f(2) character increases to approximately 1 % whilst the 25p(0) character increases to 0.1 %; a significant component as the transition moment associated with this state is around five times greater than for states of *n*f(2) character. It would be expected that the increase in intensity is driven by a significant change in the composition of the s state as it joins the manifold. This is not observed here, possibly highlighting a missing coupling mechanism in the matrix diagonalisation code.

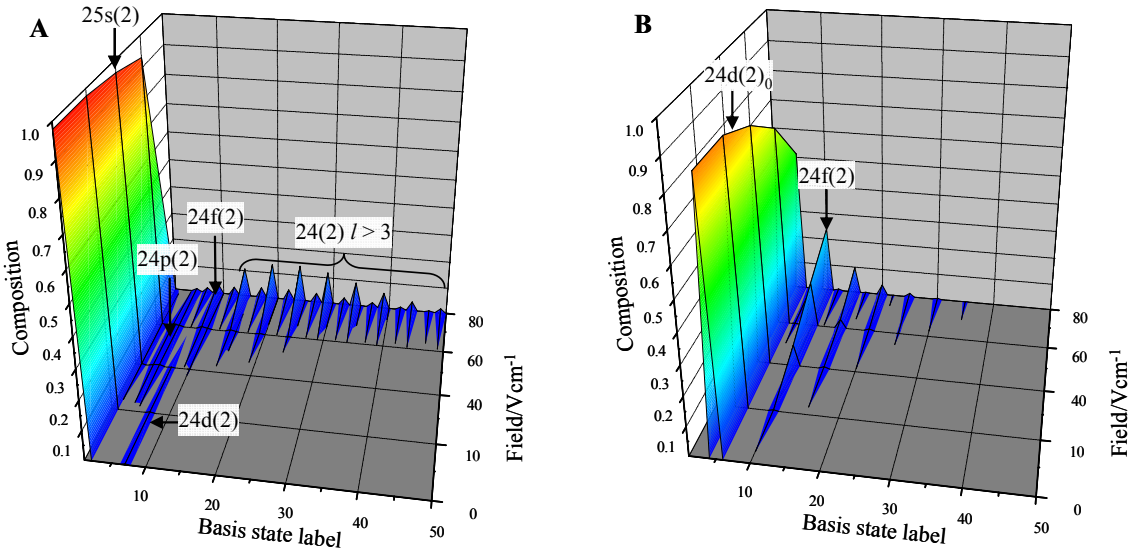

Figure 4.4.7: Surface plots showing the composition of two Stark states at five different fields. **A:** The Stark state of predominantly 25s(2) character at zero fields shows only a small increase in 24p(2) and 24f(2) character as the field is increased. The state quickly mixes with the high l 24(2) manifold at 80 V cm^{-1}. the states are labeled using $nl(N^+)$ notation.

B: The Stark state of predominantly 24d(2)$_0$ character, labeled using $nl(N^+)_N$ notation, in zero fields shows a significant increase in 24f(2) character as the field increases.

Alternatively, this could suggest that the intensity gain is actually driven by the nearby 24d(2)$_0$ state, labelled using $nl(N^+)_N$ notation, joining the manifold (figure 4.4.7B), . At 0 V cm^{-1} the 24d(2)$_0$ state is 86 % pure with 12 % 26s(0)$_0$ character arising from sσ-dσ mixing (not shown in figure 4.4.7 for clarity). Intensity is first observed at 40 V cm^{-1} and at this field the 24d(2)$_0$ character has dropped to 80 %, whilst the 24f(2)$_1$ character has increased to almost 10 %. The observed intensity reaches a peak at 80 V cm^{-1}, and the composition of the Stark state at this field is 51 % 24d(2)$_0$, 24 % 24f(2)$_1$, and 4 % 26s(0)$_0$ with over 15 % from states belonging to the high-l 24(2) manifold. The significant change in composition of the 24d(2)$_0$ state during the field range of interest could suggest that the intensity increase is driven by the increasing f(2) character in the Stark state. However, the position of the 23s(2)$_0$ Stark state is a better match to the position of the observed peak and the appearance of

a shoulder on the low energy side of the peak at 70 V cm^{-1} could be explained as arising from the $24d(2)_0$ state mixing into the manifold.

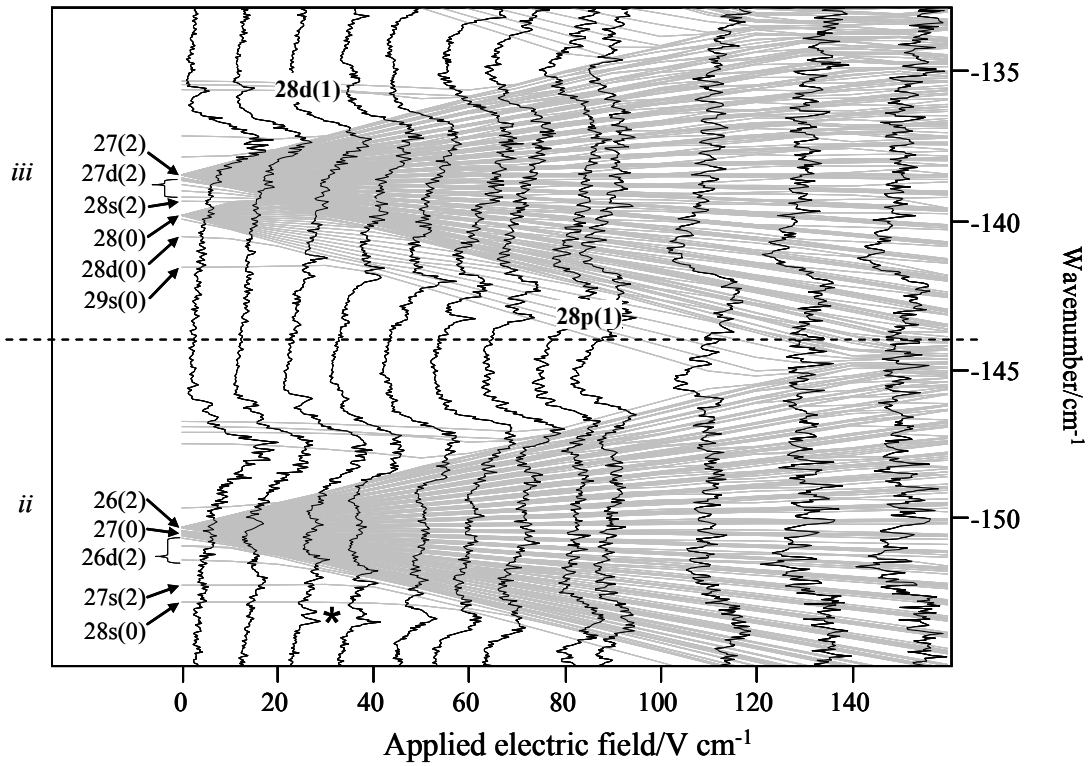

Figure 4.4.8: Zoom of Stark spectra of the predissociating Rydberg states of NO converging to the $v^+ = 0$ ionisation limit as shown in figure 4.4.5, superimposed on Stark maps calculated using the matrix diagonalisation method outlined in the text and including Rydberg states with even core rotational angular momentum quantum numbers $N^+ = 0$ and 2. Individual Rydberg states are labeled $nl(N^+)$. The positions of the zero field manifolds ($l > 3$) are labeled using the notation $n(N^+)$. In the region shown 27(0) manifold is almost degenerate with the 26(2) (region *ii*) and the 27(2) manifold lies higher in energy than the 28(0) manifold (region *iii*). The 28p(1) and $28d(1)_1$ states are labeled and the asterisk marks the positions of the 25d(3) and 26s(3) states at –153.2 and –153.6 cm^{-1} respectively.

Figure 4.4.8 shows a section of figure 4.4.5 containing region (ii) and a portion of region (iii). In region (*ii*), the 26d(2), 27s(2) and 28s(0) states just below the 27(0) and 26(2) manifolds gain intensity as they mix into the high-*l* manifold, but because these manifolds are almost degenerate, the effect is less pronounced. A matrix diagonalisation analysis of the composition of the eigenstates in this region of the

spectrum shows that $\Delta N^+ = \pm 2$ mixing is very efficient (figure 4.4.9). At 0 V cm^{-1} the 27*l*(0) and 26*l*(2) states with $l \geq 2$ have almost pure $N^+ = 0$ or 2 character; however, even at 10 V cm^{-1}, the most red shifted Stark states originating from the higher energy $N^+ = 2$ manifold (*i.e.* those closest to the $N^+ = 0$ manifold) possess up to 40% $N^+ = 0$ character (figure 4.4.9B). This mixing also dilutes the $N^+ = 2$ character of the d and f states. For example, the 26d(2) state furthest from the $N^+ = 0$ manifold is predominantly $26d(2)_0$ in character. At 10 V cm^{-1} the Stark state has gained significant $N^+ = 0$ character, *via* sσ-dσ mixing with the 28s(0) state (figure 4.4.9B). The $26d(2)_4$ state, located close to the $N^+ = 0$ manifold at 10 V cm^{-1}, shows stronger $\Delta N^+ = \pm 2$ mixing with the high *l* 27(0) manifold. Although the state is of predominately $26d(2)_4$ character in zero-field, at 10 V cm^{-1} the compositions is 27% $26d(2)_4$, 20% $26f(2)_5$ and over 45 % 27*l*(0) ($l \geq 2$) (figure 4.4.9D). Therefore, the $N^+ = 2$ state can no longer be considered as unperturbed by the presence of the $N^+ = 0$ Rydberg states, and the observed intensity gains are much weaker.

In region (*iii*), the 28s(2) and 27d(2) states do not appear with any significant intensity (figure 4.4.8). This could be attributed to $\Delta N^+ = \pm 2$ mixing. In this region, the fields at which the 28s(2) and 27d(2) states lying just below the 27(2) manifold would be expected to merge into this manifold coincide with the fields where the low energy edge of the 27(2) manifold begins to overlap with the high energy edge of the 28(0) manifold.

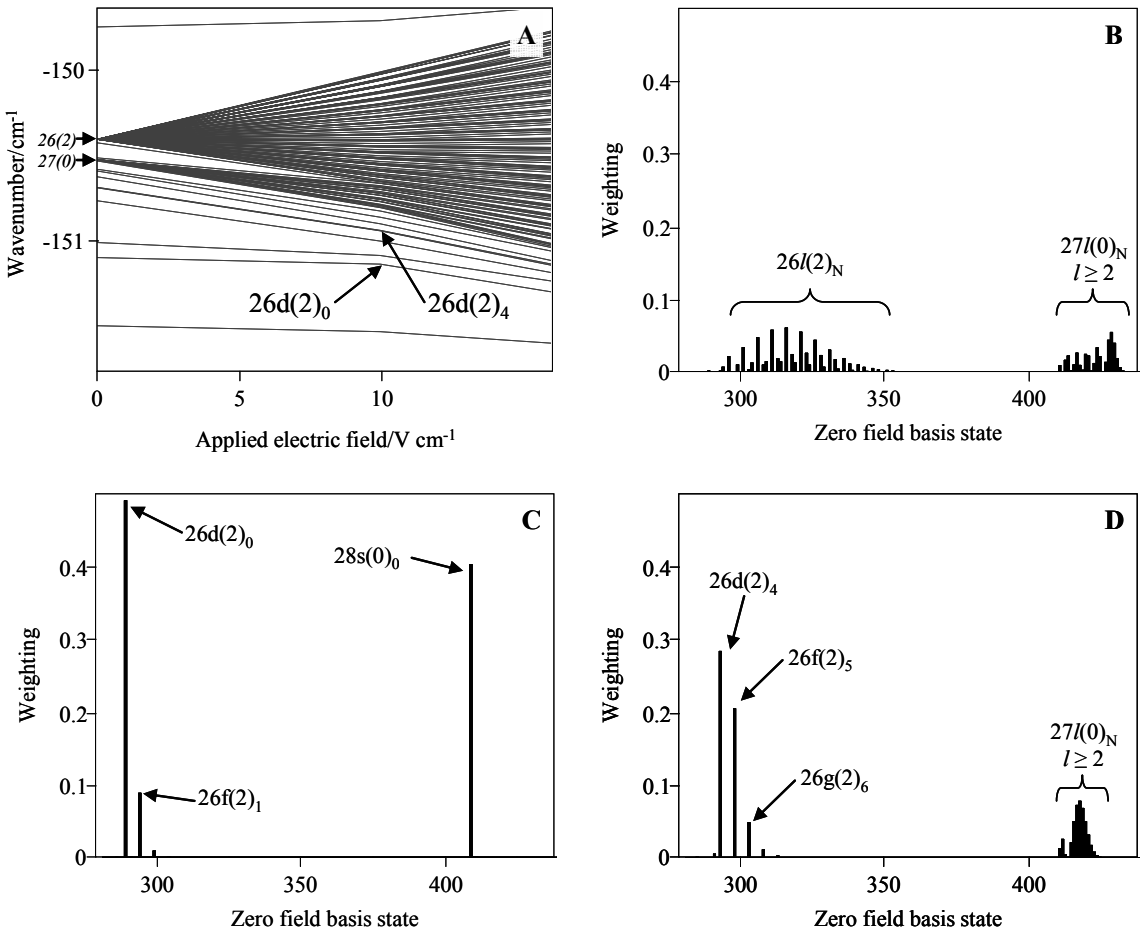

Figure 4.4.9: **A:** Stark map of region (ii) showing the 26(2) and 27(0) high *l* manifolds separated by 0.1 cm^{-1}. The composition of the $26d(2)_0$ and $26d(2)_4$ states is shown in C and D respectively.

B: Analysis of the composition of the Stark state located at -150.79 cm^{-1} at 10 V cm^{-1}. This corresponds to a state located at the point where the 26(2) and 27(0) manifolds cross. The composition of the Stark state is approximately 62 % 26(2) and 38% 27(0) showing the strong mixing between the two manifolds at relatively low fields. **C:** Composition of the $26d(2)_0$ state at 10 V cm^{-1}. The state shows 60 % 26(2) character. The remaining 40 % of $26s(0)_0$ character arises from the strong sσ-dσ mixing. **D:** Composition of the $26d(2)_4$ state at 10 V cm^{-1}. The state shows 27 % $26d(2)_4$ and 20% $26f(2)_5$ character. The proximity to the high *l* 27*l*(0) manifold results in 45 % 27(0) $l \geq 2$ character.

Zero-field $\Delta N^+ = \pm 2$ mixing between states with the same *l* character redistributes the transition intensity throughout both manifolds. In effect, the 27d(2) and 28s(2) states are diluted by the 28(0) manifold as they mix into 27(2) manifold, reducing the intensity gain compared to that observed in region (*i*). The 29s(0) state located on the low energy side of the 28(0) manifold gains intensity when it joins the manifold at

around 40 V cm^{-1} but the 28d(0) state gains little intensity when it mixes in at 20 V cm^{-1}. This is consistent with the previously proposed mechanism for intensity gain *via* mixing of the high transition strength of the f state with the fast predissociation rate of the s and d states. The lower transition strength of the f(0) series with respect to the f(2) series means that the low predissociation rate of the d states is not enough to observe the resulting Stark state. However, the presence of the s(1) series in figure 4.4.2 implies that s states possess significant predissociation character. Therefore, a Stark state can be observed that results from the mixing of the strongly predissociating s state with the small transition intensity of the f(0) state. The observation of significant intensity gain at 50 V cm^{-1} in the absence of a nearby d state suggests that the intensity gain in region (i) is driven by the ns$(2)_2$ state mixing into the N^+= 2 manifold, rather than the nd$(2)_0$ state.

There are a few additional peaks that cannot be explained using the Stark maps in 4.4.6 and 4.4.8 that were calculated including only states with even values of the rotational quantum number of the core, N^+. At fields < 40 V/cm, small peaks are observed on the high energy sides of the 27p(0) – 30p(0) states (figure 4.4.5). These peaks can be assigned by analyzing the position of the Stark states calculated using our matrix diagonalisation procedure. Using the notation $nl(N^+)_N$, it turns out that these small peaks correspond to transitions to members of the nd$(1)_1$ series, which due to their small negative quantum defects, lie just on the high energy sides of their corresponding n(1) manifolds. At higher fields the np(1) states gain intensity by mixing into the n(1) manifolds. The assignment of the 28p(1) and 28d$(1)_1$ states is shown in figure 4.4.10 and are labelled in figure 4.4.8.

In this region of the spectrum the N^+ = 1 and 3 series are well separated from each other; however, the N^+ = 1 manifolds lie close to the p(0) series. Any intensity gained by the ns(1) and nd$(1)_{N \neq 1}$ states mixing into the n(1) manifolds is

indistinguishable from the intense broad *n*p(0) peaks. The only significant intensity gain observed for s or d states belonging to the odd N^+ series are for 25d(3) and 26s(3) at –153.2 and –153.6 cm^{-1} respectively (figure 4.4.10 and labelled with an asterix in figure 4.4.8).

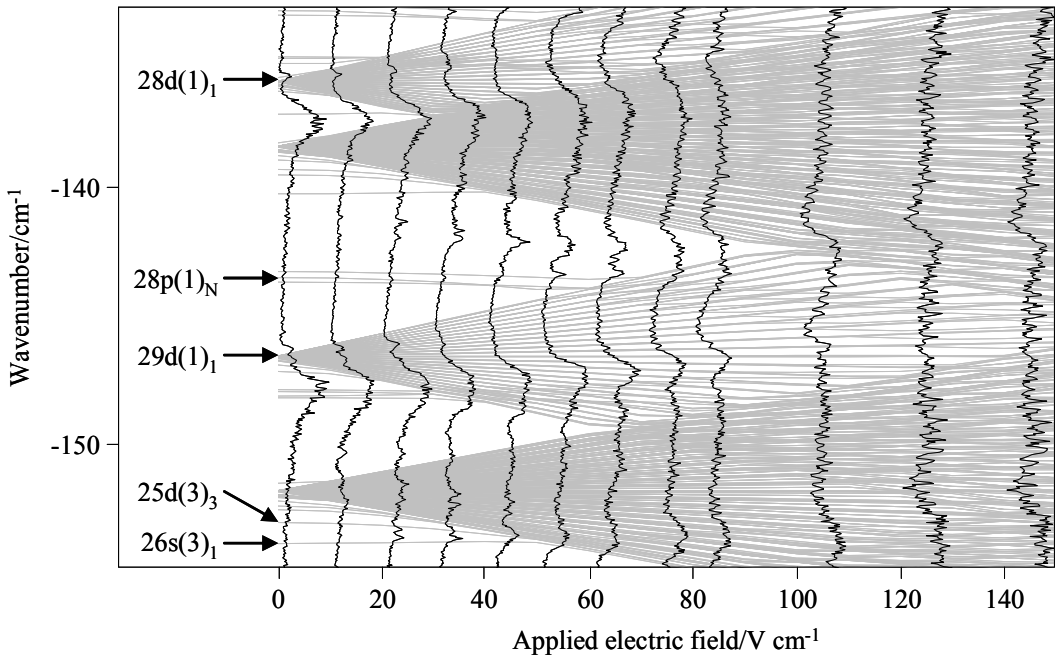

Figure 4.4.10: Zoom of Stark spectra of the predissociating Rydberg states of NO converging to the $v^+ = 0$ ionisation limit as shown in figure 4.4.5, superimposed on calculated Stark maps including Rydberg states with odd core rotational angular momentum quantum numbers N^+ = 1 and 3. Individual Rydberg states are labeled *nl*(N^+). The labeled states show the assignments of the 28p(1), 28d(1)$_1$, 25d(3) and 26s(3) as labeled in figure 4.4.8 as well as the position of the 29d(1)$_1$ state.

For all regions of the Rydberg spectrum, when the field is increased >100 V cm^{-1}, some individual Stark states can be resolved. Due to the overlap between the $N^+ = 0$ and 2 manifolds at these higher fields it is difficult to assign the peaks. However, based on the fact that most of the transition intensity is to *n*p(0) states, it is likely that Stark states belonging to the $N^+ = 0$ manifold are dominant. The observed Stark splittings are consistent with this suggestion. For example, in the vicinity of the 27(0) manifold, peaks in the spectrum at 150 V cm^{-1} are separated by 0.51 cm^{-1} which agrees well with the calculated hydrogenic splitting 0.52 cm^{-1} ($\Delta E = 3nF$ in atomic

units). Table 4.4.1 shows two more examples of the agreement between the calculated Stark splitting based on a hydrogenic system, and the average observed splitting between resolvable Stark states in the vicinity of different manifolds at 150 V cm^{-1}.

$n(N^+)$	F/V cm^{-1}	Calculated. hydrogenic/cm^{-1}	Experimental/cm^{-1}	Δ_{H-NO} /cm^{-1}
15(0)	600	1.15	1.13	+0.02
26(0)	150	0.50	0.48	+0.02
27(0)	150	0.52	0.51	+0.01
30(0)	150	0.58	0.60	-0.02

Table 4.4.1: Table showing the measured and calculated energy separation between resolvable Stark states at different fields in the vicinity of four different manifolds.

A second set of Stark spectra was recorded in the vicinity of the 15(0) manifold, so that higher fields could be applied before manifolds of the same N^+ were mixed. Figure 4.4.11 shows the Stark spectra of the region around the 15(0) state under five different applied fields. The Stark splitting of the 15(0) manifold measured at 600 V cm^{-1} is also listed in table 4.4.1, and again shows excellent agreement with the calculated value. At this field the 15(0) manifold has mixed with the nearest 15p(2) manifold, but not the 16(0) or 14(0) manifolds and so the manifold splitting can be clearly resolved. Figure 4.4.11 also shows the 15p(0) Stark spectra with the exciting laser pulses polarisation both parallel (upper traces) and perpendicular (inverted lower traces) to the polarisation of the applied electric field and, as discussed in Chapter 1, this relative polarisation of the two fields leads to $\Delta m = 0$ and $\Delta m = 1$ selection rules respectively. In a hydrogenic system, if $\Delta m = 1$ the maximum intensity will be located in the centre of the manifold, whilst if $\Delta m = 0$ the maximum intensity is located at the edges of the manifold. In a molecular system the manifold behaviour will deviate

from the simple hydrogenic picture due to the extensive mixing between manifolds of different N^+ even at relatively low fields.

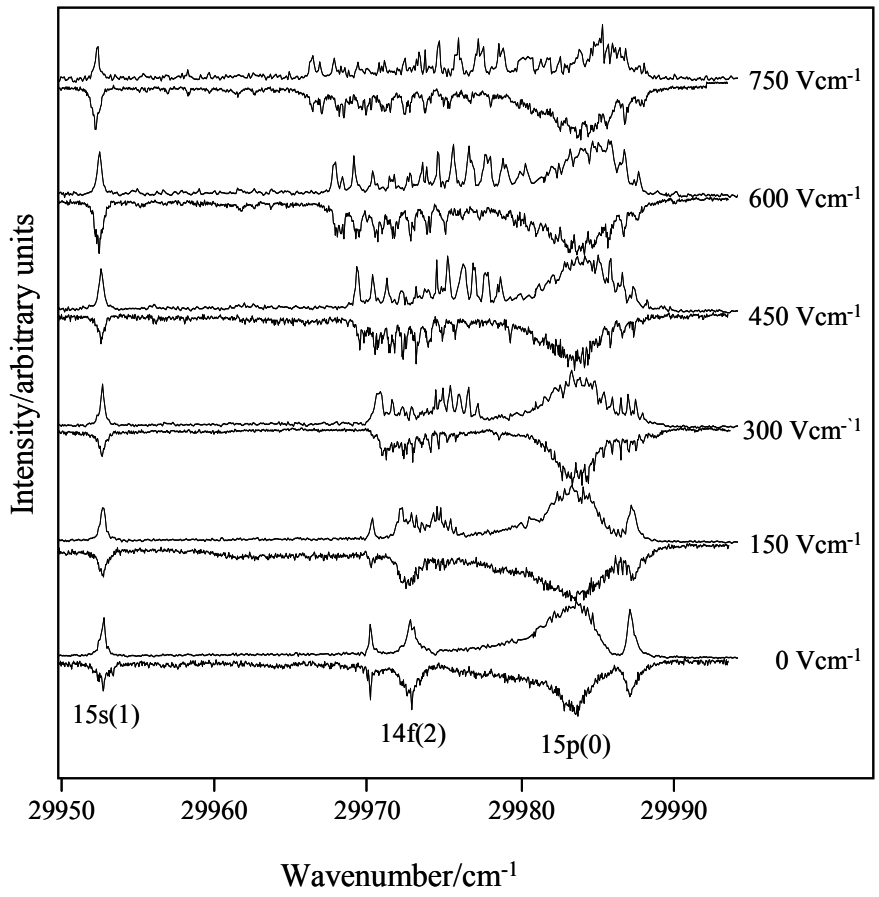

Figure 4.4.11: Stark spectra of the predissociating Rydberg states of NO converging to the $v^+ = 0$ ionisation limit in the vicinity of the 15p(0) state. Upper traces show spectra recorded with the polarizations of the laser pulse and electric field parallel, and the lower inverted traces show the same energy region recorded with the two polarizations perpendicular.

In the spectra recorded with a parallel arrangement of the laser pulse and electric field polarisations, zero field intensity is observed in the 15p(0), 14f(2) and 15s(1) states. As the field is increased the intensity from the 15p(0) and 14f(2) states is mixed into the edges of the 14(2) manifold located between the two states. As the field increases further the intensity spreads along the whole of the manifold and also begins to mix into the 14(0) manifold located on the low energy side of the 14f(2) peak. The 15s(1) state is isolated from any nearby manifolds and undergoes no splitting and little

intensity variation as the field is increased. The spectra recorded with perpendicular arrangement of the laser pulse and electric field polarisations show a similar zero field spectra. However, as the field is increased the intensity of the 14f(2) state is preferentially shared into the adjacent 14(0) manifold and only at higher fields does it begin to mix into the 14(2) manifold. Even at high fields the perpendicular and parallel spectra look distinctive, with intensity located mainly in the 14(0) or 14(2) manifolds respectively, and so must be taken into account when creating simulated spectra.

4.4.3. Predissociation spectra excited via A2Σ+($N' = 2$, $v' = 0$) in the presence of an electric field

A series of predissociation Stark spectra recorded *via* the $A^2\Sigma^+(N' = 2, v' = 0)$ intermediate state are presented in figure 4.4.12. To analyse the spectra, Stark maps were calculated from 0 to 160 V cm^{-1} containing states from 24(0), 23(2), and 21(4) to 33(0), 31(2) and 29(4) forming a total basis of 3291 elements. Figures 4.4.13 and 4.4.14 show the recorded spectra overlaid onto the calculated $N^+ = 0$, 2 and 4 manifolds.

A one photon transition from an intermediate state with non-zero rotational angular momentum can access more Rydberg series than a one photon transition from a $N' = 0$ intermediate. Selection rules predict that the dominant transition from the $N' = 2$ intermediate will be to states of p(2) character. There will also be contributions from states belonging to the p(0), p(4), f(0), f(2) , and f(4) series, with a smaller contribution from the odd N^+ series; s(1), s(3), d(1), and d(3). The presence of these extra series, when compared to the $N' = 0$ spectra, leads to a higher density of states and can make assignment difficult. This is especially true as a field is applied, and the large number of states begins to mix. The rapid mixing by the field makes the kind of

analysis performed on the $N' = 0$ spectra difficult, as the zero field Hund's case (d) states are quickly obscured by the high l manifolds. As observed previously, the dominant series in zero fields is p(2). The next two most prominent are f(0) and f(2) with a significant contribution from the s(3). Assignment of the other peaks is not possible due to the many overlapping series, but they can be assigned as either belonging to the d(1), d(3) or f(4) series. The large peak at -128.3 cm^{-1} lies on an accidental resonance between states belonging to the f(2), p(0), d(1) and d(3) series. Whilst the spectrum is more congested, it is still possible to observe states gaining intensity by mixing into the high l manifolds, in a similar process to that observed in the spectra recorded *via* $A^2\Sigma^+(N' = 0, v' = 0)$. Examples of this are shown in figures 4.4.13, 4.4.14 and 4.4.15. The intensity gained is usually due to a $ns(2)_2$ state mixing into the nearest high l $N^+ = 2$ manifold, although it can also be driven by other Rydberg states as discussed below.

Figure 4.4.13 shows a region of the Rydberg spectra from 25p(2) to 27p(2) overlaid onto the calculated Stark maps with even core rotational angular momentum of $N^+ = 0$, 2 and 4. The p(2) Rydberg states dominate the spectra at zero fields, with contributions from the f(0), f(2) and f(4) series. As the field is increased, a number of peaks can be observed to grow in intensity. The three $ns(2)$ states included in this region of the spectra all gain intensity as they mix into the nearest high l $N^+ = 2$ manifold: at 178.9, 153.3 and 165.4 cm^{-1}. A fourth peak can also be seen to appear at 169.0 cm^{-1} as the field increases, which can be assigned as the 23d(4) state joining the 23(4) manifold.

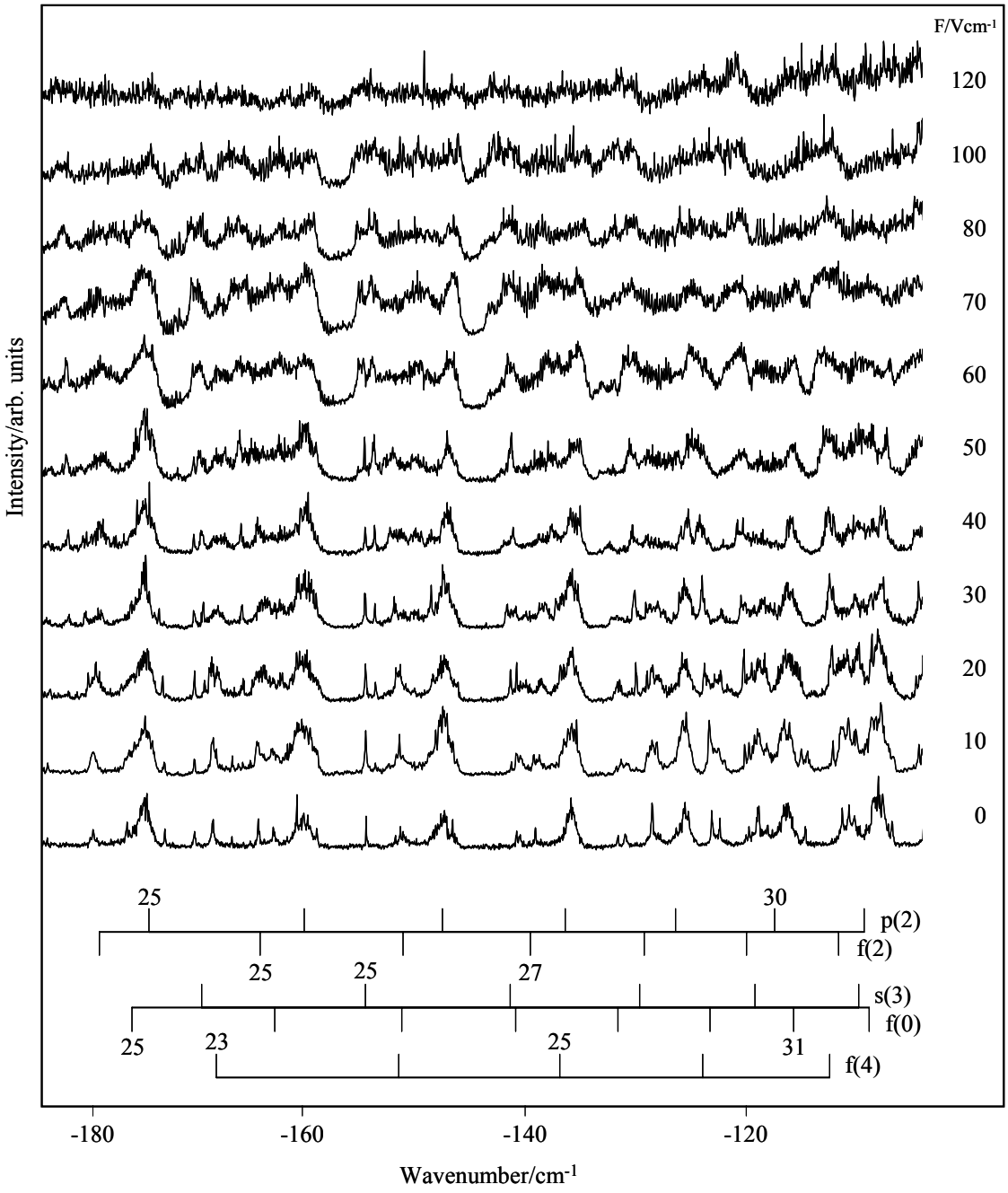

Figure 4.4.12: Stark spectra of the predissociating Rydberg states of NO converging to the $v^+ = 0$ ionisation limit with principal quantum number n = 25 – 31 excited *via* the $A^2\Sigma^+(N' = 2, v' = 0)$ state. The x-axis is the binding energy with respect to the lowest ionisation limit ($N^+ = 0$, $v^+ = 0$). The y-axis is the intensity of the nitrogen REMPI signal in arbitrary units. The spectra are arranged from bottom to top in order of increasing applied electric field. The zero-field positions of the *n*p(2), and *n*s(3) Rydberg states are marked, together with the zero-field positions of the *n*f series, which are almost degenerate with the high-l manifolds associated with the $N^+ = 0$, 2 and 4 ionisation limits.

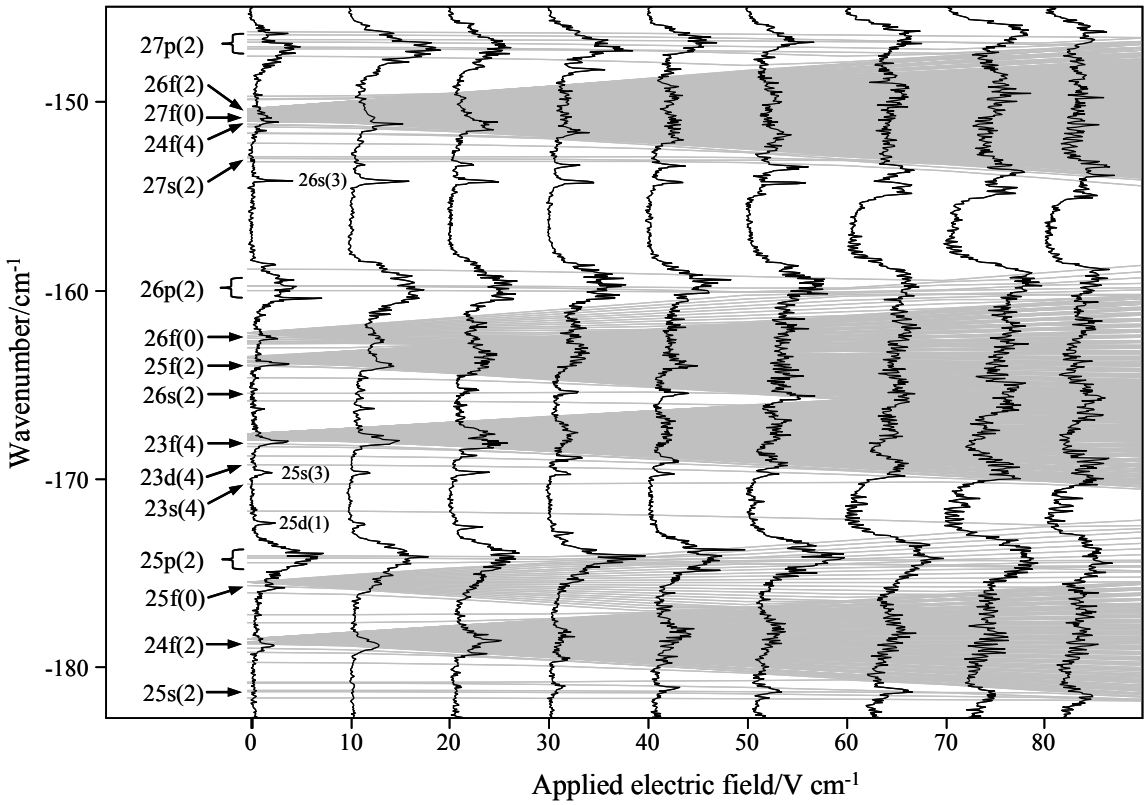

Figure 4.4.13: Zoom of Stark spectra of the predissociating Rydberg states of NO converging to the $v^+ = 0$ ionisation limit as shown in figure 4.4.12, superimposed on Stark maps calculated using the matrix diagonalisation method and including Rydberg states with even core rotational angular momentum quantum numbers $N^+ = 0$, 2 and 4. Individual Rydberg states are labeled *nl*(N^+).

Figure 4.4.14 shows a higher region of the spectra from 28p(2) to 30p(2) again overlaid onto the calculated Stark maps with even core rotational angular momentum of $N^+ = 0$, 2 and 4. This region is analogous to region (iii) in the spectra recorded *via* the $N' = 0$ intermediate, as the $N^+ = 0$ manifold sits on the red side of the $N^+ = 2$ manifold, and the mixing of the s(2) states into the *nl*(2) manifold is diluted by simultaneous mixing into the *nl*(0) manifold. As the energy increases, the *nl*(2) manifold moves away from the *nl*(0) manifold. This allows the s(2) states to once again mix freely into the *nl*(2) manifold such that a significant intensity gain can be observed at -120.0 cm^{-1}. Even at lower binding energies (-130.4 cm^{-1}), the strength of the field induced increase in the transition moment of the *n*s(2) Stark state is such that

it can be observed even after it has began to mix into the *nl*(0) manifold (marked by a * in figure 4.4.14)

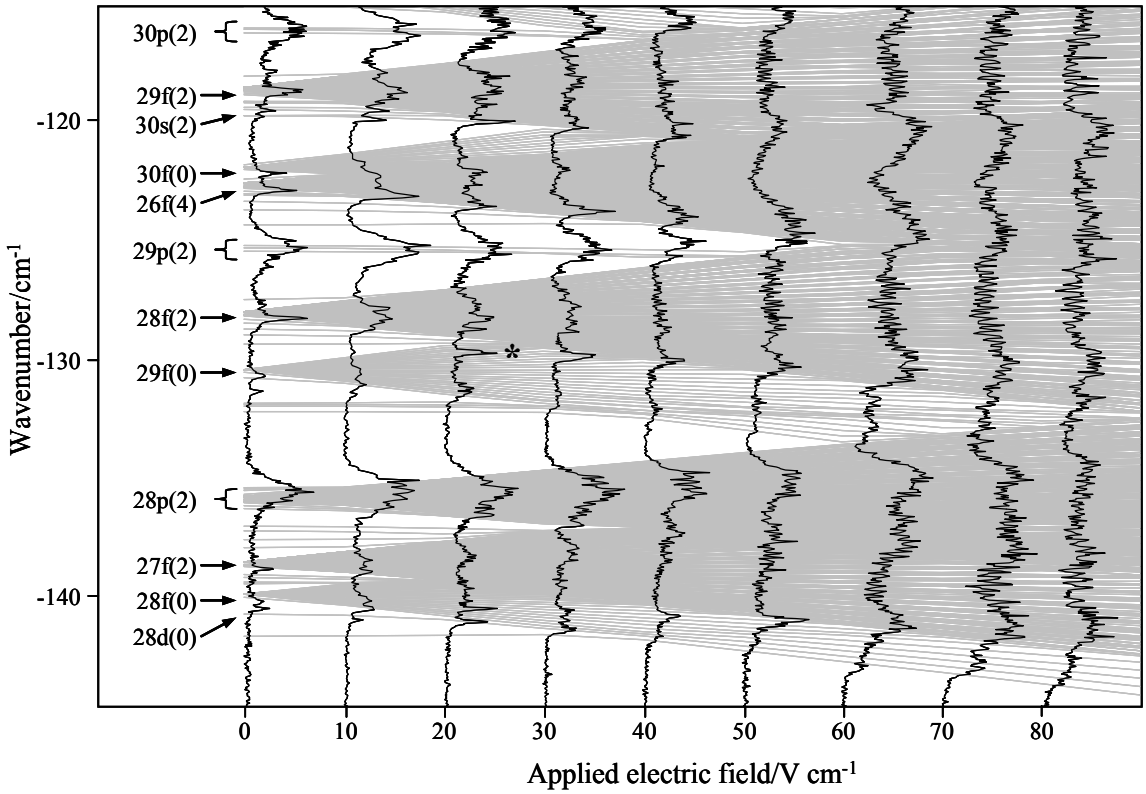

Figure 4.4.14: Zoom of Stark spectra of the predissociating Rydberg states of NO converging to the $v^+ = 0$ ionisation limit as shown in figure 4.4.12, superimposed on calculated Stark maps with $N^+ = 0$, 2 and 4. Individual Rydberg states are labeled $nl(N^+)$. The * corresponds to the intensity gained by the 29s(2) state as it mixes into both the 29(0) and 28(2) manifolds.

The spectra recorded *via* the $N' = 2$ intermediate shows many strong zero field peaks arising from s and d states with odd values of N^+. Figure 4.4.15 shows a region of the spectra from 25p(2) to 28p(2) overlaid onto Stark maps calculated for odd values of N^+. All of the states from the s(3) series are observed, and the 27s(1) and 25d(1) states can also be seen. The 27s(3) state (at -140.6 cm^{-1}) appears to grow in intensity as the field mixes it into the 26(3) manifold, and peaks at 50 V cm^{-1}.

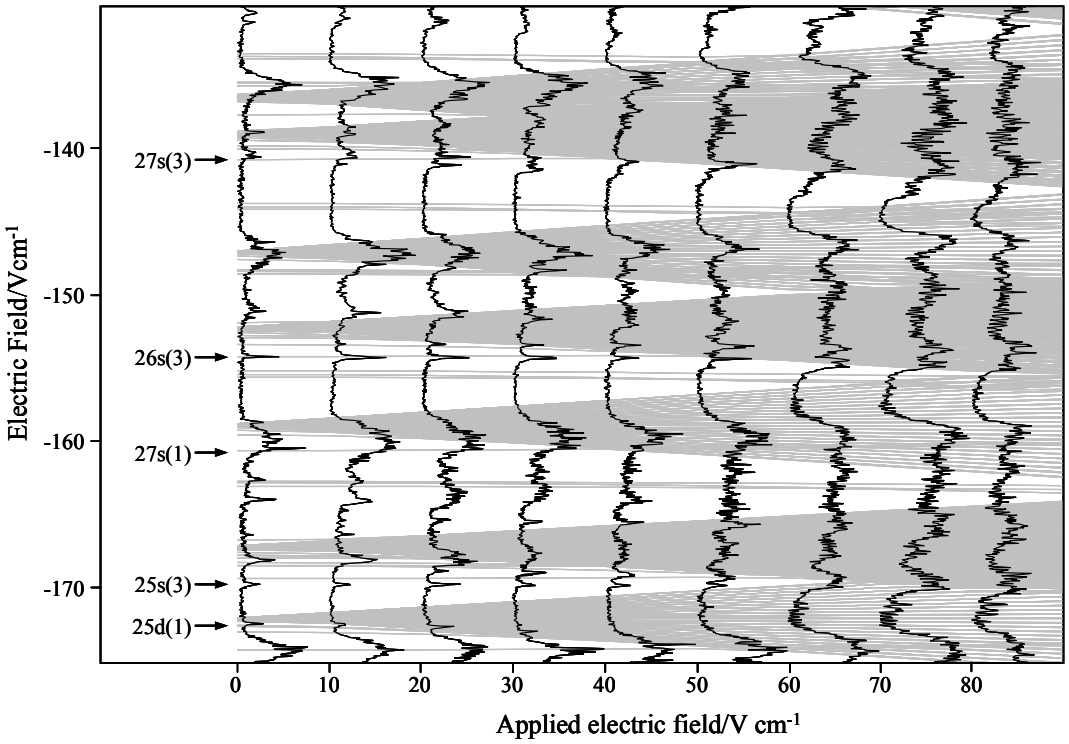

Figure 4.4.15: Zoom of Stark spectra of the predissociating Rydberg states of NO converging to the $v^+ = 0$ ionisation limit as shown in figure 4.4.12, superimposed on calculated Stark maps with $N^+ = 1$, and 3. Individual Rydberg states are labeled $nl(N^+)$. The * corresponds to the intensity gained by the 29s(2) state as it mixes into both the 29(0) and 28(2) manifolds.

A comparison between the $N' = 2$ and $N' = 0$ spectra is shown in figure 4.4.16. In the section of the $N' = 0$ spectra previously defined as region (*i*) both spectra show similarities due to the p(2) and f(2) series. However, the remainder of the zero field spectra show little similarities due to the absence of the p(0) and many other series in the $N' = 2$ spectra. As the field is applied peaks due to states of predominantly 27s(2) and 28d(0) character can be observed in both spectra. The 24f(2) peak in both spectra takes on a similar structure as the field is increased. The structure arises from the 24f(2) state mixing into the red side of the 24(2) manifold whilst the 25(0) manifold mixes into the blue side. Both of these manifolds are well separated from the nearest *nl*(4) manifolds and so at small voltages the mixing involves only the 24(2) and 25(0). As the field increases to 40 V cm^{-1}, the 24p(4) states begin to mix into the 24(2) manifold and the similarity is lost.

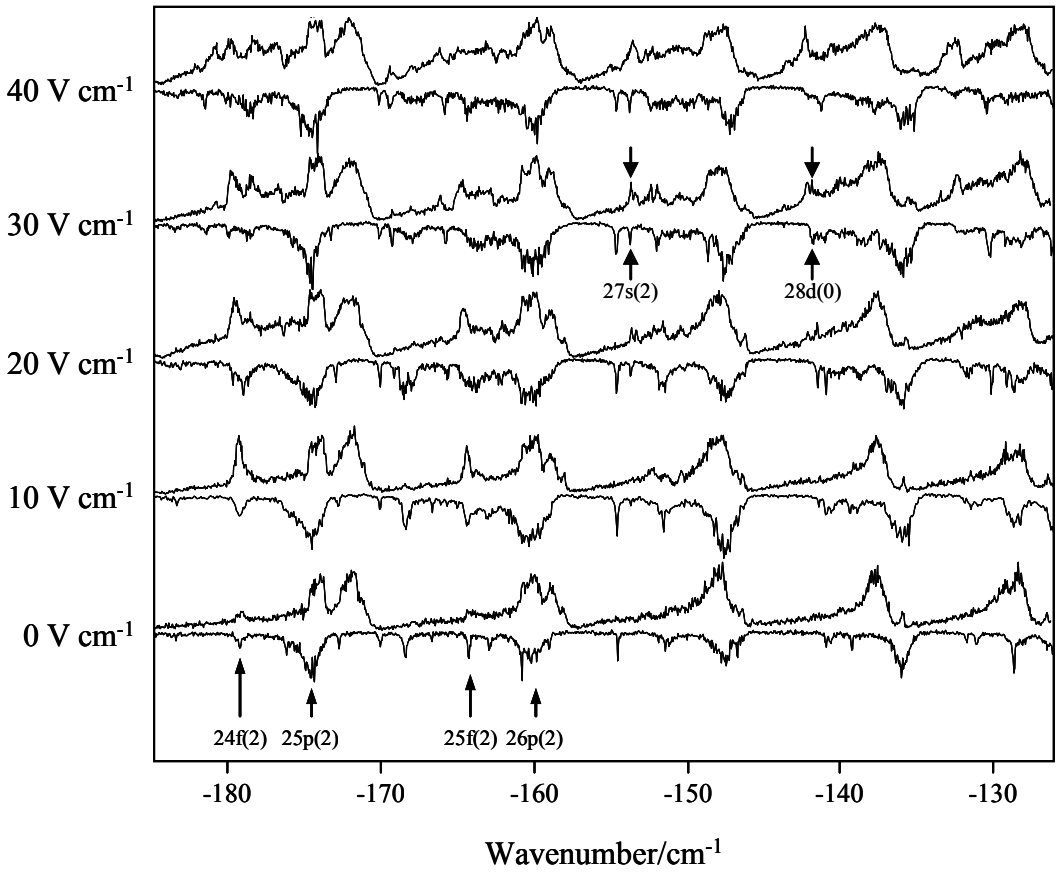

Figure 4.4.16: Comparison of the Stark predissociation spectra recorded *via* the $N' = 0$ (upper trace) and $N' = 2$ (lower inverted trace) intermediate states. States appearing in both spectra are labeled using $nl(N^+)$ notation.

4.4.4. Predissociation spectra excited *via* $A^2\Sigma^+(N' = 4, v' = 0)$ in the presence of an electric field

Selection rules predict that the dominant transition *via* the $A^2\Sigma^+(N' = 4, v' = 0)$ intermediate would be to Rydberg states of p(4) character. Transitions will also occur to states of f(2), f(4), f(6), p(2), and p(6) character, with a smaller probability of transitions to the s(3), s(5), d(1), d(3), d(5) and d(7) states. Many of these states can be accessed *via* the $N' = 2$ intermediate; therefore many of the observed states can be assigned by comparing the two spectra. The comparison between the already assigned $N' = 2$ and $N' = 4$ spectra is presented in figure 4.4.17.

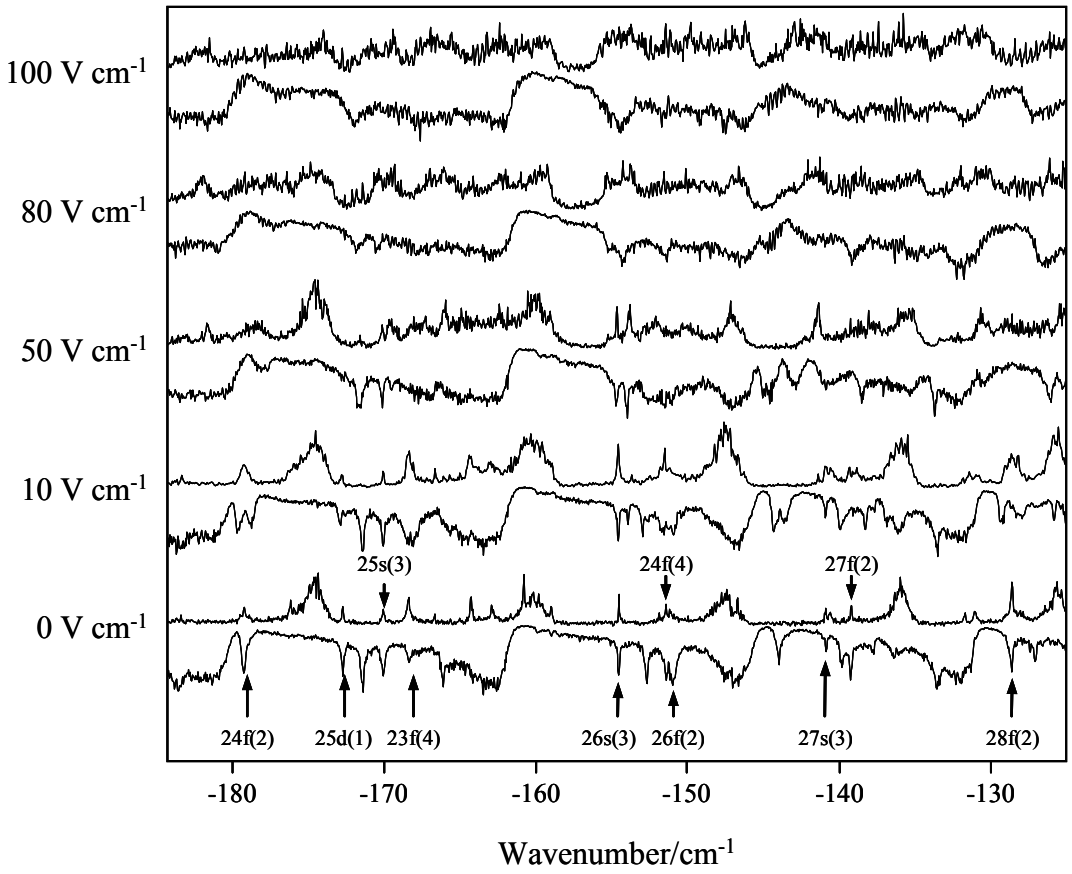

Figure 4.4.17: Comparison of the Stark predissociation spectra recorded *via* the $N' = 2$ (upper trace) and $N' = 4$ (lower inverted trace) intermediate states. States appearing in both spectra are labeled using $nl(N^+)$ notation.

The large broad peaks of the $N' = 4$ spectra are not observed in the $N' = 2$ spectra; however, states belonging to the f(2), f(4), d(1) and s(3) series are observed. The agreement between the spectra from -168 cm^{-1} to -145 cm^{-1} is surprising, as this range contains both a $N^+ = 0$ and 6 manifold. The similarities of the spectra in this range imply that these manifolds have little effect on the intensity as it spreads through the $N^+ = 2$ and 4 manifolds, which are common to spectra recorded *via* the two intermediates.

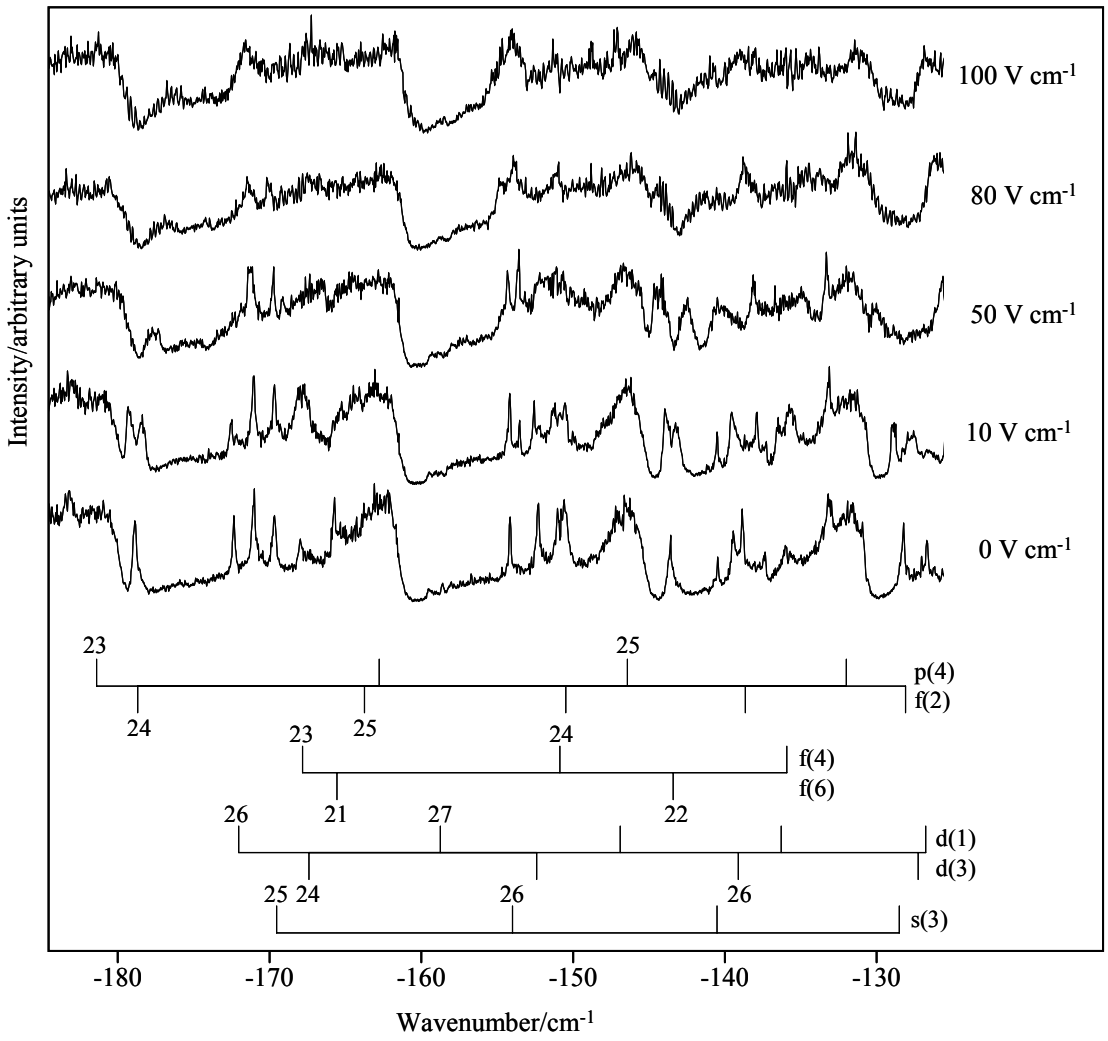

Figure 4.4.18: Stark spectra of the predissociating Rydberg states of NO converging to the $v^+ = 0$ ionisation limit with principal quantum number n = 25 – 30 excited *via* the $A^2\Sigma^+(N' = 4, v' = 0)$ state. The x-axis is the wavenumber with respect to the lowest ionisation limit ($N^+ = 0$, $v^+ = 0$). The y-axis is the intensity of the nitrogen REMPI signal in arbitrary units. The spectra are arranged from bottom to top in order of increasing applied electric field. The zero-field positions of the *n*p(4), *n*s(3), *n*d(1) and *n*d(3) Rydberg states are marked, together with the zero-field positions of the *n*f series, which are almost degenerate with the high-l manifolds associated with the $N^+ = 2$, 4 and 6 ionisation limits.

The remaining peaks were assigned using Stark maps calculated from 24(2), 23(4), and 21(6) to 30(2), 29(4), and 27(6) forming a total basis set of 4291 states. The spectra and assignments can be seen in figure 4.4.18. The extra peaks are due to the 21 and 22 f(6) states, the 26 and 30 d(1) states, and the 24 to 27 d(3) states. An extra

peak at -171.1 cm^{-1} does not match the positions of any of the expected series, and may be an interloper state from a series converging to an higher value of υ^+. As the field is increased $\Delta N^+ = \pm 2$ mixing increases the influence of the N^+ = 6 manifold and the similarities between the two spectra quickly vanish.

4.4.5. Predissociation spectra excited *via* $A^2\Sigma^+(N' = 1, \upsilon' = 0)$ in the presence of an electric field

Selection rules predict that the dominant transition *via* the $A^2\Sigma^+(N' = 1, \upsilon' = 0)$ intermediate would be to Rydberg states of p(1) character, with transitions of a smaller probability to the f(1), f(3), p(3), s(0), s(2), d(0), and d(2) states. Figure 4.4.19 shows the Stark spectra recorded with four different applied fields. At zero field the spectra is dominated by the *n*p(1) series, with smaller contributions from the *n*f(1) and *n*d(0) series. The remaining states can be assigned as *n*p(3), *n*f(3), *n*s(0), *n*s(2), and *n*d(2). The dominant p(1) series shows a broad asymmetric line shape, whilst the other series show sharper symmetric peaks. The p(1) and f(1) series are present through the whole spectrum, whereas the other series show a large *n*-dependence. For example, the d(0) series show intensity for the *n* = 25, 26 and 29 states but not for *n* = 27 and 28 states. Similarly, the *n* = 27 and 28 states can be observed in the f(3) series but not the *n* = 26 state. This strong *n*-dependency on the intensity of states was also observed in the studies of Fuji and Morita [74] and was often found to correspond to predissociation through a different decay channel.

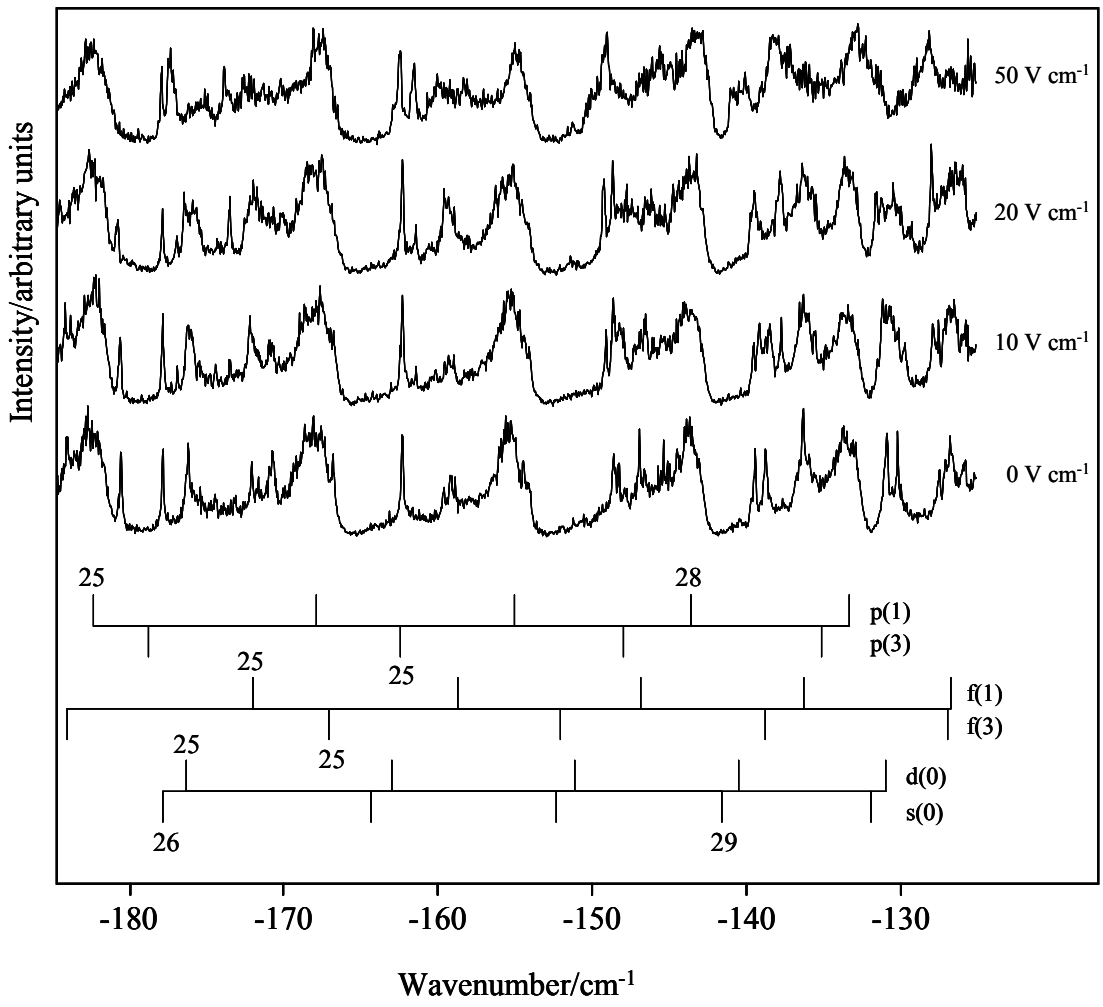

Figure 4.4.19: Stark spectra of the predissociating Rydberg states of NO converging to the $v^+ = 0$ ionisation limit with principal quantum number n = 25 – 29 excited *via* the $A^2\Sigma^+(N' = 1, v' = 0)$ state. The x-axis is the binding energy with respect to the lowest ionisation limit ($N^+ = 0$, $v^+ = 0$). The zero-field positions of the *n*p(1), *n*p (3), *n*f(1), *nf* (3), *n*d(0) and *n*s(0) Rydberg states are marked.

A comparison of the zero field spectra recorded *via* four different intermediates is shown in figure 4.4.20. The spectrum recorded *via* the $N' = 0$ intermediate is the simplest, showing only the p(0) and p(2) series with a small contribution from the f(2) series. The spectrum recorded *via* the $N' = 2$ intermediate shows a thinner Fano shape than the other three. This is to be expected, as the Fano line shape depends on the transition to the quasi-bound state, not the quasi-bound state itself (see equation 5.5.10). Therefore, the line shape parameter will vary for transitions from different intermediate states. As previously described, the spectra recorded *via* the $N' = 2$ and

$N' = 4$ show a number of similar peaks. However, there are few peaks that are shared between any other combinations of spectra.

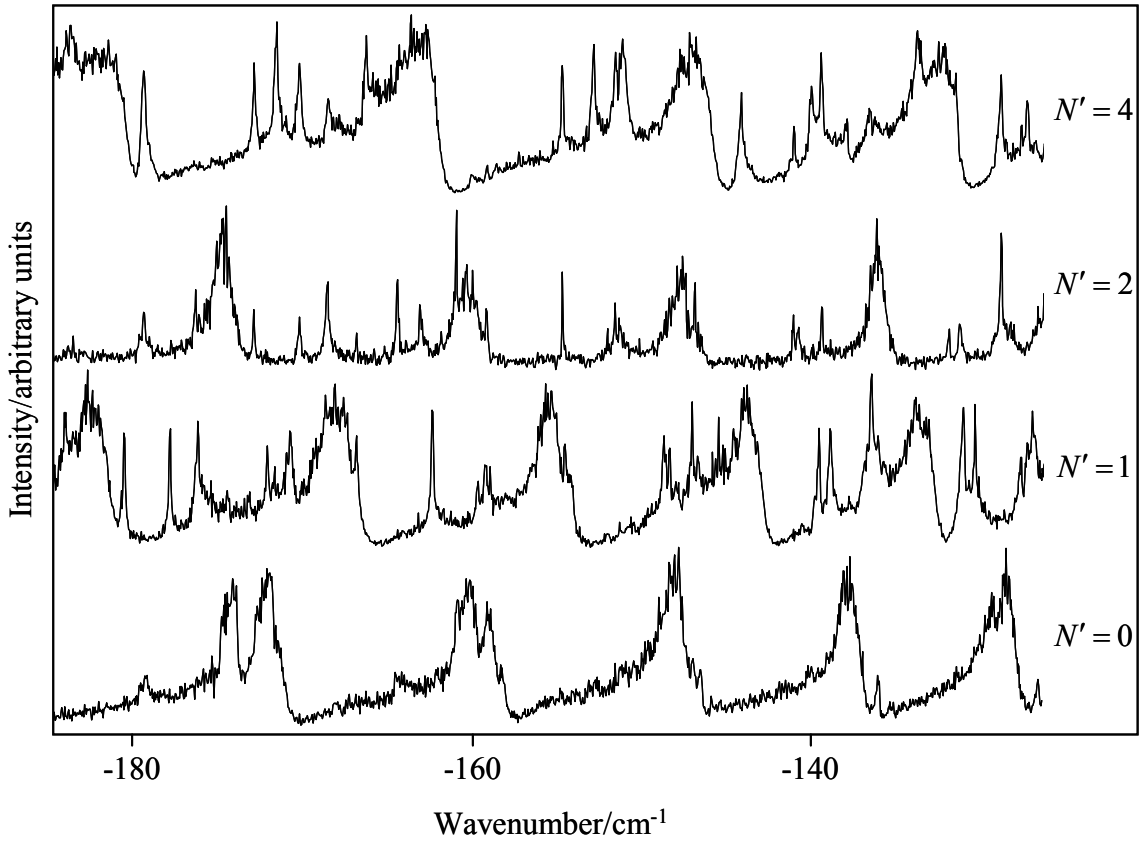

Figure 4.4.20: Zero field spectra of the predissociating Rydberg states of NO converging to the $v^+ = 0$ ionisation limit with principal quantum number n = 25 – 30 excited *via* the $A^2\Sigma^+(N', v' = 0)$ state. The x-axis is the binding energy with respect to the lowest ionisation limit ($N^+ = 0$, $v^+ = 0$). The y-axis is the intensity of the nitrogen REMPI signal in arbitrary units.

4.5. Summary

The spectra presented in this chapter are the first Rydberg predissociation Stark spectra of NO to be taken in this region and complement bound Rydberg spectra previously obtained [32]. In fact there are few Stark studies of predissociating Rydberg states [78, 79], and to the best of our knowledge only one other study has investigated the predissociating states of NO in an electric field: a recent investigation

of the low-*n* Rydberg states [80]. The spectra have been analysed using a hybrid quantum defect matrix diagonalisation technique, which has identified a number of intensity sharing processes as low-*l* states mix into the high-*l* manifolds. In the spectra recorded *via* the $N' = 0$ intermediate, three regions can be defined that show different states gaining intensity as the field mixes them into the nearest manifold. In region (*i*) the *n*d(2) and *n*s(2) states gain intensity, whilst in region (*iii*) only the *n*s(0) states see any significant intensity gain. In the spectra recorded *via* the $N' = 2$ intermediate, a similar intensity gain can be seen as the field mixes the low-*l* states into the high-*l* manifold. A field-driven intensity gain is observed mainly in the *n*s(2) states although it can also be seen for the 23d(4) and 27s(3) states. The zero field spectra recorded *via* the $N' = 0$ intermediate also show interesting behaviour; the intensity of the p(2) states gain intensity as they pass through the position of the p(0) states before suddenly disappearing. The mechanism by which this occurs is currently unknown, and requires further investigation. The zero field spectra taken *via* the four different intermediates show a strong *n*-dependence on the intensities of certain states in a series. It would be interesting to probe the other predissociation channels, especially the N(^{4}S) channel, to gain a fuller picture of the decay behaviour of these states.

5. A comparison between bound and predissociating Rydberg spectra: experiment and matrix diagonalisation calculations

5.1. Introduction

Above the first ionisation limit no Rydberg state can be thought of as purely discrete; all states are embedded in the ionisation continuum of a lower rovibrational state of the ion core and have a non-zero probability of decaying *via* autoionisation. States can also be embedded in the dissociative continuum belonging to a dissociative state and can decay *via* ion core fragmentation; a process termed predissociation. Below the lowest ionisation limit autoionisation can not occur, and the predominant decay pathway is predissociation; however other radiative and collisional decay processes are possible. Monitoring both the main predissociation and bound channels below the first ionisation limit effectively builds a map of the Rydberg wave function both within the molecule and also outside it in the dissociation continuum.

A Rydberg state can be labelled predissociating, autoionising or bound, and this label essentially arises from the sensitivity of that state to the experimental probe. For example, a Rydberg state can be called a predissociating state if it can be detected by probing the products of the core fragmentation, and thus has a short predissociation lifetime. However, that state may also undergo significant autoionisation if the autoionisation lifetime is comparative. If the same state was observed whilst monitoring the formation of the positively charged ion core it would be labelled an autoionising state. Only in the extremes of a short predissociation lifetime and long

autoionisation lifetime could a state be labelled purely predissociating (and vice versa). Bound Rydberg states are usually detected by pulsed field ionisation (PFI), in which an applied field pulse tips the Coulomb potential and strips an electron from the ion core. Therefore, only those states with a lifetime longer than the delay between excitation and ionisation will be detected. The Rydberg state is labelled bound, as it is relatively immune to predissociation and autoionisation with respect to the delay before ionisation.

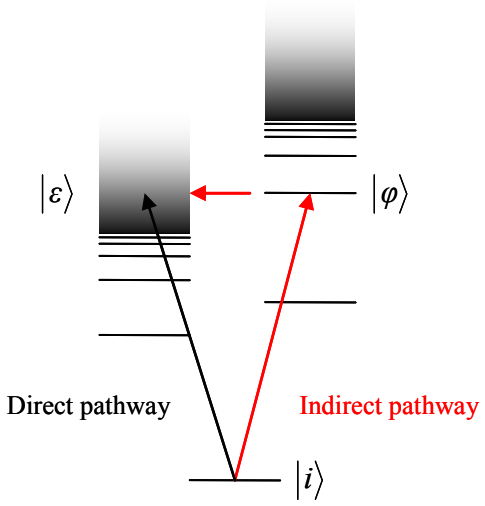

Figure 5.1.1: Schematic showing the two possible pathways to access a 'continuum state', $|\varepsilon\rangle$, from an initial state, $|i\rangle$. The first pathway is direct excitation to the 'continuum state' (black arrow), and the second is indirect excitation to the 'continuum state' *via* the degenerate discrete state $|\varphi\rangle$ (red arrows). Interference between the two pathways leads to the asymmetric Fano line shape.

The line shapes observed for a bound state and state which is strongly coupled to a continuum can be quite different. Bound states show a combination of Lorentzian and Gaussian line shapes, which arise from the finite state lifetime and imhomogeneous sample conditions respectively. However, a state embedded in a continuum is neither purely discrete nor purely continuous. In effect, two pathways are created to the continuum; one direct and one indirect *via* the autoionising or predissociating Rydberg state. On top of the Lorentzian profile, interference between the two pathways creates an asymmetric line shape known as a Fano profile (see figure 5.1.1)

[26]. A full derivation of the Fano line shape is given in appendix A but the main steps will be outlined in the following section. The remainder of this chapter will describe the differences between the experimental spectra of the bound and predissociating spectra and the different requirements of simulating the Stark spectra including line shape from the output of the matrix diagonalisation calculation.

5.2. The Fano parameter

The interaction between the discrete state, $|\varphi\rangle$, and continuum, $|\varepsilon\rangle$, can be considered as a perturbation. The wave function of the resulting hybrid state can be written as

$$|E\rangle = a_\varphi|\varphi\rangle + \int b_\varepsilon|\varepsilon\rangle d\varepsilon\,, \tag{5.1.1}$$

where the integral takes into account the continuous nature of the continuum. The Schrödinger equation for the perturbed system is

$$\begin{pmatrix} H & V \\ V & H \end{pmatrix}\begin{pmatrix} a_\varphi|\varphi\rangle \\ \int b_\varepsilon|\varepsilon\rangle d\varepsilon \end{pmatrix} = E\begin{pmatrix} a_\varphi|\varphi\rangle \\ \int b_\varepsilon|\varepsilon\rangle d\varepsilon \end{pmatrix}, \tag{5.1.2}$$

where H is the unperturbed Hamiltonian, V is the perturbation coupling the discrete state to the continuum, and E is the total energy of the hybrid state. Solving the Schrödinger equation to find b_ε and then normalising 5.1.1 to find a_φ leads to equation (5.1.3).

$$|a(E)|^2 = \frac{|V_E|^2}{\pi^2|V_E|^4 + \left[E - E_\varphi - F(E)\right]}, \tag{5.1.3}$$

where V_E is the off-diagonal coupling caused by the perturbation at energy E and $F(E)$ is a function introduced to simplify the expression (see A9). This can be related to a Lorentzian line shape (see A.20) by defining the half width as

$$\Gamma / 2 = \pi \left| V_E \right|^2 , \qquad (5.1.4)$$

and the mean energy position

$$E_0 = E_\varphi + F(E) , \qquad (5.1.5)$$

where $F(E)$ is assumed to be constant over the width of the resonance. Therefore, the discrete state has been diluted into the continuous band of energy states belonging to the continuum. This dilution is completely symmetrical about the mean position of the resonance, E_0, and has a Lorentzian shape as a function of the energy.

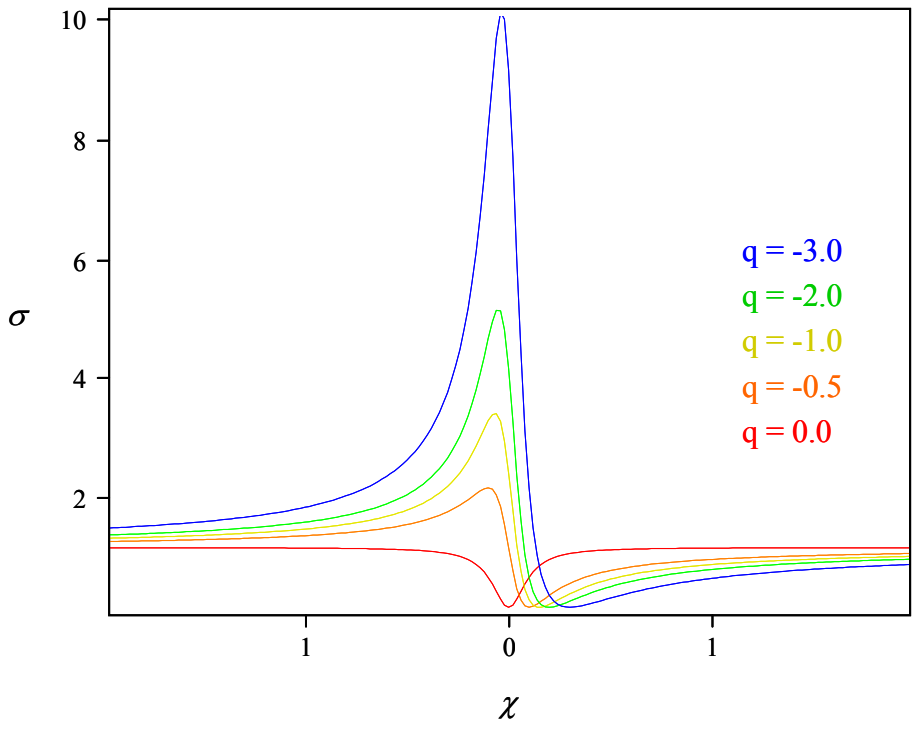

Figure 5.2.1: Fano line shapes generated with five different values of the Fano shape parameter q. The line shapes were calculated using $\sigma = \sigma_\phi (q + \chi) / (1 + \chi^2) + \sigma'_E$, with $\sigma_\phi = 1$, $\sigma_\varepsilon = 0.1$, $\Gamma = 1600$ and $n = 20$.

To understand the asymmetric Fano profile, the ratio of the transitions from an initial state, $|i\rangle$ to the hybrid state, $|E\rangle$ and continuum, $|\varepsilon\rangle$ must be considered. The strength of the transition is described by the dipole moment operator, D.

$$R = \frac{\left|\langle E|D|i\rangle\right|^2}{\left|\langle \varepsilon|D|i\rangle\right|^2}. \tag{5.1.6}$$

Substituting in the expanded form of $|E\rangle$, and derived values for b_ε leads to the equation 5.1.7.

$$R = \left|a_\varphi\right|^2 \left|\frac{\langle \Phi|D|i\rangle}{\langle \varepsilon|D|i\rangle} + V_\varepsilon Z(\varepsilon)\right|^2. \tag{5.1.7}$$

Defining two new parameters simplifies equation 5.1.7 further into the familiar Fano line shape formula.

$$R = \frac{(q+\chi)^2}{(1+\chi)}, \tag{5.1.8}$$

where χ is the detuning parameter

$$\chi = \frac{2(\varepsilon - E_0)}{\Gamma}, \tag{5.1.9}$$

and q is the Fano line shape parameter

$$q = \frac{\langle \Phi|\widetilde{D}|i\rangle}{\pi V_\varepsilon \langle \varepsilon|\widetilde{D}|i\rangle}. \tag{5.1.10}$$

It is this shape parameter that governs the symmetry of the line. If $q = 0$ the line shape is a symmetrical window resonance and as $q \to \infty$ the line shape approaches a symmetrical Lorentzian shape. For values of q between these two extremes the line shape will show an asymmetric shape as shown in figure 5.2.1.

5.3. Comparison of bound and predissociation spectra under no applied field

Figure 5.3.1 shows a comparison of the zero field Rydberg spectra taken using pulsed field ionisation (bound states) and (2 + 1) REMPI of the N(^{2}D) photodissociation fragment (predissociating states). The most noticeable difference arises from the broad asymmetric Fano profile of the predissociating *n*p states with respect to the relatively sharp symmetric Lorentzian peaks of the bound *n*f states. The bound spectra also show less congestion, as the observation of states is governed by the 'lifetime rule' that only states that are longer lived than the delay between the laser pulse and electric field pulse will be observed. As would be expected, the three p states previously identified in the zero-field bound spectrum recorded *via* the $A^2\Sigma^+(v'=0,N'=0)$ intermediate are also observed in the predissociation spectrum recorded *via* the same intermediate (labelled with red arrows in figure 5.3.1).

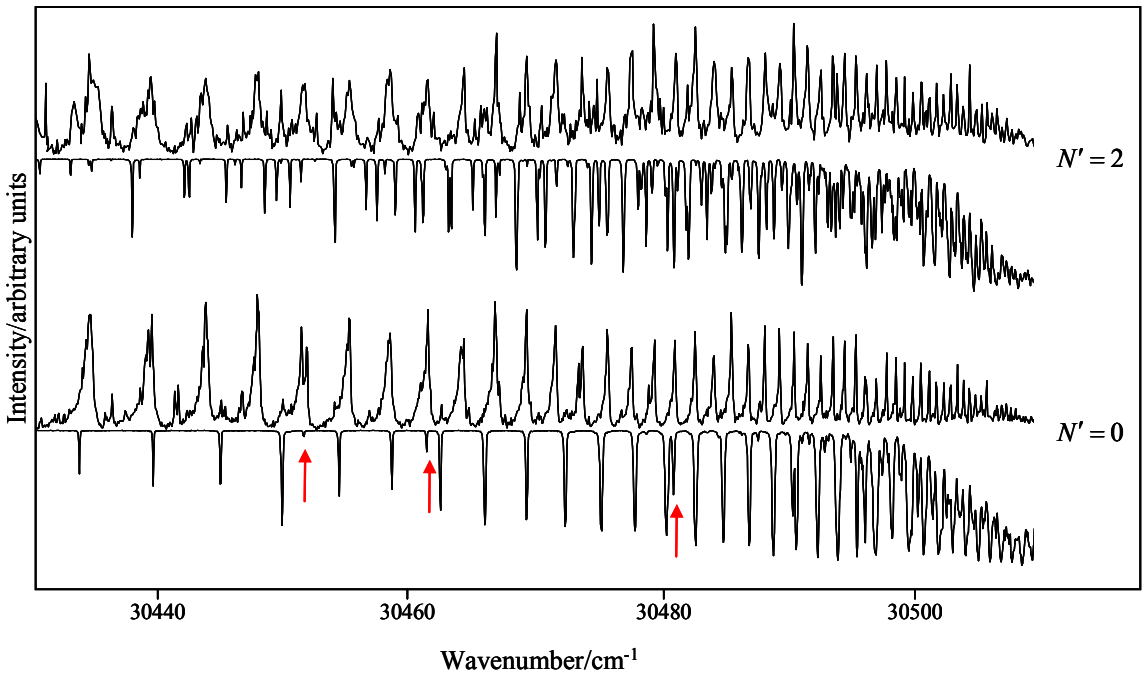

Figure 5.3.1: Zero field Rydberg spectra recorded *via* the $A^2\Sigma^+(v'=0,N'=0)$ (top pair of traces) and $A^2\Sigma^+(v'=0,N'=2)$ (bottom pair of traces) intermediates. The inverted traces are bound spectra recorded using pulse field ionisation, and the upper traces are dissociation spectra recorded by monitoring the N(^{2}D) photodissociation fragment.

In both sets of data, the various f states observed in the bound spectra can also be observed in the predissociation spectra. This is one reason why the bound and predissociation spectra recorded *via* the $A^2\Sigma^+(v'=0, N'=2)$ intermediate are more complex than the corresponding spectra recorded *via* the $A^2\Sigma^+(v'=0, N'=0)$ intermediate; the f(0), f(2) and f(4) series are present in the $N'=2$ spectra, but only the f(2) series is observed in the $N'=0$ spectra.

5.4. Comparison of bound and predissociation Stark spectra recorded *via* the $A^2\Sigma^+(v'=0, N'=0)$ intermediate

In this section we compare the predissociation Stark spectra with previously recorded bound Stark spectra [32]. Together, these bound and predissociating spectra provide an almost complete picture of the Rydberg state dynamics, effectively mapping the Rydberg wave function both within the molecule and outside the molecule in the dissociation continuum, although it should be noted that there are other minor predissociation channels that are not monitored. Both spectra were recorded using the same $(1+1')$ multiphoton excitation scheme. As with the zero field spectra, the bound spectra were recorded using pulsed field ionisation, whereas the predissociation spectra involved a $(2+1)$ REMPI scheme to ionize the $N(^2D)$ produced by the core fragmentation. The dipole transition moments coupling the A-state to the bound Rydberg states of mainly f character are much smaller than those coupling the A-state to the predissociating states and require the laser accessing this transition to be five times higher in power.

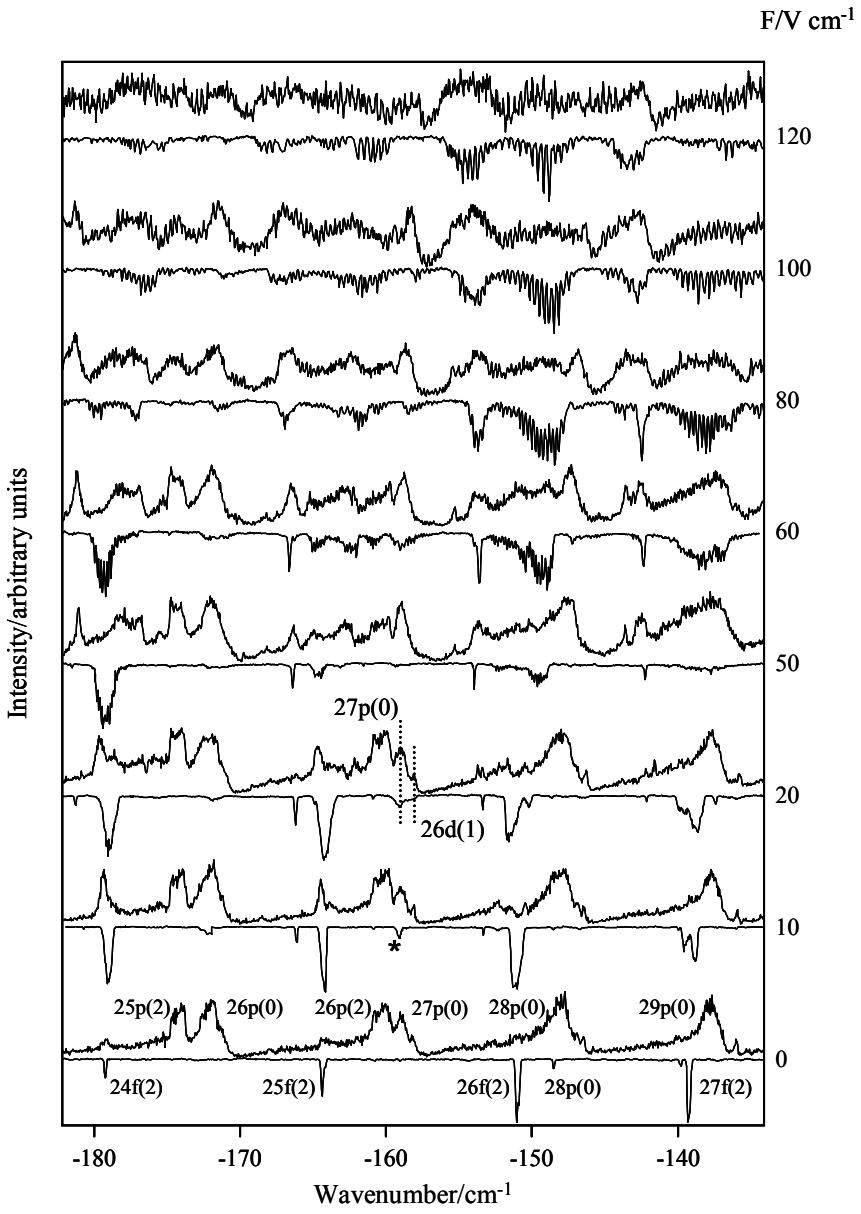

Figure 5.4.1: Stark spectra of the Rydberg states of NO recorded *via* the $A^2\Sigma^+(v' = 0, N' = 0)$ intermediate and converging to the $v^+ = 0$ ionisation limit with principal quantum numbers in the range $n = 24 – 29$. The upper traces are the dissociation spectra recorded by monitoring the $N(^2D)$ photodissociation fragment and the lower flipped traces are the pulsed-field ionisation spectra monitoring the bound component. The *x*-axis is the binding energy with respect to the lowest ionisation limit $(v^+ = 0, N^+ = 0)$. The discrete and continuum spectra are initially very different but, as the field-induced mixing increases, the spectra become remarkably similar. The asterisk labels the 27p(0) state as discussed in the text.

The predissociating and pulsed-field ionization spectra are compared in figure 5.4.1. The upper traces in figure 5.4.1 are the predissociation spectra and the lower flipped

traces are the bound spectra. Initially, as would be expected, both spectra are quite different. The bound spectra are dominated by the *n*f(2) series and have sharp symmetric line profiles whereas the predissociation spectra are dominated by the *n*p(0) series with some contributions from the *n*p(2) series and a weak *n*d(2) series. The *n*p(0) peaks are extremely broad and have asymmetric Fano line shapes; however, as the field is increased and the l states mix, the transition intensities and lifetimes are also mixed throughout the Stark manifolds and the predissociation and bound spectra begin to appear similar.

Expanded portions of these spectra are reproduced in figure 5.4.2. Figure 5.4.2A displays the spectrum over the energy region –170 cm^{-1} to –155 cm^{-1} at 0 V cm^{-1} (lower trace) and 60 V cm^{-1} (upper trace). At 0 V cm^{-1}, the bound spectrum is dominated by the 25f(2) state and by comparison with the predissociation spectra it is possible to assign tentatively the two tiny peaks that are just visible as the 26p(2) and 27p(0) states. In the predissociation spectrum the 26p(2) and 27p(0) peaks are broad, and weak transitions to the 26d(1) and 25d(2) states are also observed. At 60 V cm^{-1}, the spectra are rather similar (the intensity of the lower bound state spectrum is magnified by a factor of 1.5 for clarity). From left to right, the peaks labeled with arrows have predominantly 26s(2), 25d(2), 27s(0), 26p(2) and 27p(0) character.

Figure 5.4.2B displays the spectrum over the energy region –141 cm^{-1} to –157 cm^{-1} at 60 V cm^{-1} (lower trace) and 120 V cm^{-1} (upper trace). At 60 V cm^{-1}, the intensity in the predissociation spectrum is distributed quite evenly across the 27(0) manifold; however, there is a distinct “intensity gap” in the bound spectrum around the 28p(0) state. In the bound spectrum, the intensity of the Stark states is attributed to mixing of the *n*f(0) series into the lower energy edge of the Stark manifold. Conversely, in the predissociation spectrum, the intensity of the Stark states associated with the *n*(0) manifold derives from the higher energy (n + 1)p states and the lower energy (n + 1)s

and *n*d states which results in a more uniform distribution of intensity across the manifold. By 120 V cm^{-1}, adjacent manifolds with the same rotational quantum number begin to cross (the Inglis-Teller limit) and this "intensity gap" becomes less pronounced as the 28p(0) state mixes into both the 27(0) and 28(0) manifolds.

A number of well-resolved "dark" states are observed to gain intensity in both the bound and predissociating spectra. For example, at –166 cm^{-1} a peak appears in the bound spectrum at 10 V cm^{-1} (figure 5.4.1) and at 50 V cm^{-1} in the predissociation spectrum. From our matrix-diagonalisation analysis it can be assigned as the transition to the 27s(2) state, which mixes first with Rydberg states of 26p(2) character. The *n*p(2) states do not have significant transition intensity in the bound spectra and so we must assume that the early appearance of 27s(2) in the bound spectrum is due to zero-field $s\sigma - d\sigma$ coupling [53, 84] and d(2) – f(2) Stark mixing. The fact that the 27s(2) peak appears at weaker fields in the bound spectrum implies that this s state is being stabilized against predissociation by $s\sigma - d\sigma$ coupling. Another "dark" state is visible at –159.0 cm^{-1} in the 10 V cm^{-1} bound state spectrum (marked with an asterisk in figure 5.4.1). Initially, we assigned this as 26d(1) [32], but comparison with the predissociation spectrum leads us to reassign this peak as the 27p(0) state with 26d(1) appearing as a small shoulder on the low energy side of 27p(0).

It is clear from this comparison that at low fields the predissociation spectra show many more peaks than the bound spectra, and a broader line shape. From the analysis carried out in Chapter 4, the predissociation spectra show more complex behaviour in zero field as witnessed by the changing intensity of the p(2) series as it scans through the p(0) series. This complex behaviour was not observed in the previous bound state Stark investigations, as the p states were only weakly observed.

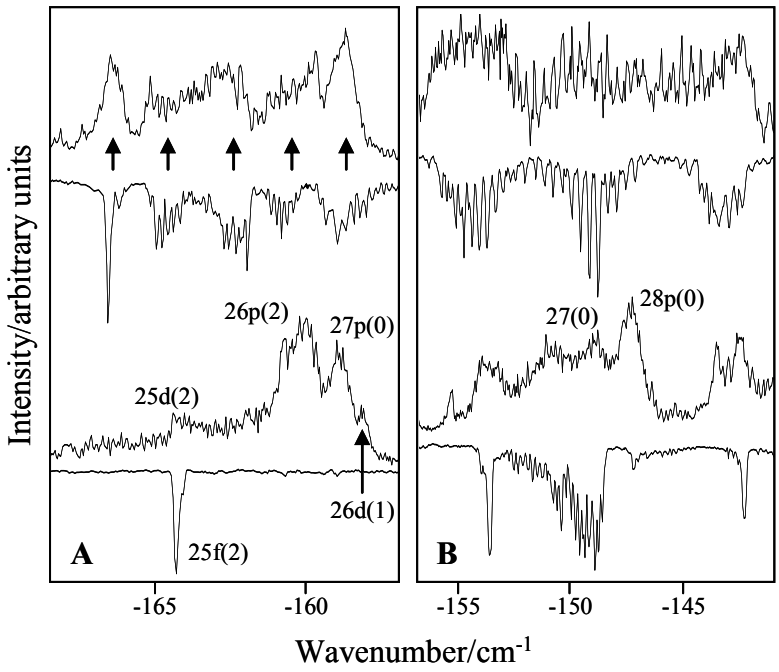

Figure 5.4.2: Enlarged portions of Stark spectra taken from figure 5.4.1: the upper traces are dissociation spectra recorded by monitoring the N(^{2}D) photodissociation fragment, and the lower flipped traces are the pulsed-field ionisation spectra monitoring the bound component. The *x*-axis is the binding energy with respect to the lowest ionisation limit $(v^+ = 0, N^+ = 0)$.
A: Energy region -170 cm^{-1} to -155 cm^{-1} at 0 V cm^{-1} (lower traces) and 60 V cm^{-1} (upper traces). The intensity of the lower bound spectrum has been multiplied by a factor of 1.5 for clarity. From left to right, the peaks labeled with arrows have predominantly 26s(2), 25d(2), 27s(0), s6p(2) and 27p(0) character.
B: Energy region -141 cm^{-1} to -157 cm^{-1} at 60 V cm^{-1} (lower trace) and 120 V cm^{-1} (upper trace).

5.5. Simulating the bound Rydberg spectra

As introduced in Chapter 4, the output of the matrix diagonalisation calculation gives the resonance energy of a Stark state, $|k\rangle$, at the specified field, and the composition of the state in terms of the mixing of the case (d) basis, $|k\rangle = \sum_{nl} |\phi_0^{(d)}\rangle$, where $|\phi_0^{(d)}\rangle$ is the zero field case (d) state and a_{nl} is a weighting coefficient. The output is a line spectrum, with all lines of equal intensity. To calculate the transition intensity from the intermediate A state to a specific *k* state the transition moment, $\langle \varphi_k | T | \varphi_A \rangle$, is

calculated as a linear combination of the Hund's case (d) zero field transition moments, $\left\langle \varphi_i^{(d)} \middle| T \middle| \varphi_A \right\rangle$, weighted by the eigenvectors of the Hamiltonian matrix, c_{ki}.

$$\left| \left\langle \varphi_k \middle| T \middle| \varphi_A \right\rangle \right|^2 = \left| \sum_i c_{ki} \left\langle \varphi_i^{(d)} \middle| T \middle| \varphi_A \right\rangle \right|^2 . \tag{5.5.1}$$

The zero field case (d) transition moments are calculated using

$$\left\langle \varphi_i^{(d)} \middle| T \middle| \varphi_A \right\rangle = \sum_{l'} (2N'+1)^{\frac{1}{2}} (2N+1) \begin{Bmatrix} N' & l & N^+ \\ l' & N & 1 \end{Bmatrix} \begin{pmatrix} l & N^+ & N' \\ 0 & 0 & 0 \end{pmatrix} A_{l'}(l) , \tag{5.5.2}$$

where $A_{l'}(l)$ are adjustable parameters chosen to give the best fit to the zero-field spectra and the 6-j and 3-j symbols are used to add the various angular momenta. As shown by the missing p series in the bound spectra, the transition intensity also depends strongly on the decay rate. Below the first ionisation limit this is determined by the rate of predissociation. The decay rate of a *k* state is given as the weighted sum of the case (d) decay rates

$$\Gamma_k = \sum_i c_{ik} \Gamma_i^{(d)} . \tag{5.5.3}$$

The total transition intensity, *I*, is then given by

$$I = \left| \sum_i c_{ki} \left\langle \varphi_i^{(d)} \middle| T \middle| \varphi_A \right\rangle \right|^2 e^{(-2\pi\Gamma_k t / h)} , \tag{5.5.4}$$

where *t* is the delay between the laser pulse and ionising electric field pulse, and is set as the experimental value. Finally, the line spectrum is convoluted with a Gaussian frequency profile with full width half maximum of 0.15 cm^{-1}. This technique is able to produce accurate simulations of the Stark frequency bound spectra [32] (figure 5.5.1), which were calculated using the values for $A_{l'}(l)$ as listed in table 5.5.1, and decay rates listed in table 5.5.2.

$l' - l$	$A_{l'}(l)$
p – s	0.1
s – p	0.7
d – p	0.1
d – f	1.0

Table 5.5.1: Table of $A_{l'}(l)$ values used for simulations *via* the $A^2\Sigma^+(v' = 0, N' = 0)$ intermediate state.

l	$\Gamma_l^{(d)}$ /cm^{-1}
s	500
p	1610
d	1000
f	43

Table 5.5.2: Table of decay rates used for the bound state simulations reproduced in this thesis. All values are taken from ref [24].

The zero field experimental spectrum is dominated by the 25f(2) and 26f(2) Rydberg states, and this is reproduced in the calculated spectrum. The 28p(0) state is not observed in the calculated spectrum, and although it is possible to increase the zero field intensity by increasing $A(1)$ this reduces the agreement with the experimental data as a field is applied. The addition of an electric field causes both peaks to split as intensity is shared over the $n(2)$ manifold and nearest $n(0)$ manifold. As the field increases, the mixing between manifolds increases and intensity is shared over both the $n(0)$ and $n(2)$. This complex mixing is well reproduced in the calculated spectra. A number of "dark" states also gain intensity as the field is increased. The 26d(1) state can be observed in both the calculated and experimental spectra, although the simulation over estimates the extent of mixing of the d state into the nearest $n(1)$ manifold. The 26s(2) and 27s(2) states also gain intensity due to field induced

coupling with optically accessible Rydberg series. The calculated spectra fail to reproduce the extent of this gain, and this will be seen again in the predissociation calculations in the next section. An analysis of the dependence of these peaks on the d quantum defect shows that the appearance is due to sσ-dσ coupling followed by field induced d(2)-f(2) mixing.

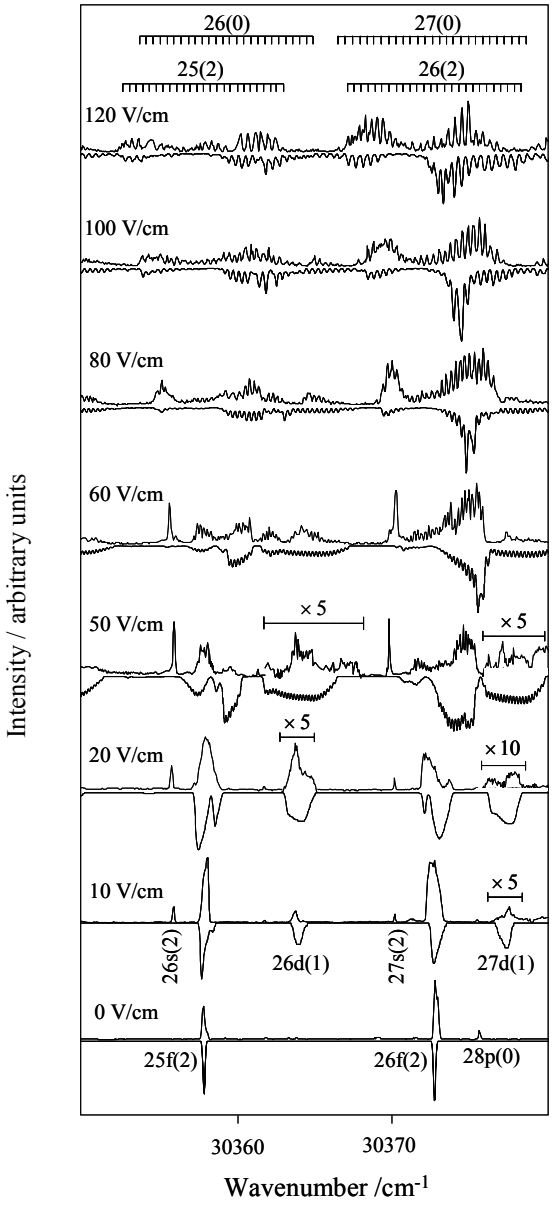

Figure 5.5.1: Experimental (upper) and simulated (lower inverted traces) Stark spectra of the bound n = 25 and 26 Rydberg states recorded *via* the $A^2\Sigma^+(v' = 0, N' = 0)$ intermediate state [32]. From bottom to top, the spectra correspond to increasing applied electric field. The intensities of some sections of the spectra have been magnified for clarity.

5.6. Simulating predissociation spectra

To obtain predissociation spectra in an approximate form, it is possible to change the exponential decay term in equation 5.5.4 to an exponential recovery by subtracting it from 1. A simulation of the predissociation Stark spectra can then be produced using a Lorentzian line shape. This approximation has previously been used to model the Stark effect on the predissociating states of molecular hydrogen [79] and NO [80], and although a comparison between figures 5.4.1 and 5.6.1 shows that in this case the approximation is inaccurate, the method will be discussed here briefly. Figure 5.6.1 shows Stark spectra simulated using the 'Lorentzian' approximation for both exponential decay and recovery using the decay parameters listed in table 5.5.2 and fitting parameters listed in table 5.6.1.

$l' - l$	$A_{l'}(l)$
p – s	0.1
s – p	1.5
d – p	1.0
d – f	2.0

Table 5.6.1: Table of $A_{l'}(l)$ values used for bound and predissociation simulations *via* the $A^2\Sigma^+(v' = 0, N' = 0)$ intermediate state as shown in figure 5.6.1.

The Lorentzian approximation does not accurately reproduce the predissociation spectra; however the mixing behaviour in the field gives information that is harder to deduce from a spectrum with a broad Fano line shape. As would be expected, in zero field the bound spectrum is dominated by the f(2) series, whilst the predissociation spectrum is dominated by the p(0) and p(2) series. The calculated zero-field predissociation spectrum also shows strong f(2) peaks, in contrast to the weak peaks observed experimentally. It is necessary to increase the zero field transition strength to

states of f(2) character in order to replicate the experimentally observed gain in s(2) intensity due to field induced mixing with the high-*l* *n*(2) manifold. This also reproduces the reduction in intensity gain in region (*iii*) where the mixing is diluted by the presence of the *n*(0) manifold. Therefore, by increasing the f(2) zero field intensity, the accuracy of the high field spectra is enhanced at the expense of the zero field spectrum. Whilst increasing the f(2) intensity does lead to a field induced intensity gain for the s(2) states, it does not have the same effect on the d(2) states, which are only weakly observed in the calculated spectra. Similarly, the high-*l* manifolds can be observed at modest fields (30 V cm^{-1}) in the experimental predissociation spectra (figure 4.4.5), but do not show significant intensity in the calculated spectra. This can be explained as follows. States of f character have a small quantum defect and are rapidly mixed into the high-*l* manifolds. The large transition intensity of the f states in the bound spectra leads to the high-*l* manifolds having significant intensity at 20 V cm^{-1}. In contrast, the high-*l* states are stable with respect to predissociation and so in the calculated predissociation spectra the field induced mixing rapidly decreases the intensity of the f(2) states. The dominant series in the predissociation spectra are of p character, which have large quantum defects and do not mix into their associated manifolds until higher fields (greater than 80 V cm^{-1}). Thus in the calculated predissociation spectra the p states dominate the spectra, and the high-*l* manifolds show little intensity.

These problems suggest that the current calculations are missing a low field coupling mechanism between the p states and the high-*l* manifolds. A coupling of this form would increase the high-*l* transition intensity at low fields, which in turn would increase the intensity gained by states of d(2) character due to field induced mixing. States of s(2) character would also gain intensity *via* this mechanism, removing the need to exaggerate the zero field f(2) transition strength.

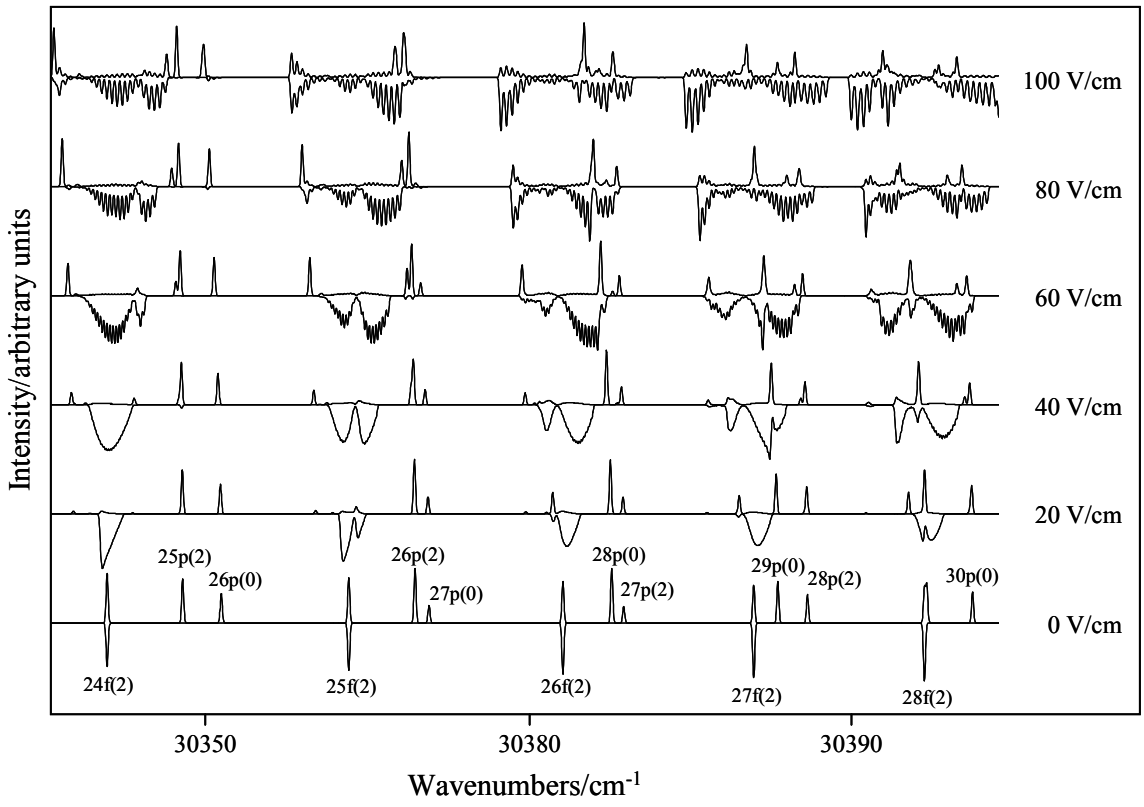

Figure 5.6.1: Simulated spectra using a Lorentzian line shape recorded *via* the $A^2\Sigma^+(v' = 0, N' = 0)$ intermediate state. The upper traces are the predissociation spectra whilst the lower inverted spectra are the bound spectra.

Finally, the simulated spectra does not reproduce the intensity gain and sudden disappearance of the p(2) series in this region. This is not surprising as the model employed includes neither continuum interference effects, nor dissociation limits.

As introduced in Section 5.2, the interaction between a discrete state and continuum creates a line shape with an asymmetry controlled by the Fano asymmetric parameter *q*. The photoionisation cross section can be calculated using equation 5.6.1 for a system with many non-interacting closed channels and many open continuum channels [88].

$$\sigma = \sum_k \sigma_{\varphi k} \frac{\left(q_k + \chi_k\right)}{\left(1 + \chi_k{}^2\right)} + \sigma'_E . \qquad (5.6.1)$$

χ_k and q_k are given by equations 5.1.9 and 5.1.10. As the value of q depends on the closed channel being considered, closed channels of different quantum numbers l, and N^+ will have different q values. $\sigma_{\varphi k}$ and σ'_E represents the portion of the cross-section relating to transitions to states in the continuum that do or do not interact with the discrete state respectively. The quantities q_k, E_{0k}, Γ_k, $\sigma_{\varphi k}$ and σ'_E are used to fit equation 5.6.1 to the experimental data and there are a number of papers discussing various fitting procedures [89-92]; however many of these parameters can be found from the output of the matrix diagonalisation code. The resonance energy, E_{0k}, is given as the eigenvalues output of the diagonalisation calculation and $\sigma_{\varphi k}$ is essentially the transition moment as calculated using equation 5.5.1. The decay rate, Γ_k, is calculated using equation 5.5.3; however the decay of states no longer reduces the intensity and so the exponential decay term is no longer necessary. With respect to the bound simulations, the only additional fitting parameters are q_k and σ'_E; σ'_E is simply a baseline measurement found by observing the signal intensity when off resonance with a predissociating state, such that only transitions direct to the continuum are observed.

$A_{l'}(0)$	1.0
$A_{l'}(1)$	2.0
$A_{l'}(2)$	0.1
$A_{l'}(3)$	3.5
$q_{l=1}\, q$	-3.5
$q_{l\neq 1}$	-8

Table 5.6.2: Table of parameters used to calculate the zero field spectrum presented in figure 5.6.2.

Figure 5.6.2 shows the zero field spectrum recorded *via* the $A^2\Sigma^+(v'=0,N'=0)$ intermediate and the corresponding simulated spectrum using the decay parameters

listed in table 5.5.2 and the adjustable parameters listed in table 5.6.2. The simulated spectrum reproduces the intensities and positions of the p(0), s(1) and f(2) series but currently incorrectly exaggerates the slight asymmetry in the s(1) peaks. The p(0) series is also too thin, although this effect can be artificially matched by convoluting with a Gaussian of a wider FWHM. In general the zero field simulation reproduces the zero field spectrum sufficiently to calculate Stark spectra using a similar set of parameters; however, as also observed in the "Lorentzian" simulations (figure 5.6.1), attempts to do this so far have been unsuccessful mainly due to the lack of intensity gained by the high-*l* manifolds as the field increases.

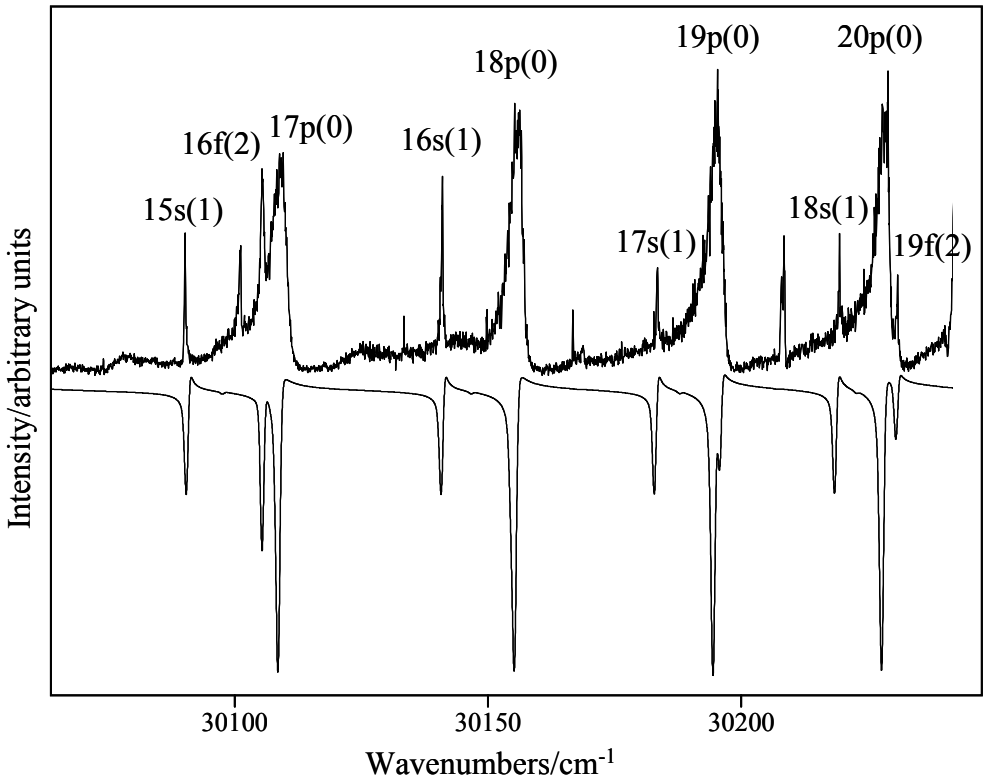

Figure 5.6.2: Experimental (upper) and simulated (lower inverted traces) Stark spectra of the predissociating n = 17 – 20 Rydberg states recorded *via* the $A^2\Sigma^+(v' = 0, N' = 0)$ intermediate.

5.7. Summary

The work presented in this chapter compares the previously obtained bound Stark spectra with the predissociating Stark spectra and details the current progress in calculating the predissociation Stark spectra using the output from the matrix diagonalisation procedure.

A comparison of the bound and predissociating spectra have identified a number of important issues that need to be addressed to simulate the predissociating spectra accurately; the most obvious of which is the Fano line shape and this has begun to be implemented. Another observation is that the mixing in the predissociation spectra shows greater complexity, owing to the larger number of observed states in zero field with respect to the bound spectra.

Prior to carrying out the simulations the matrix diagonalisation procedure was separated from the simulation procedure, as the diagonalisation process is the slowest stage in calculating the spectra. Instead the simulation procedure now reads in the eigenvectors and eigenvalues from input files created by the diagonalisation code. Using the separate simulation program a number of simulations have been made of both the bound and predissociating spectra. An analysis using a Lorentzian line shape has identified a number of issues that need to be identified before predissociating Stark spectra can be produced. The zero field spectra has been accurately reproduced, although further work is needed to remove the asymmetry from the s(1) series.

6. Selective Field Ionization in Bound Rydberg States of NO

6.1. Introduction

As introduced in Chapter 1, the application of an external electric field to a Rydberg system lifts the symmetry. This creates a saddle point in the Coulomb potential of the ion core, which moves to lower potentials as the field is increased (figure 6.1.1). If the saddle point is lower than the binding energy of an electron in a Rydberg state then the electron will no longer be bound and is field ionised. Field ionisation has been used to investigate bound Rydberg states in pulsed field ionisation (PFI) experiments in which Rydberg electrons are laser excited, rapidly stripped from the core by a fast electric pulse and subsequently detected [31-33].

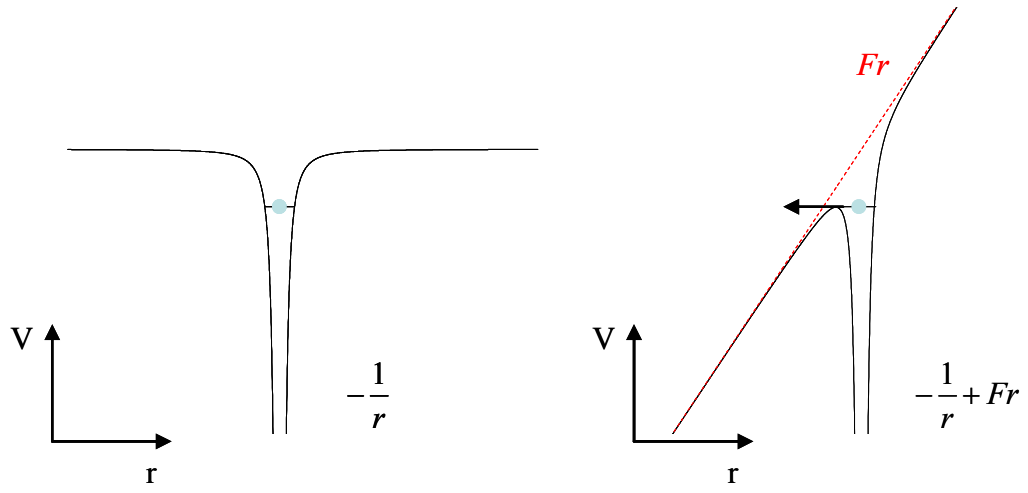

Figure 6.1.1: Schematic showing Coulomb potential in zero field (left) and the combined Coulomb-Stark potential in an applied electric field (right). The black curve shows the total potential. The dotted red line shows the applied electric field potential. The blue dot represents an electron, bound at zero field, but field ionized under the applied field, *Fr*.

A second important effect of an applied field is to split the degenerate high orbital angular momentum states into a manifold of Stark states. The field mixes states of orbital angular momentum $\Delta l = \pm 1$, and so l is no longer a good quantum number. To be separable the Schrödinger equation requires a transformation into parabolic coordinates, and a new quantum number, k, is defined as k = -n+1, -n+3,…., n-1. The frequency of a Stark state, ω_{nk}, as a function of the applied external field, F, is given by equation 6.1.1 in atomic units,

$$\omega_{nk} = -\left(2n^2\right)^{-1} + 3nkF/2 + ... \qquad (6.1.1)$$

For non-hydrogenic systems, the ion core couples all levels of the Stark manifold creating avoided crossings at the points where different Stark states cross, as shown in the inset of figure 6.1.2 [93, 94]. If population is transferred to a single Rydberg state at zero field and then a ramped field is applied, the population travels through the Stark manifolds towards the field ionisation limit. At each avoided crossing there is some probability of the population crossing to another adiabat *via* a diabatic transition through the crossing, or continuing along the same adiabat *via* an adiabatic transition through the crossing. The probability distribution along each pathway depends on the separation of the two states at the crossing, $W_{12,}$ and the speed at which the crossing is approached. The speed of approach depends on the gradient of the potential curves, dE/dt, and the slew rate of the field, dF/dt. The probability for a diabatic crossing is given by equation 6.1.2.

$$P_{diabatic} = \exp\left[\frac{2\pi|V_{12}|^2}{|dE_1/dF - dE_2/dF|dF/dt}\right]. \qquad (6.1.2)$$

V_{12} is the coupling matrix of the interaction between the two states causing the avoided crossing, and is related to the separation by $V_{12} = W_{12}/2$ (in atomic units). If the ramped field is sufficiently slow, the electron is ionised at the classical field

ionisation threshold *i.e.* each crossing is traversed adiabatically (green arrow in figure 6.1.2). This is related to principal quantum number, n, in equation 6.1.3.

$$F_{adiabatic} = \frac{1}{16n^4} . \qquad (6.1.3)$$

For fields of sufficiently fast slew rate, all crossings are traversed diabatically (orange arrow in figure 6.1.2) and the electron is ionised at the diabatic field ionisation threshold given by equation 6.1.4. This is derived assuming only the first order Stark effect applies and that $k = n$, which is valid for high n.

$$F_{diabatic} = \frac{1}{9n^4} . \qquad (6.1.4)$$

Field ionisation using ramped fields has been studied in a number of atomic systems and both adiabatic and diabatic ionisation has been observed [95-101]. The use of ramped fields has also become an important tool in wave packet experiments [16, 34-36]. Selective field ionisation (SFI) employs a slowly ramped field to field ionise the electron wavepacket, and the subsequent ionisation profile is used to identify the relative populations of different energy states within the wave packet. For a wave packet as defined by equation 6.1.5, SFI provides a measurement of the amplitude a_i of the eigenstates in the wavepacket. This corresponds to the weighting of the different $\psi(r,\theta,\varphi)$ basis states within the wavepacket, which for an electronic Rydberg wavepacket are the Hund's case (d) zero field states.

$$\Psi(r,t) = \sum_i a_i \psi(r,\theta,\varphi) \mathrm{e}^{-iE_i t/\hbar} \qquad (6.15)$$

where E_i is the energy of the i state and $\hbar$ is the reduced Planck's constant.

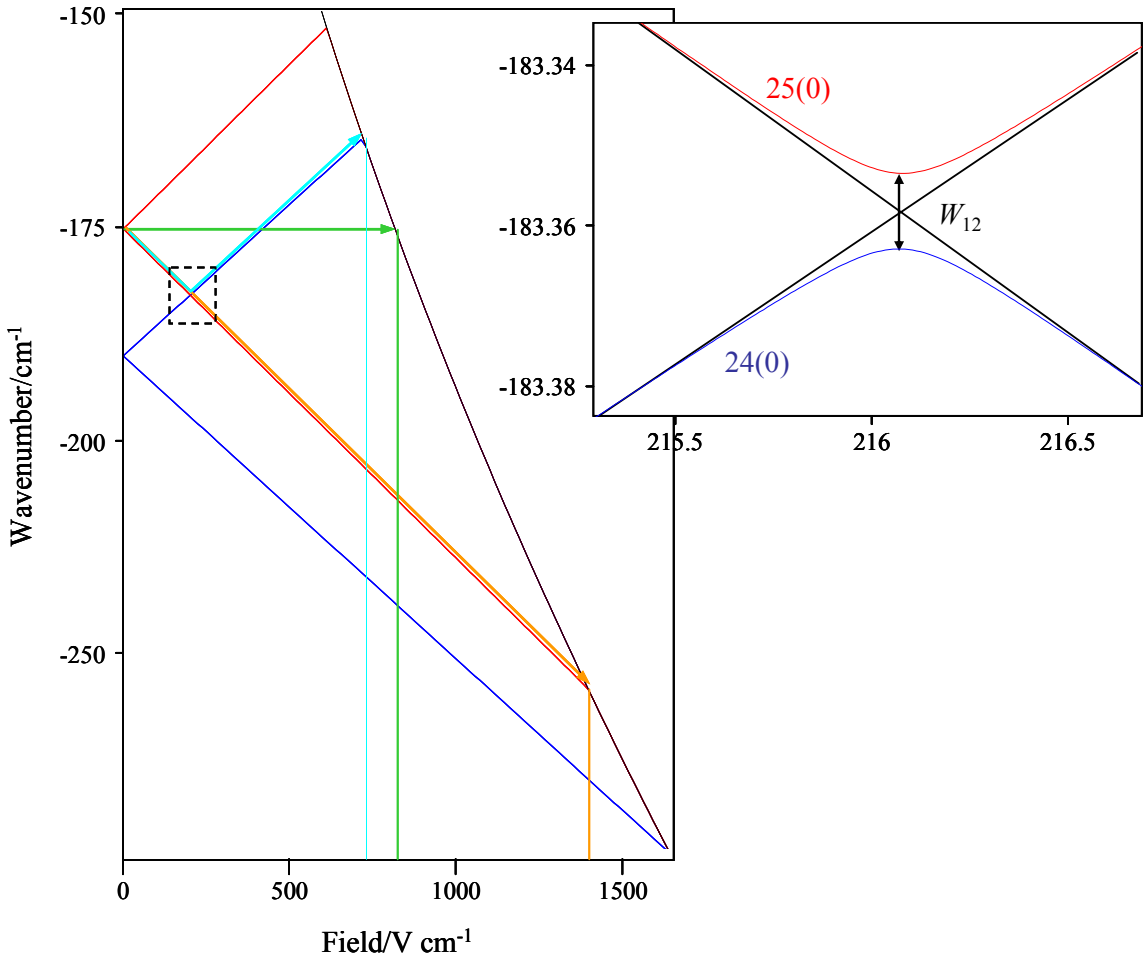

Figure 6.1.2: Energy diagram showing extreme levels of the 25(0) and 24(0) manifolds (red and dark blue lines respectively). The y-axis is wavenumbers below the adiabatic zero field ionization limit, and the x-axis is applied field in V cm^{-1}. The black line shows the adiabatic ionization limit for $N^+ = 0$ as it lowers with increasing field. The green and orange arrows show the route for pure adiabatic and diabatic ionization respectively. The light blue arrow shows the route to ionization if the first avoided crossing is traversed adiabatically, followed by a pure diabatic route to ionization. All three pathways result in the ionization of the electron occurring at different fields. The inset shows the 24(0) and 25(0) crossing in more detail. To calculate the probability of a diabatic route at the crossing, equation 6.1.2, it is necessary to calculate the gradients of the two potentials (black lines), and the separation of the potentials at the crossing, W_{12}.

Experiments have been performed that use shaped electrical pulses or sequences of pulses to increase the selectivity of field ionisation [102, 103], or to control the path of the electron to ionisation by manipulating the proportion of diabatic and adiabatic transitions at selected crossings [104-106]. In an experiment by Tada and co-workers,

two shaped electric field pulses were used to control the ionisation of a Rydberg electron in atomic rubidium [106]. The pulses were generated using a waveform generator and then amplified by a fast amplifier. The 111s and 111p states were investigated, due to their respective positions below and above the n = 108 manifold. The first pulse investigated was composed of two sections; an initial slow rise to around 50 mV cm^{-1}, followed by a fast rise to around 15 V cm^{-1} (figure 6.1.3 I). A peak was observed when an electron initially in the 111s state was ionised and another peak was observed at a slightly higher voltage when an electron initially in the 111p state was ionised. Both peaks could be explained in terms of the first avoided crossing for both states being traversed adiabatically, transferring population to the top and bottom of the 108 manifold (a similar process is shown in figure 6.1.2 as a light blue arrow). The second part of the pulse then drove the electrons diabatically towards ionisation along the top and bottom of the manifold *i.e.* the initial p state population travelled along the blue side of the manifold, whilst the s state population travelled along the red. The second shaped electrical pulse investigated had a similar shape, however this time the slow ramp was in the opposite direction, and the fast ramp crossed though 0 Vcm^{-1} (figure 6.1.3 II). This permutes the parabolic quantum number, so that k becomes $-k$. The first avoided crossing was again traversed adiabatically, and population was transferred to one side of the 108 manifold. However, as the fast ramp passes through zero the side of the manifold that the initial p and s population travelled along was swapped *i.e.* the p now travelled along the red side of the manifold, whilst the s now travelled along the blue. As expected, the positions of the two peaks had also swapped *i.e.* the p peak was now at a lower voltage than the s.

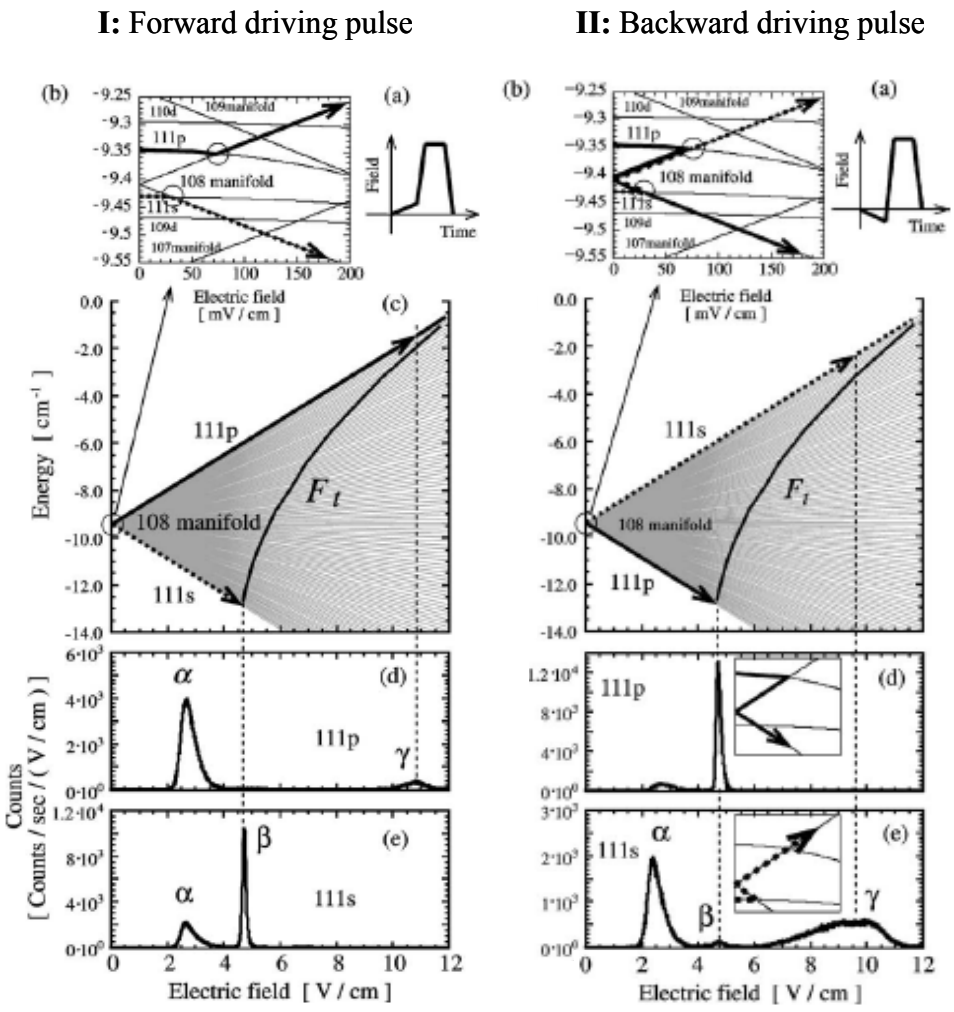

Figure 6.1.3: Taken from ref [106]. (a) shows shaped electric field pulse, (b) shows zoom of manipulated crossing (showing only extreme levels of manifold) , and (c) shows Stark manifold from zero to the ionisation field. (d) and (e) show field ionisation profiles from initially populating 111p and 111s states respectively. β and γ correspond to tunneling ionisation from population traveling along the red and blue extreme of the manifold respectively. α corresponds to autoionisation like ionisation. See text for a description of the experiment.

Our own work has demonstrated ramped field ionisation of the Rydberg states of NO around $n = 35$ with a variety of ramped fields. A molecular system offers many more times the complexity of an atomic system due to the extra Rydberg series belonging to each rovibrational state of the molecular more ion core. This high density of states creates many avoided crossings. The motivation for the work presented in this thesis was to use the ionisation profiles of known states as a basis set for a linear

combination fit to SFI profiles obtained from wavepacket experiments. This would allow the composition of the wavepacket to be quantitatively assigned. We found that by varying the ramp of the ionising field, it was possible to observe the electron crossing from one rotational state of the core to another. Therefore, by changing the slew rate of the ionising field, control was possible over the rotational quantum state of the field ionised molecules. In order to carry out these experiments it was necessary to adapt our experimental chamber for a number of reasons, outlined in Section 6.2. Our initial results are presented in Section 6.5. Further development of the chamber is then described throughout the remainder of this chapter along with the most recently obtained results. This development is ongoing and future ideas and modifications are outlined in the summary in Section 6.15.

6.2. Initial design of experimental vacuum chamber

The original design of the experimental chamber was for ion detection, with a field free time-of-flight (TOF) to separate ions of different mass. The chamber was split into two main sections; an interaction chamber and a detection chamber (figure 6.2.1). The interaction chamber was held at 10^{-5} mbar by a diffusion pump (Edwards 160/700M), and the detection region was maintained at 10^{-6} to 10^{-7} mbar by a turbo molecular pump (Edwards EXT-250).

Both pumps were backed by a two stage rotary pump (Edwards E2M18) at 10^{-3} mbar. A pulsed solenoid valve (General Valve Corporation 9-442-900) hung from a xyz translation stage situated at the top of the interaction chamber. During operation the opening duration of the valve was kept such that the operating pressure of the interaction chamber never rose above 10^{-4} mbar. The interaction region, where the lasers crossed the molecular beam, was situated between two plates, and a pulsed electric field was applied to the repeller plate. This extracted the ions through a field

free time of flight tube into the detection chamber where they were collected by a multi-channel plate (MCP). Detection of electrons was possible, if the polarity of the field on the extraction plates was swapped, and the ion MCP was replaced with one suitable for electron detection. The rods that supported the time-of-flight apparatus were screwed into a PTFE block that was clamped into place using the farthest flange from the MCP.

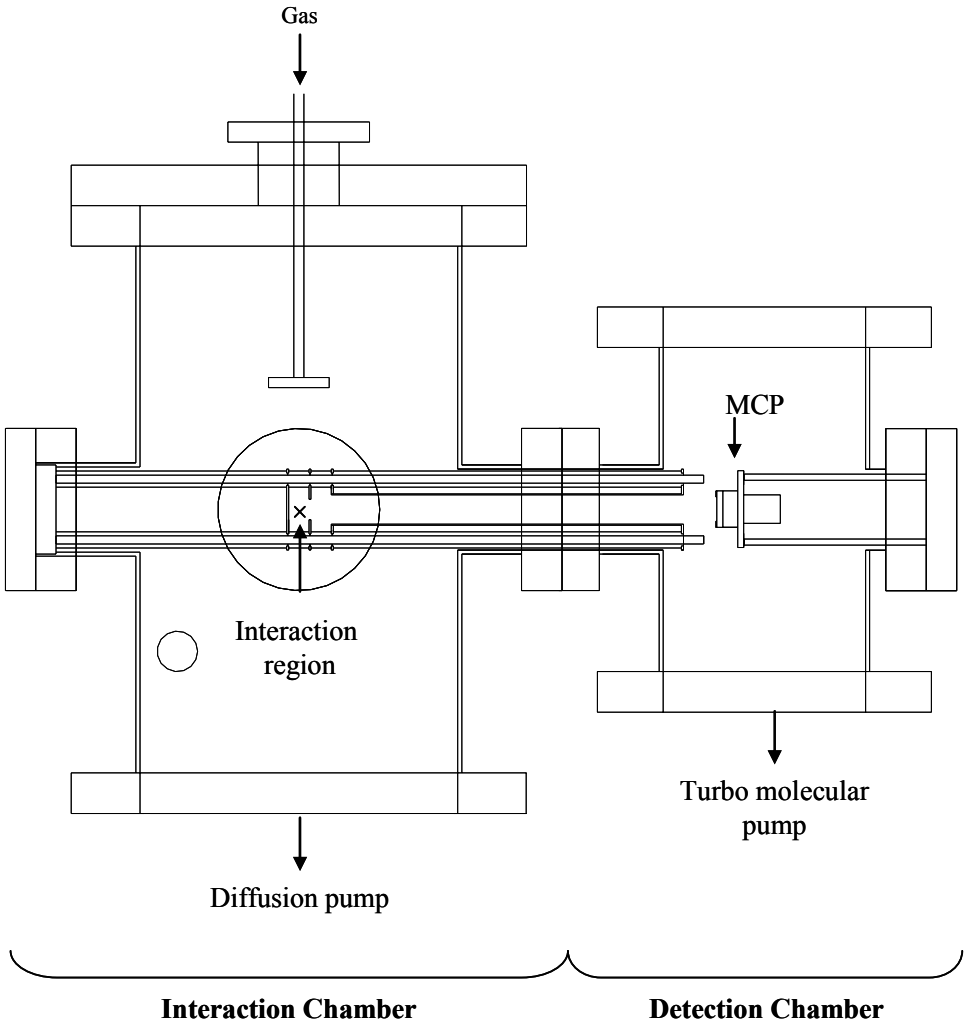

Figure 6.2.1: Initial design of the experimental chamber for ion time of flight mass separation. The molecular beam from the nozzle crosses the laser beam at X, between the two field plates. The repeller plate then field ionizes either electrons or ions and accelerates them through the field free time-of-flight to the MCP detector.

The molecule chosen to be investigated was NO. The spectroscopy of NO is well documented, and it is an ideal system to study molecular wave packets. Elsewhere in this thesis the spectroscopy of the bound states has been investigated in the presence of an applied electric field [32], and the experimental data has been simulated using a matrix diagonalisation code, producing accurate Stark maps with which to analyse ionisation profiles. Experimentally, the Rydberg states of NO in the region of interest can be easily reached using the doubled output of two dye lasers in a muli-photon $(1+1')$ scheme. Initially, the SFI profiles were recorded in preparation for future wave packet experiments, by exciting states in the region of n = 37-39 (with respect to the $N^+ = 0,\ v^+ = 0$ ionisation limit), field ionising the states with ramped fields and then recording the subsequent electron intensity against time. The recorded profiles were almost identical regardless of the state originally excited (figure 6.2.2) and this was attributed to the long field free TOF tube. Electrons ionised at higher fields are accelerated more than those ionised at lower fields. During the long time of flight electrons released at late times and therefore higher voltages caught up with electrons released at earlier lower voltages. This focuses the arrival times of the electrons at the detector resulting in ionisation profiles with no distinguishing structure. To solve this, the chamber was redesigned so that the electron MCP was closer to the interaction region, and both the electron and ion MCP could be used without the need to dismantle the chamber and rewire the field plates. Placing the MCP closer to the interaction region would result in a higher number of electrons striking the MCP, reducing its lifetime. For this reason it was necessary to reduce the gas load reaching the interaction region. To do this the nozzle was removed from the interaction chamber, and placed in a new section, the source chamber, described in the following section.

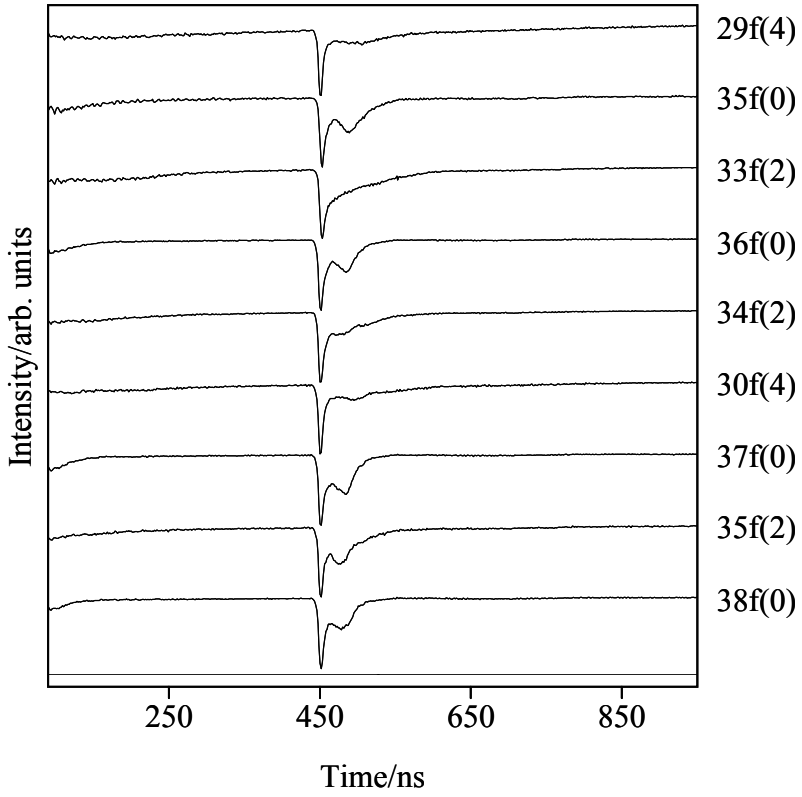

Figure 6.2.2: Ionization profiles recorded with the setup shown in figure 6.2.1 and using an ionizing pulse with a rise time of 540 μs. The labels on the right denote the initial Rydberg state populated. The y-axis is the electron intensity recorded by the MCP in arbitrary units, and normalized to the maximum peak. The x-axis is the time base of the trace taken directly from the scope.

6.3. The source chamber

A new region was added to the vacuum chamber to separate the pulsed gas nozzle from the interaction chamber. The separation was achieved by placing a molecular beam skimmer between the source and interaction chamber. It is therefore necessary to briefly introduce molecular beams, and skimmers.

A molecular beam is generated by the pressure difference on either side of a small aperture. As the gas expands through the aperture, the internal energy is cooled. This expansion can be extremely complex, especially in the region immediately outside the nozzle where the number of collisions between molecules is high. Further from the

nozzle a collision free state is obtained, and this is the region usually probed experimentally. A beam skimmer is an aperture that separates the source beam from the interaction region. It extracts the centre of a molecular beam, isolating it from interference from the rest of the expansion. To reduce interference between the skimmer and the beam, it should have an orifice with sharp edges, a small exterior angle (to reduce the reflection of molecules from the exterior surface of the skimmer), and a large interior angle (to reduce the build up of gas in the skimmer through interior collisions). Our skimmer is based on a design of Gentry and Giese [107], and was purchased from Beam Dynamics Inc. The flared design is a compromise between the conflicting requirements of the interior and exterior angles, whilst the orifice is electrochemically sharpened. A model-2 nickel skimmer was chosen because the smaller skimmers are able to withstand higher pressure differences (see figure 6.3.1 for the dimensions of the skimmer). The nickel is polished to avoid build up of beam material during operation. After twelve months of sustained operation, the surface had dulled slightly and there was a slight build up of material on the inside and base of the skimmer. However, the orifice was clear of build up and the performance of the skimmer was not noticeably affected. The tip of the nozzle is extremely delicate, and so great care must be taken when mounting it in the chamber. The opposite end is a great deal sturdier, and this allows the skimmer to be clamped to a flange.

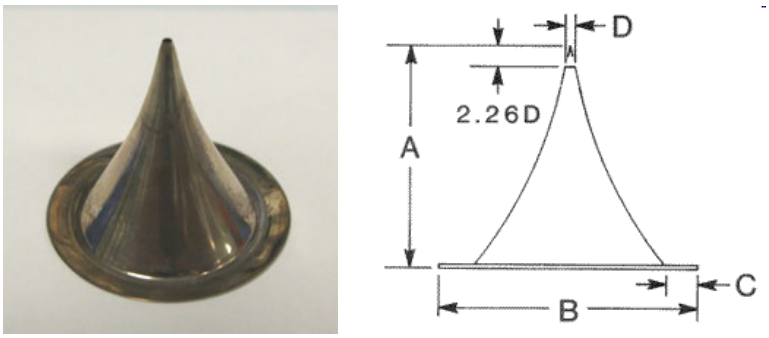

Figure 6.3.1: **Left**: Photo of skimmer used to separate the source and interaction chambers. **Right**: Cross section of skimmer taken from Beam Dynamic Inc. website. The model purchased had the following dimensions, A = 1.92 mm, B = 2.22 mm, C = 2.0 mm, D = 1 mm.

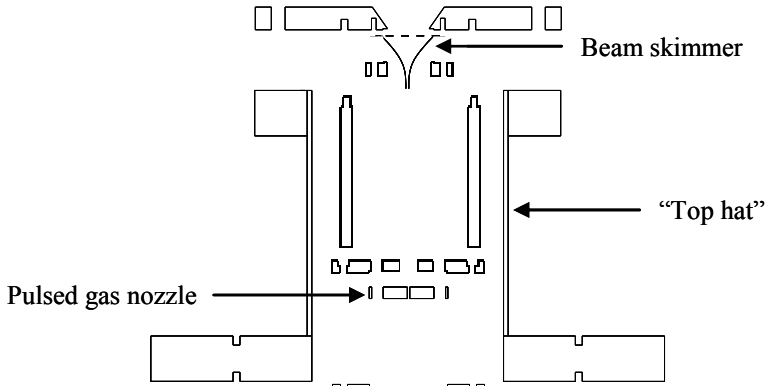

Figure 6.3.2: Cross section of top-hat. The bottom flange attaches to the standard flange at the bottom of the existing interaction chamber. A non-standard flange isolates the top hat from the interaction region. The nozzle and skimmer attach to the bottom of the non-standard flange as shown. There is no o-ring on the non-standard flange as a high vacuum seal isn't essential.

The source chamber was composed of two main parts. A "top-hat" structure (figure 6.3.2) sat directly below and projected into the interaction chamber so that the top sat close to the bottom of the field plates in the interaction region. The top hat consisted of a standard ISO NW160 flange, to connect to the bottom of the interaction chamber, and a tube of diameter 84 mm leading up to a second custom flange of outer diameter 134 mm. A 10 mm plate was then bolted to the top of the custom flange, and the nozzle and skimmer were attached to the bottom of this plate. The plate had a tapered hole located at the centre, designed to match the angle at the bottom of the skimmer. The skimmer was attached to the plate with a metal clamp as shown in figure 6.3.2. This clamped the flat edge at the end of the skimmer into a 0.5 mm indentation to help centre it onto the plate. Four metal rods were then screwed into four holes situated around the skimmer. The nozzle was attached to a small metal disc of diameter 66 mm, and screwed onto the four rods. To help centre the nozzle onto the plate, and hence to the skimmer, the nozzle sat in a 1 mm indentation, and countersunk screws were used to attach it to the legs.

The top hat is sat on an ISO NW160 tubulated flange of length 155 mm. At right angles from the tube four smaller tubulated flanges protrude at 45° to each other. These four smaller flanges are required for the electrical and gas feedthrough for the nozzle, a magnetron pressure gauge (Edwards Aim-S-NW25) and purge valve. The purge valve was necessary to reduce the pressure difference over the skimmer whilst venting the chamber. The source chamber is pumped by the diffusion pump used in the previous set-up (Edwards 160/700M). Initially the detection and interaction chambers were pumped by the single turbo molecular pump from the previous set-up (Edwards EXT-250) which was attached to the detection chamber. However, when the gas nozzle was operating the pressure in the interaction chamber quickly built up and so a second turbo molecular pump (Leybold Turbovac 361) was added to the top of the interaction chamber. Both of these pumps were backed by a new rotary pump (Leybold D16B). Under normal conditions the pressure difference across the skimmer was 10^{-1} mbar with the gas nozzle closed, and 10^{-2} mbar with it open.

Initially the valve isolating the diffusion pump from the source chamber was left open so that a 10^{-1} mbar pressure difference was maintained over the skimmer at all times. However, during a power cut the diffusion pump failed and pump oil was spread throughout the vacuum system. For this reason the diffusion pump is now isolated from the source chamber when the nozzle is not in use. In this state the source chamber is only pumped by the two turbo pumps on the other side of the skimmer causing the pressure in the source chamber to rise higher than the measurable range allowed by the pressure gauge *i.e.* greater than $1 \times 10^{+3}$ mbar. This leads to a minimum pressure difference over the skimmer of greater than 10^{-3} mbar, higher than the maximum pressure difference of 10^{-3} mbar as recommended by Beam Dynamics Inc. No structural damage to the skimmer has been observed so far, implying that the pressure difference is not much greater than 10^{+3} mbar.

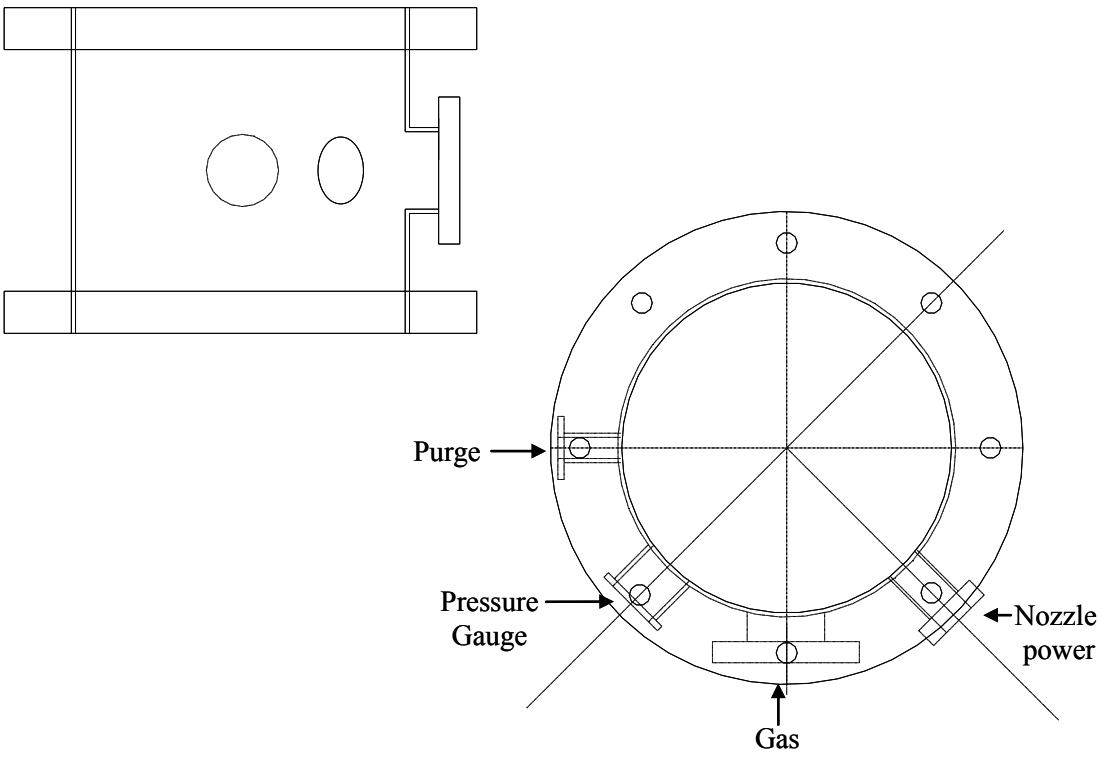

Figure 6.3.3: Cross section of extension added to bottom of top hat, lifting the top hat from the diffusion pump valve. The four external flanges were necessary to provide a feedthrough for the nozzle gas and power connections, as well as for the purge valve and pressure gauge for the source chamber.

6.4. Redesign of time-of-flight apparatus

The initial design for the time-of-flight set-up is shown in figure 6.4.1. It consists of four central rods screwed into a flange. The MCP holders, field plates, and component spacers then slot directly onto these rods. When the holding flange is attached to the chamber the other end of the rods rest in holes on the opposite flange, which adds extra horizontal stability. This design allows external construction of the TOF before it is slotted into the chamber and also guarantees greater alignment with the furthest MCP than the previous set-up. It also allows more flexibility to the design, so that future additions such as mu-metal magnetic shielding could be easily added. Unfortunately, due to time restrictions the necessary increase in size of the horizontal flanges on the detection and interaction chambers was not be completed.

A new set-up was designed and built using the existing horizontal flanges of the chamber and using converter plates to step up and down the diameter of the time of flight (TOF) apparatus. This design was a compromise between the ideal design in figure 6.4.1 and what could be built based on the restrictions of time and funding.

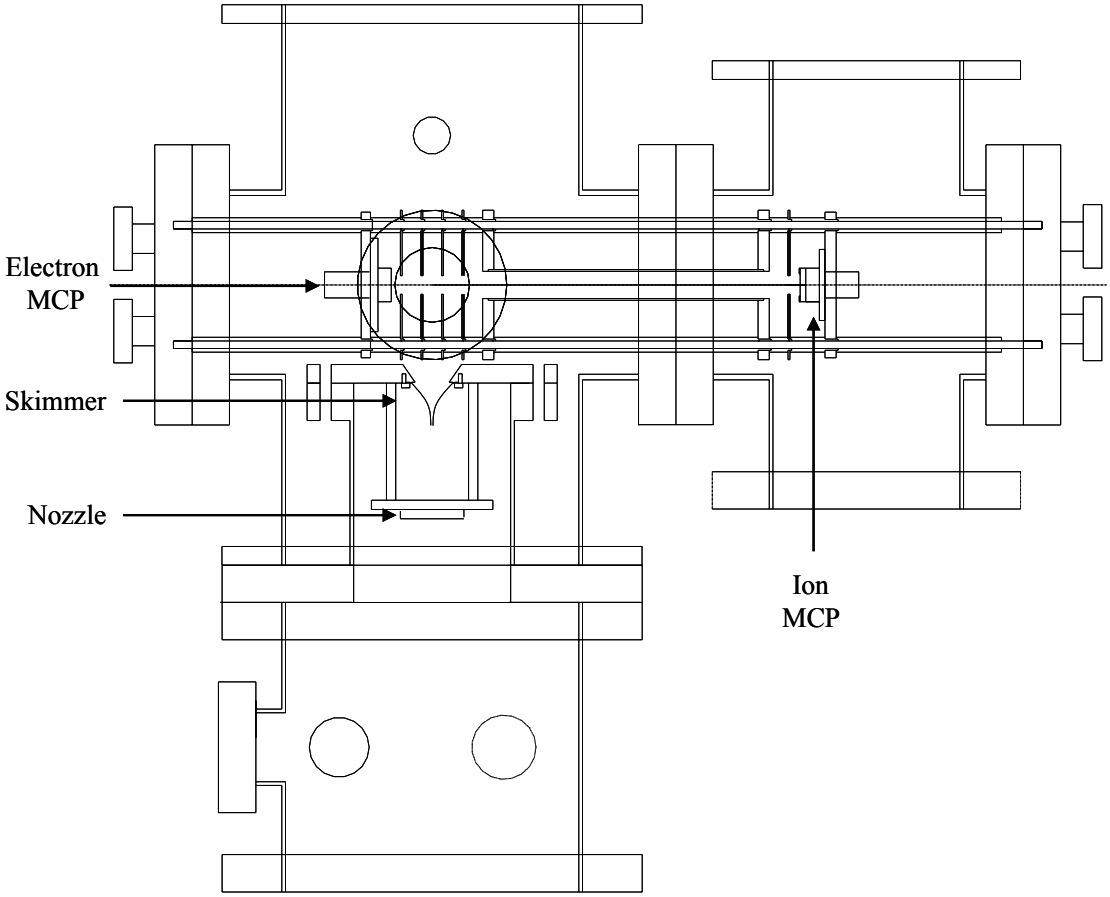

Figure 6.4.1: Cross section of initial redesign of experimental chamber. All of the ion optics and detectors slot directly onto the four central rods. The whole apparatus is held on one of the horizontal flanges and then rests in holes on the opposite flange. Tubulated flanges on both horizontal flanges act as electrical and signal feedthroughs for both MCP detectors.

The basic design can be separated into four units. The first is a flange with 4 rods that secures the whole apparatus to the chamber. The second is a step-up plate that connects the central unit of the TOF to the chamber by converting the central diameter of the apparatus from the inner tube diameter of the securing flange (30 mm) to the

field plate diameter (70 mm). The central unit holds the four field plates, the front plate of the time of flight tube and the electron MCP holder. The final section then steps back down to the 30 mm diameter to pass through the central flanges joining the interaction and detection chambers. Rods connect the remaining field plates and TOF tube to the central unit. All components are separated by PEEK spacers (figure 6.4.3B), which is favourable over PTFE spacers that were previously used due to the superior chemical resistance, and dielectric and mechanical strength of PEEK. The spacers stepped design allows them to slot through the holes on the various metal components whilst protruding slightly. The protruding end then slots into the small step indent on the reverse of the next spacer preventing any possible electrical connection between the plates and the central holding rods. All of the metal components of the time of flight are made of 316 stainless steel and were built in house.

The field plates are 1 mm thick discs of 80 mm diameter (figure 6.4.3A). A central hole of diameter 10 mm is covered with a high transmission (92.2 %) tungsten mesh purchased from Cole and Swallow and spot welded onto the plates by Kore Technology Ltd. Four holes on a diameter of 70 mm allow the front step of the PEEK spacers to slot through. Each plate has a small semi circle extension in-line with these holes with a tapped M2 hole. Electrical spade connections can be screwed to the plate using the tapped hole and a short M2 screw. It was found that these connections could become loose as the TOF is lowered into position and a locking washer and nut was used to secure them. The central unit is constructed externally before being lowered into the chamber. The electron MCP is attached to the holder and the four rods are screwed into the plate (figure 6.4.2B). The field plates and spacers are then threaded onto the rods in turn. After the front plate of the TOF tube is added, four nuts are used to secure the assembly. It is vital that the separation between the two central field

plates is a parallel 10.0 ± 0.1 mm. This can be adjusted by using a micrometer and tightening the four nuts appropriately.

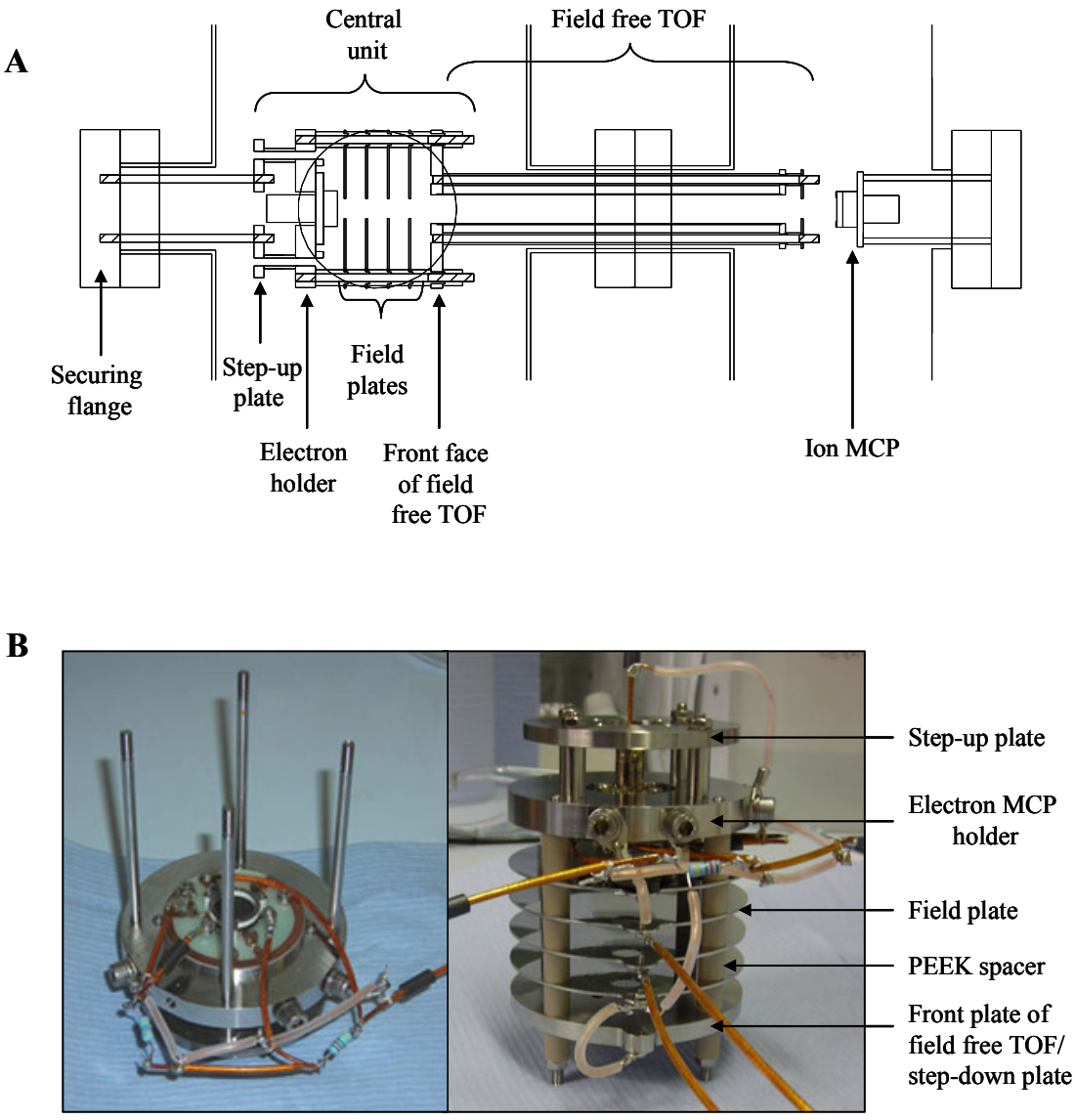

Figure 6.4.2: A – Cross section of new time-of-flight apparatus. The whole unit is secured to the left flange, and supported in the center by holes in the central flanges joining the two chambers. The molecular beam and laser beam cross at X. A field applied to one of the field plates either side of X will accelerate charged particles of opposite polarity away from the plate and towards either detector. The electron detector is positioned close to the interaction region on the left hand side, whilst the ion detector is located on the right hand side at the end of a field free time of flight. B – Photos showing construction of central unit. The left photo shows the electron MCP attached to the holding plate, with the four rods attached. The spacers and plates are then slotted onto the rods and secured by four nuts. The step-up plate is then added, allowing the unit to be secured to the chamber (right photo).

Four tapped rods are then screwed into the back of the MCP holder, four metal spacers added and the step-up plate attached. The whole unit can then be lowered into the chamber and positioned onto the four rods attached to the main flange. The opposite flange is then used to add the final components. First the four metal rods screw into the front plate of the TOF tube, and then the field free time of flight tube and remaining plates are threaded on and secured with nuts. Finally, the ion MCP is attached to the far flange and inserted into the chamber. The power and signal feedthroughs for the electron MCP are located on the interaction chamber. The electrical feedthrough for the field plates was initially a 16 pin connector; however this was later changed as discussed in Section 6.9.

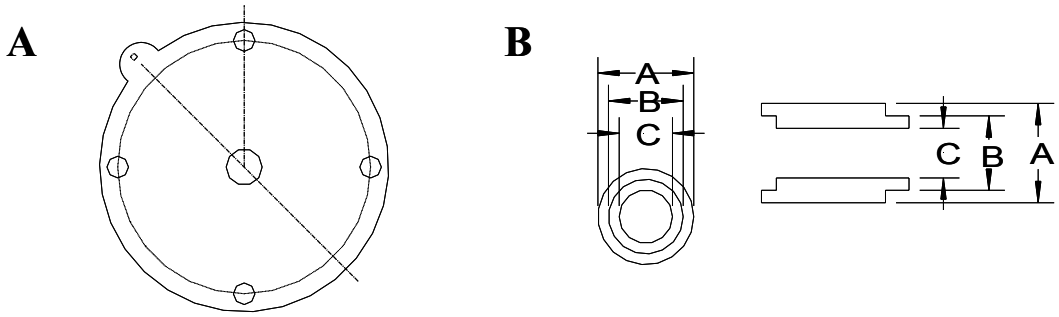

Figure 6.4.3: **A** - Cross section of field plate. The 10 mm central hole is covered in 92.2 % transmission tungsten mesh. Four holes on a diameter of 70 mm allow the plates to be fitted to the TOF apparatus. In line with the holes (at 45°) a small semi-circle projection with a tapped hole allows a spade electrical terminal to be secured to the plate. **B** – Cross section of PEEK spacer showing stepper design shown as front (left) and side (right) views. The three diameters correspond to the rod diameter, C, the field plate holes, B and the outer diameter of the spacer, A.

6.5. Initial Results

Using the set-up described in the previous two sections, ramped field ionisation profiles were recorded for a variety of Rydberg states of NO over the range of n = 37 – 39, converging to the $v^+ = 0$, $N^+ = 0$ ionisation limit. The two nanosecond lasers introduced in Chapter 2 were used to access Rydberg states around n = 37 *via* the

$A^2\Sigma^+(v' = 0,\ N' = 0)$ intermediate. The beams crossed a skimmed molecular beam of NO between two field plates, and a ramped electric field was applied to ionise the Rydberg state and draw the electrons towards the electron MCP. The ramped field was generated by adding a kΩ resistor in series with the high voltage pulse generator as shown in figure 6.5.1. The signal from the MCP was amplified using a fast preamplifier (Ortec VT120) and collected on a digital oscilloscope. The trace is taken directly from the scope using a Labview controlled program that takes a "screen dump" of the display.

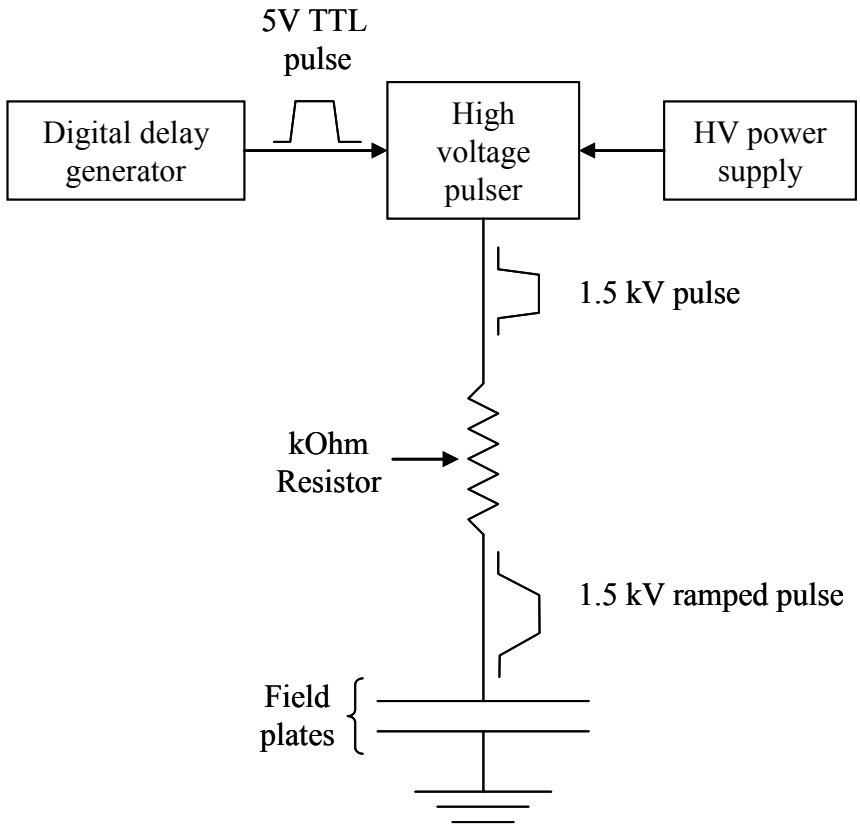

Figure 6.5.1: Schematic of apparatus used to generate the ramped fields necessary for the SFI experiments. A TTL pulse generator and high voltage power supply feed into a high voltage pulse generator creating a 1.5 kV fast ramped pulse with a rise time faster than 100 Vns^{-1}. A kΩ resistor added in series slows the ramp of the field. The pulse then passes to a field plate located on one side of the interaction region.

During the delay between the laser pulse and ionising field the low *l* states decay, and so only Rydberg states of f character are observed. The low quantum defect of these

states means that an applied field rapidly mixes the state into the adjacent manifold. As the field is ramped, the population initially in the f state moves along the manifold with some probability of transferring to other manifolds at each avoided crossing. Each state of the ion core has an associated series of Rydberg states, leading to a high density of states and a large degree of mixing between these states due to the field. Considering the extent of mixing, it is remarkable how distinct the ionisation profiles of the different states appear. A selection of profiles recorded with a slew rate of 2.3 V cm^{-1} ns^{-1} is shown in figure 6.5.2. The states are labelled using $nl(N^+)$ notation where n is the principal quantum number, l the electronic orbital angular momentum and N^+ the rotational angular momentum of the core.

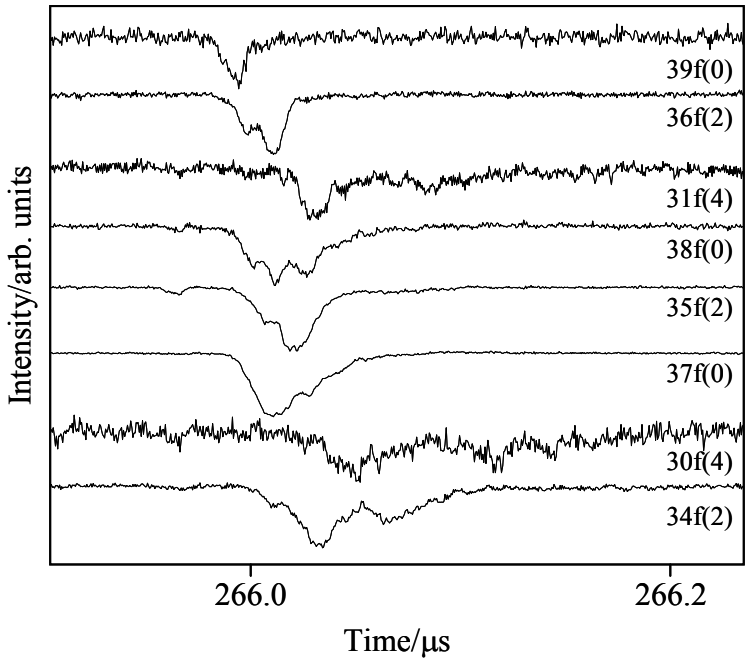

Figure 6.5.2: SFI profiles recorded for Rydberg states initially populated under no external field and then ionized with a ramped field with slew rate 2.3 V cm^{-1} ns^{-1}. The y-axis is the signal intensity as detected by the MCP, and normalized to the most intense peak. The x-axis is the time of arrival of the electron at the detector, where time zero is defined as the first experimental TTL trigger.

In general, it can be observed that the most intense peak (*i.e.* the peak corresponding to diabatic ionisation) appears at earliest times in the nf($N^+ = 0$) spectra followed by

$nf(N^+ = 2)$, and finally $nf(N^+ = 4)$. This is due to lower energy of the $N^+ = 0$ ionisation potential, which means a lower field is required for ionisation. The $nf(N^+ = 4)$ series has the highest ionisation limit and so requires higher electric fields for ionisation. The *n*f (4) profiles show the most complex structure, but are also the weakest as a consequence of the higher ionisation potential and subsequent greater number of avoided crossings. This leads to extensive mixing sharing the population throughout many manifolds. The $nf(N^+ = 0)$ and $nf(N^+ = 2)$ profiles show similar structure, *i.e.* one main intense peak with one or two weaker side peaks, but are still distinguishable. At lower slew rates it would be expected that the differences between profiles would increase as more crossings are traversed adiabatically. The time separation between the main peaks of the *n*f (0) and *n*f (2) profiles would also become greater with decreasing slew rate.

The structure of the 35f(2) profile was analysed by considering the extremes of the closest $m = 0$, hydrogenic Stark manifolds calculated using the first order Stark effect. The time profiles were converted to voltage profiles using the slew rate of the ionising field and assuming that the main peak was due to a purely diabatic route to the $N^+ = 2$ ionisation potential (~370 V cm^{-1}). As the slew rate is decreased a shoulder appears on the low voltage side of the main peak and begins to grow. A second peak also appears at 120 Vcm^{-1} and grows as the slew rate decreases.

A comparison between the ionisation profile recorded using a ramped field with a slew rate of 2.3V cm^{-1} ns^{-1} and the Stark map is shown in figure 6.5.3. The first peak can be explained as an adiabatic crossing at the first avoided crossing between the bottom of the 35(2) manifold and the top of the 37(0) manifold. The population then continues diabatically along the 37(0) manifold to the $N^+ = 0$ ionisation potential. It is possible to calculate the probability of a diabatic transition at this first avoiding crossing using equation 6.1.2. For a slew rate of 1.3 V cm^{-1} ns^{-1} $P_{dia} = 0.98$ which is in

good agreement with the experimental ratio of the two peaks of 0.97. A similar analysis of the 31f(4) profile at 6.9 V cm^{-1} ns^{-1} showed that the complex profile could be explained by transitions to manifolds with quantum number $N^+ = 2$ and 6.

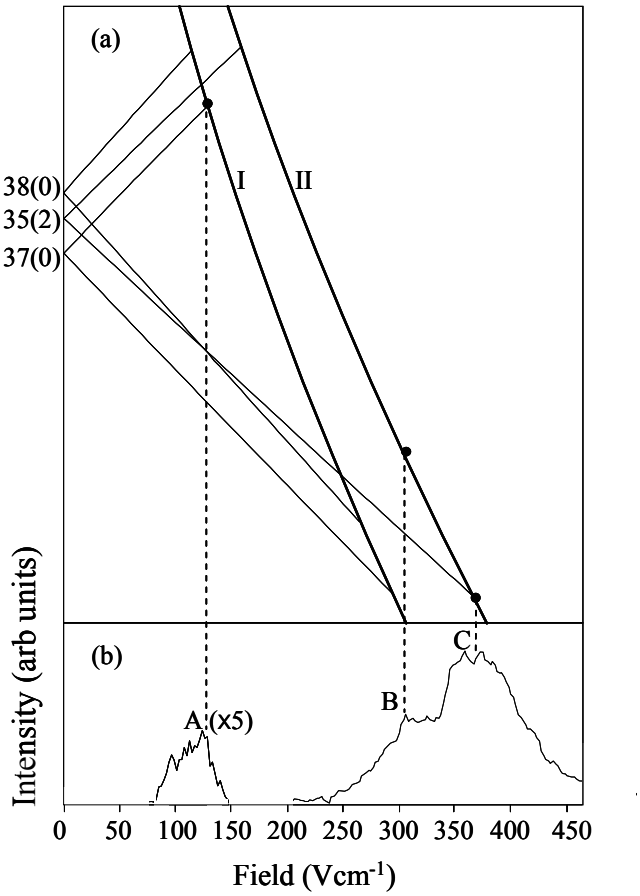

Figure 6.5.3: (a) - Extreme states of the $m = 0$ hydrogenic Stark manifolds for the high-l 37(0), 38(0) and 35(2) manifolds. The manifolds are calculated using first order perturbation theory. The curves labeled I and II represent the change in the classical field ionization limit under an applied field.
(b) - Ionization profile of the 35f(2) Rydberg state ionized by a pulsed field with a slew rate of 2.3 V cm^{-1} ns^{-1}. This figure is taken from ref [108].

The initial results were encouraging. However, due to the close proximity of the electron MCP to the field there were two electrical issues requiring further investigations. As shown in figure 6.5.4 multiple signals were observed along the time base of the scope. The identification of the source of these multiple peaks is discussed in Section 6.11. For the SFI profiles discussed above, the large distance from the first

two peaks and electronic noise made the third peak (C in figure 6.5.4) the most suitable to record. To resolve the two earliest peaks (A and B) it was necessary to subtract the noise trace from the signal profile. However, the resulting peaks showed a strong structural dependence on the noise with peaks appearing in phase with the noise structure. The identification and reduction of this noise is discussed in the Section 6.9. First, it is necessary to discuss the methods by which electronic noise is generated, and how it is introduced into a system.

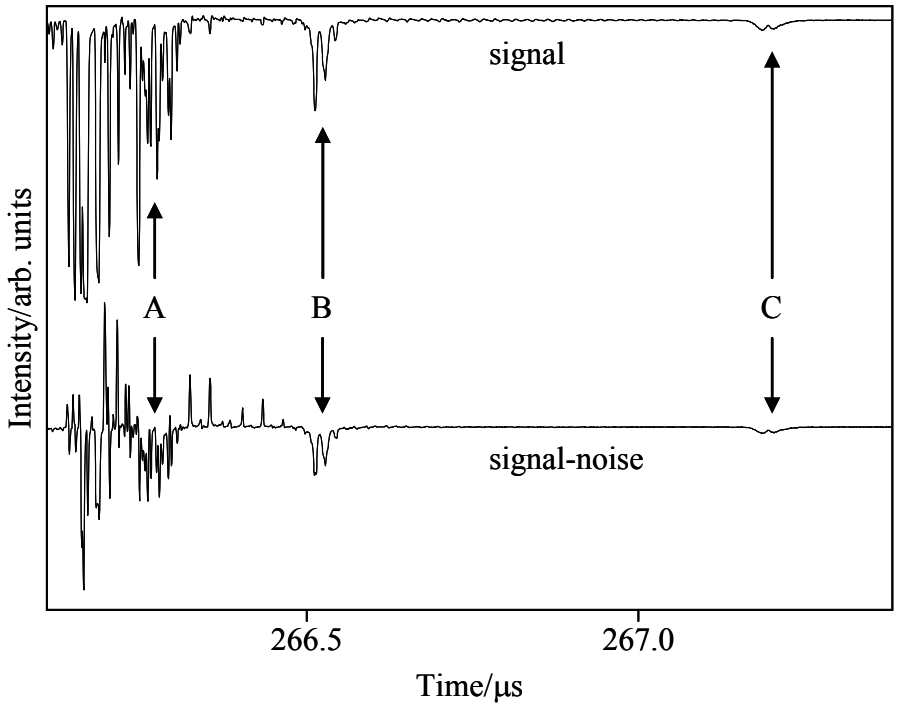

Figure 6.5.4: Ionization profile of the 36f(2) state recorded using a pulsed field with a slew rate of 11.8V cm^{-1} ns^{-1}. The top trace shows the ionization trace as it appears on the scope. The bottom trace shows the same profile once the noise has been subtracted in the time domain. Three signals can be identified, and are labeled A, B and C. The y-axis is the signal intensity in arbitrary units, and the x-axis is the arrival time of the signal at the detector.

6.6. Noise Pathway

Chapters 2, 3 and 6 of reference [109] and Chapters 2, 4 and 6 of reference [110] provide an excellent introduction into electronic noise, grounding schemes and

shielding techniques. The following three sections will now briefly review these concepts, and Section 6.9 will discuss how they have been applied to the current set-up.

Noise becomes a problem when three elements are present; a noise source, a receptor circuit sensitive to noise and a coupling channel to transmit the noise (figure 6.6.1).

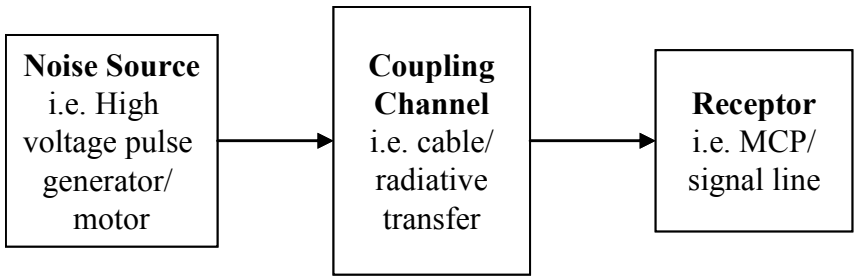

Figure 6.6.1: Schematic of the noise pathway that must be present for electronic noise to affect a system.

To remove electronic noise, each section of the noise path can be considered. Firstly, the noise source itself can be isolated from the system or suppressed. In our set-up the source is integral to the experiments and its use cannot be avoided. The mechanism by which the square high voltage pulses are generated creates a large amount of radio frequency emissions, and this is the main source of noise. In order to suppress the AC noise emitted, the pulse generated can be slowed using a RC (resistor/capacitor) circuit. This is described in greater detail in Section 6.9.

The second section of the noise path to consider is the receptor. Electronic noise can be removed by making the receptor insensitive to noise. In our set-up the detection system is composed of “out of the box” units and modification is undesirable and difficult. Filters placed along the signal line would interfere with the output of the MCP and the effect on our final signal would be difficult to remove.

Finally, the coupling channel must be taken into account. There are three main coupling mechanisms for electronic noise; common impedance coupling, conductive coupling, and electric and magnetic field coupling. Common impedance coupling is predominantly due to the grounding scheme of the relevant circuits, which will be discussed in Section 6.8. Conductive coupling arises from a conductor transferring noise directly to the receptor. Electrical and magnetic coupling will now be discussed in greater detail.

6.7. Electric and Magnetic Field Coupling

Electromagnetic fields are generated when charge is moved around a circuit and also radiated by various pieces of electronic equipment. A high voltage square pulse generator is a major source of radio frequency electromagnetic radiation emission. Mathematically, a square pulse is generated by a Fourier series of sin waves as shown by figure 6.7.1 and equation 6.7.1, where *f* is the frequency of the square pulse, and *t* is time. To generate a high voltage square pulse with a fast rise time a combination of a large number of high frequency sine waves is required, and this produces a large amount of MHz radiation.

$$x_{square}(t) = \frac{4}{\pi}\sum_{k=1}^{\infty}\frac{\sin\left((2k-1)2\pi ft\right)}{(2k-1)}. \qquad (6.7.1)$$

It is necessary to define two regions with respect to a source of radiated noise; the near and far field. The near field is defined as distances closer than the radiated wavelength divided by 2π, whilst the far field is distances greater than $\lambda/2\pi$. In the far field, only the combined electromagnetic radiation is considered. In the near field the electric and magnetic coupling need to be considered separately as capacitive and inductive coupling respectively. The dominant coupling mechanism is determined by the ratio *E*/*H* where *E* and *H* are the electric and magnetic fields. In the far field, this

ratio is equal to the characteristic impedance of the medium, *e.g.* in air $E/H = 377\ \Omega$, the electric field dominates, and only capacitive coupling needs to be considered. In the near field this ratio is determined by the characteristics of the source. A high current and low voltage source leads to predominately magnetic fields, but for a low current and high voltage source, the near field is dominated by electric fields.

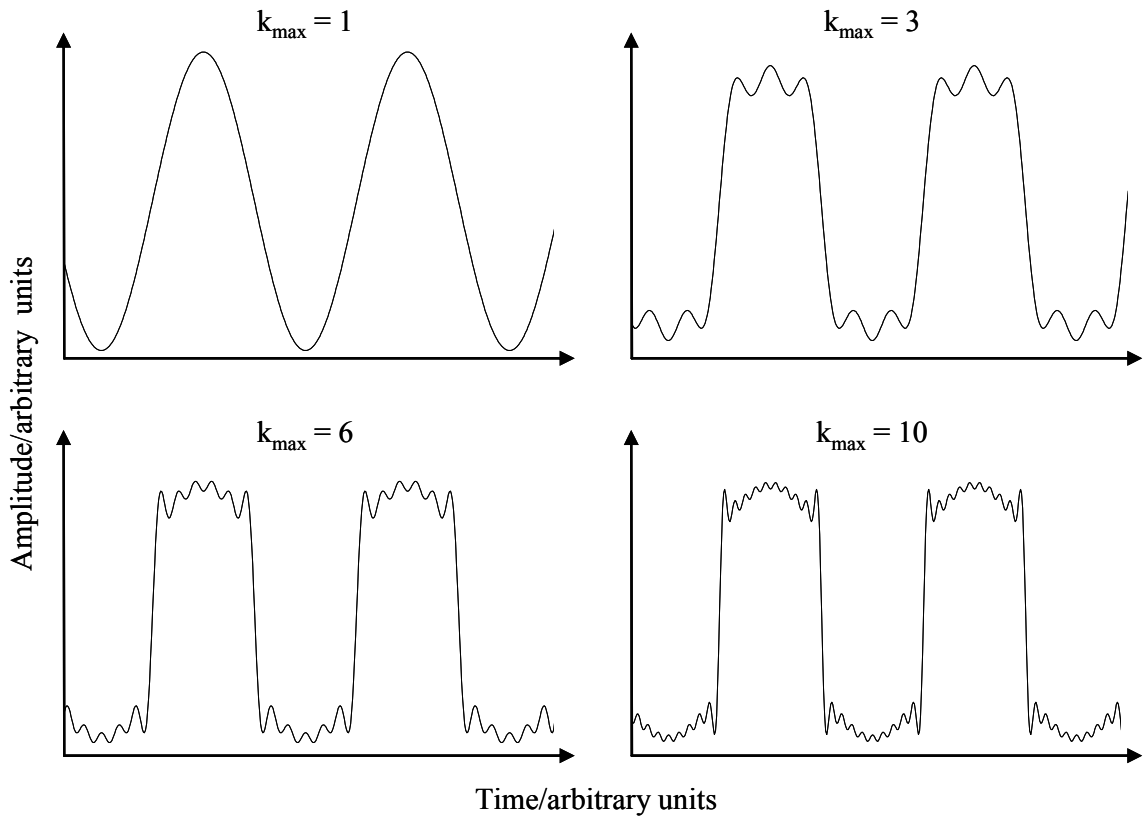

Figure 6.7.1: Time-amplitude graphs showing the generation of a square pulse by the Fourier series given in equation 6.7.1 where k_{max} is the highest harmonic used in the series. As k_{max} increases, the Fourier series generates cleaner square pulses. The best electric pulse shape is generated by addition of a large number of sine functions, including many of high frequency.

The radio-frequency radiation emitted by our source is of the order of 10 to 50 MHz, and so $\lambda/(2\pi)$ is equal to 1 to 5 m. Most of the chamber in the current set-up can be thought of as lying within the near field region, with only a small number of cables continuing out into the far field. However, our circuit is essentially a high voltage source connected to a capacitor (the two field plates); therefore it is a high voltage,

low current system. This allows the set-up to be thought of as dominated by capacitive coupling at all distances. For this reason, capacitive coupling will now be discussed in detail with only a brief introduction to inductive coupling.

Capacitive coupling can be considered as a circuit comprised of two conductors (figure 6.7.2A). Conductor 1 is the source of the interference with voltage V_1. Conductor 2 is the receptor circuit with resistance to ground, R, due to any attached circuitry. An electric field creates a capacitance between the two conductors of value C_{12}. Both conductors have a capacitance to ground due to the conductor and any attached circuitry, $C_{xG,}$ where x denotes either conductor 1 or 2. The capacitance between the two conductors creates a noise voltage, V_N, between conductor 2 and ground.

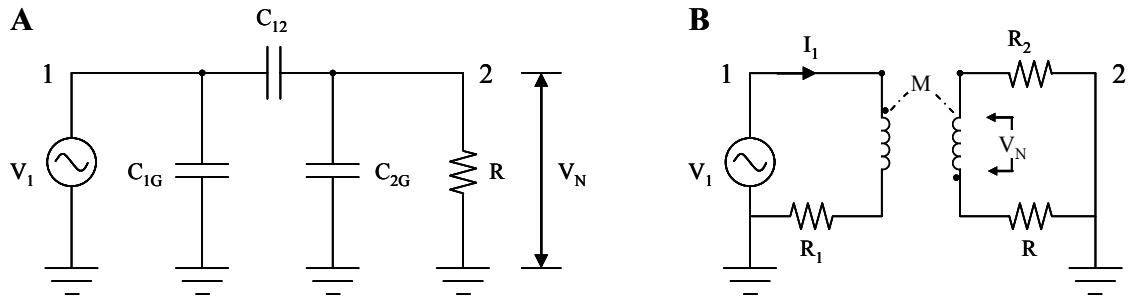

Figure 6.7.2: Equivalent circuits to describe (A) capacitive and (B) inductive coupling. The wire labeled 1 is the conductor carrying an interference of voltage V_1. 2 labels the conductor connected to the receptor circuit that receives a subsequent noise voltage of size V_N.

Assuming the resistance R, is of lower impedance than the impedance of the stray capacitance then the noise voltage created in the receptor circuit, V_N, can be expressed in terms of the voltage on the noise circuit, V_1, the resistance to ground of the receptor circuit, R, the capacitance between the two conductors, C_{12}, and the frequency of the noise, $f = \omega / 2\pi$. This relationship, as shown in equation 6.7.2, can be modelled as a current generator connected in series between the receptor circuit and ground.

$$V_N \propto \omega R C_{12} V_1 \qquad (6.7.2)$$

Equation 6.7.2 shows that for a usual system in which ω and V_1 cannot be changed, the noise voltage can be reduced by minimising C_{12} or R. The capacitance can be reduced by shielding either conductor or increasing the physical distance between them. The capacitance is related to the distance, D, between two parallel conductors of diameter d by equation 6.7.3, where $\varepsilon = 8.85 \times 10^{-12}\ \mathrm{Fm}^{-1}$ for free space.

$$C_{12} = \pi\varepsilon / \cosh^{-1}(D/d). \qquad (6.7.3)$$

A fully shielded conductor is no longer coupled to the noise source by C_{12} (black circuit in figure 6.7.3). The voltage picked up by the shield is given in equation 6.7.4.

$$V_S = \left(\frac{C_{1S}}{C_{1S} + C_{SG}} \right) V_1 \ . \qquad (6.7.4)$$

As no current flows through C_{2S} the noise voltage picked up by conductor 2 is $V_N = V_S$. For a shield connected to ground $V_S = 0$ and so V_N is also zero.

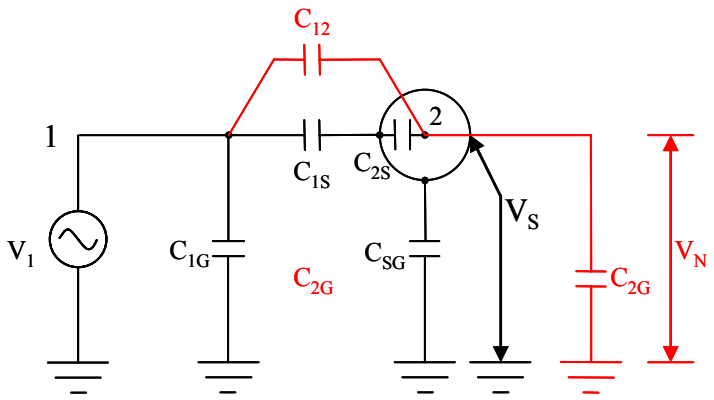

Figure 6.7.3: Circuit representing the addition of a shield fully covering (black lines) conductor 2. If the conductor extends any distance outside of the shield then extra couplings exist as shown by the red lines.

In a real system, the conductor extends some distance out of one or both ends of the shield allowing coupling between the two conductors, *via* C_{12} (shown by the red lines in figure 6.7.3). C_{12} may also be increased by a non-perfect shield *e.g.* a standard BNC cable uses a braided shield to increase the flexibility of the cable, but small gaps

in the braid allow conductor 1 and 2 to couple. The noise voltage is now given by equation 6.7.5.

$$V_N = \left(\frac{C_{12}}{C_{12} + C_{2S} + C_{2G}} \right) V_1 \ . \qquad (6.7.5)$$

As a general rule, shielding from electrical radiation should be grounded at one end only to avoid the flow of noise current. This is discussed in greater detail in the next section.

Inductive coupling arises when a charge flows through a conductor, creating a magnetic flux in a second conductor. Figure 6.7.4 shows a physical representation of inductive coupling in which conductor 2 passes through the magnetic field created by conductor 1 with current I_s. The position and orientation of conductor 2 passing through this field determines the size of the inductive coupling. The equivalent circuit is shown in figure 6.7.2B.

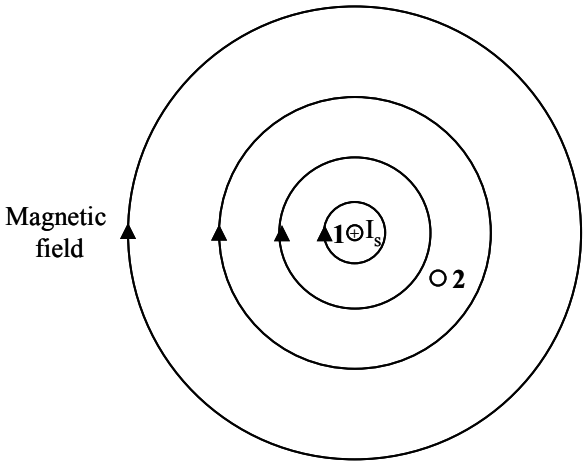

Figure 6.7.4: Magnetic field created by a current I_s flowing through conductor 1. This induces a noise voltage in conductor 2 as it passes through the field.

The noise voltage induced by the field is given by equation 6.7.6 where I_1 is value of the current in the interfering circuit, ω is the frequency of the field, and M is the

mutual inductance, which depends on the geometry and magnetic properties of the medium between the two circuits.

$$V_N \propto \omega M I_1 . \qquad (6.7.6)$$

Magnetic shielding requires grounding at both ends *i.e.* the opposite situation to electrical shielding. This is discussed in the next section.

6.8. Grounding

In this section, shield and circuit grounding will be introduced. Safety grounds will not be covered as this is implicit to the high voltage equipment used. A signal ground is a low impedance path for the current to return to the source. For physically separated ground points, this implies a potential difference. Therefore, to reduce noise it is usually best to implement a single point ground system (figure 6.8.1)

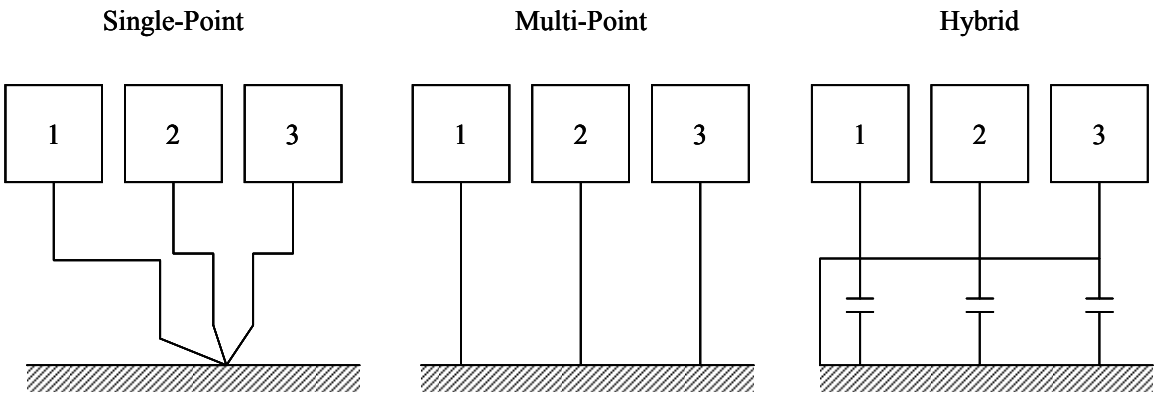

Figure 6.8.1: Schematic representation of possible ground circuits. For a single-point ground, all three circuits are ground at a single physical point. A multi-point system has grounds physically separated with impedance between them. A hybrid ground acts as a single-point ground at low frequencies, but a multi-point ground at high frequencies.

A multiple ground system is the simplest system to implement but the series nature of the ground connection leads to non-zero impedance between each ground point. In practise, a single point ground can require a large amount of wiring to achieve. For

high frequency noise, it is preferable to use short cables to reduce emission and so a multi-point set-up may be utilised. Alternatively, a hybrid ground uses capacitors to act as a single point ground for low frequencies, and multi point at high frequencies.

When grounding many cables it is important to avoid ground loops. If a circuit is attached to ground in a number of physically separated places, a noise voltage is introduced. If one or more of the grounds in the loop is a mains ground, this can be an extra source of noise.

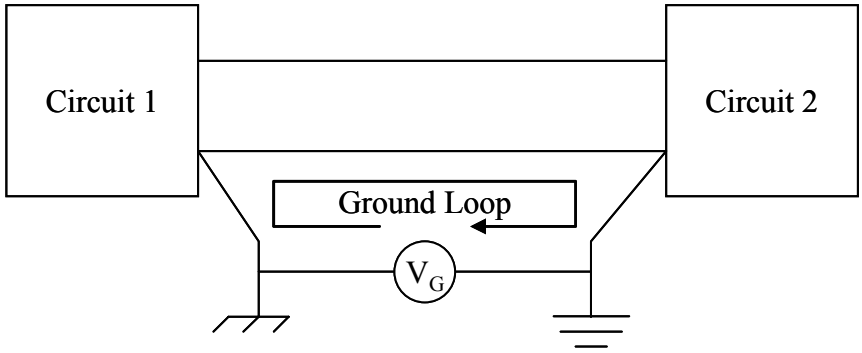

Figure 6.8.2: Schematic showing a noise voltage generated by a ground loop created between two circuits. The loop occurs due to the physically separated grounds associated with both circuits

The grounding applied to shielding depends on the purpose of the shield. An electrical field shield should only be grounded at one end, to avoid the flow of current. For coaxial cables, a current flow in the shield creates a noise voltage due to a drop in the shield resistance. However for high frequencies of noise (*i.e.* >1 MHz), or for cables longer than one twentieth of the noise wavelength, it may be necessary to ground at multiple points to ensure a constant ground potential along the whole shield and to reduce the amount of shielding emitting electromagnetic radiation. However, this requires a grounding point close to the noise source to keep any ground leads short. A shield against magnetic fields requires the opposite set-up. A shield grounded at one end has no effect on the geometry or magnetic properties of the medium between two

conductors, and therefore no effect on the voltage picked up by the shielded conductor. If the shield is grounded at both ends, and it is ensured that the current in the shield flows in the opposite direction to the field in the conductor, then the resulting magnetic field will be in the opposite direction to the field generated by the conductor. Therefore, this type of shielding can be used on a noise source to cancel the magnetic field around a noise conductor.

6.9. Application of noise reduction techniques

To reduce the electronic noise in the experimental set-up, it was first necessary to identify the source of the noise. Whilst vacuum pumps typically generate a large amount of noise, the source of the high frequency noise shown at early times in figure 6.5.4 can be easily identified as resulting from the high voltage pulse generator. The noise is observed at the time of arrival of the high voltage pulse at the field plates, and disappears as soon as the generator is disabled. If a BNC cable is placed near to the pulse generator, a similar signal can be observed directly on an oscilloscope. The receptor can be identified as the signal line in the apparatus, including the MCP, the oscilloscope and the cable between. The coupling channel is more complex, and could feasibly be any of the many internal and external cables and also the metal components of the chamber acting as antennas. The direct noise from the pulse generator is low, being on the order of less than 500 mV. However, the fast preamplifier is extremely noise sensitive and amplifies it to over 5 V. Therefore, it is important to reduce the amount of noise reaching the receptor circuit, and its subsequent amplification.

The initial method to reduce noise focused on physically separating electronically noisy cables from the signal cables. External cables were reduced to the shortest length possible and the MCP-to-scope signal cable was separated from all other power

and high voltage cables. At the chamber, a new tubulated flange was added to the blank flange holding the time-of-flight so that the distance between the output of the MCP and signal feedthrough was as short as possible. The 16 pin high voltage feedthrough was also removed, and a new extension with extra tubulated flanges added to the top of the chamber. The flanges were used as electrical feedthroughs for the two repeller plates, the MCP power cable, and the two ground field plates. The central unit of the time of flight was also altered to reduce the possibility of capacitive coupling between the repeller plate, and metal holding rods. These rods were attached directly to the electron MCP holder plate so any noise present in the high voltage pulse line could be transferred to the signal ground of the MCP by capacitive coupling to the rods. The rods were isolated by shortening them, and adding a long PEEK spacer for the rods to screw into (figure 6.9.1). These spacers were then attached to the electron MCP holder with a screw.

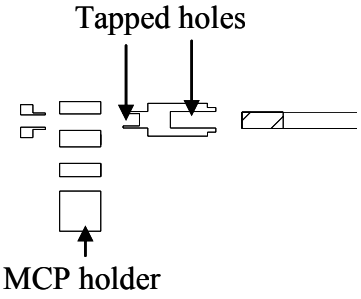

Figure 6.9.1: Cross section of PEEK spacers used to isolate the rods supporting the field plates of the central TOF unit from the MCP holder.

It is possible to remove noise from the pulse generator output by slowing down the pulse using a RC (resistor-capacitor) circuit, with a resistor in series and a capacitor parallel to ground (figure 6.9.2). The ramped field experiments themselves require slowly ramped pulse to be generated from the fast pulses produced by the pulse generator, but in the past only a small reduction in noise has been observed as the slew rate of the ramped field is reduced. The previous method used a BNC cut in the

middle with resistors in series. Therefore the exposed section was unshielded and susceptible to radiated noise. A new circuit box was built to allow greater control over the ramp of the field, whilst maintaining the shield around the circuit (figure 6.9.2B). The shielding was maintained by a thick metal box with a lid, and the ramp could be altered by either adding more resistors in series, or by changing the capacitor. This had a dramatic effect on the noise, and a small decrease in slew rate reduced the observable noise by as much as 10 times.

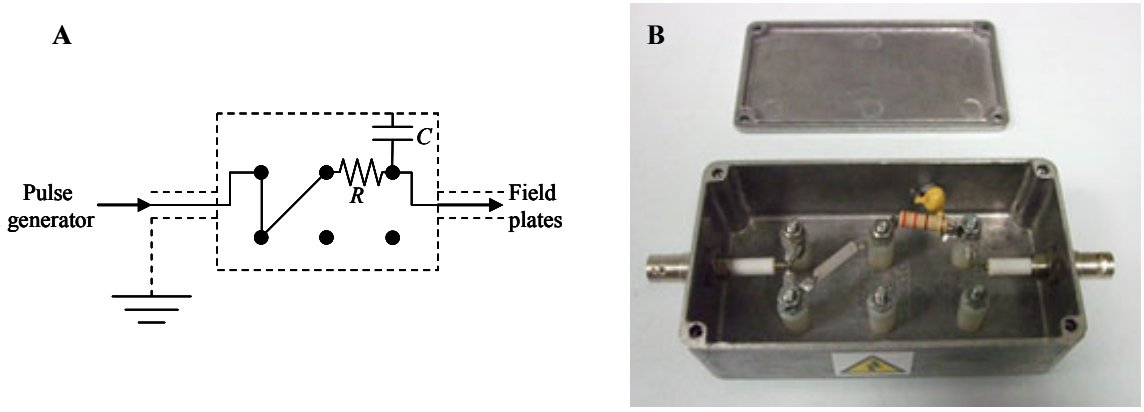

Figure 6.9.2: **A** – Circuit diagram of RC circuit used to decrease the slew rate of the ionizing electrical pulse. The output pulse enters from the left, passes through a series of resistors and wires screwed into the 6 terminals, and continues on to the field plates. The dotted line shows the shielding due to the coaxial cable and metal box. **B** – Photo of RC circuit, contained with box. The capacitor ground is connected to the box, which itself is ground by the coaxial shielding.

To reduce capacitive coupling, the level of shielding on all internal components of the chamber was increased. Initially, kapton coaxial wire suitable for high vacuums was used for all internal cabling and the experiments in Section 6.10 were carried out. However, over time it was found that the multiple stranded core necessary to give the wire flexibility, also made the wire susceptible to break after a small amount of movement. The braided shield on the coaxial cable was also inadequate to provide full shielding against electric fields. Instead, a RG59 BNC cable, stripped of the outer insulation and braided shield, was used for all of the field plates, whilst stripped

URM43 BNC was used as the signal line for the electron MCP. Copper tubing replaced the shielding requiring new PEEK spacers to separate it from the field plates. Small metal clamps were also slotted onto the tubes, and then used to connect grounding wires.

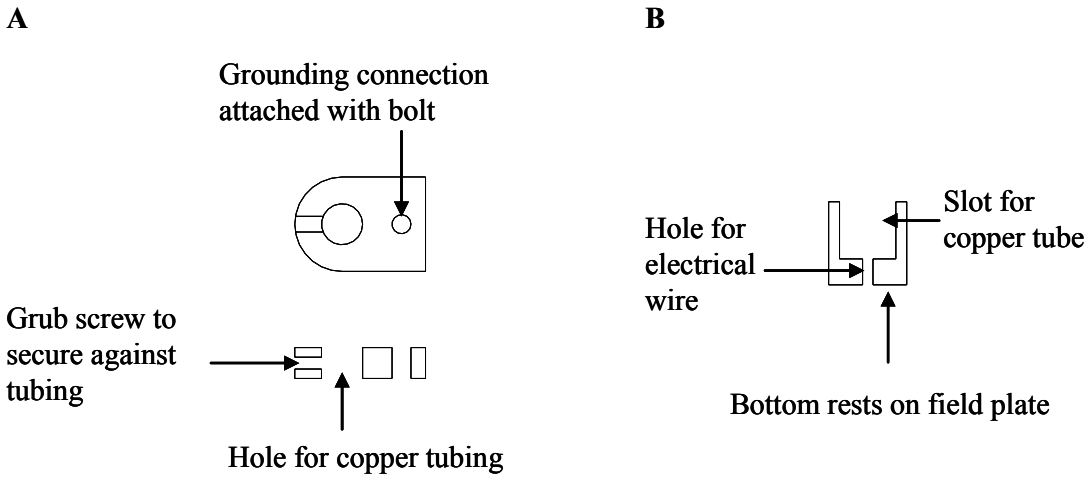

Figure 6.9.3: Cross section of grounding connection (A) and isolating spacer (B) for copper tube shielding. The grounding connection slots over the tube, and is secured with a grub screw. The tube fits into the isolating spacer, which then sits on top of the field plate.

Two new internal fittings were attached to the inside of the chamber to provide a grounding point for the external cable shielding. One was attached to a flange located on the top extension. It consisted of a metal rod with a flat ridge at the end to which shielding connections could be attached. A tapped hole was added to the external side of the flange to provide a point from which a ground wire could be attached the chamber. The second grounding point was a metal ledge attached to the inside of the flange holding the signal feedthrough and with a tapped hole to which the signal shield could be bolted.

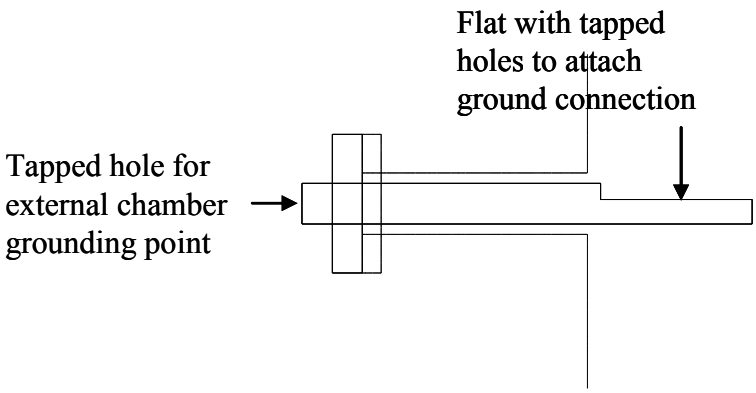

Figure 6.9.4: Cross section of grounding flange for shielding around field plate cables. The dotted line shows the tubulated flange located on the chamber extension. The grounding point consists of a metal rod, ending in a flat section with tapped holes allowing the shielding around electrical cables to be attached using screws.

Figure 6.9.5 shows the layout of the ground circuits associated with the chamber, and associated electronics. Whilst it appears complex, there are 3 main points at which the chassis/mains grounds from the electronics join to the chamber, with the potential to form noisy ground loops. These are located after the pulse generator (PG), after the pre-amplifier, and after the MCP high voltage power source. Floating feedthroughs were used to break the noisy mains ground connection carried by the BNC shielding to the chamber and these are shown in the diagram by a break in the dotted line. The chamber ground arising from the chassis earth of the vacuum pumps is difficult to remove without the use of special plastic spacers and these were found to be unnecessary. Initially the grounded field plates were attached directly to the external grounding point on the chamber. Whilst this reduced the length of cabling, the chamber acted as an antenna and the noise was increased. Instead the field plate grounds and chamber ground were sent by separate wires to a grounding point at the wall. High frequency noise requires short ground cables earthed at many points in a multipoint ground arrangement. The distance from the chamber and ground point made this impossible to achieve, however noise reduction using a single-point ground was sufficient.

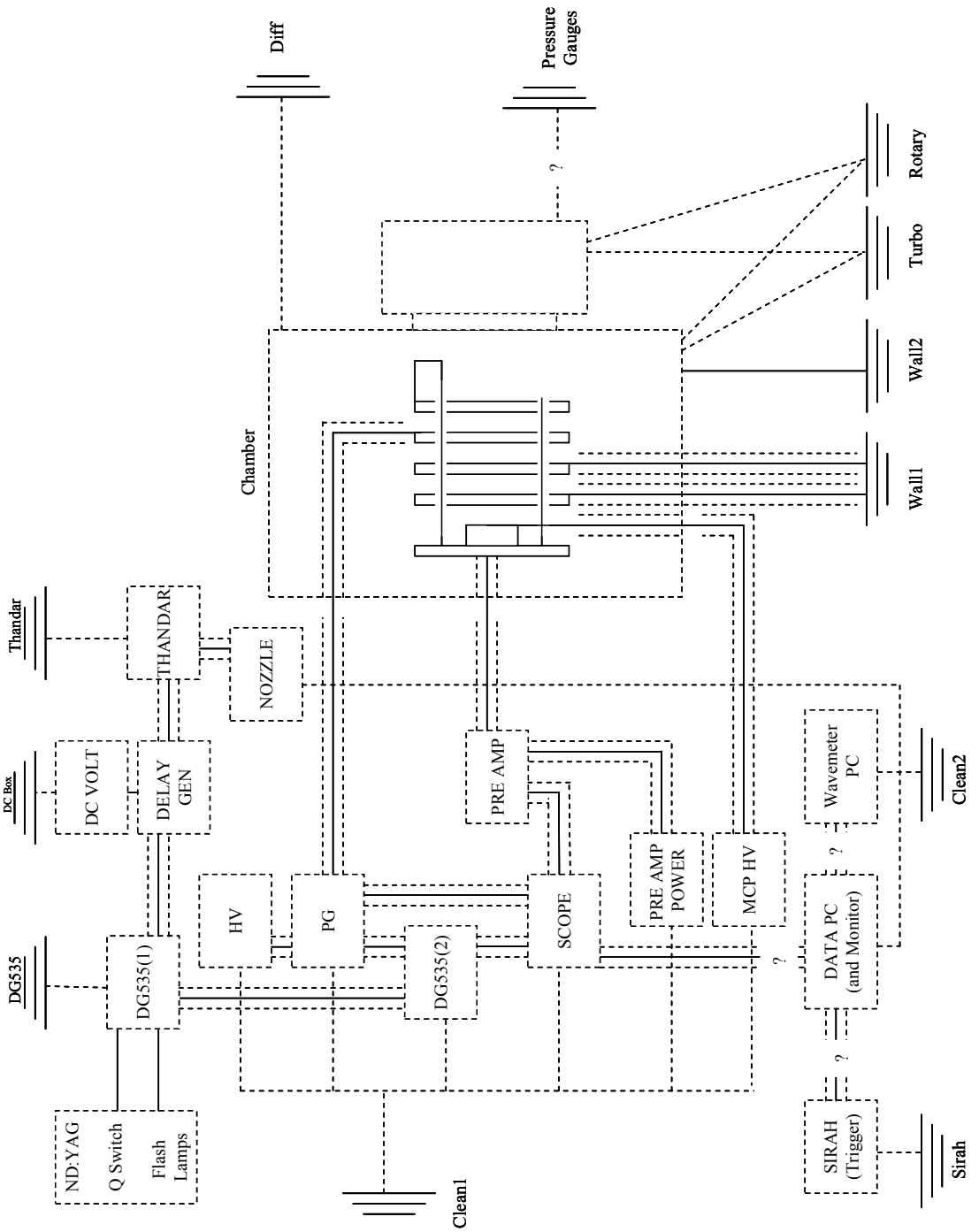

Figure 6.9.5: Grounding diagram showing the grounding pathway of the whole experimental set up. The dotted boxes represent a chassis ground, normally earthed along a mains cable, dotted line. Care was taken to isolate the chamber ground from as many grounding loops as possible, and to avoid connecting it to a mains ground. The break in the dotted line shown after the preamplifier, the pulse generator (PG) and the MCP power supply (HV) represents a floating feedthrough isolating the shielding from the chamber.

Finally, other noise sources needed to be considered including the vacuum pumps, power supplies and mains supply. Ferrite beads were used on all suitable lines to provide high frequency loss (over 1MHz) without introducing power loss. Ferrite clips (Wurth Electronics Inc) were used on power leads connected to the mains and preamplifier DC power source, whereas ferrite beads (Fair-Rite 25MHz and 100MHz) were used on both the MCP power supply and all cable shields. These cannot be used on the pulse generator line, as the high frequency loss damages the electrical pulse shape.

6.10. Selective field ionisation results

The addition of coaxial wire to the time of flight apparatus, the use of the new RC box to generate the ramped fields, and the improvement in the layout of the external cables, reduced the noise sufficiently so that the second peak could now be clearly resolved. A series of selective field ionisation (SFI) profiles were now recorded showing the partially obscured first peak and fully resolved second peak. Different states of character were populated in zero fields using the laser set-up described in Chapter 2, and were then field ionised and extracted using 1.5 kV electrical pulses of varying slew rates. The ionised electrons were detected using an electron MCP. The ramped pulses were generated using a RC (resistor/capacitor) circuit as shown in figure 6.9.2, changing the value of R by using a series of insulated wires and kOhm resistors to bridge the terminals, whilst keeping C at a constant 220 pF. The RC box gave greater flexibility to the set-up allowing a greater number of ramped pulses to be investigated. Figure 6.10.1 shows a typical ionisation profiles for the 36f(2) state ionised using a single resistor of R = 0.22 kΩ, as well as the background experimental noise (recorded with the nozzle shut) and the profile with the noise removed.

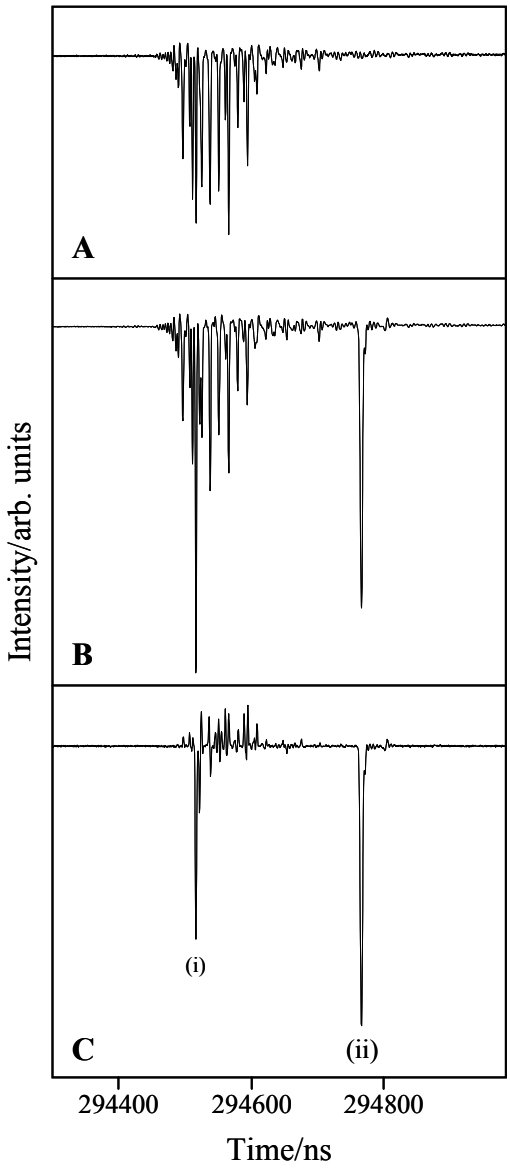

Figure 6.10.1: Traces taken directly from the oscilloscope. The y-axis is the voltage scale on the oscilloscope which is equivalent to the signal intensity. The x-axis is time in nanoseconds with respect to the initial Thandar trigger. **A** – Noise trace recorded with the nozzle closed *i.e.* no NO is present in the chamber. **B** – 36f(2) ionization trace recorded with a ramped field of 11.8 V cm^{-1} ns^{-1}. **C** – Signal trace with noise subtracted. Two peaks, labeled (i) and (ii), are now visible, and separated by approximately 180 ns.

The traces of pulses generated using a series of resistors of total resistance R were measured using high voltage probes and fitted using equation 6.10.1, where C is the total capacitance of the circuit, and V_0 is the peak voltage of the pulse *i.e.* 1.5 kV. For a total resistance of 0.22 kΩ this results in a pulse of slew rate 11.79 Vcm^{-1} ns^{-1} with a

rise time of $t_{80\text{-}20}$ = 127 ns. This rise time corresponds to the time taken for the pulse to rise from 20% to 80% of the peak voltage.

$$V = -V_0\left((1-\exp\left(-t/CR\right)\right). \qquad (6.10.1)$$

A set of ionisation profiles recorded for 36f(2) and 40f(0) are shown in figure 6.10.2 with the background electrical noise subtracted. It is clear from both traces that the two ionisation time profiles are very different. A 3.64 kΩ resistor generating a pulse with a slew rate of 0.9 $Vcm^{-1}ns^{-1}$ maximises the difference between the two profiles.

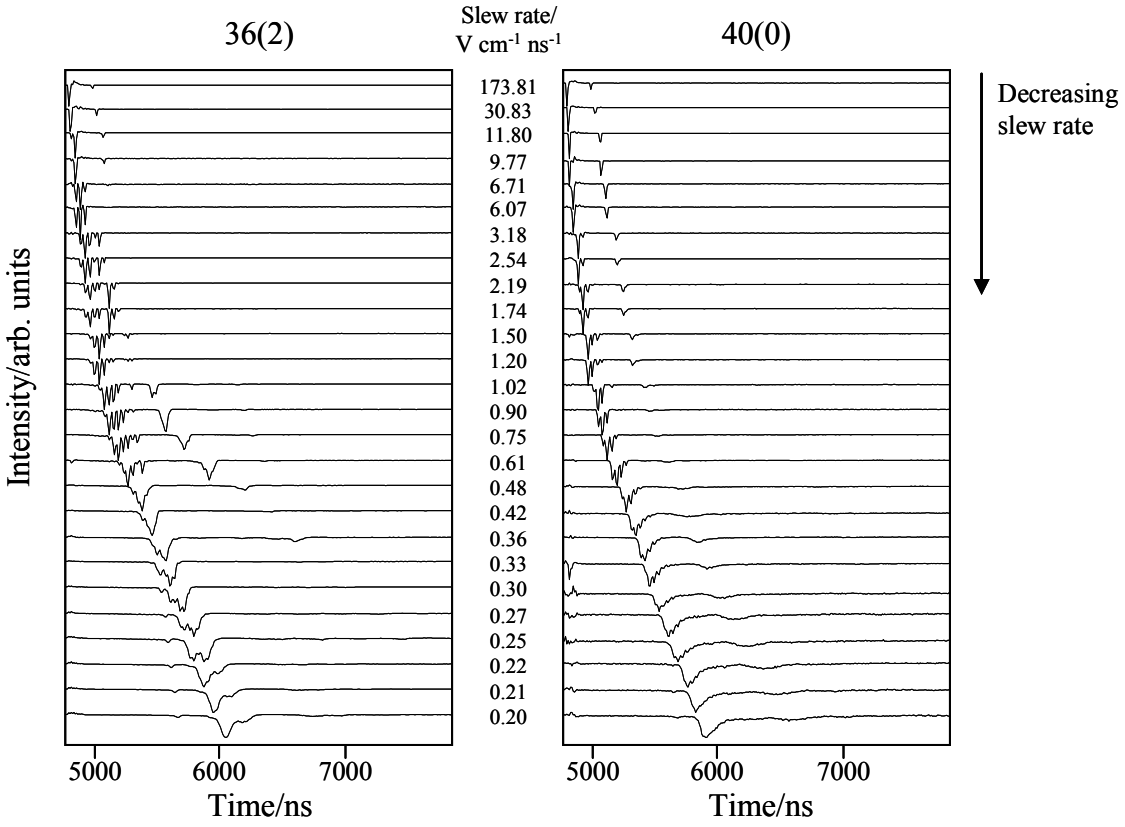

Figure 6.10.2: Ionization profiles taken for initial states of 36f(2) and 40f(0). The y-axis is intensity in arbitrary units, and the x-axis is time in ns. As the slew rate decreases the profile begins to spread and move to later times. Initially two signals can be observed but the second signal vanishes as the slew rate decreases. A comb structure can be observed on the first signal, but this disappears after the signal has moved approximately 600 ns.

There are two important observations to make on the ionisation time profiles at this point. The first concerns the multiple peaks present along the time base. Previously three peaks could be observed (figure 6.5.4), whereas now only two peaks are present, and are separated by 180 ns. As the slew rate is decreased, the second peak quickly disappears suggesting that the first peak arises from the primary field ionisation process whereas the second peak is due to some secondary process. The smaller separation between the first two peaks, in contrast to the third peak previously observed, now results in overlap between both signals as the slew rate is decreased. Therefore, it is now important that the source of this second peak can be identified so that possible removal techniques can be examined. The second important observation regards the structure of the first peak. This structure is greatly reduced with respect to the first peak of the previously recorded traces (figure 6.5.4) however the source still needs to be found and, if identified as an experimental artefact, removed.

6.11. Multiple peaks

The redesign of the time-of-flight apparatus has removed the electronic noise that previously obscured the earliest two peaks and allows the source of the multiple peaks to be probed further. Initially the different signals were assumed to be due to a reflection in the signal line. However, adding terminators into the signal line did not reduce the "reflection" as would be expected. Further calculations and experiments have instead confirmed that the second peak arises from an interaction between NO^+ ions and the repeller plate and these findings will now be discussed.

When the fastest ionising electrical pulse is used, the two peaks are separated by about 180 ns with the first arriving during the onset of the high frequency noise. Both signals are gas pressure and laser wavelength dependent, and both show components due to REMPI from an intermediate state, and field ionisation of a Rydberg state. The

relative height of the two peaks shows a large dependence on the alignment of the laser through the chamber. If the laser is aligned close to the repeller plate, the intensity of the second peak is reduced, whereas aligning close to the ground plate reduces the intensity of the first peak. The arrival time of the first peak shows little dependence on the alignment of the laser, whereas the second shifts by 50 ns as the laser beam is moved from one side of the interaction region to the other. Finally, ionisation using the fastest ramped field with a slew rate of greater than 140 V cm^{-1} ns^{-1} gives the first peak a width of 2 ns and an amplified peak width of 5 ns full width half maximum (FWHM). The second peak has a width of about 20 ns FWHM. As the slew rate is decreased, the first peak quickly broadens but the field has less influence on the width of the second.

A model of the time-of-flight (TOF) apparatus was built using Simion [111] and used to predict arrival times of the electrons at the detector (figure 6.11.1). Simion is a software package used to model electron optics and calculates the electric fields and subsequent trajectories of charged particles in those fields. For an electron ionised at 200 V cm^{-1} (approximately the field required to ionise a Rydberg state with principal quantum number 40) the time of flight to the electron MCP is 6.9 ns. Moving the position where the laser and molecular beams cross across the interaction region changes this value by ± 2 ns. For a linear TOF such as ours, the motion of the electron can be described in terms of the potential of the electric field. The kinetic energy of an electron, E_{KE} , of mass m_e and velocity v is given in equation 6.11.1.

$$E_{KE} = \frac{1}{2} m_e v^2 . \qquad (6.11.1)$$

The potential energy of charged particle in a field is equal to the charge of the particle, q, multiplied by the potential of the field, u. For an electron accelerated by a field, the potential energy is converted to kinetic energy. Using the relationship between

velocity, distance and time, the time t taken by the electron to move distance d, once it has been accelerated by the field can be expressed as equation 6.11.2.

$$t = d\left(\frac{2qu}{m}\right)^{-1/2}. \qquad (6.11.2)$$

An electron released under a constant voltage of 200 Vcm^{-1} takes 0.6 ns to travel the 5 mm required to leave the interaction region. At the fastest slew rate (≈140 V cm^{-1} ns^{-1}) the field rises by 84 V cm^{-1} ns^{-1} during this time, decreasing the time-of-flight through the accelerating region by only 0.09 ns. Therefore, it is assumed that the field the electron experiences inside the interaction region is approximately constant, in terms of the final velocity given to the electron. These calculations are all consistent with the first peak observed being due to an electron ionised by the initial field.

Field ionisation of a NO molecule also produces NO^+ ions, which experience an opposite potential due to the negative field and are accelerated towards the repeller plate. As the ion strikes the tungsten mesh covering the central hole of the field plate, electrons are released and then accelerated away from the plate and towards the detector. For ions created at 200 V cm^{-1}, the time of flight to the repeller plate is 413 ns, many times larger than the 180 ns peak separation observed. However, at the fastest slew rate the ramped field increases to 1500 V cm^{-1} in 13 ns, decreasing the time-of-flight to 152 ns. The electrons liberated at 1500 V cm^{-1} take 0.5 ns to reach the electron MCP. Therefore, electrons liberated in the way could correspond to the experimentally observed peak separation.

The assignment of the second peak as resulting from electrons liberated by NO^+ ions striking the tungsten mesh of the repeller plate is also consistent with the relationship to laser alignment. The 4 ns time of flight difference for electrons ionised at the extremes of the interaction region would not be observable on the scope, consistent

with the stationary behaviour of the first peak. However, ions created at either side of the interaction region have a 70 ns difference in time of flight at 200 Vcm^{-1} and a 50ns difference at 1500Vcm^{-1} again consistent with the experimentally observed value. Similarly, the change in relative intensity of the two peaks with changing alignment can be explained. An electron ionised near to the grounded plate would be accelerated less by the electric potential, and less would reach the detector. An ion created at the same point would be accelerated to a higher velocity, liberating more electrons from the tungsten mesh. On the opposite side of the interaction region, the lower velocity of the ion would release fewer electrons leading to a reduction in the height of the second peak.

As a final test, a voltage was applied to the field plate nearest to the detector, which is attached to ground during normal operation. This creates an electric potential barrier that the electrons must pass over to reach the detector (figure 6.11.1). As the voltage is increased, the intensity of the first peak decreases, and eventually disappears. The second signal is unaffected. The barrier blocks electrons field ionised by the rising field, *e.g.* states ionised at 200 Vcm^{-1}, but the electrons released from the mesh at a higher voltage are given enough kinetic energy to surmount the barrier and be detected.

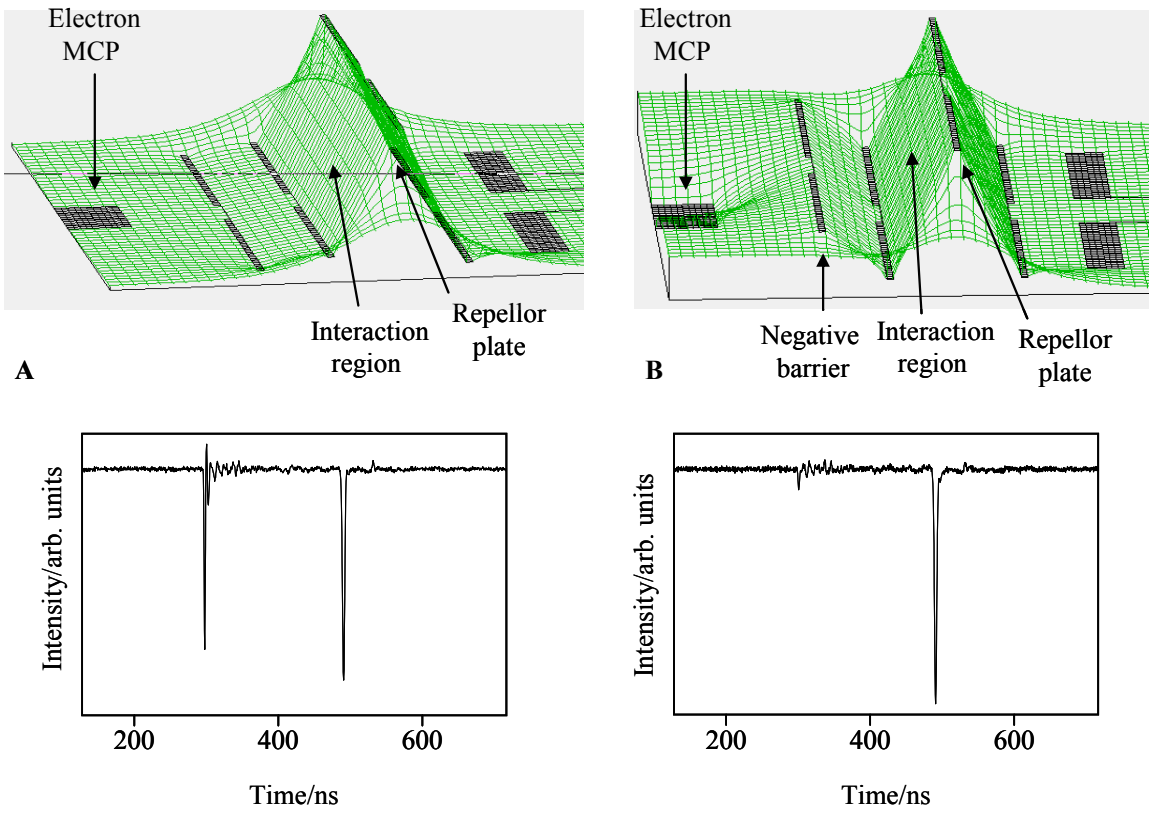

Figure 6.11.1: Simion models (top) and pulsed field ionization spectra (bottom) showing disappearance of second peak as a potential barrier is added between the MCP and interaction region. A shows the system under normal operation. A negative field accelerates the ionized electron towards the electron MCP and are detected (first signal), whilst accelerating ions towards the repeller plate. The ions then liberate electrons from the plate, and the field accelerates thee electrons to the detector (second signal). B shows the system when a negative barrier has been placed before the detector and after the interaction region. Electrons released from the plate are given enough kinetic energy to surmount the barrier, whereas initially ionized electrons are at a much smaller potential and are blocked.

6.12. Signal structure

As shown in figure 6.10.2, the signal due to a field ionised electron shows comb structure with a separation of 20 to 50 ns corresponding to a frequency of 20 to 50 MHz. This frequency corresponds closely to the radiofrequency noise generated by a high voltage pulse generator, and also to the electronic noise emitted by the pulse generator and observed on a scope. The comb structure appears as the slew rate of the

ionising field is decreased and the ionisation profile begins to spread. As the ionisation moves to later times the structure begins to wash out and after about 1 μs from the appearance of the first ionisation peak the structure has completely vanished. The comb structure also appears roughly in phase with the background electronic noise directly observed on the scope. For these reasons it was assumed that the structure arose from an additive effect between the electronic noise and signal, and so further steps were taken to enhance the shielding of the electrical cables, and improve the grounding circuit, as detailed in Section 6.9.

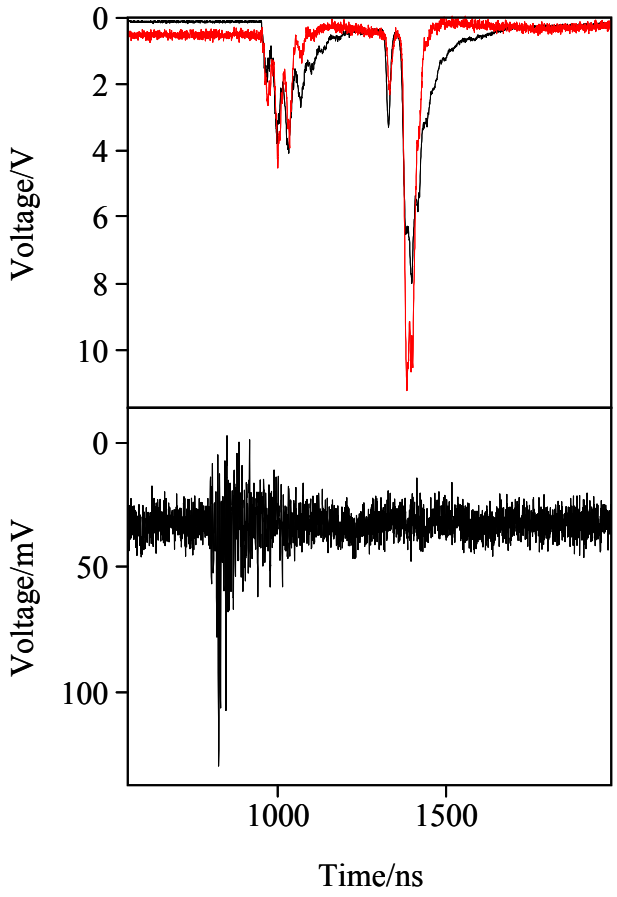

Figure 6.12.1: Ionization profile recorded for the 40f(2) Rydberg state ionized using a ramped field of slew rate 1.50 $Vcm^{-1}ns^{-1}$. The top trace shows the profiles recorded with (black) and without (red) a preamplifier. Both profiles show the same comb structure. The bottom trace shows the noise recorded with the same slew rate. The noise has now been reduced to an order of magnitude less than the magnitude of the signal and extends for approximately 300 ns, much shorter than the relative time the comb structure is observed in the signal.

This further development reduced the observable background electronic noise to around 100 mV, over an order of magnitude less than the observable signal. However, the comb structure was still present in both the pure and amplified signal, but now showed no relationship to any oscillations in the experimental noise and continuing long after any the principal experimental noise had vanished (figure 6.12.1). It was also noted that the second peak showed a similar structure albeit condensed to a lower frequency resulting in a lower prominence. This raised the possibility that the structure was a genuine ionisation process rather than an electronic artefact. However, the in-phase time behaviour of the peaks in profiles taken with decreasing slew rates seemed to contradict this (fig 6.12.2).

A number of tests were performed to identify the source of this comb structure. The SFI traces shown in previous sections were taken using an RC circuit containing carbon film resistors. A second RC box was built using a high voltage wire wound resistor and with a separate ground after the capacitor so that the circuit ground could be separated from the chassis of the box. The isolated capacitor ground had no effect on the level of electronic noise or the signal structure. Traces taken using the wire wound RC circuit are shown in figure 6.12.2A. The comb structure now appeared at twice the frequency of the previous traces (20 MHz); however the noise had remained unchanged apart from an overall reduction in amplitude. The electrical pulses generated by both methods were measured using high voltage probes and a digital scope. The pulses produced with the wire wound RC circuit showed larger structural defects due to the higher inductance of the resistor, but neither pulse showed any radiofrequency oscillations. However, it is difficult to measure an electrical pulse directly as the probes themselves possess impedance, adding an extra load to the pulse generator and possibly dampening any AC noise present.

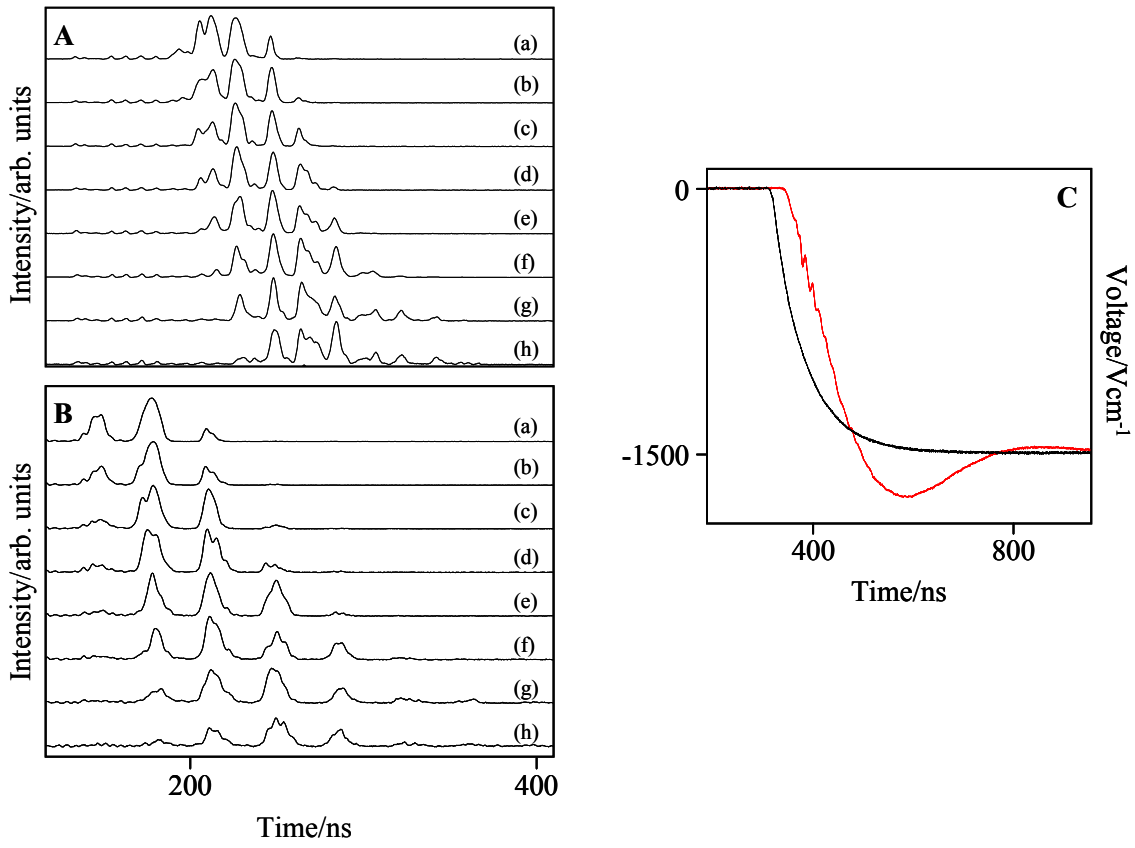

Figure 6.12.2: Ionization traces recorded using the RC box containing a wire wound (A) and carbon film (B) resistor. The comb structure is present for both resistors; however the frequency is doubled when using the wire wound. C shows the electrical pulse, measured on a scope using high voltage probes. The wire wound trace (red) shows larger structural defects than the carbon film trace (black). (a) to (h) label ionisation traces recorded with electric field pulses with a maximum voltage of 850 V to 500V in 50 V steps, corresponding to a decreasing slew rate.

A second measurement technique was applied, using a RC circuit designed to measure the AC noise directly on a DC field *via* a 50Ω terminated channel on a scope. A trace measured using the carbon film resistor circuit (figure 6.12.3) showed a 10 to 20 MHz oscillation. Whilst it is unlikely that the oscillation of the electrical pulse is large enough to ionise electrons in packets, none of the techniques attempted so far have provided a full explanation of the source of the comb structure. Further investigations are required, and these are detailed in the summary in Section 6.15.

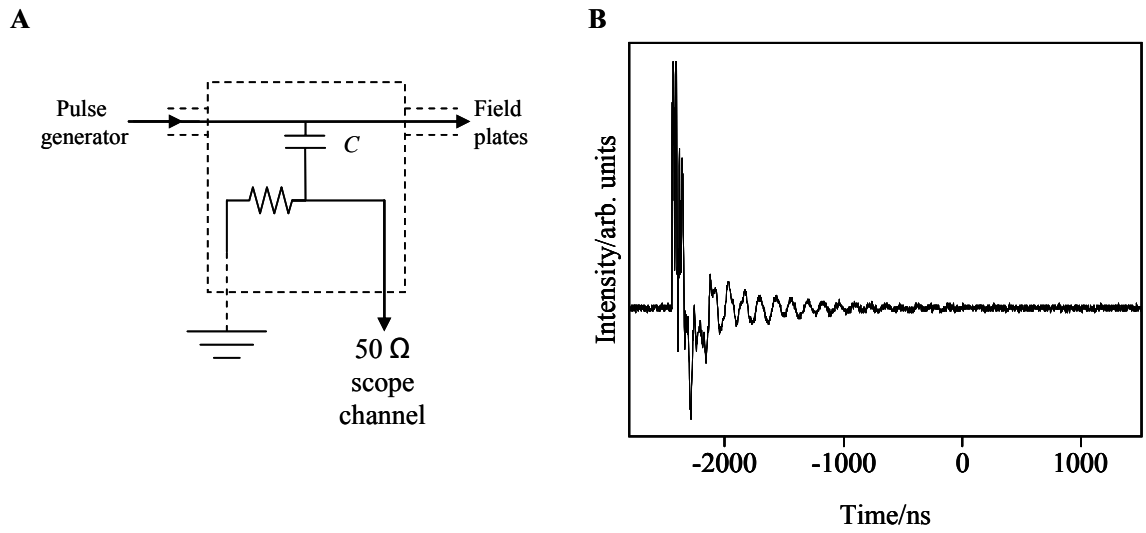

Figure 6.12.3: **A** – RC circuit designed to measure the AC ringing on top of the high voltage pulse directly using the 50 Ω channel on a scope. This reduces the dampening of the AC ringing.
B – Trace recorded using circuit shown in A. A clear AC oscillation can be observed, with a frequency of 10 to 20 MHz. The RC circuit possesses impedance and so will affect the high voltage pulse and any AC noise. Therefore, the 10 to 20 MHz oscillation could be the source of the 20 to 50 MHz comb structure observed in the signal.

6.13. Signal processing

It is possible to remove frequency components from the signal using a Fourier transform signal filtering technique. A FORTRAN program was written that takes the SFI intensity file, and the timebase from the scope used to record the trace, and then performs a Fourier transform to produce a frequency spectrum. High frequency components are present in both the noise and signal spectra, however in the important 10 to 60 MHz range, the noise spectra shows no clear structure (figure 6.13.1).

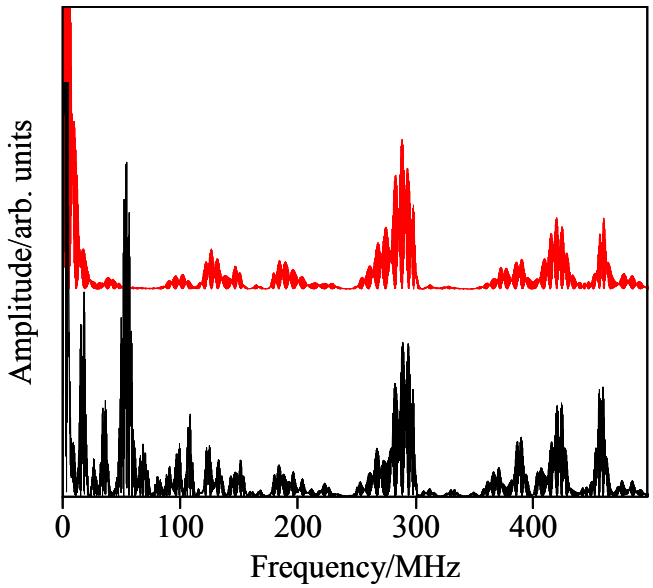

Figure 6.13.1: Fourier transform of the signal (black) and noise (red) ionization time profiles recorded for the 41f(0) Rydberg state with an ionizing field of slew rate 2.54 $Vcm^{-1}ns^{-1}$. The noise frequency spectrum shows little structure in 20 to 80 MHz region corresponding to the frequency of the comb structure of the signal profile observed in the time domain. As expected, the signal spectrum shows a large peak at around 50 MHz corresponding to this comb structure.

As would be expected, the signal profile shows a strong peak in this region. To remove this oscillation a filtering technique must be performed to remove frequencies higher than a cut off value before the spectrum is transformed back into the time domain. This kind of technique is called a low pass filter. The simplest low pass filter is a box function, which sets all frequencies higher than the cut-off to zero. However, the Fourier transformation of a box function is a sinc function that oscillates to infinity, *i.e.* the peak exhibits strong ringing. A Gaussian filter appears the same in both domains and so exhibits no ringing. A Butterworth filter [112] is a combination of these two filters; a Gaussian at the edges with as a flat a top as possible during the pass band (figure 6.13.2).

A Butterworth function is given by equation 6.13.1, where n is the order, ω_c is the cut-off frequency, ω is the frequency.

$$B(\omega) = \frac{1}{1 + (\omega / \omega_c)^{2n}} \qquad (6.13.1)$$

To filter a time profile it must first be Fourier transformed to the frequency domain, multiplied by the filter function and transformed back to the time domain. It was found that the best retrieval of the signal envelope was achieved using a Butterworth filter of order 3 and with a frequency cut off value of 24 MHz.

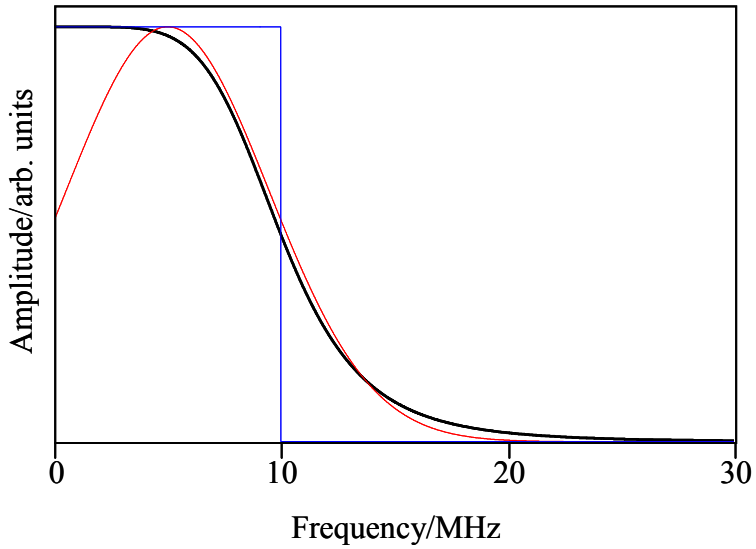

Figure 6.13.2: Plot showing a Butterworth function (black line) of order 3 and with a frequency cut-off of 10 MHz. The function closely resembles a box function (blue line) during the pass band *i.e.* below the cut-off frequency. At the edges the Butterworth resembles a Gaussian function (red line) to reduce the ringing due to edge effects when transformed back to the time domain.

Filtered ionisation profiles, plotted over the original data, are shown in figure 6.13.3. The red traces show the unfiltered data and the black show the results of the frequency filter. The filter brings out the envelope of the first peak, and can make the differences clearer between spectra taken from different initial states. This would help in the analysis of composition of a wavepacket SFI trace. All five spectra initially start off almost identical with two sharp peaks observed as discussed in the previous section. As the slew rate decreases the peaks begin to spread. The *n*f(2) traces all show the main peak arriving at around 6000 ns for the slowest slew rate. The two *n*f(0) profiles

would be expected to show a earlier peak, due to the lower ionisation potential, which is the case for the 41f(0) profile with a peak at around 5700 ns. The 40f(0) profile is more complex, showing a small peak at around 5800 ns, but then a large broad structure around 6000 ns, possibly arising from population transferring to a *n*(2) manifold.

Label	**Slew rate/V cm^{-1} ns^{-1}**
(a)	173.81
(b)	30.83
(c)	11.80
(d)	9.77
(e)	6.71
(f)	6.07
(g)	3.18
(h)	2.54
(i)	2.19
(j)	1.74
(k)	1.50
(l)	1.20
(m)	1.02
(n)	0.90
(o)	0.75
(p)	0.61
(q)	0.48
(r)	0.42
(s)	0.36
(t)	0.33
(u)	0.30
(v)	0.27
(w)	0.25
(x)	0.22
(y)	0.21
(z)	0.20

Table 6.13.1: Table of labels used in figure 6.13.3 with associated slew rate in V cm^{-1} ns^{-1} of the ionizing field pulse.

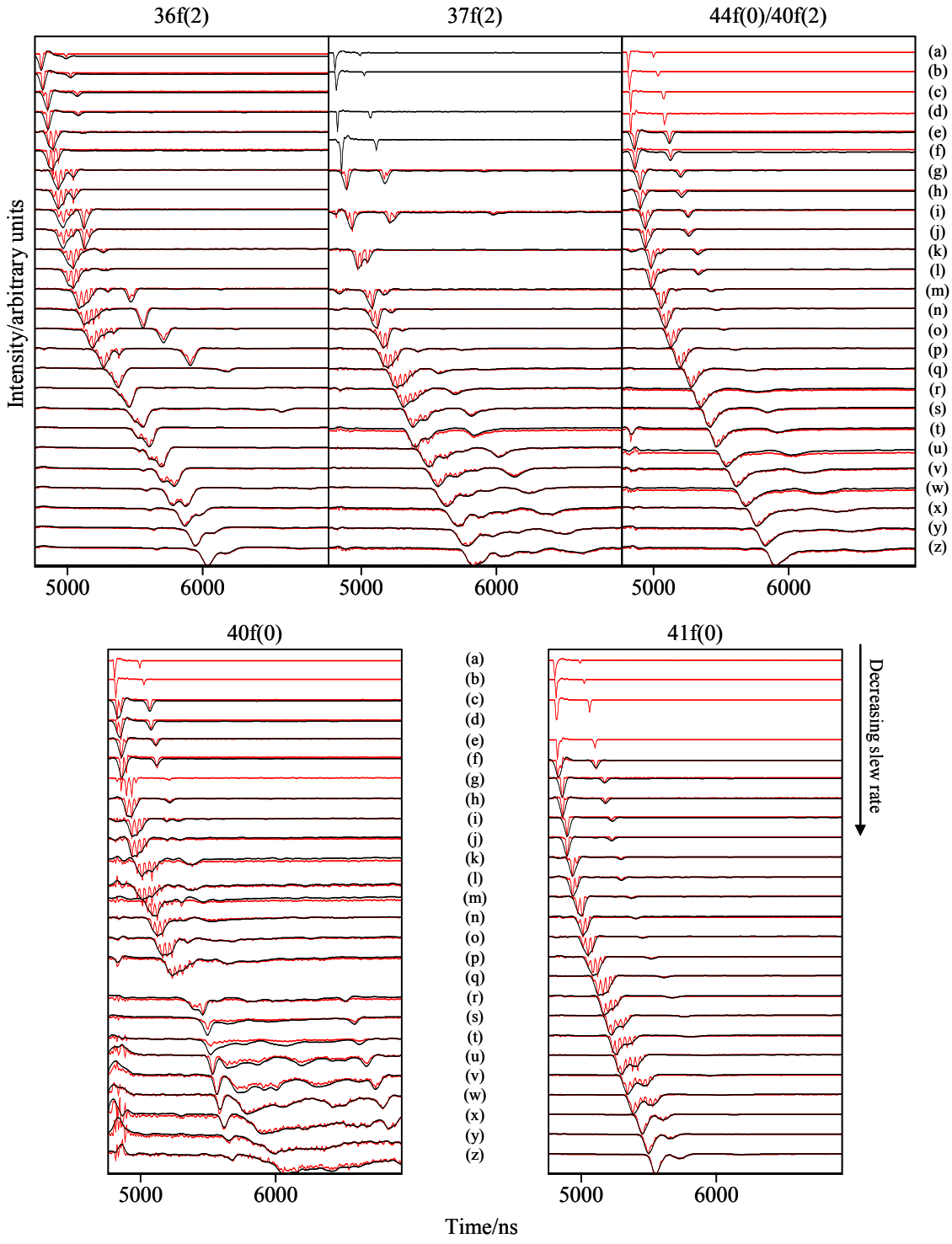

Figure 6.13.3: SFI profiles for five different states. The red lines are the original traces, and the black the filtered profiles. The profiles for the five states show significant differences allowing the different states to be identified from a wavepacket SFI analysis. The labels (a) – (z) correspond to the slew rate of the ionizing field and are tabulated in table 6.13.1.

6.14. Time scale to voltage conversion

To convert an ionisation profile from time to voltage, the slew rate of the ionising field is found. This is done by fitting equation 6.10.1 to a trace of the electrical pulse, measured using a high voltage probe. Next, the arrival time of the main diabatic ionisation peak in the ionisation profile is matched to the voltage at which diabatic ionisation occurs, approximately $1/16n^4$. By working backwards from the diabatic ionisation voltage the start time of the pulse, t_0, is found. This is then used along with the slew rate to convert the time base to voltage.

In an ideal system, diabatic ionisation of a single electron would results in a delta function ionisation time profile. However, the large number of electrons probed and other factors (*e.g.* size of interaction region, laser profile, instrument function, initial energy of molecular beam) lead to a Lorentzian profile of finite width. During the conversion, this leads to an exaggeration of the peaks width on a voltage scale. A peak with an initial width of 10 ns FWHM, converted to a voltage scale using the fastest slew rate of 140 $Vcm^{-1}ns^{-1}$ results in a peak of width 1400 Vcm^{-1} FWHM. In contrast, the same peak converted to a voltage scale using a slew rate of $10Vcm^{-1}ns^{-1}$ results in a peak of 100 Vcm^{-1} FWHM. It should be expected that as the slew rate decreases, the ionisation profile will spread as the probability of adiabatic population transfer increases at each avoided crossing. However, this base scale conversion effect has the opposite effect of exaggerating the spread of peaks at fast slew rates. As the slew rate decreases, this effect no longer dominates and the voltage profiles begin to converge to a true appearance (Fig 6.14.1).

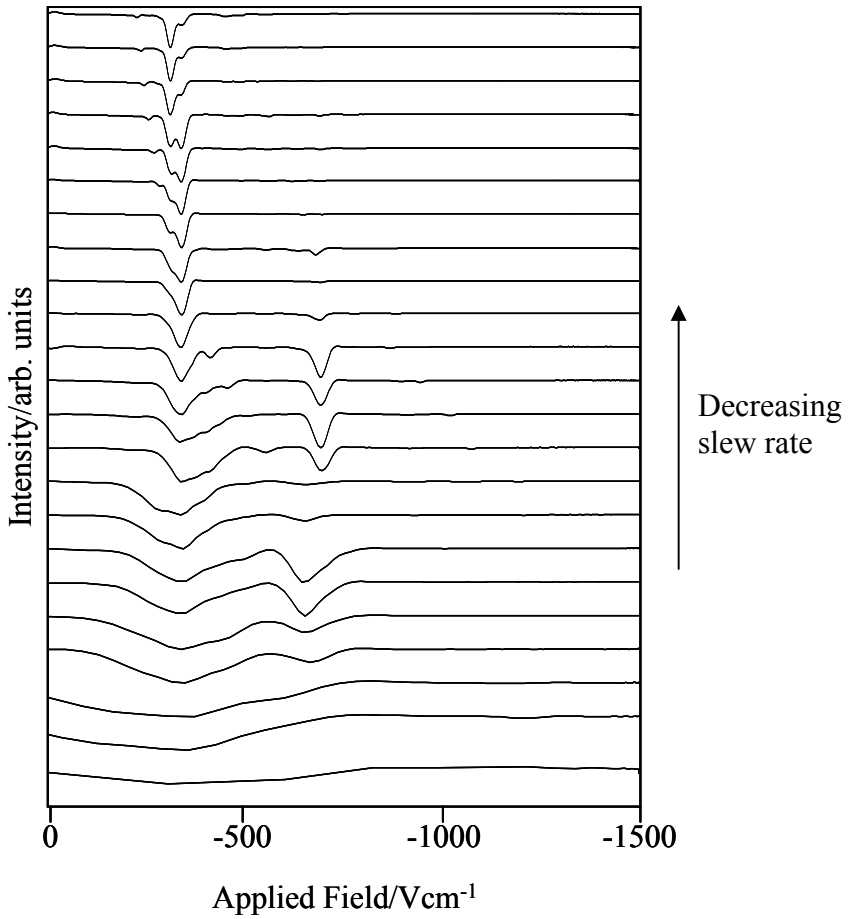

Figure 6.14.1: SFI profiles converted to a voltage scale. At fast slew rates the ionization profile is stretched horizontally and loses any useful information. As the slew rate decreases, it no longer dominates. And the true voltage ionization profile can be observed.

The second peak is less affected by the time base conversion. The time-of-flight of the NO^+ ions is focused by the field. Ions released at later times gain more kinetic energy from the higher field and catch up with ions released earlier at a smaller voltage. This causes the ions to bunch up in time, and compresses the subsequent detection peak. The compression of the peak in time means the subsequent conversion to voltage is less prone to exaggerated spreading.

6.15. Summary

A large proportion of the time of this PhD has been the design and subsequent development of the experimental chamber. Whilst the design was based on well established time-of-flight designs within the group, there have been no previous detailed investigations into electronic noise. This has been a success, reducing the background noise picked up by the detector circuit from a saturated 5 V signal, to a workable few 100 mV. With these developments, a number of ionisation profiles have been recorded using a large number of different slew rates. The use of these state ionisation time "fingerprints" will greatly simplify analysis of future wavepacket experiments. The conversion to a voltage timescale has so far been unsuccessful. Further work is need to either focus the electron signal in time, or to create a more rigorous time-voltage conversion technique.

The investigation into the presence of the multiple signals has also been successful providing for the first time a full explanation of signals previously hidden behind the electronic noise. This allows us to justify the use of the different peaks for different experimental purposes.

Further work is necessary to explain the comb structure, although it seems likely that it is generated by electrical interference from the pulse generator. There are a number of further tests to investigate and possibly eliminate the structure. By far the most informative test would be to generate the ramped field by a different method. A high voltage arbitrary pulse generator, or high voltage amplifier and low voltage arbitrary pulse generator, would allow us to test if the RC circuit is the source of the problem. Further techniques could be employed to reduce the electronic noise further. The coaxial shielding of the various external shielding could be passed through a large ferrite ring to remove any AC noise either from the ground itself or coupled to the

shield from the pulse generator. An RC circuit in series with the pulse generator may filter out any AC ringing through the capacitor whilst leaving the DC pulse unaffected.

Future modification of the chamber could also be desirable. An extra feedthrough would allow a second connector to be added to the repeller plate. This would allow the voltage on the plate to be measured directly during the recording of an ionisation profile and may also help to reduce any ringing in the applied voltage pulse. If the horizontal flanges on the interaction and detection chambers could be widened then the initial TOF design could be used. This would allow extra magnetic and electrical shielding to be placed around the TOF. The mesh on the repeller plate could be altered or removed to remove the second signal, but the effect on the ion detection scheme would need to be examined. A second nozzle could also be added to the set-up, outside of the source region. This would allow sensitive ion detection experiments to be performed where a skimmer is either unnecessary, or inhibitive.

Finally, although not shown in this thesis, a number of experiments were attempted to allow control over the path an electron takes to ionisation. In the control experiment by Tada and co-workers, the high value of principal quantum number, n, investigated required only a single pulse to control and ionise the Rydberg state. For the values of n around 35 that are currently probed in this set-up, two pulses are required. First, a slowly ramped low voltage pulse (< 15 V) to adiabatically transfer population at the first avoided crossing to a manifold belonging to a different rotational state of the ion core. A fast high voltage pulse then diabatically ionises the electron, although this pulse needed to have a slew rate low enough that the two ionisation limits separated by some voltage are an observable time distance apart. It was hoped that the arrival time of the electron would change dramatically when the slow pulse is added and the electron ionised at a different rotational ionisation limit. However, the timing between

the two pulses was difficult to control and the comb structure at early times made analysis of the peaks impossible. It would be interesting to further develop the set-up to remove the timing jitters and comb structure and attempt this kind of control, which would be the first of its kind in a molecular system.

7. Summary and outlook

7.1. The predissociating Rydberg spectra of NO

In Chapter 4, the zero field spectra of the predissociating Rydberg states of NO in the range n = 15 – 100, recorded *via* the $A^2\Sigma^+(v'=0, N'=0)$ and $A^2\Sigma^+(v'=0, N'=2)$ intermediates, are presented. Both spectra show distinct examples of broad asymmetric Fano line shapes and show many more Rydberg series than previously obtained from bound Rydberg spectra recorded using pulsed field ionisation (PFI); PFI will only detect states with a lifetime longer than the delay between the excitation laser pulse and ionising electric pulse. The p(2) series observed in the predissociating spectrum recorded *via* the $A^2\Sigma^+(v'=0, N'=0)$ intermediate also shows a strong intensity dependence on n, slowly increasing to a maximum before suddenly vanishing. This appears to show a correlation with the relative position of the p(0) series; the p(2) intensity increases as the states approach the positions of the p(0) states and vanish just after the p(2) states have passed to the high energy side of the p(0) states. In Chapter 4, the Stark spectra of the predissociating Rydberg states of NO are also presented recorded *via* the $N'=0$, 1, 2, and 4 rotational states of the $A^2\Sigma^+(v'=0, N')$ intermediate. Selection rules dictate that the spectrum recorded *via* the $N'=0$ intermediate is the least congested and this allows a number of interesting spectroscopic features to be observed clearly. A number of low-l dark states are observed gaining intensity as the field mixes them into the high-l manifold. This behaviour is most clearly observed for the 24d(2), 25d(2), 25s(2) and 26s(2) states. These states lie in a region in which the n(0) manifold sits on the opposite side

of the $n(2)$ manifold to the position of the low-l states. Therefore, the mixing of the states of s and d character into the high-l manifold is approximately hydrogenic. In contrast, in the region where the $n(0)$ manifolds lie on the same low energy side of the $n(2)$ manifolds as the low-l $nl(2)$ states the mixing is diluted and the intensity gain is reduced. Whilst more congested, the Stark spectra recorded *via* the $A^2\Sigma^+(v'=0, N'=2)$ intermediate also reveals a number of "dark states" gaining intensity by mixing into the high-l manifold of predominantly s character. The analysis of the Stark spectra was carried out using a matrix diagonalisation technique to produce a Stark map that could then be overlaid onto the experimental data. The analysis of the spectra is then relatively straightforward and the composition of the zero field states mixed to form a Stark state can be quickly determined.

Chapter 5 compares the predissociation spectra to previously obtained bound spectra [32]. The most striking difference is the line shape: broad and asymmetric for the predissociating and sharp and symmetric for the bound. As already mentioned, many more states can be observed in the predissociation spectra than the bound, and this high density of states can sometimes make assignment difficult. The high-l manifold gains intensity as a field is applied due to the mixing with states of non-zero transition intensity. This intensity gain is noticeably different at moderate fields in the predissociation and bound states; in the predissociating states it is almost symmetrical, arising from mixing of the p and f states from either side of the manifold, whereas the bound manifolds show an asymmetric intensity gain arising from just the f states. The comparison also highlights the different techniques used to model the bound and predissociating spectra. Progress has been made on adapting the matrix diagonalisation code to reproduce the Fano line shape in zero field however further work is needed to simulate the Stark spectra quantitatively.

A ramped field can be used to characterise a wave packet, by giving a time dependant ionisation signal that can be used to calculate the initial composition of the wave packet. This was the initial motivation for the work in Chapter 6, which details the application of a ramped field to ionise bound Rydberg population; however early experiments revealed the possibility of controlling the rotational angular momentum of an ionised molecule by the use of a shaped electric pulse. The development of the experimental chamber to achieve this took a large proportion of the time of this PhD. One requirement of the new chamber was a short distance between the detector and repeller plate and this resulted in a substantial increase in background noise requiring a detailed investigation into electrical noise. These investigations have identified the source of the noise, and reduced it to manageable levels whilst also pinpointing the source of the multiple signal peaks. With these developments, a number of ionisation profiles have been recorded using a large number of different slew rates, and are suitable for use in characterising a bound Rydberg wave packet excited in the same energy region. The development is ongoing, with a number of issues identified and possible solutions discussed in the summary of Chapter 6.

7.2. Outlook

7.2.1. Time-resolved wave packet experiments

The overall motivation for much of this work has been to develop the background necessary for wavepacket coherent control experiments in NO. A wavepacket is a coherent super position of states excited with a broadband pulse. To understand the phase information within the molecule it is necessary to know the positions of the various Rydberg states and this has been achieved with the frequency spectra presented in this thesis. The direct population in each Rydberg state excited in a wave packet can be measured using selective field ionisation (SFI); therefore the state

ionisation time "fingerprints" presented in Chapter 6 will greatly simplify analysis of future wavepacket experiments. The fingerprints will also help choose a slew rate that provides the maximum resolution between the different Rydberg states that may be present in a wave packet. Initially, a predissociating wave packet will be excited below the lowest ionisation limit and the subsequent motion observed using a time resolved pump-probe experiment. Once this has been achieved the aim is to excite a wave packet above the first ionisation limit, and then to control the predissociation and autoionisation branching ratio, which has previously been demonstrated in NO by monitoring the bound components with the optical Ramsey method (ORM) [20]. However, in these experiments the predissociating component is only inferred by the decay of the bound component, and so the planned experiments will instead directly probe the predissociation fragments. A pair of ultrafast pulses will be used to excite the wave packet and then ionise the nitrogen fragments produced by photodissociation. This pump-probe technique will provide a time-resolved direct measurement of the predissociation process.

7.2.2. Frequency resolved predissociation investigations

Although the dominant predissociation channel has been probed, it would be of interest to monitor the different fragmentation channels; especially the N(^{4}S) channel, which is the main decay route for states of s character. The intensity of many of the Rydberg series observed in the zero field spectra recorded *via* different intermediates show a strong *n*-independence. Previous work by Fuji and Morita [76] observed that the absence of states in the N(^{2}D) REMPI spectra often corresponded to the observation of the missing states in a different decay channel. It would be of interest to study this effect as a field is applied, especially to observe if the intensity gained by the low-*l* states mixing into a high-*l* manifold was observed in any other decay channels. Further experiments could also be performed above the first ionisation limit,

and probe both the predissociation and autoionisation spectra in zero field and also with an applied field.

7.2.3. Control of rotational angular momentum using shaped electric field pulses

The field ionisation studies have also opened up the possibility of controlling the rotational angular momentum of an ionised molecule by using a shaped electric field pulse, as has been previously demonstrated in atomic systems [106]. An initially slow ramp would be used to drive the population on a predominantly adiabatic passage through the first avoided crossing. The second part of the pulse would have a fast slew rate, driving the population along a diabatic pathway to ionisation. Through this method the population would be ionised from a different manifold and hence at a different voltage than if an ionising pulse with a purely fast or slow slew rate. This would provide the first example of this kind of field control in a molecular system. It may be possible to use this method to increase the difference in ionisation profiles from different Rydberg states, and therefore to increase the resolution of the wave packet characterisation using SFI. To carry out this kind of field control the chamber will need further development to fully understand the cause of the comb structure in the ionisation profiles, and also to remove the signal peak that occur at later times. A different molecular system may also be necessary to increase the lifetime of the Rydberg state, and to give a longer time to apply the control pulse. Finally, it would of interest to develop a method that could simulate the ionisation profiles of Rydberg states under different slew rates. This has previously been carried out in Lithium, using the Landau-Zener equation and a WKB approximation to follow the population through the Stark manifold to ionisation [101]. If this could be adapted to simulate the greater number of crossing present in a molecular system it could help with further analysis of the ionisation profiles.

Appendix A: Derivation of Fano parameter

A state embedded in a dissociation continuum is neither purely discrete nor purely continuous. The state acts as an indirect pathway to the dissociation continuum, and the interference between the direct and indirect pathways results in an asymmetric line shape known as a Fano profile [26]. The Fano shape parameter can be derived by considering the interaction between the discrete state and continuum as a perturbation. The interaction is not strictly a perturbation, as it cannot be turned off, but as a hypothetical concept it is convenient to assume that the perturbation can be removed and the resulting Schrödinger equation for the system is solvable [87]. The unperturbed basis consists of a discrete state labeled $|\varphi\rangle$, and a degenerate continuum labeled $|\varepsilon\rangle$. First the unperturbed (diagonal) Hamiltonian is constructed, H_0, and can be written as

$$\begin{pmatrix} H_{\varphi\varphi} & 0 \\ 0 & H_{\varepsilon\varepsilon'} \end{pmatrix}\begin{pmatrix} |\varphi\rangle \\ |\varepsilon\rangle \end{pmatrix} = \begin{pmatrix} E_\varphi|\varphi\rangle \\ \varepsilon|\varepsilon\rangle \end{pmatrix}. \qquad \text{(A.1)}$$

The perturbation is then added as an off-diagonal element, V, and the wave function of the hybrid state is defined as

$$|E\rangle = a_\varphi|\varphi\rangle + \int b_\varepsilon|\varepsilon\rangle d\varepsilon\,. \qquad \text{(A.2)}$$

As introduced in the discussion on the matrix diagonalisation technique (equation 4.3.1), the total Hamiltonian is the sum of the unperturbed Hamiltonian, plus the Hamiltonian describing the perturbation. The perturbation is added as an off-diagonal coupling, V; the form of this off-diagonal coupling is not important for the general theory. The Schrödinger equation describing the perturbed system is

$$\begin{pmatrix} H & V \\ V & H \end{pmatrix}\begin{pmatrix} a_\varphi|\varphi\rangle \\ \int b_\varepsilon|\varepsilon\rangle d\varepsilon \end{pmatrix} = E\begin{pmatrix} a_\varphi|\varphi\rangle \\ \int b_\varepsilon|\varepsilon\rangle d\varepsilon \end{pmatrix}, \tag{A.3}$$

which is equivalent to the pair of coupled equations

$$\begin{aligned} E_\varphi a_\varphi + \int V_{\varphi\varepsilon} b_\varepsilon d\varepsilon &= E a_\varphi \\ V_{\varepsilon\varphi} a_\varphi + \varepsilon b_\varepsilon &= b_\varepsilon E \end{aligned}. \tag{A.4}$$

Solving the bottom equation gives b_ε

$$b_\varepsilon = \frac{V_{\varepsilon\varphi} a_\varphi}{E-\varepsilon}. \tag{A.5}$$

b_ε approaches a singularity at $E = \varepsilon$, and so to avoid infinities when integrating, a new function is defined where

$$b_\varepsilon = V_{\varepsilon\varphi} a_\varphi \left(\frac{1}{E-\varepsilon} + Z(E)\delta(E-\varepsilon) \right). \tag{A.6}$$

Any integral involving b_ε takes the principle part of $(E-\varepsilon)^{-1}$ and the function $Z(E)$ is defined by the problem being considered [87]. Substituting b_ε back into the first of the paired equations (A.4) gives

$$a_\varphi E_\varphi + P\left\{ \int \frac{V_{\varepsilon\varphi} a_\varphi V_{\varphi\varepsilon}}{E-\varepsilon} d\varepsilon \right\} + Z(E) a_\varphi V_{\varepsilon\varphi} V_{\varphi\varepsilon} \delta(E-\varepsilon) = E, \tag{A.7}$$

where P means 'take the principal part of' the integral over $(E-\varepsilon)^{-1}$. H is Hermitian and so $V_{\varepsilon\varphi} = V_{\varepsilon\varphi}^*$. It is possible to drop the φ subscript as only one discrete state is being considered therefore $V_{\varepsilon\varphi} V_{\varphi\varepsilon} \equiv |V_\varepsilon|^2$. Also, considering that $f(a)\delta(b-a) = f(b)$ [113] equation A.7 can be written

$$a_\phi E_\phi + P\left\{ \int \frac{|V_\varepsilon|^2 a_\phi}{E-\varepsilon} d\varepsilon \right\} + a_\phi Z(E) |V_E|^2 = E a_\phi. \tag{A.8}$$

For simplicity, a new function is defined containing the principle part integration

$$F(E) = P\left\{\int \frac{\left|V_{\varepsilon\varphi}\right|^2}{E-\varepsilon} d\varepsilon\right\}. \tag{A.9}$$

a_φ factors out and $Z(E)$ can be written as

$$Z(E) = \frac{E - E_\varphi - F(E)}{\left|V_E\right|^2}. \tag{A.10}$$

To find a_φ the wave function of the hybrid state must be normalised

$$\left\langle \widetilde{E} \middle| E \right\rangle = a_\varphi^*(\widetilde{E}) a_\varphi(E) + \int b_\varepsilon^*(\widetilde{E}) b_\varepsilon(E) d\varepsilon = \delta(\widetilde{E} - E). \tag{A.11}$$

Substituting in the value of b_ε from A.6 gives

$$a_\varphi^*(\widetilde{E}) a_\varphi(E) + \int V_\varepsilon^* a_\varphi^*(\widetilde{E}) \left\{\frac{1}{\widetilde{E}-\varepsilon} + Z(\widetilde{E})\delta(\widetilde{E}-\varepsilon)\right\} V_\varepsilon a_\varphi(E) \left\{\frac{1}{E-\varepsilon} + Z(E)\delta(E-\varepsilon)\right\} d\varepsilon = \delta(\widetilde{E} - E) \tag{A.12}$$

Integrating $(\widetilde{E}-\varepsilon)^{-1}(E-\varepsilon)^{-1}$ over ε leads to a double singularity at the point $E = \widetilde{E}$; however it can be resolved into partial fractions plus a singular term (as shown in Appendix A of reference [26]).

$$[(\widetilde{E}-\varepsilon)(E-\varepsilon)]^{-1} = (\widetilde{E}-\varepsilon)^{-1}\left((\widetilde{E}-\varepsilon)^{-1} - (E-\varepsilon)^{-1}\right) + \pi^2 \delta(\widetilde{E}-E)\delta[\varepsilon - (\widetilde{E}+E)/2]. \tag{A.13}$$

Expanding out bracket in A.12 and substituting in A.13 gives

$$a_\phi^*(\widetilde{E}) a_\phi(E)\left[1 + \int d\varepsilon \left|V_\varepsilon\right|^2 \left\{\left(\frac{1}{\widetilde{E}-E}\right)\left(\frac{1}{E-\varepsilon} - \frac{1}{\widetilde{E}-\varepsilon}\right) + \pi^2 \delta(\widetilde{E}-E)\delta[\varepsilon - (\widetilde{E}+E)/2] + Z(\widetilde{E})Z(E)\delta(\widetilde{E}-\varepsilon)(E-\varepsilon) + \frac{Z(\widetilde{E})\delta(\widetilde{E}-\varepsilon)}{\widetilde{E}-E} + \frac{Z(E)\delta(E-\varepsilon)}{E-E}\right\}\right] = \delta(\widetilde{E}-E) \tag{A.14}$$

Equation A.14 can be further simplified to

$$|a(E)|^2 |V_E|^2 \left[\pi^2 + Z^2(E)\right]\delta(\widetilde{E} - E) +$$
$$a_\varphi^*(\widetilde{E}) a_\varphi(E)\left\{1 + \left(\frac{1}{\widetilde{E} - E}\right)\left(F(E) - F(\widetilde{E}) + Z(E)|V_E|^2 - Z(\widetilde{E})|V_{\widetilde{E}}|^2\right)\right\} = \delta(\widetilde{E} - E) \tag{A.15}$$

where

$$F(E) = P\left\{\int \frac{|V_\varepsilon|^2}{E - \varepsilon} d\varepsilon\right\}. \tag{A.16}$$

Finally, considering equation A.10 allows the terms in the curly bracket to cancel and A.15 can be further simplified to

$$\begin{aligned} |a(E)|^2 &= \frac{1}{|V_E|^2\left[\pi^2 + Z^2(E)\right]} \\ &= \frac{|V_E|^2}{\pi^2 |V_E|^4 + \left[E - E_\varphi - F(E)\right]} \end{aligned} . \tag{A.17}$$

Therefore, A.16 shows that the discrete state E_φ is diluted by the configuration interaction throughout a continuous band of stationary states that can be represented by a resonance curve with a half width given by A.18 and symmetrical about a mean position E_0 as given in A.19

$$\Gamma/2 \equiv \pi|V_\varepsilon|^2 , \tag{A.18}$$

$$E_0 = E_\varphi + F(E) . \tag{A.19}$$

Substituting A.18 and A.19 into A.17 reveals that this resonance curve has a Lorentzian shape as a function of energy E (as given in equation 1.6.2)

$$|a(E)|^2 = \frac{1}{\pi}\frac{\Gamma/2}{(\Gamma/2)^2 + \left[E - E_0\right]} . \tag{A.20}$$

In an experimentally recorded predissociation spectrum, the observable is the transition to an energy level, rather than the level itself. Therefore, the ratio of the

transitions to the mixed state, E, and continuum, ε, must be considered from the same initial state, i, with a transition strength governed by the dipole operator D.

$$R = \frac{\left|\langle E|D|i\rangle\right|^2}{\left|\langle \varepsilon|D|i\rangle\right|^2}. \tag{A.21}$$

Substituting in the expanded equation for E introduced previously (equation A.2) gives

$$R = \frac{\left|a_\varphi \langle \varphi|D|i\rangle + \int b_\varepsilon \langle \varepsilon|D|i\rangle d\varepsilon\right|^2}{\left|\langle \varepsilon|D|i\rangle\right|^2}. \tag{A.22}$$

Substituting in b_ε as previously defined in equation A.6 give

$$R = \frac{\left|a_\varphi\right|^2}{\left|\langle \varepsilon|D|i\rangle\right|^2}\left|\langle \varphi|D|i\rangle + P\left\{\int \frac{V_\varepsilon \langle \varepsilon|D|i\rangle}{E-\varepsilon} d\varepsilon\right\} + V_\varepsilon Z(\varepsilon)\langle \varepsilon|D|i\rangle\right|^2. \tag{A.23}$$

A new shifted state is defined as

$$|\Phi\rangle = |\varphi\rangle + P\left\{\int \frac{V_\varepsilon \langle \varepsilon|D|i\rangle}{E-\varepsilon} d\varepsilon\right\}. \tag{A.24}$$

This allows a simplified form of A.23 to be written.

$$R = \left|a_\varphi\right|^2 \left|\frac{\langle \Phi|D|i\rangle}{\langle \varepsilon|D|i\rangle} + V_\varepsilon Z(\varepsilon)\right|^2. \tag{A.25}$$

Combining the definition of E_0 as given by A.19 with A.10 gives a term describing the detuning from resonance

$$Z(E) = \frac{E - E_0}{\left|V_E\right|^2}. \tag{A.26}$$

Substiutuing A.18 gives

$$Z(E) = \frac{2\pi(E - E_0)}{\Gamma} = \chi \,. \tag{A.27}$$

The Fano shape parameter, q, is now defined as

$$q = \frac{\langle \Phi | D | i \rangle}{\pi V_\varepsilon \langle \varepsilon | D | i \rangle} \,. \tag{A.28}$$

Finally, using A.27 and A.28, equation A.20 and A.21 can now be rewritten

$$|a(E)|^2 = \frac{1}{\pi^2 |V_\varepsilon|^2 (\chi^2 + 1)}, \tag{A.29}$$

$$R = |a_\varphi|^2 |q\pi V_\varepsilon + V_\varepsilon \chi|^2 \,. \tag{A.30}$$

Substituting A.29 into A.30 leads to the familiar Fano line shape formula, A.31 expressed in terms of q and χ. It can also be expressed in terms of the half width $\Gamma/2$ and detuning, $E - E_0$.

$$\begin{aligned} R &= \frac{1}{\pi^2 |V_\varepsilon|^2 (\chi^2 + 1)} |q\pi V_\varepsilon + V_\varepsilon \chi \pi|^2 \\ &= \frac{(q + \chi)^2}{(\chi^2 + 1)} \\ &= \frac{(q(\Gamma/2) + (E - E_0))^2}{(E - E_0)^2 + (\Gamma/2)^2} \end{aligned} \tag{A.31}$$

8. References

1. J.J. Balmer, *Annalen der Physik und Chemie*, 1885. **N.F. 25**: p. 80.
2. J.R. Rydberg, *Philosophical Magazine*, 1890. **29**: p. 331.
3. J.J. Thompson, *Philosophical Magazine*, 1897. **44**: p. 293.
4. E. Rutherford, *Philosophical Magazine*, 1911. **21**: p. 669.
5. H. Geiger and E. Marsden, *Proceedings of the Royal Society of London. Series A, Containing Papers of a Mathematical and Physical Character (1905-1934)*, 1909. **82**(557): p. 495-500.
6. N. Bohr, *Philosophical Magazine*, 1913. **26**: p. 1.
7. P.M.W. French, *Reports On Progress In Physics*, 1995. **58**(2): p. 169-262.
8. E. Schrödinger, *Naturwissenschaften*, 1926. **28**: p. 664
9. A. ten Wolde, L.D. Noordam, A. Lagendijk and H.B. van Linden van den Heuvell, *Physical Review Letters*, 1988. **61**(18): p. 2099.
10. V.G. Stavros and H.H. Fielding, *Physical Review A (Atomic, Molecular, and Optical Physics)*, 1999. **60**(6): p. 4774.
11. V.G. Stavros, J.A. Ramswell, R.A.L. Smith, J.R.R. Verlet, J. Lei and H.H. Fielding, *Physical Review Letters*, 1999. **83**(13): p. 2552-2555.
12. M.W. Noel and C.R. Stroud, *Physical Review Letters*, 1995. **75**(7): p. 1252-1255.
13. H. Wen, C. Rangan and P.H. Bucksbaum, *Physical Review A*, 2003. **68**(5).
14. R. van Leeuwen, K. Vijayalakshmi and R.R. Jones, *Physical Review A*, 2001. **6303**(3).
15. M.L. Bajema, R.R. Jones and T.F. Gallagher, *Physical Review A*, 2004. **70**(6).
16. R.E. Carley, E.D. Boleat, R.S. Minns, R. Patel and H.H. Fielding, *Journal Of Physics B-Atomic Molecular And Optical Physics*, 2005. **38**(12): p. 1907-1922.
17. J.R.R. Verlet, V.G. Stavros, R.S. Minns and H.H. Fielding, *Physical Review Letters*, 2002. **89**(26).
18. J.R.R. Verlet, V.G. Stavros, R.S. Minns and H.H. Fielding, *Journal Of Physics B-Atomic Molecular And Optical Physics*, 2003. **36**(17): p. 3683-3696.
19. R.S. Minns, R. Patel, J.R.R. Verlet and H.H. Fielding, *Physical Review Letters*, 2003. **91**(24): p. 243601.
20. R.S. Minns, J.R.R. Verlet, L.J. Watkins and H.H. Fielding, *Journal Of Chemical Physics*, 2003. **119**(12): p. 5842-5847.
21. A. Fowler, *Proceedings of the Royal Society of London. Series A, Containing Papers of a Mathematical and Physical Character (1905-1934)*, 1915. **91**(627): p. 208.
22. W.C. Price, *Physical Review*, 1935. **47**(6): p. 444.
23. H. Kato and M. Baba, *Chemical Reviews*, 1995. **95**(7): p. 2311-2349.
24. M.J.J. Vrakking, *The Journal of Chemical Physics*, 1996. **105**(17): p. 7336.

25. A.L. Goodgame, H. Dickinson, S.R. Mackenzie and T.P. Softley, *The Journal of Chemical Physics*, 2002. **116**(12): p. 4922-4937.
26. U. Fano, *Physical Review*, 1961. **124**(6): p. 1866.
27. J. Stark, *Berl. Akad. Wiss*, 1913. **40**: p. 932
28. P.S. Epstein, *Annalen der Physik*, 1916. **50**: p. 489.
29. K. Schwarzschild, *Sitzungsberichte der Koniglich Preussischen Akademie der Wissenschaften*, 1916: p. 548.
30. T.F. Gallagher. 1994, Cambridge: University Press.
31. S.R. Mackenzie, E.J. Halse, E. Gordon, D. Rolland and T.P. Softley, *Chemical Physics*, 1996. **209**(2-3): p. 127-141.
32. R. Patel, N.J.A. Jones and H.H. Fielding, *Journal Of Physics B-Atomic Molecular And Optical Physics*, 2007. **40**(7): p. 1369-1381.
33. M.J.J. Vrakking and Y.T. Lee, *Journal Of Chemical Physics*, 1995. **102**(22): p. 8818-8832.
34. J.H. Hoogenraad, R.B. Vrijen and L.D. Noordam, *Physical Review A*, 1998. **57**(6): p. 4546-4552.
35. S.N. Pisharody and R.R. Jones, *Physical Review A*, 2002. **65**(3): p. 033418.
36. T.C. Weinacht, J. Ahn and P.H. Bucksbaum, *Physical Review Letters*, 1998. **80**(25): p. 5508-5511.
37. E. Miescher, *Journal Of Quantitative Spectroscopy & Radiative Transfer*, 1962. **2**(4): p. 421-425.
38. E. Miescher, *Journal Of Molecular Spectroscopy*, 1978. **69**(2): p. 281-293.
39. E. Miescher, *Canadian Journal Of Physics*, 1976. **54**(20): p. 2074-2092.
40. E. Miescher, *Journal Of Molecular Spectroscopy*, 1974. **53**(2): p. 302-310.
41. E. Miescher, *Canadian Journal Of Physics*, 1971. **49**(18): p. 2350-&.
42. E. Miescher, *Journal Of Molecular Spectroscopy*, 1966. **20**(2): p. 130-&.
43. K.P. Huber, M. Huber and E. Miescher, *Physics Letters*, 1963. **3**(7): p. 315-316.
44. K. Dressler and E. Miescher, *Astrophysical Journal*, 1965. **141**(3): p. 1266-&.
45. E. Miescher and F. Alberti, *Journal of Physical and Chemical Reference Data*, 1976. **5**(2): p. 309.
46. S.T. Pratt, J.L. Dehmer and P.M. Dehmer, *The Journal of Chemical Physics*, 1989. **90**(4): p. 2201-2212.
47. D.T. Biernacki, S.D. Colson and E.E. Eyler, *Journal Of Chemical Physics*, 1988. **88**(4): p. 2099-2107.
48. Y. Anezaki, T. Ebata, N. Mikami and M. Ito, *Chemical Physics*, 1984. **89**(1): p. 103.
49. M. Seaver, W.A. Chupka, S.D. Colson and D. Gauyacq, *Journal Of Physical Chemistry*, 1983. **87**(12): p. 2226-2231.
50. J.W.J. Verschuur, J. Kimman, H.B. Van Linden Van Den Heuvell and M.J. Van Der Wiel, *Chemical Physics*, 1986. **103**(2-3): p. 359.
51. H. Park and R.N. Zare, *Journal Of Chemical Physics*, 1997. **106**(6): p. 2239-2247.
52. T. Ebata, Y. Anezaki, M. Fujii, N. Mikami and M. Ito, *Journal Of Physical Chemistry*, 1983. **87**(24): p. 4773-4776.
53. D. Gauyacq, A.L. Roche, M. Seaver, S.D. Colson and W.A. Chupka, *Molecular Physics*, 1990. **71**(6): p. 1311-1331.
54. J. Geng, T. Kobayashi and M. Takami, *Chemical Physics Letters*, 1997. **266**(3-4): p. 290.

55. E.F. McCormack, F. Di Teodoro, J.M. Grochocinski and S.T. Pratt, *Journal Of Chemical Physics*, 1998. **109**(1): p. 63-71.
56. F. Remacle and M.J.J. Vrakking, *Journal Of Physical Chemistry A*, 1998. **102**(47): p. 9507-9517.
57. M. Bixon and J. Joshua, *The Journal of Chemical Physics*, 1996. **105**(4): p. 1363-1382.
58. I. Rabadan and J. Tennyson, *Journal Of Physics B-Atomic Molecular And Optical Physics*, 1996. **29**(16): p. 3747-3761.
59. M. Raoult, *Journal Of Chemical Physics*, 1987. **87**(8): p. 4736-4761.
60. A. Giustisuzor and C. Jungen, *Journal Of Chemical Physics*, 1984. **80**(3): p. 986-1000.
61. A. Giusti-Suzor and J. Ch, *The Journal of Chemical Physics*, 1984. **80**(3): p. 986-1000.
62. C. Jungen, *Journal Of Chemical Physics*, 1970. **53**(11): p. 4168-&.
63. K.P. Huber and G. Herzberg. Molecular Spectra and Molecular Structure. Vol. IV. 1979, New York: Van Nostrand Reinhold Company.
64. D.B. Keck and C.D. Hause, *Journal Of Molecular Spectroscopy*, 1968. **26**(2): p. 163-&.
65. G. Herzberg, Second ed. Molecular Spectra and Molecular Structure, ed. G. Herzberg. Vol. I. 1957, London: D. Van Nostrand Company
66. G. Herzberg and K.P. Huber, ed. G. Herzberg. 1979, London: D. Van Nostrand Company
67. M. Elena, J.D.D. Martin and T.F. Gallagher, *The Journal of Chemical Physics*, 2001. **115**(15): p. 7032-7040.
68. R.A.L. Smith, J.R.R. Verlet, E.D. Boleat, V.G. Stavros and H.H. Fielding, *Faraday Discussions*, 2000(115): p. 63-70.
69. K. Kaufmann, C. Nager and M. Jungen, *Chemical Physics*, 1985. **95**(3): p. 385-390.
70. S.N. Dixit, D.L. Lynch, V. McKoy and W.M. Huo, *Physical Review A*, 1985. **32**(2): p. 1267.
71. S.T. Pratt, C. Jungen and E. Miescher, *Journal Of Chemical Physics*, 1989. **90**(11): p. 5971-5981.
72. G.E. Gadd, L.E. Jusinski and T.G. Slanger, *The Journal of Chemical Physics*, 1989. **91**(6): p. 3378-3383.
73. A. Fujii and N. Morita, *Journal Of Chemical Physics*, 1992. **97**(1): p. 327-334.
74. A. Fujii and N. Morita, *Laser Chemistry*, 1994. **13**(3-4): p. 259-271.
75. A. Fujii and N. Morita, *Journal Of Chemical Physics*, 1993. **98**(6): p. 4581-4585.
76. A. Fujii and N. Morita, *Laser Techniques For State-Selected And State-To-State Chemistry*, 1993. **1858**: p. 184-195.
77. A. Fujii and N. Morita, *Chemical Physics Letters*, 1991. **182**(3-4): p. 304-309.
78. D. Laura, J.P. Yan and J.v.d.Z. Wim, *The Journal of Chemical Physics*, 2004. **121**(7): p. 3058-3068.
79. K. Qin, M. Bistransin and W.L. Glab, *Physical Review A*, 1993. **47**(5): p. 4154-4159.
80. B.B. Clarson, S.R. Procter, A.L. Goodgame and T.P. Softley, *Molecular Physics*, 2008. **106**(9): p. 1317 - 1330.
81. S.J. Brownbill and T.P. Softley, *Molecular Physics*, 2005. **103**: p. 2347.
82. T.P. Softley, A.J. Hudson and R. Watson, *The Journal of Chemical Physics*, 1997. **106**(3): p. 1041-1056.

83. M. Grutter, O. Zehnder, T.P. Softley and F. Merkt, *Journal of Physics B: Atomic, Molecular and Optical Physics*, 2008. **41**(11): p. 115001.
84. S. Fredin, D. Gauyacq, M. Horani, C. Jungen, G. Lefevre and F. Masnouseeuws, *Molecular Physics*, 1987. **60**(4): p. 825-866.
85. R.N. Zare. 1988, New York: Wiley. 0471858927
86. A.R. Edmonds, R. Pullen, J. Picart and N.T. Minh, *Journal of Physics B: Atomic and Molecular Physics*, 1979. **12**(17): p. 2781.
87. J.-P. Connerade. 1998, Cambridge: University Press.
88. K. Ueda, *Physical Review A*, 1987. **35**(6): p. 2484.
89. B.W. Shore, *J. Opt. Soc. Am.*, 1967. **57**(7): p. 881.
90. T.K. Fang and T.N. Chang, *Physical Review A*, 1998. **57**(6): p. 4407.
91. X.J. Liu, Y.P. Huang, L.F. Zhu, Z.S. Yuan, W.B. Li and K.Z. Xu, *Nucl. Instrum. Methods Phys. Res. Sect. A-Accel. Spectrom. Dect. Assoc. Equip.*, 2003. **508**(3): p. 448-453.
92. B.W. Shore, *Physical Review*, 1968. **171**(1): p. 43.
93. M. Gatzke, J.R. Veale, W.R. Swindell and T.F. Gallagher, *Physical Review A*, 1996. **54**(3): p. 2492-2495.
94. M.L. Zimmerman, M.G. Littman, M.M. Kash and D. Kleppner, *Physical Review A*, 1979. **20**(6): p. 2251.
95. Y. Kishimoto, M. Tada, K. Kominato, M. Shibata, S. Yamada, T. Haseyama, I. Ogawa, H. Funahashi, K. Yamamoto and S. Matsuki, *Physics Letters A*, 2002. **303**(4): p. 279-284.
96. J.H.M. Neijzen and A. Donszelmann, *Journal Of Physics B-Atomic Molecular And Optical Physics*, 1982. **15**(13): p. 1981-2000.
97. J.L. Vialle and H.T. Duong, *Journal Of Physics B-Atomic Molecular And Optical Physics*, 1979. **12**(8): p. 1407-1423.
98. J. Han and T.F. Gallagher, *Physical Review A*, 2008. **77**(1).
99. T.F. Gallagher, L.M. Humphrey, W.E. Cooke, R.M. Hill and S.A. Edelstein, *Physical Review A*, 1977. **16**(3): p. 1098.
100. T.H. Jeys, G.W. Foltz, K.A. Smith, E.J. Beiting, F.G. Kellert, F.B. Dunning and R.F. Stebbings, *Physical Review Letters*, 1980. **44**(6): p. 390-393.
101. F. Robicheaux, C. Wesdorp and L.D. Noordam, *Physical Review A*, 2000. **62**(4): p. 043404.
102. H.J. Dietrich, K. MullerDethlefs and L.Y. Baranov, *Physical Review Letters*, 1996. **76**(19): p. 3530-3533.
103. U. Hollenstein, R. Seiler, H. Schmutz, M. Andrist and F. Merkt, *Journal Of Chemical Physics*, 2001. **115**(12): p. 5461-5469.
104. A. Gurtler and W.J. van der Zande, *Physics Letters A*, 2004. **324**(4): p. 315-320.
105. R.C. Shiell, E. Reinhold, F. Magnus and W. Ubachs, *Physical Review Letters*, 2005. **95**(21).
106. M. Tada, Y. Kishimoto, M. Shibata, K. Kominato, S. Yamada, T. Haseyama, I. Ogawa, H. Funahashi, K. Yamamoto and S. Matsuki, *Physics Letters A*, 2002. **303**(4): p. 285-291.
107. W.R. Gentry and F.G. Clayton, *Review of Scientific Instruments*, 1975. **46**(1): p. 104.
108. R. Patel, N.J.A. Jones and H.H. Fielding, *Physical Review A*, 2007. **76**(4).
109. H.W. Ott, Second ed. 1988, New York: John Wiley & Sons Ltd.
110. P.A. Chatterson and M.A. Houlden, First ed. 1992, Chichester: John Wiley & Sons Ltd.

111. A.D. Appelhans and D.A. Dahl. *Ion Optics Through the Eyes of SIMION 6.0*. 1996 [cited; Available from: http://www.simion.com/docs/class-handout.pdf.
112. S. Butterworth, *Wireless Engineer*, 1930. **7**: p. 536-541.
113. P.A.M. Dirac, 4th ed. 1981, Oxford: Oxford University Press.